Fluid and deformation induced partial melting and melt escape in low-temperature granulite-facies metasediments, Damara Belt, Namibia.

Robert Alexander Ward

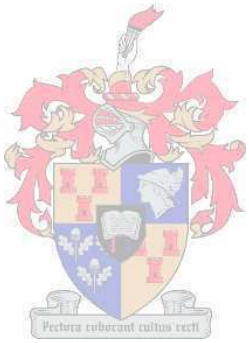

Dissertation presented for the degree of Doctor of Philosophy at Stellenbosch University

With promoters: **Professor Gary Stevens and Professor Alex Kisters**

March 2009

Declaration

By submitting this dissertation electronically, I declare that the entirety of the work contained therein is my own, original work, that I am the owner of the copyright thereof (unless to the extent explicitly otherwise stated) and that I have not previously in its entirety or in part submitted it for obtaining any qualification.

Signature: . . . . . Date: . . . . . .

Abstract

Fluid-present partial melting has generally been regarded a poor candidate for effecting crustal differentiation. In this study I report on anatectic metasediments from the Pan-African Damara Belt in Namibia that have undergone fluid-present biotite melting at a relatively low temperature, yet appear to have lost a significant volume of melt. *In situ* anatectic features have been identified on the basis of the existence of new generations of cordierite and/or garnet produced as the solid products of incongruent anatexis within or adjacent to leucosomes, that most commonly occur as lens shaped pods at a high angle to the lineation and formed during extension in a direction parallel to the long axis of the orogeny. Within these sites biotite underwent incongruent melting via the reaction Bt + Qtz + Pl + H_2O = Melt + Grt + Crd. Cordierite nucleated on pre-existing crystals within the bounding gneiss; garnet nucleated within the fracture sites (leucosomes) and typically occurs as individual, large (50 to 120 mm in diameter) poikiloblastic crystals. Thermobarometry applied to the anatectic assemblage yields low-temperature, granulite-facies peak conditions of 750 °C, 0.5 GPa. This temperature is approximately 100 °C lower than the accepted conditions for the onset of fluid-absent biotite melting. This, coupled to the focussing of anatexis on extensional fractures, suggests that anatexis occurred through water-present biotite incongruent melting. In order to better understand this process, both fluid-absent and water present partial melting experiments were conducted within the temperature interval 700 to 900 °C at 0.7 GPa. In the fluid-absent experiments, biotite incongruent melting started between 800 and 850 °C to produce melt coexisting with peritectic garnet and cordierite. In contrast, in water-saturated experiments, biotite melted via the reaction Bt + Pl + Q + H_2O = Grt + Crd + Melt, between 700 and 750 °C, to produce melt, cordierite and garnet in the proportions 73:24:3. The garnet compositions produced in these low temperature experiments matches very well with the relatively high spessartine content (10 %), low Mg# garnets formed with the leucosomes, consistent with the water-saturated, low temperature nature of anatexis in the study area. In general, the melting focused on individual fracture sites has produced 6 dm^3 of melt in conjunction with 0.25 dm^3 of garnet. This melt has been sourced from some 0.08 m^3 of rock, a volume that coincides well with the typical frequency of extensional fracture spacing. This was probably important in enabling efficient melt extraction which has caused a slight shift towards more refractory compositions in the granulites over amphibolite-facies equivalents. Extraction of melt from the leucosomes hosted in extensional fractures was possible due to hydraulic gradients created by upwardly migrating sills whose orientation was controlled by the pre-existing anisotropy in the host metasediments.

Uittreksel

Fluïde-teenwoordige gedeeltelike smelting is in die verlede oor die algemeen gesien as ‘n swak kandidaat vir die bewerkstelliging van kors differensiasie. Hierdie studie handel oor anatektiese metasedimente van die Pan-Afrika Damara Gordel in Namibië, wat, hoewel dit fluïde-teenwoordige biotiet smelting ondergaan het by ’n relatiewe lae temperatuur, dit tog blyk of die gesteentes ’n beduidende volume smelt verloor het. In-situ anatektiese eienskappe is geïdentifiseer op grond van die teenwoordigheid van nuwe generasies van kordiëriet en/of granaat wat gevorm het as die soliede produkte van inkongruente anatekse binne of naby aan leukosome, wat gewoonlik voorkom as lensvormige peule teen ’n hoë hoek met die lineasie en wat gevorm het gedurende ekstensie in ’n rigting parallel aan die lang as van die orogenie. Biotiet het binne hierdie gebiede inkongruente smelting ondergaan deur middel van die reaksie Bt + Qtz + Pl + H_2O = Smelt + Grt + Crd. Kordiëriet het op voorafbestaande kristalle binne die omringende gneis om ’n kern saamgetrek; granaat het binne die breuk-gebiede (leukosome) om ’n kern saamgetrek, en kom gewoonlik voor as individuele, groot (5 0 tot 120 mm) poikiloblastiese kristalle. Termobarometrie soos toegepas op die anatektiese versameling gee resultate wat lae temperatuur, granuliet fasies maksiumum kondisies van 750 °C, 0.5 GPa aandui. Hierdie temperatuur is ongeveer 100 °C laer as die aanvaarde kondisies vir die begin van fluïde-afwesige biotiet smelting. Gepaardgaande met die fokusering van anatekse op ekstensionele breuke, dui dit daarop dat anatekse plaasgevind het deur water-teenwoordige biotiet inkongruente smelting. Beide fluïde-afwesige en water-teenwoordige gedeeltelike smeltingseksperimente is uitgevoer binne die temperatuur interval 700 tot 900°C by 0.7 Gpa, om hierdie proses beter te verstaan. In die fluïde-afwesige eksperimente, het biotiet inkongruente smelting begin tussen 800 and 850 °C om smelt te produseer wat gelyktydig bestaan saam met peritektiese granaat en kordiëriet. In kontras hiermee, het biotiet in die water-versadigde eksperimente gesmelt deur middel van die reaksie Bt + Pl + Q + H_2O = Grt + Crd + Smelt tussen 700 and 750 °C om smelt, kordiëriet en granaat in die verhoudings 73:24:3 te vorm. Die granaat samestellings wat in hierdie lae temperatuur eksperimente verkry is, korreleer baie goed met die relatiewe hoë spessartien inhoud (10%), lae Mg# granate wat gevorm het in die leukosome, en dit bevestig die water-versadigde, lae temperatuur aard van die anatekse in die studiegebied. Oor die algemeen het die smelting wat gefokus het op individuele breuk-areas, 6 dm^3 smelt opgelewer tesame met 0.25 dm^3 granaat. Hierdie smelt het sy oorsprong uit ongeveer 0.08 m^3 rots, ‘n volume wat goed saamval met die tipiese frekwensie van ekstensionele breuk spasiëring. Dit was waarskynlik belangrik vir die voorkoms van genoegsame smelt ekstraksie wat ’n effense skuiwing na meer refraktiese samestellings in die granuliete oor amfiboliet fasies ekwivalente teweeggebring het. Ekstraksie van smelt uit die leukosome wat voorkom in ekstensionele breuke was moontlik as gevolg van hidroliese gradiënte wat gevorm het deur opwaarts-migrerende plate waarvan die oriëntasie beheer is deur die voorafbestaande anisotropie in die gasheer-metasedimente.

Table of Contents

List of Figures

List of Tables

1. Introduction

1.1 Our current understanding of granite genesis

Granitoid rocks are the dominant constituent of the Earth's continental crust, having formed the nuclei to the oldest cratonic fragments (Anhaeusser, 1973) and having been produced and continually recycled through successive episodes of intrusion, erosion, metamorphism and melting mainly at active continental margins (Kusky & Polat, 1999). Consequently, an understanding of all aspects of granitoid petrogenesis is essential to understanding the formation and evolution of the planet's continental crust. The movement of granitoid magma through the crust is a very important mechanism of mass transfer, moving vast amounts of material of a fairly specific chemistry together with heat from the deeper-level source into the mid- to upper crust. This process enriches the upper part of the crust with elements compatible within granitic magma, leaving deeper parts depleted, more refractory and more thermally stable (granulites). This is probably an important process in craton stabilisation.

What are the conditions required to produce mobile granitoid magmas, apart from obviously exceeding the solidus temperature of the source? Some studies have proposed that very high temperatures, allowing for complete breakdown of biotite and/or hornblende via fluid-absent melting reactions, are necessary for generating mobile batches of magma (Figure 1.1).

However, the refractory products of such high temperature anatectic events (very refractory aluminous granulites) are rare in the rock record and the temperatures required (> 900 °C) cannot readily be attained in thickened crust without major addition of mantle heat (Chapman, 1986, Warren & Ellis, 1996, Vigneresse, 2004). Despite this, granite plutons that are far removed from their source rocks are known from orogens where only crustal sources of heat appear to be involved (such as the Damara Orogen, Namibia and the Himalayas). This suggests that melts developed during relatively low temperature

anatexis do mobilise efficiently. The mechanisms of melt segregation and ascent must be highly efficient, but remain poorly understood.

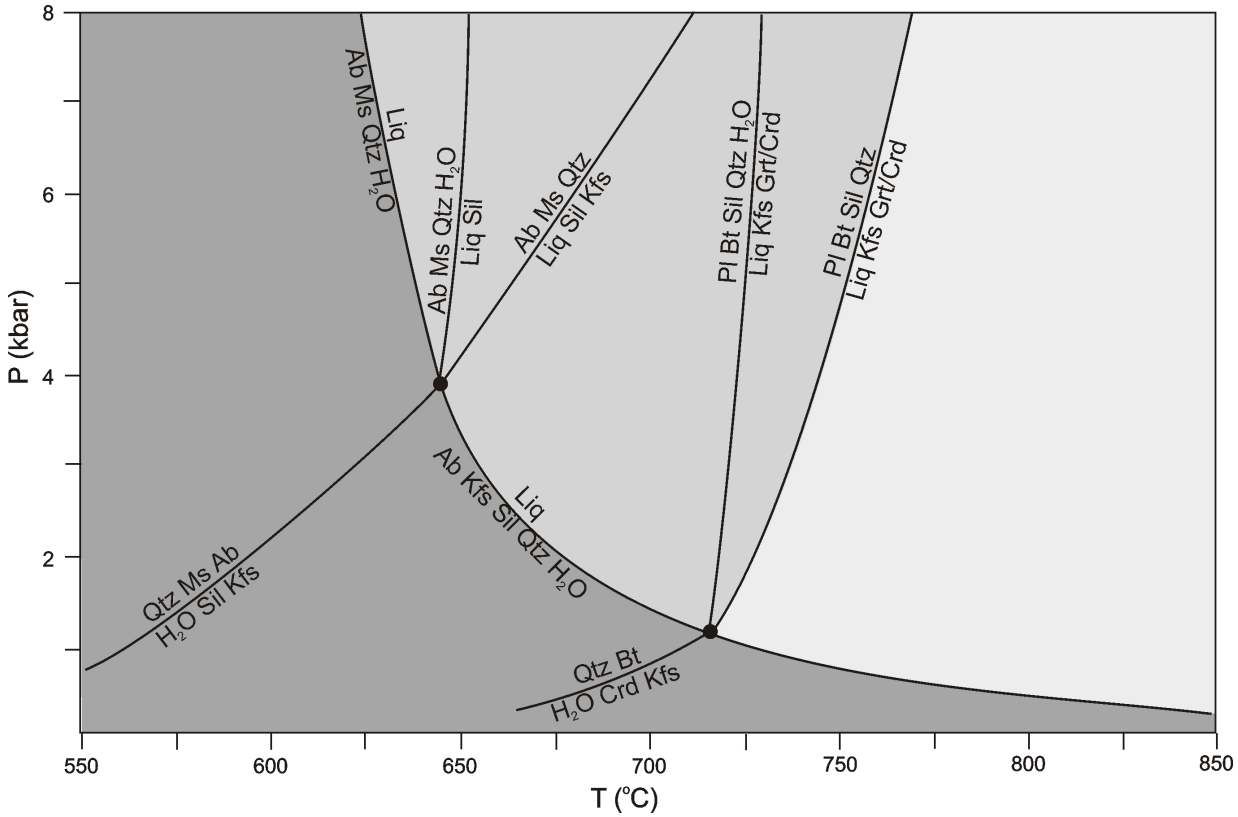

Figure 1.1. P-T diagram indicating the position of melting reactions relevant to metapelitic rocks (after Spicer et al. (2004)). In essence the intersection of the subsolidus dehydration reactions with the wet granite solidus in quartz-bearing rocks spawn two possible incongruent melting reactions; one fluid-present at lower temperature, and a higher temperature fluid-absent reaction (Clemens and Watkins, 2001). The (lightest grey shading) field at high temperature is the pressure-temperature realm commonly proposed as the source of granitoid magmas. Lower temperature melting, by fluid present biotite breakdown, muscovite melting and melting at the wet granite solidus (medium grey shading) is typically regarded as being important only as reactions that absorb water, making the system fluid absent and allowing for the occurrence of the higher-temperature fluid-absent processes.

The production of a large granite body from the partial melting of a suitable source rock requires the focussing of melt from small, inter-grain pockets, via progressively larger melt bodies and melt conduits to the final emplacement site of a pluton, commonly assembled from multiple batches of magma (Brown, 2007 and references therein). Traditionally, the removal of small quantities of melt from a partially melted host-rock was thought to be problematic, since large-scale melt transport was believed to occur

only after a threshold melt percentage was reached (the Rheological Critical Melt Percentage of Arzi (1978)). However, more recent studies have emphasised that melt segregation is greatly enhanced by the presence of deviatoric stress during deformation, not only providing hydraulic gradients that drive melt flow, but also permeabilities in the otherwise largely impermeable high-grade rocks (Sawyer, 1994; Vigneresse et al., 1996, Brown & Rushmer, 1997). For this reason, the leucosomes of migmatitic terrains are often observed to reside in specific structural sites, such as foliation-parallel veins, shear bands and shear zones, or boudin necks and/or fold-hinges (Hand & Dirks, 1992, Davidson et al., 1994, Brown & Solar, 1998, Kisters et al., 1998, Vanderhaeghe, 1999). Furthermore, fluid-absent melting reactions induce a positive change in volume in the source which favours fracturing and dyking for the ascent of the buoyant melts (Brown & Solar, 1999, Weinberg, 1999, Bons et al., 2001, Brown, 2004). Hydraulic gradients and permeabilities formed during deformation can potentially tap even low melt fractions, possibly explaining small-scale isotopic and geochemical variations in some granites that appear to indicate inheritance of source rock heterogeneity (Brown, 1994, Clemens, 2003 and references therein, Brown, 2007).

However, the link between the formation of melt segregation features and the rheology of partially molten rocks is still poorly understood. For this reason experimental investigations into the mechanical behaviour of partially melted rocks have been conducted. These include experimental deformation of small cores of natural rock (e.g. Rushmer, 1995, Rutter & Neumann, 1995, Rosenberg & Handy, 2005) which indicate a drop in strength with the development of melt-bearing shear bands as well as analogue modelling of deformation in suitable materials such as paraffin and wax (here the wax acts as the partially molten lithology) (e.g. Rosenberg & Handy, 2000, Barraud et al., 2001, Barraud et al., 2004). What is less well constrained is the possible feedback that exists between deformation and partial melting, or the influence of deformation on the initiation of partial melting in structural sites that host the magmas of partially molten rocks.

The range of temperatures required for partial melting of metasedimentary rocks and the generation of granitic magma overlap with those of granulite-facies metamorphism. Furthermore, the similarities of granulite-facies mineral assemblages and the peritectic products of partial melting reactions are no coincidence and many granulites have an anatectic history and have lost melt (e.g. Fyfe, 1973, Clemens, 1990, Thompson, 1990, Clemens & Watkins, 2001). This can be readily observed in granulite-facies migmatites which demonstrate the link between developing granulite-facies metamorphic assemblages and the generation, and segregation of water-undersaturated partial melts (e.g. Stevens & Van Reenen, 1992, Srogi et al., 1993). The solid products (residues) of melting (or lack thereof) are useful in identifying the nature of the melting reactions that have occurred in the rocks (Guernina & Sawyer, 2003). The presence of ferromagnesian phases such a garnet, cordierite or orthopyroxene commonly indicate the occurrence of incongruent biotite breakdown, whereas leucosomes not associated with such peritectic phases could be the result of a congruent melting reaction such as Qtz + Fsp + H_2O (Figure 1.1). The products of the melting reaction may help to identify the reactant minerals, but they are rarely able to identify the details of the melting reaction such as the fluid regime at the time of anatexis (Clemens & Watkins, 2001).

It may be possible to estimate the PT conditions of melting from the phases present in the sites of melting by using conventional geothermobarometry. This approach can indicate the temperatures of the reactions, which can then be compared to applicable thermodynamically modelled systems and experimental investigations. So, indirectly, such temperature estimates of the reactions may indicate whether they were fluid-present or fluid-absent. A problem with this approach for most studies of anatexis in crustal rocks is that the temperatures of melting are very high and that many of the minerals are open to diffusion at these conditions. Peak temperatures of granulite-facies rocks are often under-estimated as a result (e.g. the granulite-facies uncertainty principle of Frost & Chacko, 1989), recording only the retrograde path.

Partial melting to produce *mobile* granitoid magmas is commonly considered to occur via a fluid-absent incongruent melting process only (Brown, 1994, Clemens & Droop, 1998,

Brown, 2007). However, the substantial temperature interval that exists between the onset of fluid-absent incongruent melting equilibria and the water saturated solidus in metapelitic and metapsammitic rocks, creates the possibility that during upper amphibolite- and lower granulite-facies metamorphism, such rocks may melt via these fluid-present reactions if a fluid can become available. Indeed, models for the formation of granulite-facies assemblages by processes other than carbonic fluid fluxing, commonly involve some fluid-present melting at temperatures close to the wet granite solidus to absorb the water-rich, grain boundary fluid film that may be present from subsolidus dehydration reactions (e.g. Stevens et al., 1995). This process is generally not considered to yield any significant volume of melt due to the very low porosity of high grade metamorphic rocks.

The rocks of the Damara Orogen in Namibia provide a unique natural laboratory for the study of anatectic processes of relatively low-temperature mid-crustal levels. Along the Khan and Swakop rivers, an E-W section through the mid- to upper-crustal levels of the orogen exposes rocks that range from granulite-grade of metamorphism in the West to lower amphibolite-grades in the East. Aluminous metasediments of the Kuiseb Formation are exposed along much of the length of this section and metapelites from the higher grade domain have been considered as potentially important source rocks for the S-type granitic plutons that intrude the lower-grade metasediments (Jung, 2005). However, within the high-grade domain no rock units of significant volume have been reported that might readily represent the refractory residua left after the extraction of abundant S-type magma. More typically, reported anatectic features vary from widely spaced stromatic leucosomes (in the lowest grade anatectic rocks) (McDermott et al., 1996b, Jung & Mezger, 2001) to diatexic migmatites in the isolated exposures of the highest grade reported material from near the coast (Hartmann et al., 1983, Masberg et al., 1992). Additionally, reported metamorphic temperatures for the anatectic rocks range from 700 ºC to 820 ºC (Masberg, 2000, Jung & Mezger, 2003). These temperatures are generally below the beginning of the experimentally determined biotite fluid-absent melting (e.g. LeBreton & Thompson, 1988, Vielzeuf & Montel, 1994, Patiño Douce & Beard, 1995, Stevens et al., 1997, Buick et al., 2004).

1.2 Aims and methodology for the present study

Partial melting via biotite incongruent melting is intimately associated with distinct structural sites in the Kuiseb Formation metapelites of the Blauer Heinrich Syncline of the Damara Orogen, Namibia. Leucosomes with peritectic garnet are hosted in fracture arrays that relate to the stretching lineation of the main phase of deformation in the southern Central Zone of the Damara Belt and these features display evidence of significant melt loss. The production of mobile granitic magmas by biotite breakdown is believed to occur under fluid-absent conditions at high temperatures. The rocks of the Blauer Heinrich Syncline seem to be at odds with this dogma, considering the relatively low peak metamorphic temperatures estimated for this part of the belt. Either the metamorphic conditions have been grossly under-estimated, or our understanding of the formation of granitic magmas is too narrow to understand the phenomena recorded in these rocks.

Melting in the migmatitic metasediments of the Kuiseb Formation was explored with a view towards understanding the nature of the anatectic process, the fluid regime of anatexis, the physical mechanisms of melt migration and the consequences for the genesis of the Damaran S-type plutons. To this end the work followed a multi-disciplinary approach;

- Firstly identifying leucosomes formed through *in situ* anatexis by the presence of associated peritectic phases resulting from incongruent melting reactions as well as documenting the orientation, geometry, connectivity and progressive deformation of melt conduits in order to identify the melt extraction mechanism, ascent paths and controls thereof.
- Secondly establishing the peak metamorphic conditions via conventional thermobarometry on the best suited assemblages developed in or close to the anatectic rocks, and,

- Thirdly, by experimentally melting the likely protoliths over a range of temperatures under both fluid-absent and water-present conditions.

The study is based on 5 weeks of field work in the Blauer Heinrich Syncline (1 week in March and 2 weeks in July 2005, and 2 weeks in March 2007). The initial work involved detailed sampling of relevant lithologies of the Kuiseb Formation and the description and initial structural investigation of the inter-relationship between melting and deformation. The final field season was dedicated to the structural analysis of the Blauer Heinrich Syncline and the structural setting of the melt-related features with respect to the regional geology. Detailed petrography was conducted on the samples retrieved from the field together with whole-rock major and trace-element analysis with XRF as well as mineral chemical analysis with SEM-EDS.

PT estimates from modelling and thermobarometry were determined and this guided the detailed experimental investigation of the melting behaviour of typical Kuiseb Formation metapelites. Over 3000 hours of experiments were conducted and the run-products of the 19 successful experiments analysed with SEM-EDS to determine textural relationships and phase compositions. All phase abbreviations used in the text are from Kretz (1983), except in chapter 10 where Thermocalc notation (Powell et al., 1998) is used.

Image analysis and least-squares mixing (mass-balance) calculations were done to determine the phase proportions of the experiment that most closely matched the field relations. This allows estimates to be made of the volume of the host/source rocks involved in producing the melt and peritectic products that are preserved in so many of the former melt-bearing structures.

All structural data were measured with a Freiberg compass. Readings have been corrected for a magnetic declination of 21 °W (according to 1:50 000 topographic sheet). Structural data are presented on Schmidt equal area stereographic projections (lower-hemisphere). Structural readings are presented as the azimuth of the dip and the dip (dip-

direction/dip) for planar elements and azimuth of the plunge and plunge (plunge direction/plunge) for linear elements.

2. Field Setting

2.1 Introduction to the Damara Belt, Namibia

The Damara Belt of central Namibia formed by the convergence and subsequent collision of the Kalahari and Congo Cratons at around 550 Ma (Miller, 1983, Stanistreet et al., 1991, Tack et al., 2002). It forms the NE trending inland branch of the larger Pan-African Damara orogen that also includes the coastal Kaoko and Gariep Belts (Figure 2.1). The Damara Belt is a superbly exposed example of a bivergent collisional belt. Either side of a high-grade central part of the orogen are foreland fold-and-thrust belts that verge away from the core of the orogen. Beyond these fold belts, foreland basins developed and now host the Mulden and Nama Group sediments. The core of the orogen provides a mid-crustal oblique section through the internal parts of the collisional belt.

Miller (1983) divided the Belt into four main tectonostratigraphic zones parallel to the orogen; namely the Northern Zone (NZ), the Central Zone (CZ), the Southern Zone (SZ) and the Southern Marginal Zone (SMZ), together with the Southern Foreland (SF) and the Northern Platform (NP) flanking the orogen to the south and north, respectively. The Northern Zone is a N-verging fold-and-thrust belt of low metamorphic grade. The Central Zone contains high-grade metamorphic rocks and abundant granites and is divided into a northern and a southern part according to the dominant presence of the upper and lower stratigraphy of the Damara Supergroup, respectively. The CZ is separated from the Southern Zone by the Okahandja Lineament Zone (OLZ). To the south of the OLZ metamorphic temperatures are lower, but high pressure conditions existed in the SE-verging thrust belt of the SZ.

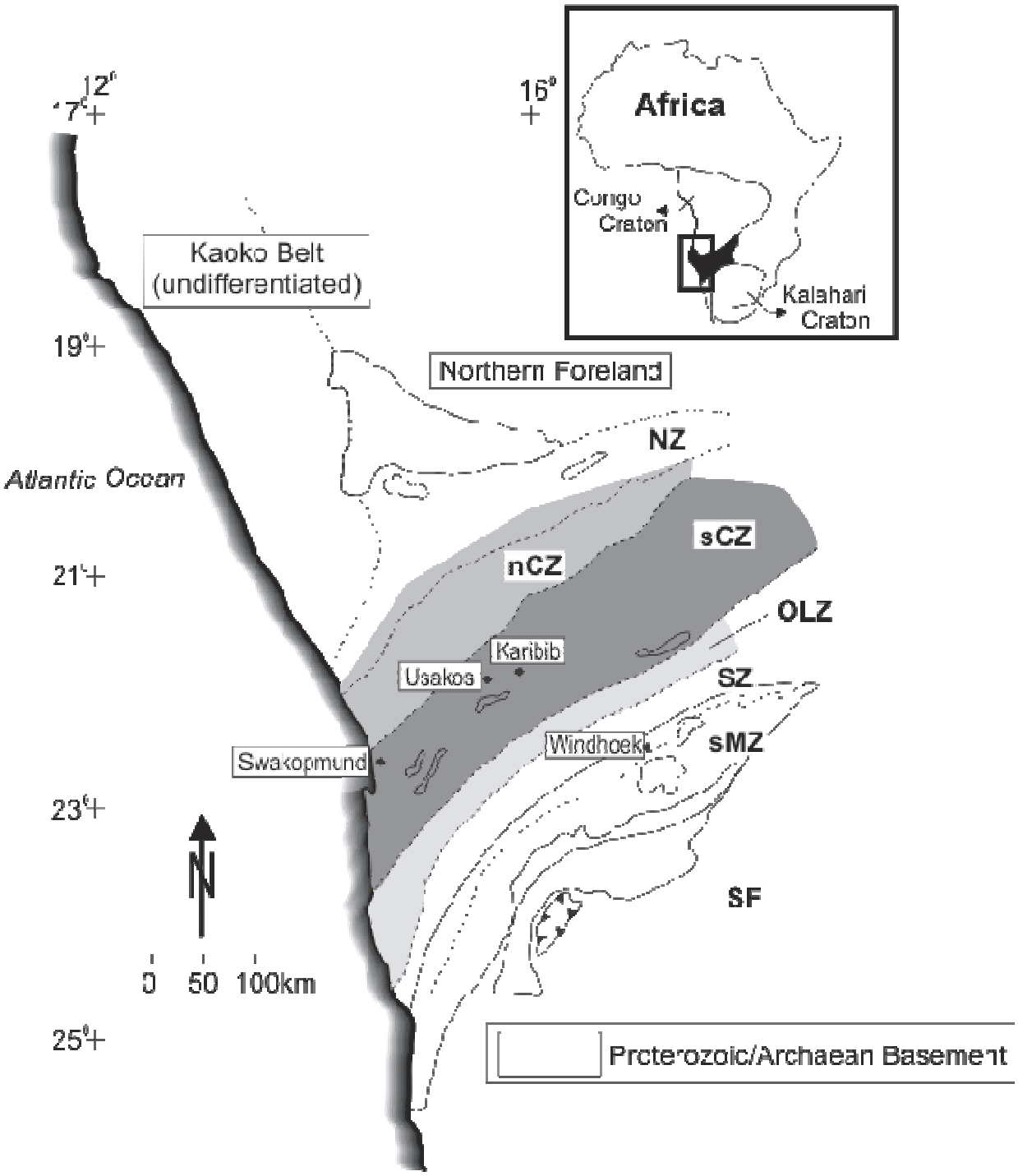

Figure 2.1. The Damara Belt of Namibia is a typical bivergent orogen. It has been divided into several tectonostratigraphic zones (Miller, 1983). The dark grey area represents the medium P, high T southern Central Zone which is the focus of this study.

Preceding the convergence, the Congo and Kalahari cratons had undergone rifting to produce a succession of volcanic and coarse-clastic sediments. Hoffmann et al. (1996)

found U-Pb zircon ages of ca. 750 Ma for volcanic horizons in the rift-related Nosib Group rocks, which unconformably overlie Mesoproterozoic basement gneisses. Jung et al. (2007) found the same age using U–Pb geochronology on euhedral titanite of inferred magmatic origin for the rift-related syenites and together these ages define the onset of continental rifting. The subsequent passive margin sediments of the Swakop Group were deposited shortly before the onset of convergence at ca. 600 Ma. The immature siliciclastic pelites of the Kuiseb Formation represent the youngest sediments of the Damara Supergoup, forming a thick (>> 1000 m) sequence of flysch-type turbidites associated with the closure of the Khomas Sea between the Kalahari and Congo Cratons (Stanistreet et al., 1991). Basement rock types include quartzo-feldspathic gneisses, metasediments and some amphibolites and are mainly Mesoproterozoic in age. The basement as exposed in the core of the orogen is generally referred to as the Abbabis Metamorphic Complex (AMC) and formed part of the leading edge of the Congo Craton (Jacob et al., 1978, Kröner et al., 1991).

2.2 Stratigraphy

2.2.1 The Damara Supergroup

In the Central Zone, the late-Neoproterozoic Damara Supergroup overlies the AMC. At the base of the Supergroup, the siliciclastic Nosib Group represents a rift-related sequence that contains mainly metasediments and volumetrically minor, intercalated metavolcanic rocks. The Etusis Formation was deposited unconformably on the basement gneisses c. 750 Ma (Hoffmann, 1994; Hoffmann et al. 1996) and consists mainly of arkoses and quartzites with some rhyolites also preserved in the CZ. These rocks are overlain by the Khan Formation that contains abundant greenish calc-silicate rocks and amphibole-pyroxene gneisses together with feldspathic quartzites.

The Swakop Group overlies the rift-related Nosib Group and consists of a several thousand metre thick sequence of deep-water mixed carbonate-siliciclastic sequence (Hoffmann, 1983). At the base, the marbles and psammitic gneisses of the Rössing

Formation are well developed in the lower parts of the Khan and Swakop Rivers, but this Formation is largely absent from the Usakos region further inland. The carbonates, minor iron-formations and the characteristic glaciogenic diamictites make the Chuos Formation a distinctive marker horizon in the Swakop Group. The diamictites are related to the Sturtian glaciation of the late-Neoproterozoic.

Stratigraphically above this lies a package of schists, marbles and calc-silicate rocks that comprise, in order, the Spes Bona, Okawayo and the Oberwasser Formations. The latter contains glaciogenic deposits which formed during the Marinoan glaciation. Felsic volcanics near the top of the Oberwasser Formation. have recently been dated at 635 ± 1 Ma (Hoffmann et al., 2004).

The Karibib Formation is a thick succession (up to 1000 m) of well-bedded marbles and occasional calc-silicate horizons that overlies the Oberwasser Formation. In the field area of this study, a large part of the stratigraphy between the Chuos Formation and the Karibib marbles has not been preserved, partly as a result of primary facies variations and partly due to thinning as a result of the strong deformation in the area.

Most importantly for this study, the dark-coloured metapelites and metapsammites of the Kuiseb Formation form a very thick package of well over 1000 m in parts of the sCZ. They display bedding characteristics that are very indicative of turbidite sequences and formed during convergence of the Congo and Kalahari cratons. These rocks were deposited before c. 580 Ma, as constrained by intrusive granites (Miller, 1983).

2.2.2 Granites in the Damara Belt

The Central Zone and southern parts of the Northern Zone are invaded by a great many plutons that consist almost entirely of granite (*sensu stricto*) with gabbro, diorite and granodiorite forming only some 4 % of the > 70 000 km^2 of exposed granitoid outcrop (Miller, 1983). Individual plutons with rounded forms in map section are common,

however, the most common mode of granite occurrence is as pervasive and extensive dyke- and sill-complexes (Kisters et al., 2007).

Miller (1983) classified the granitoids into three major groups that have intruded largely syn- to late-tectonically:

1) Older diorites and granodiorites, red and grey granites;
2) Commonly porphyritic biotite monzogranites and associated (grano-) diorites, collectively referred to as Salem-type granites.
3) Fine- to coarse-grained leucogranites and pegmatites.

Intrusive rocks with an I-type character can be found among the early diorites and the titanite- and hornblende-rich phases of the Salem granites, whereas the more leucocratic Salem granites are peraluminous and commonly garnetiferous S-type granites. Most of the leucogranites are garnet- and cordierite-bearing, strongly-peraluminous S-type granites. These rocks have been regarded as being derived from (1) the partial melting of mid-crustal metasediments of the Damara Supergroup, or (2) partial melting of metasediments and meta-igneous rocks of the Mesoproterozoic basement (Haack et al., 1982, McDermott et al., 1996a, Jung et al., 2000, Jung et al., 2001). The post-tectonic plutons are mainly A-type granitoids, derived from the melting of basement gneisses and also containing a mantle component (Jung et al., 2000).

Although a large geochronological data set is available for granitoids of the Damara Belt, many of these ages are Rb-Sr and Pb-Pb whole rock and model ages that are poorly constrained and lack the resolution necessary to decipher magmatic and/or related metamorphic events. Moreover, there is compelling evidence that the rocks of the Damara Belt underwent a complex and long-lived thermal evolution following the collisional event that this prolonged residence at high temperature resulted in the resetting and overprinting of many isotopic systems (Jacob et al., 2000).

The history of granite magmatism in the belt may largely reflect this protracted high-temperature evolution of the deeper portions of the orogen. Broadly speaking, there are

three main episodes of granite magmatism at 570-540, 535-510 and 505-485 Ma, with the youngest granites having intruded at 465 Ma.

570-540 Ma – convergence and collision-related granitoids.

The first magmatic episode corresponds to the convergence stage and collision between the Kalahari and Congo Cratons. During this time, volumetrically subordinate mafic plutons and syenites, as well as early diorites, granodiorites and I- and S-type Salem granites were intruded. Jacob et al. (2000) report U-Pb SHRIMP ages of 564 ± 5 and 546 ± 6 Ma for early, early- to syn-thrusting (D2) diorites of the Goas Dioritic Suite, namely the Mon Repos diorite and granodiorite, outside Karibib. These ages compare well with older U-Pb zircon ages and some Rb-Sr whole rock ages for diorites of the Goas Suite, although Jung et al. (2002) report a relatively wide range of Pb-Pb titanite ages from the Goas type locality between ca. 560 and 520 Ma. Most ages for the compositionally heterogeneous group of Salem-type granitoids cluster between 560-540 Ma (Miller, 1983, Jacob et al., 2000, Johnson et al., 2006). Importantly, the Salem-type granites are syntectonic with regard to the formation of regional-scale folds and thrusts (D2/D3) in the Damara Belt, thus, constraining the timing of the main collisional event in the belt. For the rare syenites in the Damara Belt that yield ages of ca. 540 Ma, a mantle source with crustal assimilation of lower-crustal Mesoproterozoic basement gneisses is inferred (Jung et al., 2005).

535-510 Ma – late- to post-tectonic granite plutonism.

This timing correlates with the thermal peak of metamorphism in the CZ after the main phase of crustal thickening. Most of the peraluminous S-type granites were intruded during this time and while some of the earlier, ca. 535-530 Ma granites are late-tectonic, younger granites are largely post-tectonic. Partial melting of the Damara Supergroup and basement gneisses can be demonstrated during this time in the highest-grade western parts of the Damara Belt around Swakopmund.

505-485 Ma – post-tectonic granite plutonism.

The large group of leucogranites and pegmatites yielding ages of ca. 505 Ma to 485 Ma represent the last and clearly post-collisional granite event recorded in the Damara Belt. The last granite plutonism is recorded at ca. 465 Ma. The heat for this regionally widespread granite event may have been supplied by the rocks of the Damara Supergroup, following crustal stacking and radiogenic heat production of the thickened rock pile (Jung et al., 2001).

2.3 Metamorphic evolution of the high-grade sCZ and previous work in the area

Considerably higher metamorphic grades exist in the CZ than in the high pressure, moderate temperature NZ and SZ. Within the CZ the metamorphic grade increases towards the SW as it is exposed at deeper structural levels, reaching granulite-facies near the coast in the vicinity of Swakopmund (Hartmann et al., 1983, Masberg et al., 1992). This has also resulted in the partial melting of parts of the sCZ and migmatites are fairly common in this part of the orogen.

The highest metamorphic conditions recorded in the belt correspond to lower-granulite-facies grades (P: 7 ± 0.5 kbar, T: 760 ± 50 °C) that are recorded in coastal outcrops of Grt-Crd-Sil-Spl-Kfs-Qtz bearing metapelites (Masberg, 2000). Here, high temperature metamorphism resulted in extensive partial melting of the rocks, as a result of biotite breakdown under fluid-absent conditions. In the Khan River, some 60 km inland, peak metamorphic conditions of P: 5 ± 1 kbar and ca. 750 °C are recorded (Jung & Mezger, 2003), whereas mid- to lower amphibolite-facies conditions of 3 ± 1 kbar and 550-600 °C prevail in the Karibib/Usakos region (Hoffer, 1977, Puhan, 1983).

The timing and magnitude of the metamorphic peak in the Khan River exposures around the study area, some 60 km inland, is the source of some controversy (see discussion in Jung and Mezger, 2003 (p. 240-241)). Masberg (2000) argues for one metamorphic event, describing a clockwise P-T path from burial-heating during the prograde evolution, via isothermal decompression during the retrograde path followed by isobaric cooling.

Kasch (1983) and Nex et al. (2001) argue for polymetamorphism with an M1 and M2 event; M1 is poorly defined and overprinted by M2, but geochronological data (U-Pb zircon and monazite ages from cross-cutting sheeted granites near Goanikontes published by Briqueu et al. (1980)) indicate it occurred at ca. 540 - 530 Ma. Oliver (1994) has shown that extensional deformation associated with mylonites in a regional high-strain zone (the Khan River detachment) can be constrained to between 534 ± 7 Ma, which is the age of foliated red granites in the high strain zone at Goanikontes, dated by concordant (isotope dilution) U-Pb zircon, and 508 ± 2 Ma, the concordant U-Pb monazite isotope dilution ages from undeformed, mineralised leucogranite sheets cross-cutting the high strain zone. Again the geochronological data is from Briqueu et al. (1980).

Jung and Mezger (2003) have applied the most rigorous approach to solving these problems and propose peak metamorphic conditions of 0.5 ± 0.1 GPa and ca. 750 °C. Furthermore, based on detailed geochronology and petrography from a number of exposures in the CZ, they propose that the rocks record three temperature peaks, at 540-530, 520-500 and 480-470 Ma. In data from the Oetmoed area (15 E, 21.5 S), the Davetsaub area (22.4 S, 16.3 E) and the Khan area (15 E, 22.7 S) the same distribution of multi-point Sm-Nd garnet whole rock ages and U-Pb monazite ages strongly indicate the existence of three peaks of metamorphism (S. Jung, pers. comm.). The use of a major rock-forming mineral and an accessory mineral (both with high closure temperatures) as well as two different decay schemes makes this the most sound approach applied to understanding metamorphism and the timing thereof in the CZ. Jung and Mezger (2003) suggest that the high-T metamorphic events are closely associated with episodes of voluminous late- to post-tectonic granitoids and that heat advection by the magmas has played an important role in driving this metamorphism.

K-Ar and Ar-Ar ages on hornblende, biotite and muscovite illustrate the differential uplift of different parts of the orogen through 550-300 °C. This uplift occurred at ca. 505-485 Ma in the SZ, but at only 480-455 Ma in the CZ, where the cooling history was also disturbed by the emplacement of post-tectonic granites (Gray et al., 2006).

2.4 The migmatites of the Damara Belt

2.4.1 Previous investigations of anatexis

The petrogenesis of migmatites and granites in the Central Zone was investigated by Winkler (1983), Winkler et al. (1975, 1977, 1978) and Hoffmann (1976). These studies were based on exposures of Kuiseb metapsammites to the west of the migmatite-in isograd (Figure 2.2) and concluded that the leucosomes formed by *in situ* melting of the metasediments, principally via quartz + feldspar + H_2O melting. An oxygen isotopic investigation by Hoernes and Hoffer (1985) focused on both the anatectic and pre-anatectic metasediments and demonstrated that both groups of rocks have similar oxygen isotopic characteristics; that only a small subset of the higher grade samples deviate from the average oxygen isotopic compositions of both populations ($\delta^{18}O$ of 14 to 16 ‰); and, that no isotopic case could be made for general fluid ingress into the anatectic metapelites. They concluded that if a fluid was involved in the anatexis of these rocks it was internally derived, or derived from similar metasediments. In addition to these characteristics, Hoernes and Hoffer (1985) documented a slight shift to lower $\delta^{18}O$ values that coincides with proposed partial melting isograds. Jung et al., (2001) have also suggested the possibility that fluids derived from underthrust low- to medium-grade metasedimentary rocks may have fluxed partial melting in overlying aluminous sediments. These results were interpreted to indicate limited fluid-present conditions during metamorphism in the highest grade parts of the belt. The combined relatively low temperatures of metamorphism and absence of isotopic evidence for large-scale fluid ingress have lead more recent workers such as Masberg (1992, 1996) and Jung et al., (1999) to interpret the migmatites as being predominantly melt-injection features, with the melt being derived from a water-undersaturated source. These authors interpret there to have been a limited amount of *in situ* melt generation by fluid-present processes in the outcrops studied. The fluid movement was interpreted to have been aided by deformation and the melting produced Na-rich melts and thus serves as a good comparison to this study.

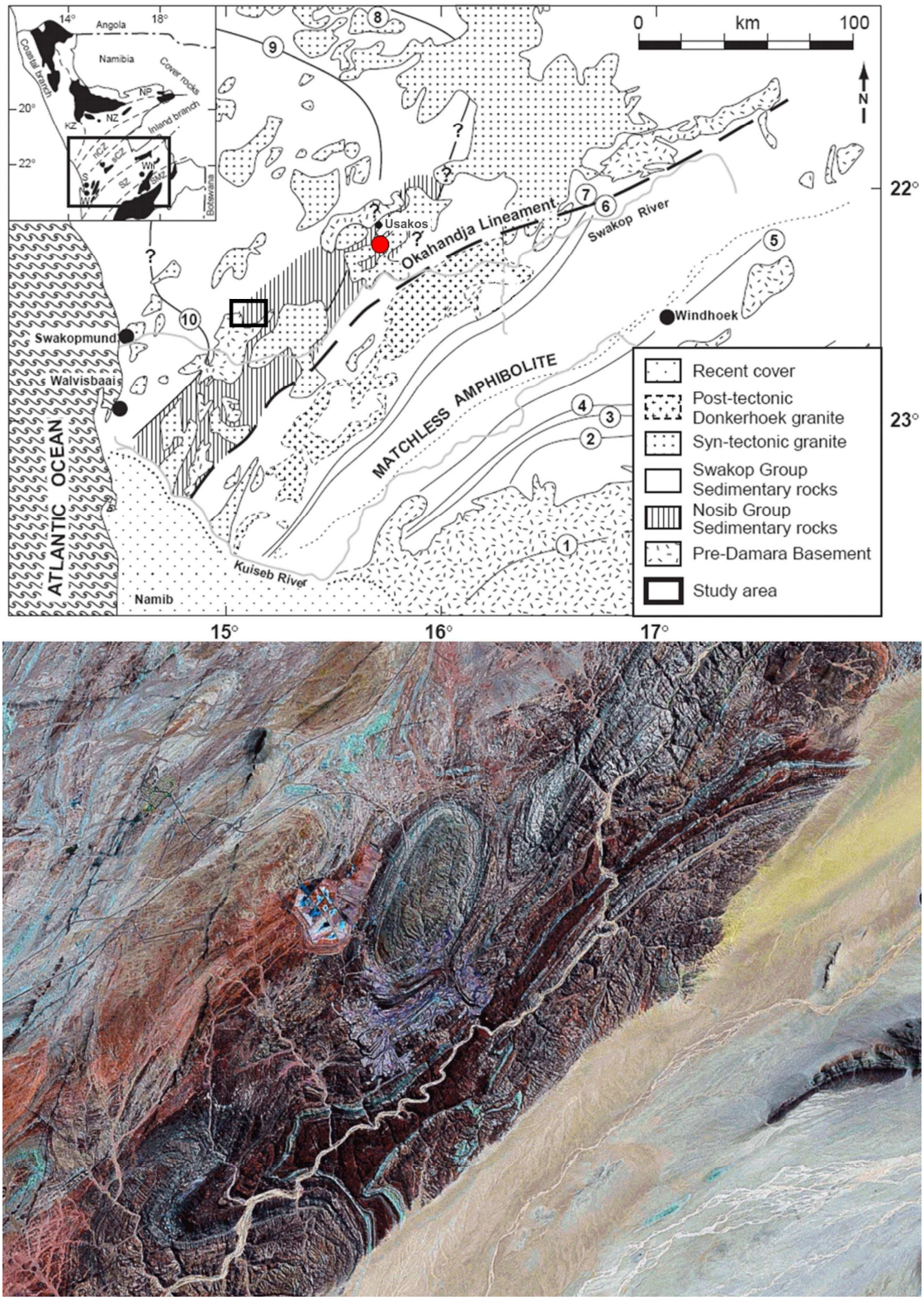

Figure 2.2. A map of the Central Zone of the Damara Orogen after Jung and Mezger (2001) and Hartmann et al. (1983) with false colour satellite-image of the study area. This generalized geological map shows the study area within the southern Central Zone of the Damara Orogen, Namibia.

Abbreviations in inset: KZ: Kaoko Zone, NP: Northern Platform, NZ: Northern Zone, nCZ: northern central Zone, sCZ: southern Central Zone, SZ: Southern Zone, SMZ: Southern Margin Zone. Isograd map (Hartmann et al., 1983) gives the distribution of Pan-African regional metamorphic isograds within the southern and central Damara orogen. Isograds: (1) biotite-in, (2) garnet-in, (3) staurolite-in, (4) kyanite-in, (5) cordierite-in, (6) andalusite sillimanite, (7) sillimanite-in according to staurolite-breakdown, (8) partial melting due to: muscovite + plagioclase + quartz + H2O --> melt + sillimanite, (9) K-feldspar + cordierite-in, (10) partial melting due to: biotite + K-feldspar + plagioclase + quartz + cordierite --> melt + garnet.

Metamorphic grade increases from east to west, as indicated by the isograds of previous studies. The study area is marked by the black block. Note that this falls entirely within the domain identified as the possible anatectic domain, but does not fall in the zone where biotite breakdown has been described. The satellite image illustrates the geology of the study area. The rocks studied were from the Kuiseb Formation (brown central band) along the Khan River. The red dot to the east of the study area on the map marks the site of sampling of lower grade Kuiseb Formation metasediments for comparison with the rocks of the study area.

2.5 Structural geology

The sCZ of the Damara Belt is characterised by the presence of km-scale domal structures, the long axes of which are sub-parallel to the ENE trend of the orogen and form part of the main structural grain (Figure 2.2). Many of these domes are cored by the Damaran Granites or by older pre-Damaran Basement gneiss (Smith, 1965), with the metasediments of the Damara Sequence draped around the domes in synformal structures. Several theories have been published to describe the formation of domes in the sCZ and are briefly discussed below.

1 Buoyant rise of older basement within the cores of domes led Eskola (1948) and Barnes and Downing (1979) to consider that density-driven diapirism led to the formation of basin and dome outcrop patterns.

2 Magmatic deformation caused by diapiric rise of magma or magmatic ballooning was suggested by Sawyer (1981), Coward (1981) and Kröner (1984). Kröner further suggested that the buoyant rise of granitic melt into antiforms was hindered by an impermeable horizon, causing doming with continued expansion.

3 Polyphase folding with several distinct deformation events created superposed fold interference patterns, and give rise to domes and basins, according to Smith (1965) and Jacob et al. (1983), after (Ramsay, 1967).

4 Coward (1983) suggested a large low-angle shear zone with an overthrust sense to the southwest produced km-scale sheath folds (dome structures) within the CZ. He suggests that the higher strain zones along the underlying antiformal limb of the sheath folds support this model.

5 Oliver (1994) suggested that the Damara Belt could represent a deeper seated equivalent to the North American metamorphic core complex. The cover was detached from the basement along a ductile extensional shear zone and developed as the Khan River Detachment (Oliver, 1994, Oliver, 1995).

6 Poli and Oliver (2001) discussed the possibility of progressive polyphase folding of the middle crust during constriction. They suggested that the sCZ was exposed to a single deformational event, however, oversteepening during the oblique collision between the Congo and Kalahari Cratons caused the Damara Sequence to extrude laterally towards the southwest resulting in a basin and dome terrain.

7 More recent structural analysis by Kisters et al (2004) led to the development of a model relating the domes within the Karibib District to tip-line folds above blind thrusts within a fold-and-thrust belt.

Different models have been proposed by authors studying different parts of the belt; Barnes and Downing (1979) pointed out that the present day erosional surface may expose the sCZ in an oblique crustal section (with progressively deeper levels to the southwest). Kisters et al. (2004) indicated that this is a fundamental aspect to consider when interpreting the dome forming mechanisms across the sCZ. They propose that domes at higher structural levels in the northeast resulted from fold-and-thrust tectonics while domes exposed further southwest developed as a result of constrictional tectonics at deeper levels as described by Poli and Oliver (2001).

The differing interpretations have also led to discussion about the number of distinct deformational events that occurred in the Damara Belt. The earliest structures preserved in the Damara Sequence are a bedding-parallel foliation (S_1). The S_1 foliation is commonly associated with bedding-parallel shear zones and large, km-scale recumbent folds that were refolded during subsequent events. The timing of the S_1 deformation is tentatively discussed for ca. 600-580 Ma. The main structural grain of the Damara belt trends ENE, parallel to the overall trend of the belt. It is characterized by regional-scale, upright, to NE or SW verging folds (F_2) and a ENE-trending axial planar foliation (S_2) (referred to by Miller, (1983), as F_3 and S_3). Regional scale thrusts are related to this event (D_2) and show a top-to-the-NW tectonic transport in the N (CZ, NZ and NP), but a top-to-the-SE tectonic transport in the S (SZ and SMZ), resulting in the overall bivergent symmetry of the belt. The high-grade mid-crustal levels of the sCZ have undergone a SW-vergent, orogen-parallel extrusion (e.g.Oliver, 1994, Kisters et al., 2004) evidenced by pervasive constrictional strains and km-scale, SW-ward closing sheath folds (Coward, 1983). The timing of the D_2 deformation is ca. 550-540 Ma (Miller, 1983, 2002; Jacob et al., 2000; Johnson et al., 2006). D_2 is generally regarded to represent the main, slightly oblique collisional stage between the Congo and Kalahari cratons that were brought together along a NW-dipping subduction zone. Late-stage strike-slip and oblique-slip movement is recorded along e.g. the OLZ, reflecting differential uplift along the belt. The Naukluft Nappe Complex is a collection of late-stage, probably gravity-driven thrust sheets that were emplaced over low-grade rocks of the Nama Group in the SF.

The deformation in the Damara has been divided into as many as four distinct events by some authors, and can be summarised as follows:

- **D_1**: Fabric forming event (bedding parallel foliation) and thrust-stacking of the Damara stratigraphy and simultaneous thinning of parts of the sequence. This event also produced the migmatitic banding around Rössing according to Basson and Greenway (2004).
- **D_2**: Some authors propose that this event formed NW trending folds that later formed the domes with interference from the NE trending folding (their D_3).

There is some evidence of polyphase folding in the CZ (Jacob et al., 1983, Buhn et al., 1993).

D_3: NE trending folds that mirror the orientation of the Belt and formed as a result of collision of the Kalahari and Congo Cratons. Johnson et al. (2006) found that the dome forming event in the Usakos Dome was the result of a progressive deformation they called D_2. The NE trending fold could not continue to grow as a result of the rheological weakening caused by sheeted granite intrusions and resulted in a collapse of the structure to the SE.

Poli and Oliver (2001) do not agree with the model that calls on superposed folding events to produce the domes of the Damara CZ. Instead, they favour a progressive deformation which initiates with the constriction of the sub-horizontal, bedding-parallel foliation. The shortening occurs along both (principal) axes in the horizontal plane but is unequal as evidenced by the elongated shape of most domes. The synclinal domains between the domes tighten with continued deformation, and as the domes amplify progressively, the synclines become sinuously wrapped around the domes and are forced to converge (e.g. The Namibfontein and Khan Mine Convergence Zones). Fossen and Tikoff (1997) predicted the general prolate strain with SL/LS fabrics and steep regional lineation trajectories formed during 'Type A' transpression, and Poli and Oliver (2001) suggest that these structures, found throughout their field areas, formed during the progressive dome growth.

Ghosh (1970) explains that the rheology of the crust is critical in determining the response to constrictional deformation. If the crust behaves in a viscous manner domes can result, if it behaves elastically folds will develop (two sets according to the principal stress directions). Kisters et al. (2004) suggested that both rheological responses are present in the Damara Belt as they compared the formation of the Usakos and Karibib Domes with the Khan, Vergenoeg and Namibfontein Domes as described by Oliver (1994) and Poli and Oliver (2001). The latter are believed to have formed in a constrictional environment by viscous flow. The Usakos and Karibib Domes, however,

behaved in a more competent manner to the crustal shortening and accommodated the movement by NW-vergent folding and thrusting (Kisters et al., 2004).

2.6 The Geology of the Khan River between the Rössing and Khan Domes

In the study area, metasediments of both the Nosib and Swakop Groups are best preserved in synclinal structures between the anticlinal Khan and Rössing Domes. The north-eastern part of the Khan Dome is the tightly folded Nose Structure Anticline (Smith, 1965). The Blauer Heinrich Syncline is an open to tight synformal structure nestled within the curve of the Nose Structure Anticline (Smith, 1965). This structure trends WSW-ENE and meets several other major syncline axes to form the Khan Mine Convergence Point (Barnes, 1981, Poli & Oliver, 2001). The Khan Syncline joins the convergence point from the NE and the Welwitschia Syncline joins from the South (Smith, 1965). The limbs of these structures generally dip steeply and are commonly overturned.

The contact between the basement and overlying Damara sediments in the Nose Structure Anticline has been interpreted to be tectonic by Oliver (1994) and part of a regional ductile shear zone, the Khan River Detachment. This has been mapped as a 2 km thick detachment shear zone in places, with an increasing dominance of L-tectonites over the regionally more common S-tectonites with increasing proximity to the basement-cover contact (Oliver, 1994).

These lineations are common in the area and have a general moderate plunge to the NE. Poli and Oliver (2001) ascribe these lineations (fold plunge, mineral lineation, and pebble strain analysis) to one progressive event of constrictional strain in the area as the result of transpression during the collision of the Congo and Kalahari Cratons. This resulted in the formation of domes surrounded by sinuous synclinal domains as the ductile crustal material was extruded to the SW.

Furthermore, they explain the formation of the Khan River Detachment as being initiated from bulk pure shear at the inherently weak basement-cover contact. In other words it acted as a favourable site for strain partitioning during dome formation (Oliver, 1994, Poli & Oliver, 2001) and the lack of shear-sense indicators shows an absence of simple shear.

3. Lithology and Petrography

3.1 Introduction

Metapelitic rocks lend themselves well to high-grade metamorphic petrology and the study of partial melting. This is the result of their generally aluminous composition being reactive to changes in pressure and temperature, as well being fertile for the production of granitoid melts. The Kuiseb Formation consists predominantly of metapelitic rocks that very commonly display evidence for partial melting. Samples were chosen to represent the most important units of the lithology, but were also chosen for the purposes of documenting the phenomena of partial melting in the area. Some samples were chosen for their relatively lower variance assemblage than commonly occurs in the Kuiseb Formation as these are useful for constraining the metamorphic conditions with thermobarometry. Samples were taken for the preparation of thin-sections for petrographic descriptions as well as for mineral chemical analyses (SEM-EDS), and for the whole-rock geochemical analysis (XRF).

Table 3.1. Sample list with locations and field descriptions. Bold face sample names indicate the samples for which whole-rock geochemical analyses are available.

Sample Name	Latitude (S)	Longitude (E)	Sample Description
KH-1/1	22º 32.476'	14º 59.879'	Grt, crd, bi-schist
KH-1/2	22º 32.476'	14º 59.879'	Grt, crd, bi-schist
KH-1/3	22º 32.476'	14º 59.879'	Grt, crd, bi-schist
KH-2/1	22º 31.884'	15º 01.567'	Crd, bi-schist
KH-2/2	22º 31.884'	15º 01.567'	Leucosomes associated with boudins in bi-schist
KH-2/3	22º 31.884'	15º 01.567'	Leucosomes associated with boudins in bi-schist
KH-3	22º 30.903'	15º 03.197'	Banded granite
KHt-1	22º 30.614'	14º 59.522'	Boudins of calc-silicates and metapsammites
KHt-2/1	22º 31.407'	15º 01.860'	Crd, bi-schist
KHt-2/2	22º 31.407'	15º 01.860'	Leucosome in crd, bi-schist
KHt-2/3	22º 31.407'	15º 01.860'	Leucosome boudins in bi-schist
KHt-2/4	22º 31.407'	15º 01.860'	Grt leucosome in bi-schist
KHt-4	22º 31.142'	15º 02.918'	Grt leucosome in bi-schist
GL-1	22º 31.101'	15º 02.925'	Large garnet straddling leucosome and bi-schist
USK-1	22º 00.458'	15º 36.50'	Low-grade schist
USK-2	22º 00.458'	15º 36.50'	Low-grade schist
USK-3	22º 00.458'	15º 36.50'	Low-grade schist
USK-4	22º 00.458'	15º 36.50'	Low-grade schist
USK-5	22º 00.458'	15º 36.50'	Low-grade schist

Sample Name	Latitude (S)	Longitude (E)	Sample Description
USK-6	22º 00.458'	15º 36.50'	Low-grade schist
USK-7	22º 00.458'	15º 36.50'	Low-grade schist
11/1	22º 31.006'	15º 03.535'	Crd gneiss
11/2	22º 31.053'	15º 03.575'	Grt-bearing migmatite
11/3	22º 31.065'	15º 03.677'	Crd migmatite
11/4 (A-C)	22º 31.065'	15º 03.677'	Crd gneiss and leucosomes
11/5	22º 31.065'	15º 03.677'	Metapsammite
11/6	22º 31.154'	15º 03.596'	Crd gneiss
11/7	22º 31.154'	15º 03.596'	Grt-crd migmatite and metapsammite
11/8	22º 32.018'	15º 01.316'	Leucosomes and granite
11/9	22º 32.018'	15º 01.316'	Garnet migmatite
11/10	22º 32.015'	15º 01.186'	Green Pl, Cpx, Hbl, Bi schist
11/11 (A-C)	22º 31.960'	15º 01.141'	Crd gneiss
12/1 (A-E)	22º 30.439'	15º 03.831'	Gneisses and metapsammites
13/1 (A & B)	22º 32.218'	15º 00.465'	Metapelite
13/2	22º 32.218'	15º 00.465'	Leucocratic coarse-grained granite
13/3	22º 32.218'	15º 00.465'	Garnet granite
13/4	22º 32.218'	15º 00.465'	Metapelite
13/5	22º 32.218'	15º 00.465'	Crd gneiss
14/1	22º 31.801'	15º 02.005'	Crd-bearing nebulitic migmatite
14/2	22º 31.801'	15º 02.005'	Sugary-textured, migmatite Crd gneiss
14/3	22º 31.801'	15º 02.005'	Grt-bearing leucosomes
14/4	22º 31.801'	15º 02.005'	Metapelite
14/5 (A & B)	22º 31.384'	15º 01.869'	Crd gneiss
15/1	22º 31.821'	15º 01.997'	Migmatite

3.2 The Kuiseb Formation migmatites

3.2.1 Cordierite-biotite gneisses (metapelites)

The rocks of the study area consist predominantly of coarse-grained metapelitic cordierite-biotite gneisses that are characterised by the assemblage Crd + Bt + Pl + Q ± Ksp ± Grt (± Ilm), which is a relatively high variance assemblage in natural rock compositional space (approximated by NCKFMASHTO). The cordierite-biotite gneisses of the study area are compositionally and mineralogically fairly homogeneous on a dm-scale and are considerably more homogeneous than their lower-grade amphibolite-facies equivalent rocks from the area around Usakos, which still display well preserved bedding on a cm-scale and cross-bedding on a mm-scale. Representative compositions for both sets of metasedimentary rocks are presented in Chapter 5 (whole-rock geochemistry).

The high-grade rocks contain abundant porphyroblasts of cordierite which display an elongated oval habit. These porphyroblasts contain rounded inclusions of quartz and biotite, and only rarely of plagioclase. Very rarely, the biotite inclusions will define a relict foliation; however, this fabric in the inclusions has not been observed to be consistent between grains of the same rock. The porphyroblasts have a significantly skeletal structure, with the inclusions making a large contribution to the overall volume of the porphyroblasts. These inclusions point to the prograde nature of the cordierite and the abundance of the porphyroblasts suggests these rocks might be restitic.

Cordierite porphyroblasts of the metapelites have also been observed to have a relatively inclusion-free rim. Cordierite displaying these halos is found in close association with garnet-bearing leucosomes and is not observed throughout the package.

The cordierite is commonly pinnitised. Despite this the cordierite porphyroblasts are more resistant to weathering than the surrounding quartz-feldspar biotite matrix and produce the (bubble-wrap) texture that is clearly illustrated in Figure 3.1. These porphyroblasts clearly define a lineation in many of the gneisses (this will be discussed in Chapter 4).

Figure 3.1. Typical weathered texture of the coarse-grained metapelitic cordierite gneiss. The dark blue cordierite crystals are resistant to weathering and give the rock this 'bubble-wrap' texture.

A coarse-grained generation of biotite can be seen to wrap around the cordierite porphyroblasts. It is common to find quartz-feldspar-biotite patches between the porphyroblasts; these are the most fine-grained part of the rock. The biotite in these patches is less coarse grained than the biotite that wraps around the porphyroblasts, but is otherwise very similar in colour and the orientation of their basal planes. Coarse-grained segregations of quartz and feldspar are also fairly common. These segregations can often be found to occur as small bodies in the pressure shadows of porphyroblasts or otherwise occur as ellipsoidal bodies similar in size and shape to the cordierite porphyroblasts. However, in rocks with a strong planar fabric, the segregations occur preferentially as foliation-parallel ribbons and sheets. In the quartz-feldspar segregations, plagioclase often displays a euhedral shape (Figure 3.2).

In certain rocks, potassium-feldspar forms porphyroblasts that are very similar in appearance and have a similar inclusion suite to the adjacent cordierite porphyroblasts. These are most easily distinguished from cordierite under the microscope by their lack of pinitisation and occasional presence of exsolution lamellae of albite.

Interlayered with the typical cordierite gneisses are rocks that are very similar in appearance and chemistry that are only distinguished by the presence of metamorphic garnet in the assemblage together with cordierite. This garnet is relatively poor in inclusions and rarely forms crystals larger than 5 mm in diameter. The biotite foliation wraps around the garnet which is thus also interpreted to be a prograde metamorphic phase.

Some of the garnet-rich metapelites host small intergrowths of biotite and quartz (Figure 3.3). In many other high-grade environments such structures have been described as the products of crystallisation-hydration reactions of minerals initially more SiO_2-rich than biotite, such as orthopyroxene or gedrite. The presence of leucocratic segregations, possibly indicating the presence of a melt in the rocks at the peak of metamorphism, suggests that these structures probably formed via the same process. The rarity of these structures and their association with low strain domains and competent lithologies within

the rocks indicates that they were easily destroyed during recrystallisation associated with deformation.

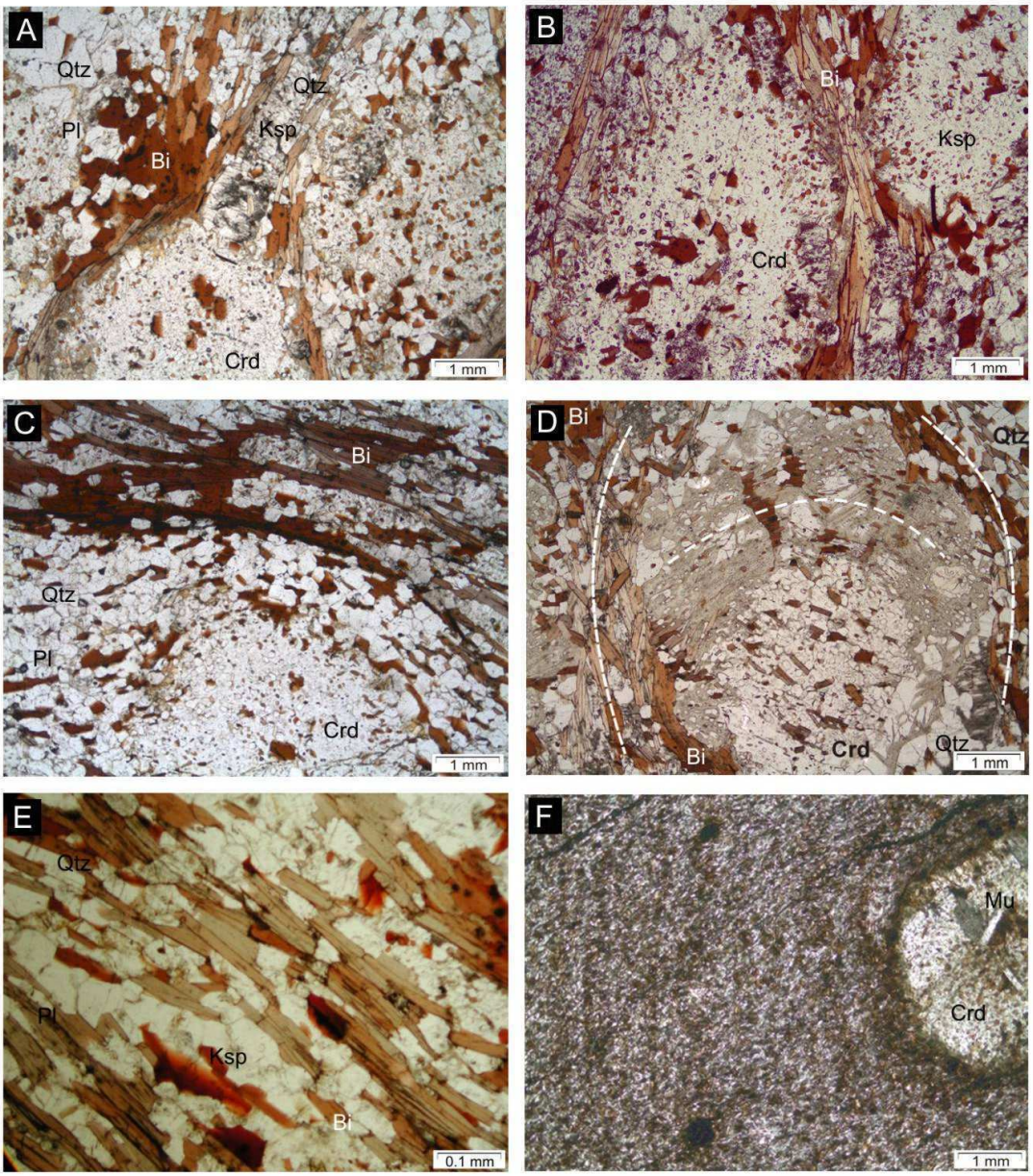

Figure 3.2. Mineral textural relationships in the Kuiseb Formation metasediments; all photomicrographs taken with plane polarised light. A shows a cordierite porphyroblast just below a stretched quartz-feldspar aggregate. B illustrates the slight textural difference between the potassium feldspar porphyroblasts (top right) compared to the more abundant cordierite porphyroblasts. Note the inclusion-poor rim of the cordierite. C shows the foliation defined by biotite wrapping around a typical, large cordierite porphyroblast. D again shows the foliation around a porphyroblast, but also illustrates the relative rotation that has occurred between the foliation and the porphyroblast during its growth; rarely cordierite preserves inclusions that define a relict foliation, which in this example was at right angles to the foliation preserved around the

porphyroblast. E is a photomicrograph of typical biotite-quartz-plagioclase schist of the study area. F is an image of the lower-grade equivalent Kuiseb Formation schist from Usakos. The cordierite porphyroblasts are typically smaller and are hosted in a much finer biotite-quartz-plagioclase matrix. The faint subvertical striations that can be seen in the left and centre of the image are the compositional variations associated with cross-bedding which is still preserved in many of these amphibolite-facies metasediments.

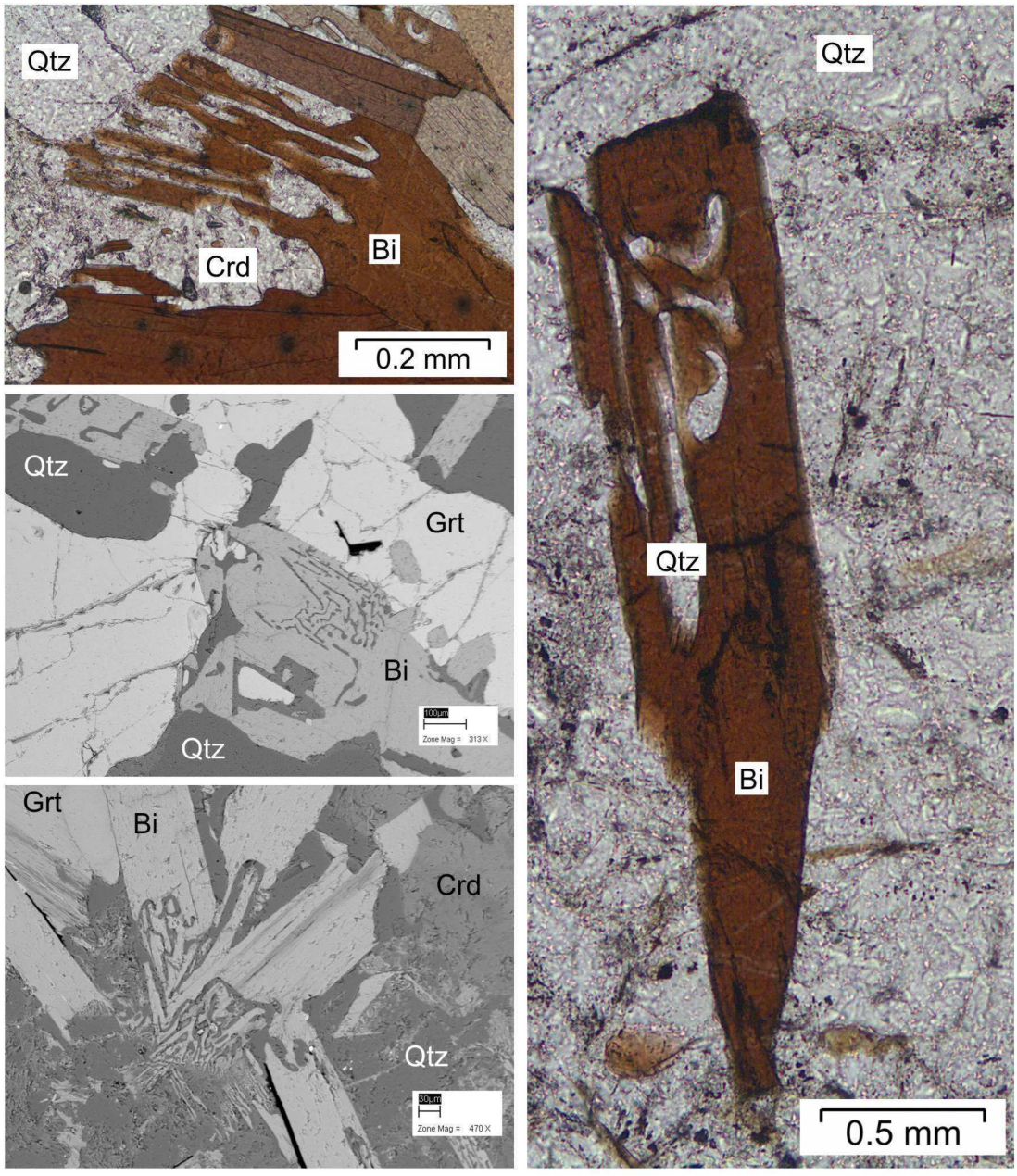

Figure 3.3. Biotite-quartz intergrowths are rare features in the rocks of the study area but testify to the presence of a pre-existing mineral that was more SiO_2-rich, such as orthopyroxene or gedrite.

Silimanite is rare in these metapelites only occurring as inclusions in cordierite porphyroblasts in one example and as a retrograde mineral in the matrix of sample KH-1/3.

The metasedimentary rocks are the host of arrays of leucocratic bodies, commonly regularly spaced, that cross-cut the lineation and foliation. These leucosomes are quartz, plagioclase and potassium feldspar segregations occasionally with biotite-rich rims. In many of these bodies garnet has developed as an intergrowth with quartz to form large rounded porphyroblasts between 50 - 120 mm in diameter. Less commonly, cordierite is developed together with, or in the place of garnet. The cordierite also forms an aggregated mass with quartz like garnet, but more commonly forms pristine, gem-quality crystals in these bodies (when present) than the garnet, which only rarely forms euhedral examples. Biotite is also present in the leucosomes and in a few examples, tourmaline was observed.

Impingement, or 'collapse', of the foliation around these garnet porphyroblasts is common and indicates that these structures formed before the end of deformation in the area. The collapse of the foliation is consistent with the formation of boudins in some of the examples, but in others there may have been a loss of volume from the vicinity of the garnet. This could be interpreted as a loss of the leucosome material (melt).

In these metapelites, small, often rounded zircon crystals are very common, as are apatite and monazite. Ilmenite is less common, and is not found as inclusions in the biotite crystals as is the case for the zircon and monazite. Apatite is often associated with the coarse poikilitic garnets of the leucosomes.

3.2.2 Biotite schists (metapsammites)

Also within the metasedimentary pile are quartz-biotite schists that locally contain garnet and are lighter in colour and more fine-grained than the gneisses discussed above. They also contain porphyroblasts of cordierite, but this mineral occurs in far smaller amounts

compared to the more aluminous metapelites. These "metapsammites" are dominated by quartz and oriented grains of biotite. Plagioclase is also a constituent of these rocks but they are generally feldspar-poor. Garnet forms porphyritic grains up to 35 mm in diameter.

3.2.3 Intrusive rocks

The rocks of the Blauer Heinrich Syncline host vast numbers of intrusive sheets that are almost exclusively of leuco-granitic composition and are always coarse grained or pegmatitic. These sheets occur on all scales between centimetre-sized sheets that can be traced for several metres to decametre-scale sheets that can be followed along strike for kilometres. Small, low-aspect ratio bodies of the same coarse granitic material are less common, but these so called 'mini-plutons' can be related to blows of the larger sheets, or be fed by several smaller granite sheets. The large sheets and mini-plutons almost always display an internal compositional or textural layering.

These intrusive rocks are composed predominantly of large euhedral to subhedral potassium feldspar and plagioclase crystals. Quartz is interstitial or less commonly euhedral or occurs as a graphic intergrowth with feldspar. The granite sheets commonly host large books of biotite. Many of the larger sheets and mini-plutons host coarse poikilitic intergrowths of cordierite and quartz that form fist-sized nodules (Figure 3.4). Texturally similar intergrowths of garnet and quartz can, less commonly, be found in the granites.

Despite the presence of small amounts of garnet and cordierite, the intrusive rocks are generally not characterised by the presence of mafic selvages and do not contain, either within the sheets or within the marginal bounding gneisses, mafic minerals such as garnet, cordierite or orthopyroxene of a generation that could be interpreted to be the peritectic products of *in situ* anatexis. Thus, both the plutons and the sheets are interpreted to be largely the result of intrusion of magma into the gneisses.

Figure 3.4. Coarse-grained leucogranitic mini-pluton. The sheeted nature of the granite is clearly evident as a result of mineralogical and textural variations between individual sheets. The poikilitic cordierite nodules seen on the left of the image are intergrown with quartz.

In contrast to the rocks described above, there are several associations for which there is textural and mineralogical evidence for the granitic material being formed as the product of *in situ* anatexis. There is an important structural control on the formation of the anatectic features as well as on the orientation and style of intrusion of the granite sheets and mini-plutons. For this reason these rocks will be further discussed in Chapter 4.

3.2.4 Other rock types

A thin sequence (ca. 10 m at its thickest point) of plagioclase-hornblende-clinopyroxene schist of similar texture to the biotite schists was found. These rocks contain plagioclase in much greater abundance together with hornblende and clinopyroxene and lesser amounts of biotite and quartz. Tourmaline is a common accessory mineral in these rocks.

Occasional thin beds of calc-silicate rocks occur throughout the rocks of the study and form distinctive hard-weathering beds of up to 20 cm thick.

Collectively, these rocks constitute the Kuiseb Formation of the Damara Sequence and lie stratigraphically above the characteristically light-coloured and hard-weathering marbles of the Karibib Formation, which form a prominent ridge around the study area. These are clearly visible as the blue band in the satellite image of Figure 2.2.

In several places within the Blauer Heinrich Syncline, the Kuiseb Formation rocks display a compositional change in bedding from psammitic grading upwards into more pelitic horizons in regular repetition that is reminiscent of the Bouma sequences present in the lower-grade equivalent rocks of the Usakos area. These high-grade rocks, however, do not retain the upward-fining textures typical of Bouma Sequences. Instead, the textural variation is reversed to what would be expected. The rocks become more coarse-grained upwards towards the metapelitic beds as a consequence of the metamorphic porphyroblasts that form preferentially in the beds of pelitic compositions and are rare in the feldspar-poor metapsammites. This coarsening is characteristic of all the rock types of the study area when compared to their low-grade equivalents as sampled in Usakos.

The cordierite-biotite gneisses are the volumetrically dominant clastic metasedimentary unit and are the focus of this study, together with the granitic material that they host in several different associations.

3.3 Subsolidus Kuiseb Formation Metapelites

The Kuiseb Formation metapelites of the Usakos Dome were sampled to compare the migmatitic rocks with this likely subsolidus equivalent. Despite reaching the lower- to mid amphibolite-facies, these rocks still display cross-bedding on a mm-scale in low-strain domains and graded-bedding, which is indicative of their original deposition as

turbidite flows. The low-strain in these rocks is the result of strain partitioning into the overlying Karibib Formation dolomitic marbles (Johnson et al., 2006).

These rocks display no evidence of partial melting and are believed to have reached peak metamorphic conditions of 3 ± 1 kbar and 550-600 °C (Hoffer, 1977, Puhan, 1983). No garnet has been described to occur in these rocks. The rocks commonly contain cordierite porphyroblasts of between 2 – 5 mm in diameter (Figure 3.2 F). Porphyroblasts are not as abundant in these rocks as they are in the high-grade metasediments. Instead, the rock is dominated by a fine-grained matrix consisting of biotite, quartz and plagioclase. The fabric defined by the biotite in the rocks wraps around the cordierite porphyroblasts. Ilmenite and zircon are common accessory minerals. A late generation of muscovite grows across the foliation, and was probably formed on the retrograde path.

4. Structural geology of the Blauer Heinrich Syncline

The metapelites of the Kuiseb Formation in the BHS (Figure 4.1) are inundated with granitic leucosomes of highly variable geometries and sizes, ranging from small, irregularly-shaped leucosome patches, through pervasive networks of sill and dyke complexes to small-scale plutonic bodies (Figure 4.2). Even on first inspection of the rocks, a strong correlation between the orientation of granitic leucosomes, their emplacement styles and relative timing with respect to the main fabrics and structures of the BHS is clearly evident (e.g. Miller & Hoffmann, 1981). This suggests that the formation and emplacement of granites is structurally controlled.

Figure 4.1. Google Earth® image showing an oblique, approximately down-plunge view to the NE of the Blauer Heinrich Syncline (BHS). The Khan River Gorge runs along the length of the fold providing excellent outcrop and access. The tailings and open-pit of Rössing Uranium mine are at the top of the photo. Just south of the tailings, the steep to over-turned northern limb of the BHS can be seen. The dark-coloured metapelites of the Kuiseb Formation occupy the core of the structure with light-coloured marbles of the Karibib Formation forming the high ridges.

Figure 4.2. Typical field associations of granite in the study area. The abundant bedding-parallel sills connect to dykes and mini-plutons as can be seen in this photograph taken parallel to the subvertical bedding looking up the plunge of the Blauer Heinrich Syncline.

The present chapter outlines the structural geology of the BHS, the formation, significance and relative timing of planar and linear fabrics (Table 4.1) and their relationship to first- and lower-order structures of the BHS. Together with this

background, the actual controls of deformation on granite formation, segregation and ascent will be investigated and discussed in the second part of this chapter.

Table 4.1. Summary of fabric elements in the BHS.

Fabric Type	Pre-tectonic	Deformation D_1	Deformation D_2	Description
Planar (S)	S_0			- Bedding.
		S_1		- Bedding-parallel foliation, axial planar to intrafolial (F_1) folds.
			S_2	- Axial planar foliation to F_2 folds, NE-trending with steep- to vertical dips,
Linear (L)			L_2a	- Mineral stretching lineation, subparallel to F_2 folds.
			L_2b	- Hinge-lines of parasitic folds (F_2), mostly subparallel to L_2a
Fold (F)		F_1		- Early, isoclinal, intrafolial folds associated with D_1.
			F_2	- Upright, NE-trending, steep to shallow NE plunging folds. The BHS is the first-order F_2 fold. Second- and lower-order folds occur on all scales.

4.1 Fabric and Structural Elements

The Blauer Heinrich Syncline (BHS) is a NE-trending synclinal structure (Table 4.1; F_2, and see below), cored by rocks of the Kuiseb Formation. Anderson and Nash (1997) refer to it as the Welwitschia Syncline, but this study follows the nomenclature used by Smith (1965) and Poli and Oliver (2001). A variety of planar and linear fabric elements can be distinguished in the gneisses of the Kuiseb Formation. These fabrics are described in chronological order, based on cross-cutting and overprinting relationships (Table 4.1).

4.1.1 S_0

S_0 refers to the original sedimentary bedding. On a regional scale, bedding is evident as 10- to 100 m wide lithological packages within the Kuiseb Formation. Contacts between individual formations such as the marble units of the Karibib Formation and siliciclastics of the Kuiseb Formation can be easily followed around the closure of the BHS in the southwest of the study area. In detail, bedding is preserved in the high-grade metamorphic rocks as compositional, grain-size and/or colour variations. In the Kuiseb Formation graded bedding often defines m-scale Bouma sequences typical of turbidite deposits (Figure 4.3) (see also Chapters 2 and 3). The pelitic top parts of the Bouma cycles are now represented by coarsely recrystallised biotite-cordierite schists, whereas the psammitic bottom parts are rather fine-grained quartzo-feldspathic felses.

Figure 4.3. Centimetre- to dm scale bedding (S_0) preserved in the Kuiseb Formation metasediments. The bedding varies regularly from psammitic to pelitic in composition, displaying characteristics of a turbidite succession. The chisel is 25 cm long.

These compositional variations can be used to define the second- and lower-order folding of the metasediments or associated boudinage. Bedding is more difficult to establish with certainty in high-strain domains or in areas where extensive partial melting and/or melt injection has disrupted the succession. This, together with the lack of distinctive marker horizons, complicates the correlation of lithological packages and the mapping of the internal structure of the syncline despite the excellent 3-D outcrop.

4.1.2 D_1 fabrics - S_1 and F_1 folds

An early, bedding-parallel planar fabric, S_1, is defined by the preferred alignment of basal planes of biotite. S_1 is axial planar to cm- to dm- intrafolial, isoclinal folds (F_1), testifying to the partial transposition of bedding into the early S_1 fabric (Figure 4.4). Large-scale F_1 folding and transposition of bedding is best observed in marbles of the Karibib Formation, where calc-silicate horizons define high-amplitude, intrafolial folds within the generally light-coloured marbles. S_1 is best preserved on the limbs of the BHS where large-scale transposition of the S_1 features by a later event is less evident. This transposition is particularly strong in zones of partial melting and in high-strain zones of the BHS. The identification of F_1 folds in metapelitic horizons is hampered by later metamorphic recrystallisation, porphyroblast growth and partial melting in the metapelitic units that has largely destroyed fine bedding details that allow the characterisation of F_1 folds. The less reactive metapsammites more commonly retain these early features.

Figure 4.4. Field example of intrafolial folding (D_1) in metapsammitic units is indicative of the early F_1 fold generation. The metapelites do not retain early features, but are instead overprinted by later D_2-related fabrics, which commonly causes a strong alignment of the long-axis of cordierite porphyroblasts, the basal planes of biotite and quartz-feldspar aggregates.

4.1.3 D_2 fabrics - S_2 foliation, L_2 lineation and F_2 folds

The BHS is the first-order structure that dominates the geology of the area, forming part of the regional-scale pattern of domal and intervening synclinal structures (F_2) in the south Central Zone (Smith, 1965, Barnes & Downing, 1979, Miller, 1983). It is a moderate- to steep north-easterly plunging syncline with an upright axial plane and sub-vertical limbs that are, in places, overturned (Figure 4.5). Along its axial trace, the BHS can be followed for over 15-20 km, showing a half-wavelength of 3-4 km. On satellite images and aerial photographs, its outline is clearly illustrated by the light-coloured marbles of the Karibib Formation that form a prominent ridge around the younger and dark-coloured metaturbidites of the Kuiseb Formation. Figure 2.2 shows a false colour Aster Image of the study area.

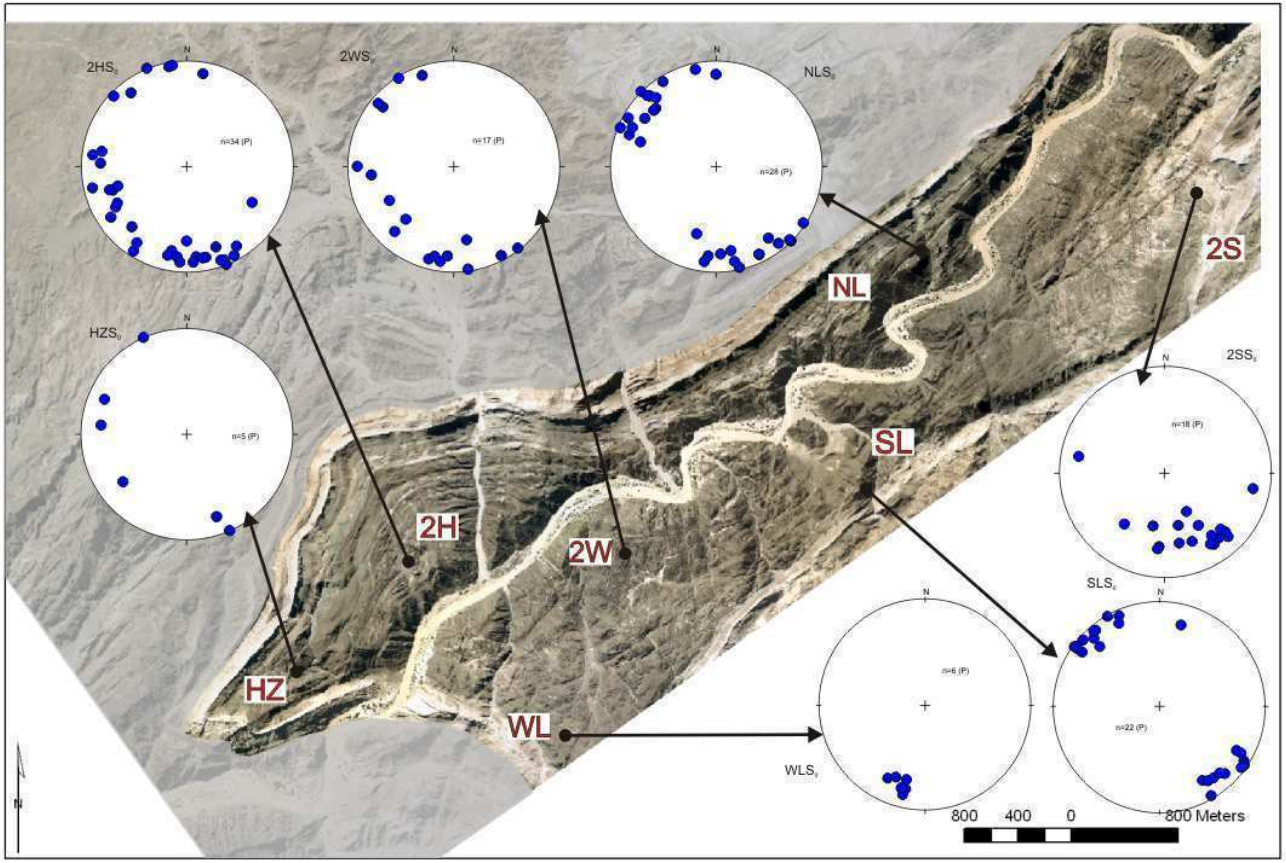

Figure 4.5. Schematic map of the BHS showing orientation diagrams (all lower hemisphere equal area projections) for poles to bedding, S_0, listed for different structural domains. S_0 defines folding in the area. The bedding-parallel foliation, S_1 is not commonly preserved. Domains: HZ – hinge zone; 2H: 2nd-order fold near the HZ, WL: Welwitschia Limb, 2W: 2nd-order fold near the WL, NL: Northern limb of BHS, SL: Southern limb of the BHS, 2S: 2nd-order fold on the SL.

The Welwitschia Syncline here refers to a second-order structure with a southerly trending axial trace that trends at a high angle to the axial trace of the BHS in the north (Figure 4.5). The axial traces of the BHS, the Welwitschia Syncline and smaller second-order folds impinge on each other to form the "Khan River Convergence point" (Poli and Oliver, 2001). The resulting, geometrically complex hinge zone of the first-order BHS seems to be moulded between the relatively regularly shaped regional-dome structures, such as the Rössing Dome, which is characteristic for synformal structures in the southern Central Zone (e.g. Smith, 1965, Jacob, 1974, Coward, 1983, Miller, 1983). Despite the overall strongly non-cylindrical fold geometry, bedding orientations in the individual domains of second-order folds still define mostly great-circle distributions around axes that plunge parallel to the consistent lineation (L_2, Table 4.1) in the cordierite gneisses. Figure 4.5 illustrates the bedding orientations of domains of the BHS as well as specific 2^{nd}-order F_2 structures. Poles to S_0 may also show small-circle distributions for some domains, such as in the second-order fold near the hinge-zone of the BHS, pointing to the non-cylindrical fold geometry of the BHS. The orientations of the L_2a and L_2b lineations have been plotted for the same domains (Figure 4.6) to illustrate their close association with the orientations of the bedding-defined fold axes.

Fold plunges of 2^{nd}- and 3^{rd}- order fold-hinges can vary considerably from the steep NE plunge of the hinge of the first-order BHS and there is a general trend for fold plunges to become shallower towards the NE and away from the SW fold closure of the BHS (Figure 4.6). This also indicates the non-cylindrical nature of the 1^{st}-order BHS, which is characteristic of the synforms of the sCZ of the Damara Belt.

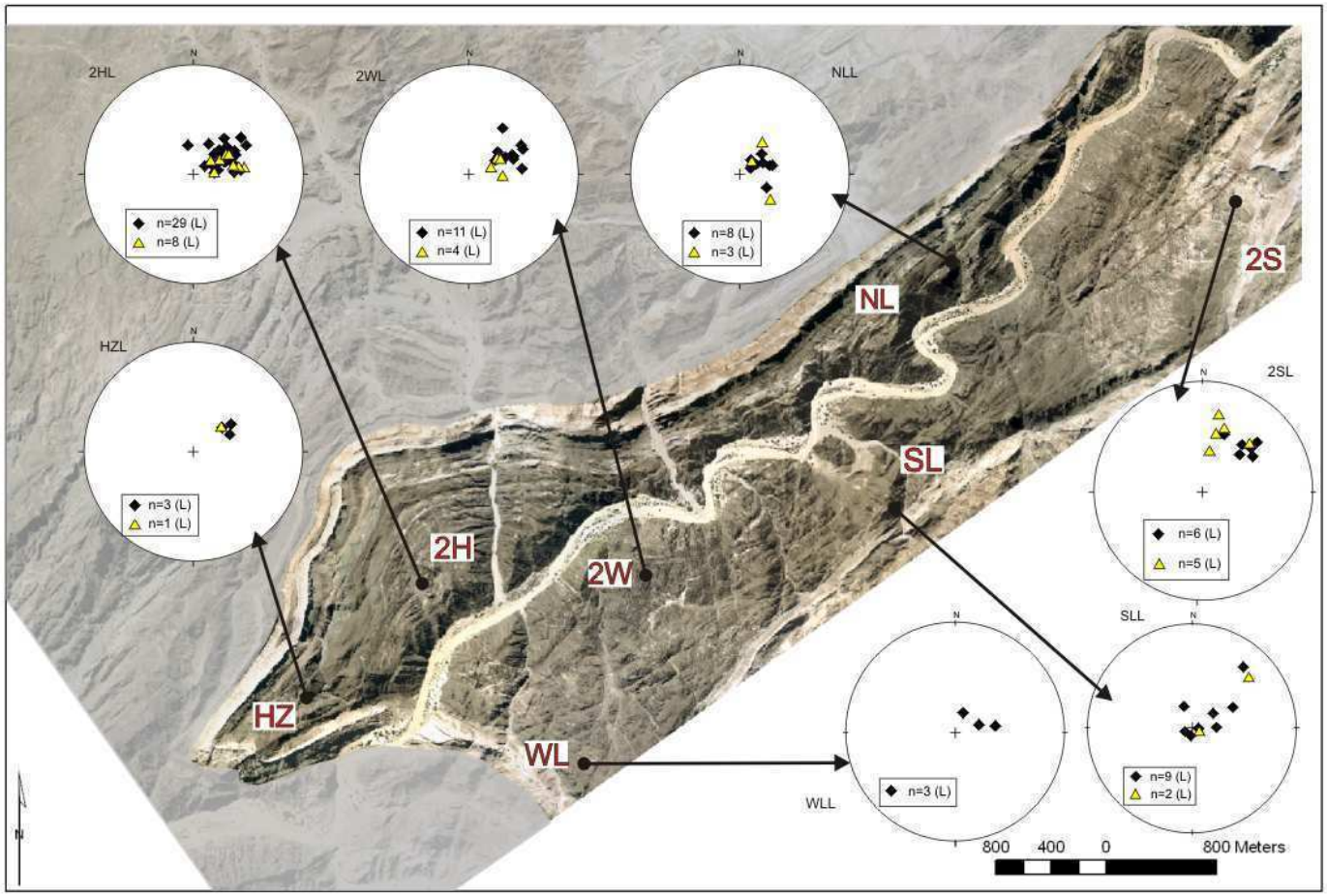

Figure 4.6. Lower hemisphere equal area projections of the trend and plunge of linear fabrics, L_2a and L_2b (table 4.1), for different domains.

F_2 folds are associated with an axial planar foliation (S_2) that overprints the S_1 foliation. S_2 is also defined by the preferred alignment of biotite as well as oriented quartz-feldspar aggregates. For the most part, S_2 is subvertical, showing NE trends, sub-parallel to S_0 and S_1 on the limbs of the BHS, but is clearly evident in the hinges of F_2 folds, where it crosscuts the bedding-parallel S_1 foliation at high angles. S_2 is best developed on the limbs of the BHS (S>L tectonites). Biotite commonly wraps around the metamorphic porphyroblasts of cordierite and occasionally potassium feldspar indicating that metamorphic cordierite, which is part of the peak metamorphic assemblage, was present before the end of the D_2 deformation. Biotite inclusions in cordierite porphyroblasts may, in places, define an older planar fabric. This fabric shows no consistent orientation with respect to the S_2 fabric defined by biotite in the matrix of the rocks, nor is it continuous between adjacent porphyroblasts. The timing of this fabric remains somewhat speculative and it may represent part of the older S_1 fabric preserved in the porphyroblasts, or part of the S_2 fabric, where the porphyroblasts record some degree of rotation during progressive deformation. The coarse-grained nature of the biotite and the granoblastic texture of quartz-feldspar domains indicate that the rocks underwent a certain degree of post-tectonic static recrystallisation.

One of the most characteristic structural features is a strong, though variably developed, linear fabric in the rocks. This stretching lineation shows consistent moderate- to steep NE plunges, parallel to the plunge of the first-order BHS and associated parasitic folds (F_2), suggesting a genetic relationship between the F_2 folding, the S_2 foliation and this stretching lineation, henceforth referred to as L_2a. The intensity of the linear fabric depends on (1) the composition of the rocks and the presence of suitable minerals and mineral assemblages that define the lineation, and (2) regional variations in strain intensity and strain type. L_2 is best developed in cordierite-biotite gneisses, where it is defined by the preferred orientation of the long axis of cordierite porphyroblasts, stretched quartz-feldspar-biotite aggregates and/or thin, rodded leucocratic segregations. It is less prominent in e.g. metapsammites, where cordierite porphyroblasts are scarce so that L_2 is very poorly developed and often not discernable.

In areas where the rocks are pervasively rodded, the S_1/S_2 foliation becomes indistinct, anastomosing around the cordierite porphyroblasts and rodded mineral aggregates. In the SW hinge zone of the BHS, this fabric is so strong that almost all planar fabrics are completely disrupted and almost no original bedding features remain (L>>S). Here, the leucosomes of migmatites occur as long cigar-shapes that plunge steeply to the NE. Indeed, this orientation of the lineation is constant throughout the area with some variation to shallower and steeper plunges around the average of 060/60 (Figure 4.7).

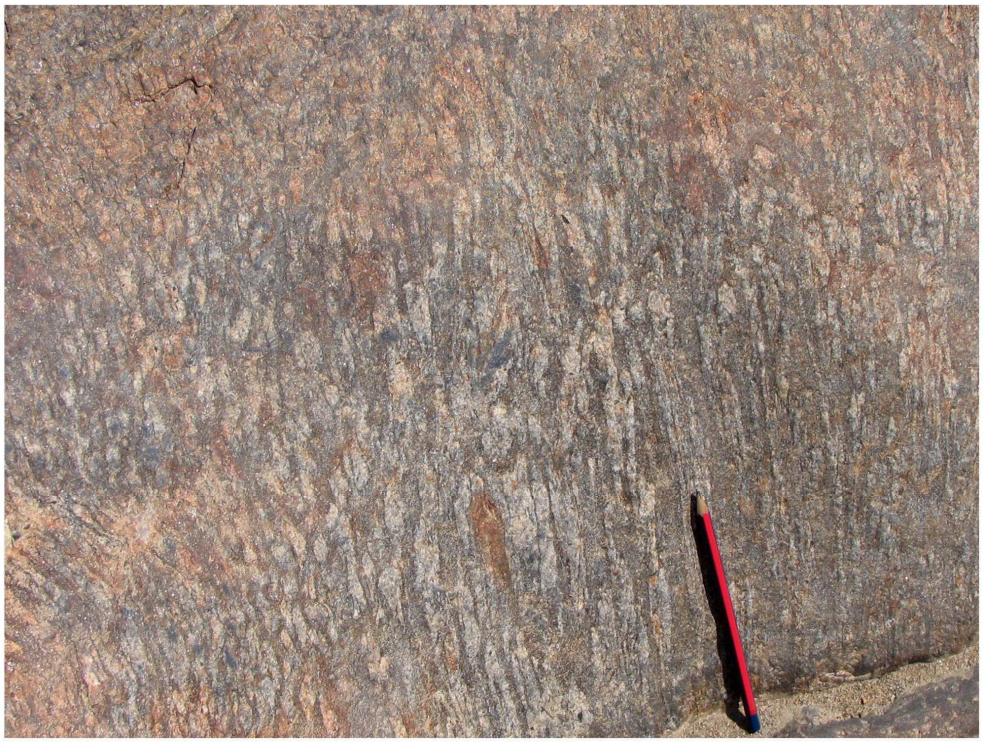

Figure 4.7. Oblique-section through the strong rodding lineation, L_2, is defined by stretched, cordierite-bearing, quartz-feldspar aggregates (parallel to the pencil) in this picture, plunging steeply to the NE.

The hinge lines of small (less than 1 m half-wavelength) folds of quartz-feldspar veins and of thin beds of metapsammite or calc-silicate define a lineation, L_2b. This lineation is parallel to the mineral lineation, L_2a, as well as the plunge of higher-order folds in which they occur. L_2b does vary in its steepness, but shows a consistent NE plunge direction.

Although L_2a and L_2b are the only observed lineations, their spatial association with F_2 folds and the S_2 foliation suggests a genetic relationship to D_2 related structures, rather than earlier S_1 fabrics

4.2 Strain in the BHS

Rocks in the BHS show characteristic variations in strain intensity and strain type with, on a regional scale, a clearly domainal distribution. The following is intended to delineate domains of constrictional, plane and flattening strains, with the aim of relating wall-rock strains to the occurrence of leucosomes that may either be sites of anatectix or zones of melt transfer. Wall rock strains are qualitatively described based on the development of linear and planar fabrics, folding and boudinage.

Constrictional strains and L>>S tectonites are particularly prominent in the SW (see above) hinge of the synform, as shown by moderate- to-steep NE-plunging rodding lineations subparallel to fold axes of the first- and lower-order F_2 folds (Poli & Oliver, 2001). Differently orientated quartz and quartz-feldspar veins are invariably tightly folded, with fold axes plunging parallel to the L_2a stretching lineation. Ptygmatically folded veins with L_2-parallel fold hinges are also common. Rodding is defined by the preferred orientation of cordierite porphyroblasts as well as by stretched quartz-feldspar segregations in the metapelitic rocks. These coarse-grained leucocratic segregations can form up to 15 cm long, cigar-shaped structures that may occur pervasively throughout the rock (Figure 4.8).

Figure 4.8. Strongly prolate fabrics are represented by pencil-shaped leucosomes near the SW closure of the Blauer Heinrich Syncline. The pen is aligned along the stretching lineation (L_2a), also corresponding to the fold axes of ptygmatically folded leucosomes and quartz veins that are common in these rocks.

The pervasive constrictional strain that has affected rocks of the Kuiseb Formation in the BHS is not always manifested as a strong rodding fabric. In places, outcrops appear to preserve contradictory evidence for both D_2-related bedding-parallel stretching and shortening. Figure 4.9 shows a folded bedding-parallel vein occurring between beds that are boudinaged and hosting tension fractures formed at a high angle to the stretching lineation. Such strain appears to be incompatible in the same outcrop, but the features can be easily explained when the orientation of the outcrop is taken into consideration with the general interpretation of constrictional strain in the field during D_2.

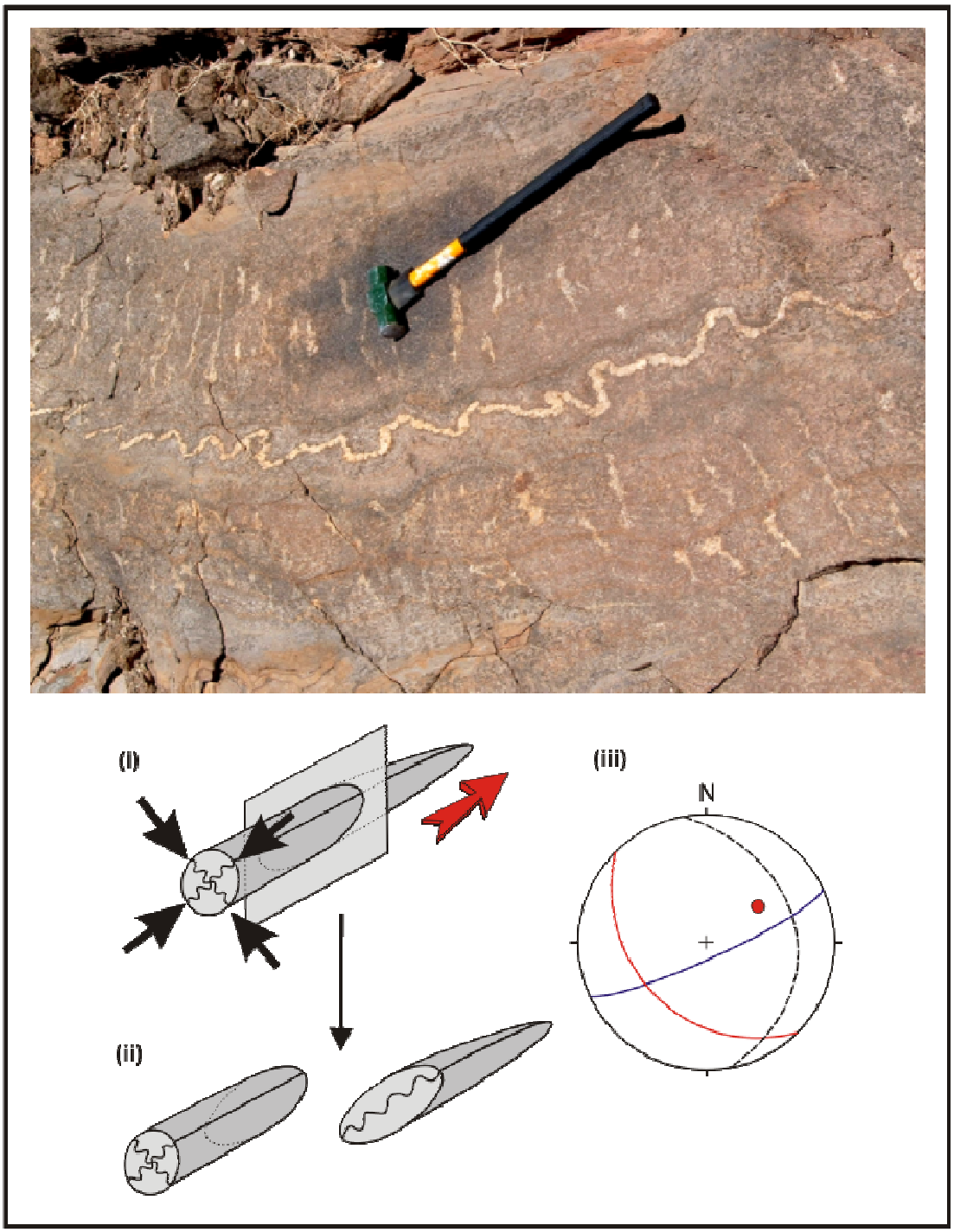

Figure 4.9. Oblique view (photo) of seemingly contradictory field evidence suggesting layer-parallel shortening (folding of central vein) and layer-parallel extension (leucosome-filled extension fractures). This ambiguous expression of folding (compressional) and fractures (tensional), both associated with D_2, together in the same outcrop can be explained by constrictional strain as shown in the strain ellipse which is cut away to reveal the nature of folding displayed in the outcrop. (i) Schematic strain ellipse is cut away (ii) in a plane parallel to the orientation of the bedding in the outcrop in the photograph. (iii) Orientation diagram indicating the lineation (red dot), S_0 (blue great circle), leucosome orientation (red great circle) and the orientation of the outcrop surface (black, dashed great circle).

The accompanying schematic sketch (Figure. 4.9 i,ii & iii) illustrates the relationship between bedding, the average leucosome orientation in this outcrop and the orientation of the surface of the outcrop with respect to the stretching lineation, L_2, which is characteristic of D_2. The strain ellipse (i) is dissected (in ii) at the same angle to the principal axis as the angle between L_2 and the outcrop surface. This illustrates that such a section would still display folding of steeply dipping sills in this outcrop. The leucosomes are developed at a high-angle to the stretching lineation and due to the fairly low angle between the outcrop and the lineation, these structures are exposed as subhorizontal veinlets. This highlights the significance of constrictional strain for the region as a whole.

On the NE-trending, sub-vertical limbs of the BHS, S>L tectonites are dominant. The chocolate-tablet boudinage of competent layers such as intrusive sills or calc-silicate horizons is common. Furthermore, conjugate sets of shear zones are present of which the bisectrix of the angle gives the direction of shortening (Figure 4.10). This, together with the nature of the folding, the orientation of the S_2 foliation and chocolate-tablet boudinage, enveloped by S_2, record a NW-SE directed, subhorizontal bulk flattening strain.

In the absence of good strain markers, the transition between the domains of strong prolate strain and the zones of flattening strain shown above is difficult to identify as a result of the gradual changes between the two endmember cases.

Figure 4.10. Chocolate-tablet boudinage of granite sills in subvertical metapelites of the Kuiseb Formation on the steep NE limb of the BHS. (a) 3-D Chocolate tablet boudinage of a leucocratic sill is evidenced on two perpendicular outcrop surfaces. (b) Cross-sectional view of boudinage and the development of conjugate sets of shears in subvertical Kuiseb Formation and granite sills, both indicating layer-normal flattening.

Synopsis: structural evolution of the BHS

The early, bedding-parallel S_1 foliation and associated intrafolial folding (F_1) recorded in gneisses of the Kuiseb Formation are a regionally observed feature, commonly related to low-angle shearing, imbrication and recumbent folding of the rocks (e.g. Miller, 1983). The recumbent F_1 folds and S_1 foliation are refolded to form the regional F_2 fold of the BHS. The NE trend and subvertical orientation of S_2 and, in particular, the chocolate-tablet type boudinage and/or symmetrical folding of e.g. granite sills contained in the S_2 fabric on the steep limbs of the BHS suggest a subhorizontal, NW-SE bulk shortening strain during D_2. The steep NE plunging rodding fabrics preserved in e.g. the SW hinge of the BHS point to the oblique and orogen-parallel extrusion of the rocks (Kisters et al., 2004). In other words, subhorizontal flattening strains observed predominantly on the limbs and oblique extrusion of rocks mainly recorded in the hinge of the BHS seem to

have developed in response to the subhorizontal shortening as, for example, has also been suggested by e.g. Oliver (1994) and Poli and Oliver (2001). However, the absence of non-coaxial fabrics in the study area does not support Poli and Oliver's (2001) assertion of an oblique collision, at least for the area of the BHS. This may reflect a regional-scale partitioning, where the non-coaxial component of the bulk strain has been partitioned into the Omaruru and Okahandhja Lineaments to the north and south of the sCZ, respectively (Poli and Oliver, 2001). The intervening areas may record the coaxial flattening component during the oblique convergence as it is recorded here in the BHS.

4.3 Structural setting of Granites and Leucosomes

4.3.1 Features related to *in situ* anatexis

Throughout the BHS, there is textural and mineralogical evidence for an *in situ* incongruent melting reaction occurring at structural sites related to extension, the details of which were discussed in Chapter 3. Four main different structural sites can be distinguished and are described in detail below, from the most to the least abundant, and illustrated in Figure 4.11 (a-f).

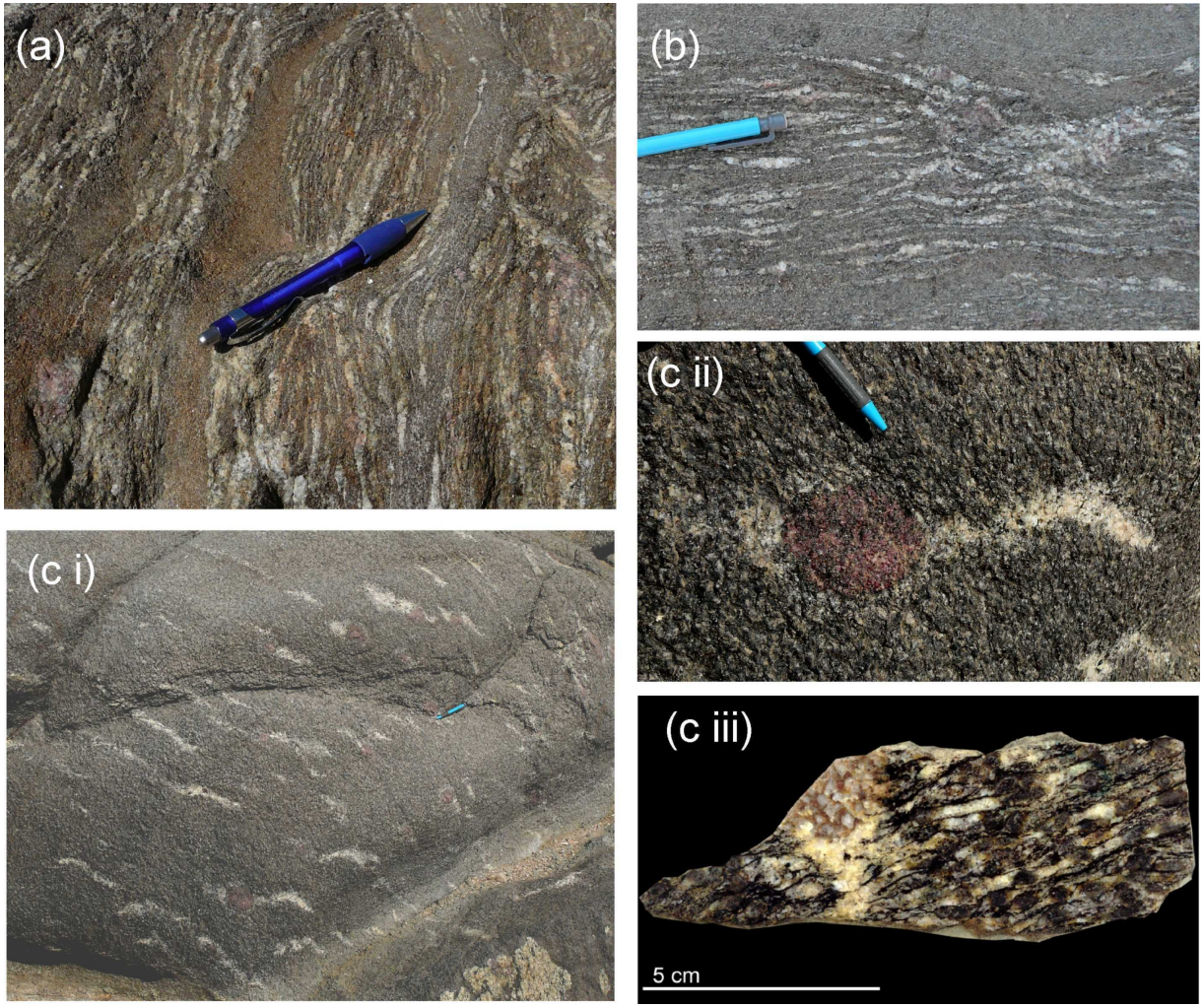

Figure 4.11.

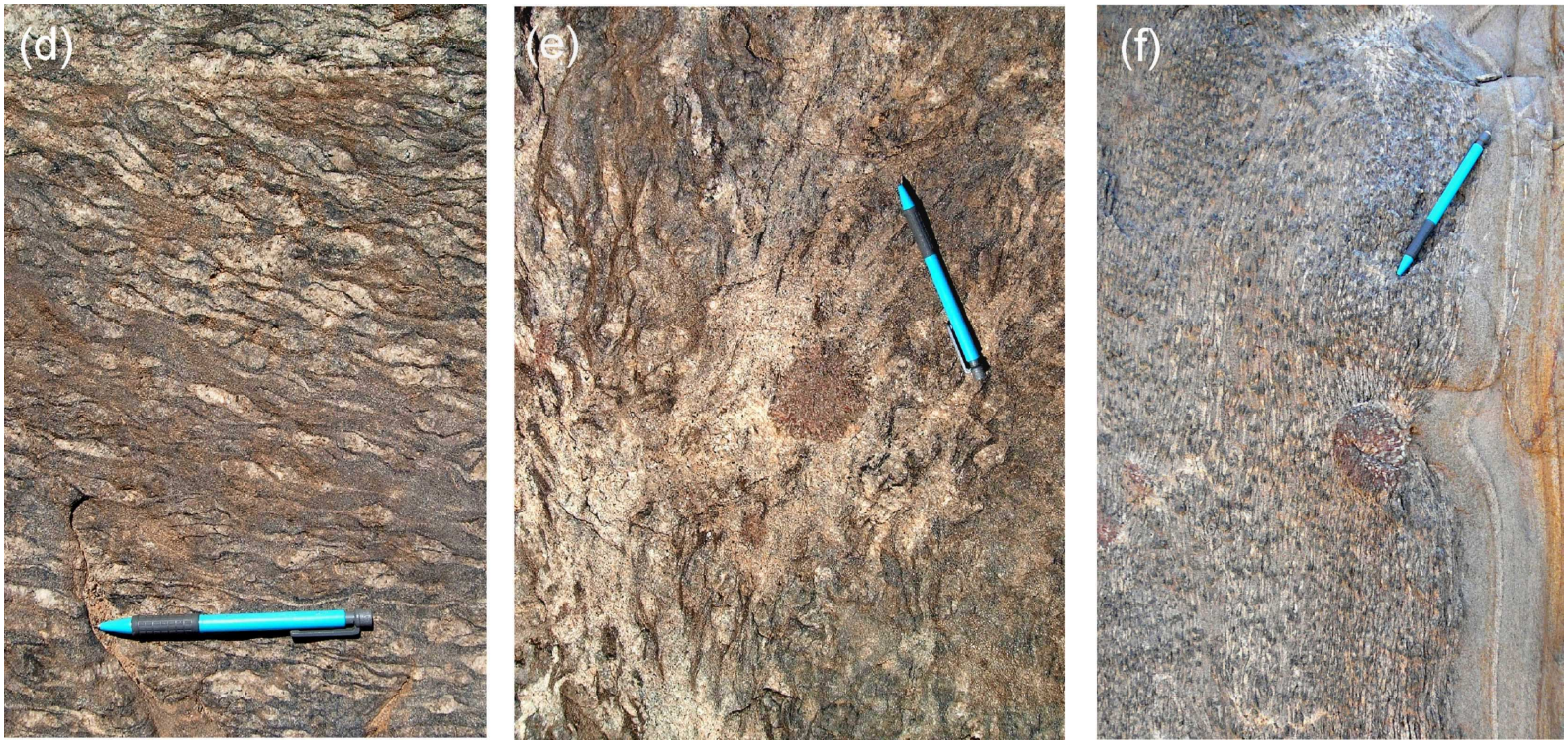

Figure 4.11 (continued). Leucosome types of the study area. a & b) Stromatic leucosomes found in thin metapelitic units separated by beds of unmelted metapsammite. A new generation of garnet and cordierite are associated with the leucosomes. c) In the dominant leucosome type large poikilitic crystals of garnet are hosted by lens-shaped leucosomes. The leucosomes occur in distinctive regularly spaced fracture arrays (c i) that occur at a high angle to the lineation in the host rocks. The garnet leucosomes are often found to have a high garnet to leucosome ratio and many display collapse of the surrounding foliation, indicating volume loss. The leucosome is not associated with a distinct mafic selvage (c ii) and has a coarse granitic texture, which is in mineralogical continuity with the quartz-feldspar segregations in the host rock. (c iii) is a polished slab of a garnet leucosome, cut parallel to the lineation; it illustrates the mineralogical continuity of the leucocratic material, garnet porphyroblast texture and shows the inclusion-poor cordierite rims on pre-existing metamorphic cordierite porphyroblasts. d & e) illustrate nebulitic leucosomes that host a new generation of garnet associated with the leucosome material. The garnet is subhedral and occurs as grains of several millimetres in diameter, but is occasionally found as coarse porphyroblasts similar to those found in the fracture arrays (e). New cordierite is also associated with these leucosomes and is most commonly inclusion-free and euhedral. (f) Shows garnet-bearing leucosomes hosted in boudin interpartitions. These structures are interpreted to represent melting features similar to those in fracture arrays (c, above) but these particular examples are almost entirely devoid of leucosome material suggesting the majority of the melt was lost.

1. The most common occurrence of leucosomes is in shallowly-dipping fracture sets that contain large, poikiloblastic garnet crystals (Figure 4.11 c (i, ii, iii)). In cross section, these leucosomes occur as 10-50 cm long lenses, characterised by a coarse-grained granitic texture and euhedral feldspar crystals, as well as typically one, or several, large (50 to 120 mm) poikiloblastic garnet crystals. Although the boundary between the leucosome and the gneiss is generally well defined, it is not a sharp contact nor is it defined by a distinct mafic selvage. There is mineralogical continuity between foliation parallel quartz + feldspar segregations in the gneissic matrix and the same minerals in the leucosome, as can be seen in Figure 4.11 c iii. The leucosomes consist of coarse-grained quartz, plagioclase and potassium feldspar with biotite present in variable amounts. Garnet is present as a peritectic product of the melting reaction occurring as large poikilitic crystals within the leucosome together with clear, inclusion-free overgrowths of new cordierite on metamorphic cordierite porphyroblasts within the gneisses adjacent to the leucosomes (Figure 4.11 c iii). In any individual outcrop, but also between outcrops on a regional scale, the leucosome lenses show a remarkably consistent orientation normal or at high angles to the mineral stretching lineation. Figure 4.12 shows a typical, shallowly dipping, garnet-bearing, lens-shaped leucosome together with stereographic plots of the orientation of 62 similar structures with respect to the average lineation of the study area. This illustrates the consistent orientation of the leucosomes at a high angle to L_2a and L_2b. Conjugate sets do occur as a variation from the dominant sub-normal orientation of the leucosomes to the lineation; this accounts for some of the scatter in the data. The solidified leucosomes remained largely undeformed, but the progressive steepening of fold limbs and associated passive rotation of the leucosomes may also cause some of the scatter in the data. The consistent orientation of the structures with respect to the stretching lineation, together with the lack of lateral displacement along fracture walls, suggest they are mainly extensional fractures. A component of shear displacement must be expected for fractures that occur in conjugate arrays. The leucosomes occur in sets/arrays that have a variable spacing, but are generally in the order 0.5 – 1.0 m apart. The spacing varies in adjacent lithologies,

indicating that fracture spacing is also controlled by rheological variations between beds and the relative competencies of units. However, the leucosomes do not seem to cross lithologies into adjacent metapsammitic rocks. The ratio of leucosome to garnet is commonly highly variable and individual fractures may, in places, only show a very small leucosome to garnet ratio. In fact, large, cm-size garnet crystals can be observed to be entirely embedded in biotite schist with no evidence of leucosome material. This is interpreted to indicate melt loss from the melting sites (e.g. Kriegsman, 2001) causing the collapse of the wall-rock foliation into the garnet-bearing dilatant sites, forming characteristic "pucker-structures" (Figure 4.11 c ii and f).

2. Garnet-bearing leucosomes are also developed in the inter-boudin spaces of thin, competent metapelitic beds. These leucosomes have the same mineralogy and textures as the leucosomes in the fracture arrays (point 1, above). Boudin-neck leucosomes also show large poikiloblastic garnet crystals developed in the coarse-grained granitic material without any melanosome. As with the leucosomes developed in the sets of dilatant fractures, these structures often contain relatively little leucosome around the large poikiloblastic garnets (Figure 4.11 f). Spacing between the boudin-necks is variable, but in the order of 0.5 – 1.0 m and commonly form in beds less than 0.3 m thick. These structures are more common on the limbs of the BHS, where, as described in chapter 4.2., a bulk flattening strain is recorded in the rocks.

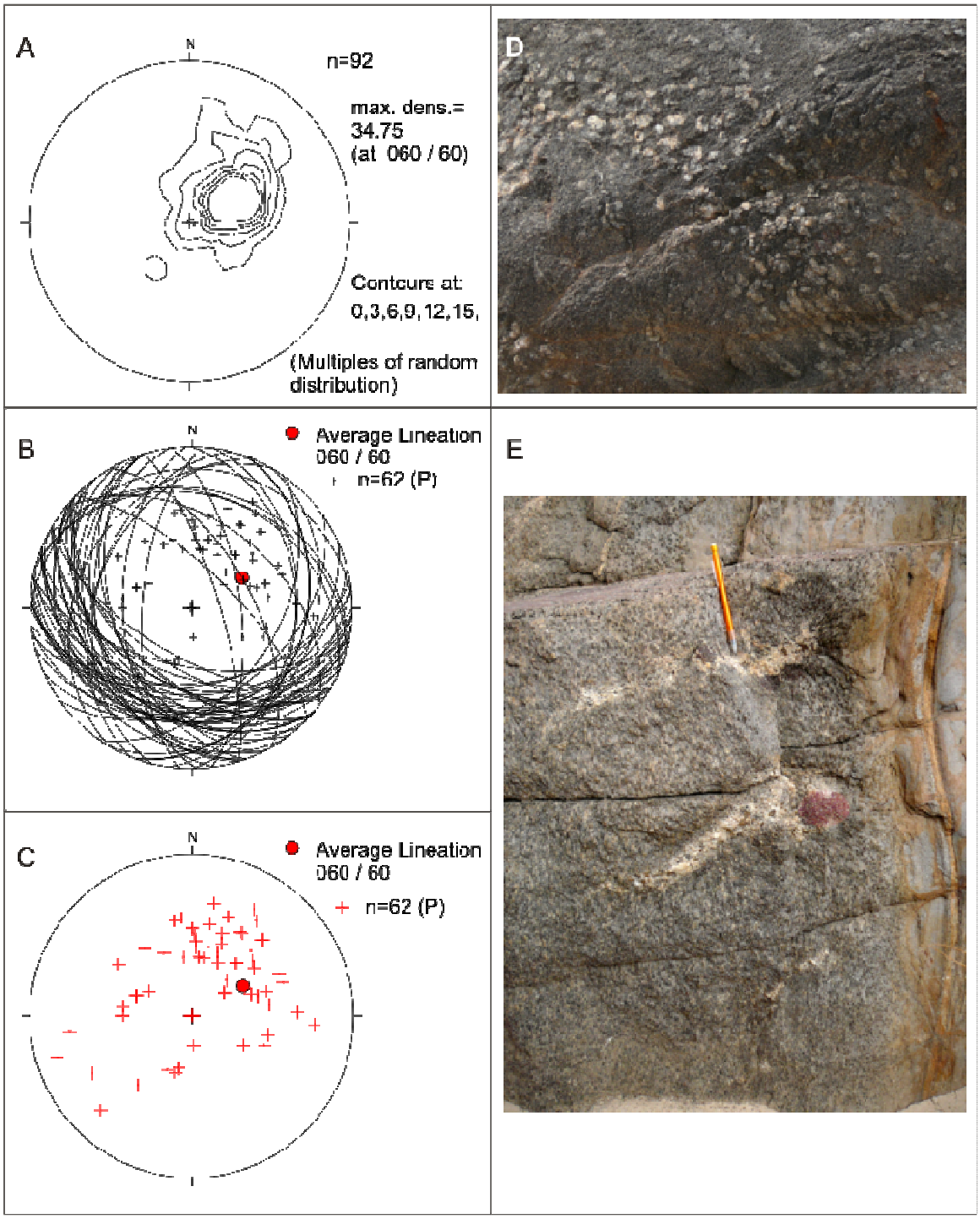

Figure 4.12: A. The average lineation (L_2a) plotted by means of a density distribution in the orientation diagram. B. and C. Show the leucosome orientations as great circles and pole to the planes respectively for comparison to the average lineation. D. Typical example of rodded leucosomes, defining the lineation. E. Typical fracture-hosted, garnet-bearing leucosomes. The variation in the orientation of the leucosomes may be as a result of a primary control with variation in the orientation of the lineation and/or variations due to conjugate sets of shear fractures, or as a result of deformation and folding (rotation of the leucosomes) subsequent to their crystallisation.

3. Elongated leucosome pods that are pervasively developed in regions of strongly constrictional strains. These are largely restricted to the SW hinge of the Blauer Heinrich Syncline. These leucosomes form 1-3 cm wide, but up to several decimetre long rods parallel to the mineral stretching lineation (L_2a). In plan view, the spacing between the leucosomes is in the order of 5 – 10 cm, but they can occur tightly clustered and pervasively developed throughout the rock (see Figures 4.8, 4.11 d and 4.12 d). The pencil-shaped pods of granitic-textured leucocratic material contain a texturally distinct generation of cordierite and/or garnet. Garnet is generally absent from the matrix of these rocks, which became highly disrupted during anatexis and the high degree of deformation. In the rare cases where garnet is found in the matrix as well as in the anatectic patches of the rock, the mineral is distinctly coarser in the leucosomes (up to 15 mm in diameter). Cordierite is abundant in the matrix of the metapelites but is inclusion rich and anhedral, whereas cordierite associated with the leucosomes is inclusion-free and commonly euhedral. Although garnet is more commonly subhedral and somewhat less poikiloblastic, these rocks also contain examples of garnet poikiloblasts similar to those described for the leucosome fracture arrays (Fig 4.11 e).

4. The least common of the migmatite types in the study area is developed as typical stromatic leucosomes (Ashworth, 1985) that form thin (< 1.5 cm wide, ca. 2 cm apart), bedding-parallel stroma that contain garnet and/or cordierite (Fig. 4.11 a,b). The peritectic phases in these leucosomes show distinctly different textures compared to the occurrence of the metamorphic varieties of these minerals within the host gneisses. Cordierite is typically almost inclusion free and euhedral, whereas it is anhedral and poikiloblastic in the wall-rock gneisses. Garnet is typically absent from the cordierite gneiss and where it does occur, is much smaller (< 3 mm) than the garnet occurring within these leucosomes, which forms grains between 5 – 10 mm in diameter. The typical leucosome – melanosome association is commonly developed in these migmatites. The stromatic

leucosomes are associated with areas of pronounced flattening strain, particularly on the southern limb of the BHS.

4.3.2 Intrusive/ascent features

Figure 4.13 and Figure 4.14 illustrate a range of typical field associations between the cordierite-biotite gneisses of the Kuiseb Formation and granite bodies of various scales. Bedding- and foliation- parallel sills of granite are very common in the study area and often appear to feed into small plutons that show clear intrusional relationships with the host gneisses. Cross-cutting dykes are less common. The textural and mineralogical similarity of the leucosomes, granite sheets and mini-plutons in the study area, together with the nature of their juxtaposition, suggests a close genetic relationship between these former melt-bearing features, which will be discussed here. Furthermore, marbles of the Karibib Formation that bound the field area seem to be a highly effective barrier to propagating granites. This has shielded the siliciclastic metasediments of the Kuiseb Formation in the core of the BHS from the intrusion of late cross-cutting leucogranite sheets that are common in the underlying rock types of the Chuos, Khan and Rössing Formations. Thus, all field evidence points to the fact that the granitic material emplaced in the Kuiseb Formation in the BHS is mostly internally derived from partial melting of these Kuiseb Fromation metasediments.

Figure 4.13. Melt injection features in the Blauer Heinrich Syncline are most commonly sills and mini-plutons. The outcrop displays the typical bedding-parallel sills (centre); some of the sills display pinch and swell and can begin to resemble mini-plutons (top right). Northern limb of the BHS, looking to the SW.

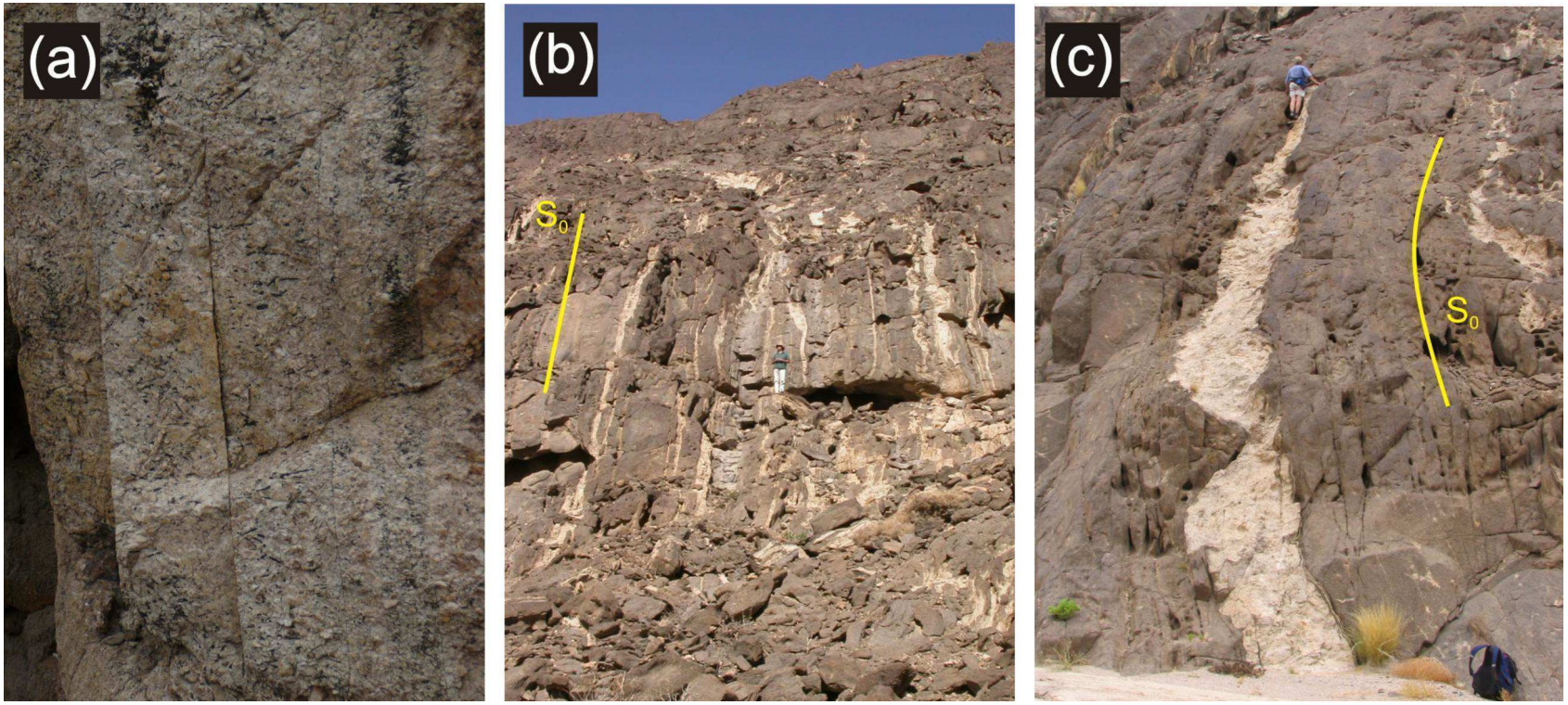

Figure 4.14. a) Sills and plutons commonly display compositional and textural layering that is parallel to the orientation of the sills. The width of the sill is 0.8 m b) Bedding-parallel sheets showing a self-organisation towards fewer, larger sills. These sheets are also associated with 'ladder-structures' that link the leucosomes that bear evidence of *in situ* melting with granite sills. c) Cross-section through the tip of a large sill, illustrating the sharp lateral and vertical terminations of sills in the BHS.

4.3.2. a *Sills*

For the purpose of this study, the term "sill" is used to denote bedding and/or foliation concordant intrusive bodies, irrespective of orientation, whereas as the term "dyke" is used to describe sheet-like intrusives that cross-cut bedding and/or the foliation. Granitic sills are the most abundant intrusive rocks in the study area. They vary in width from a few centimetres to wide bodies of over 25 metres that contain, in places, abundant rafts of the wall rock. Sills of between 0.5 and 1.5 metres are the most common. The largest sills can have strike extents of over several hundred metres. The spectacular 3-D outcrop provides vertical sections of up to 200 metres through the predominantly subvertical stratigraphy and the bedding-parallel sills. The 3-D outcrop reveals the penny-shaped nature of the sills and occasionally also the gradual taper towards the sharp lateral terminations of the sills (Figure 4.14 c). In a study combining field work and GIS analysis of aerial photographs, Barrow (2007) investigated the dimensions of granite bodies in the BHS. He found that the larger granite bodies (minimum thickness of 2 m) had moderate aspect ratios and that the dimensions also depended on the location of the granite body with respect to 1st and 2nd order D_2 structures. The average length:width ratio of intrusive bodies of domains within the BHS range between 30:1 and 75:1. This study did not consider the thinner granite sheets and also did not consider the possibility that the larger bodies are commonly constructed of many smaller sheets (see below).

As discussed in Section 3.2.3, the sills are interpreted to be intrusive features as they are not associated with a mafic selvage or peritectic minerals of a generation that would indicate that they formed by *in situ* anatexis.

There are numerous areas where the sills occur as dense clusters separated by as much as 100-150 m thick packages of schists belonging to the Kuiseb Formation that are devoid of sills (Figure 4.15). Large sills are commonly internally sheeted and display multiple intrusive relationships, i.e. a sill is made up of distinct, individually intrusive smaller sills. The clusters also display multiple sheeting that has become so pervasive that only a 'ghost-stratigraphy' of the pre-existing bedded schists is preserved in nearly massive

granite. Closer inspection reveals the sheeted nature of the leucocratic material as shown in Figure 4.14 a.

Figure 4.15. On a regional scale, sills tend to be clustered into 20-50 m wide zones characterized by the close spacing of intrusive sills and multiple intrusive relationships. These clusters are separated by 100-150 m wide packages of biotite schist that are largely devoid of intrusive granites.

The granite sills are variably deformed. Many of the sills have been folded by tight to isoclinal F_2 folds, together with the wall rocks. It is also common to find chocolate-tablet boudinage of sills on the limbs of the BHS, indicating the layer-normal co-axial flattening of the wall rocks and intrusives. The size and shape of boudins is related to the thickness of the sills as well as to the competency contrasts between the intrusive material and the host rocks, as illustrated in Figure 4.16 (See also Figure 4.10). Despite having undergone D_2 strains, the sills rarely contain any fabric or evidence of internal deformation,

emphasizing the large rheological contrast between the coarse-crystalline, feldspar-dominated granite and the foliated, biotite-rich and finer-grained metasedimentary rocks.

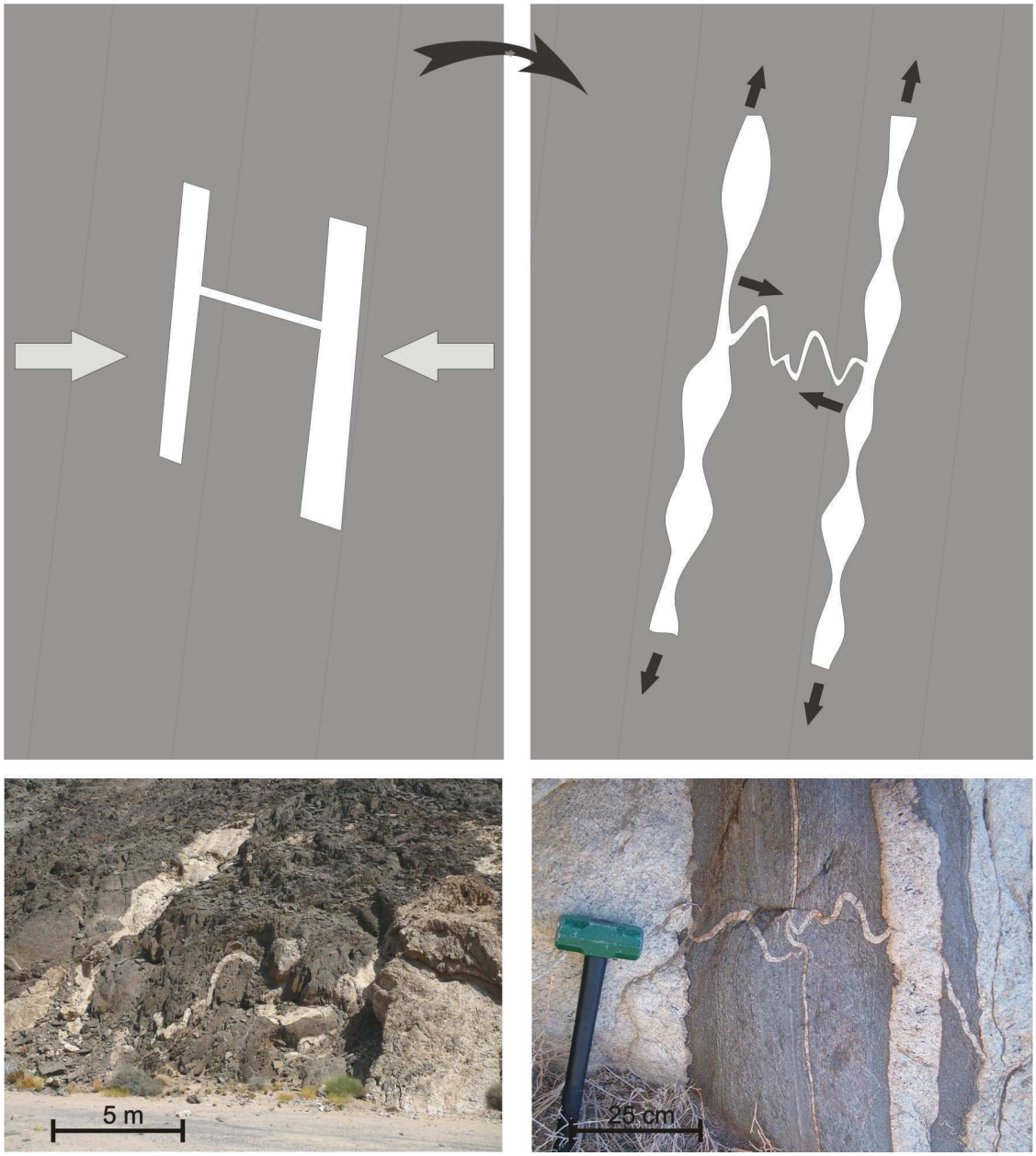

Figure 4.16. The deformation of the syntectonic granite sills and dykes indicate sub-horizontal shortening during D_2. The bedding-parallel sub-vertical sills are stretched and commonly display boudinage or pinch-and-swell, whereas the shallowly dipping dykes are folded in response to the shortening. Field examples of this are evident on a variety of scales.

4.3.2. b *Dykes*

Dykes show very similar compositions, compositional variations and textural appearance to the bedding-parallel sills. The dykes occur on a variety scales, but are most commonly less than 2 metres wide and rarely exceed 20 metres in length. They do not generally form large, cross-cutting features, but instead appear to be mainly short connecting features between sub-vertical sills. Where dykes are abundant a stockwork-like pattern of sills with large strike and up-dip extents, connected by shorter high-angle dykes is formed (Figure 4.17 (A-E)). Cross-cutting relationship between dykes and sills are highly variable and, importantly, not consistent. Two end-member cases can be observed at dyke-sill intersections. In the first case, dykes sharply cross cut sills or vice versa. The cross-cutting relationships are clear when dykes and sills differ texturally and compositionally from each other. In contrast, cross-cutting relationships may be difficult to identify and resolve if compositional and textural variations are subtle. There are also cases where mineralogical and textural continuity is maintained across dyke-sill intersections. When the dykes and sills show evidence of continuity, the dykes can be seen to terminate or widen upon intersection with the sills. Sills can also be seen to terminate on the dykes and occasionally show a biotite rind (mafic selvedge) marking the position of the 'collapsed' sill (Figure 4.17 C). The interconnectivity is shown in Figure 4.17 D where a swarm of closely spaced sills intersects a shallowly dipping dyke. Below the intersection there is a greater number of sills than sills that connect from above. However, the sills above the dyke are larger than those below, possibly indicating a focusing of many sills into fewer, but larger conduits along the dyke during upward migration of the melt. The figure also shows the biotite selvedges that occasionally preserve evidence of sill collapse. This is interpreted to be a common process, but evidence for it is rarely preserved, or recognised, because the bedding-parallel sills do not have significant reaction halos that would mark the passing of the melt and any thin biotite rind, as shown in the figure, would be susceptible to destruction by recrystallisation.

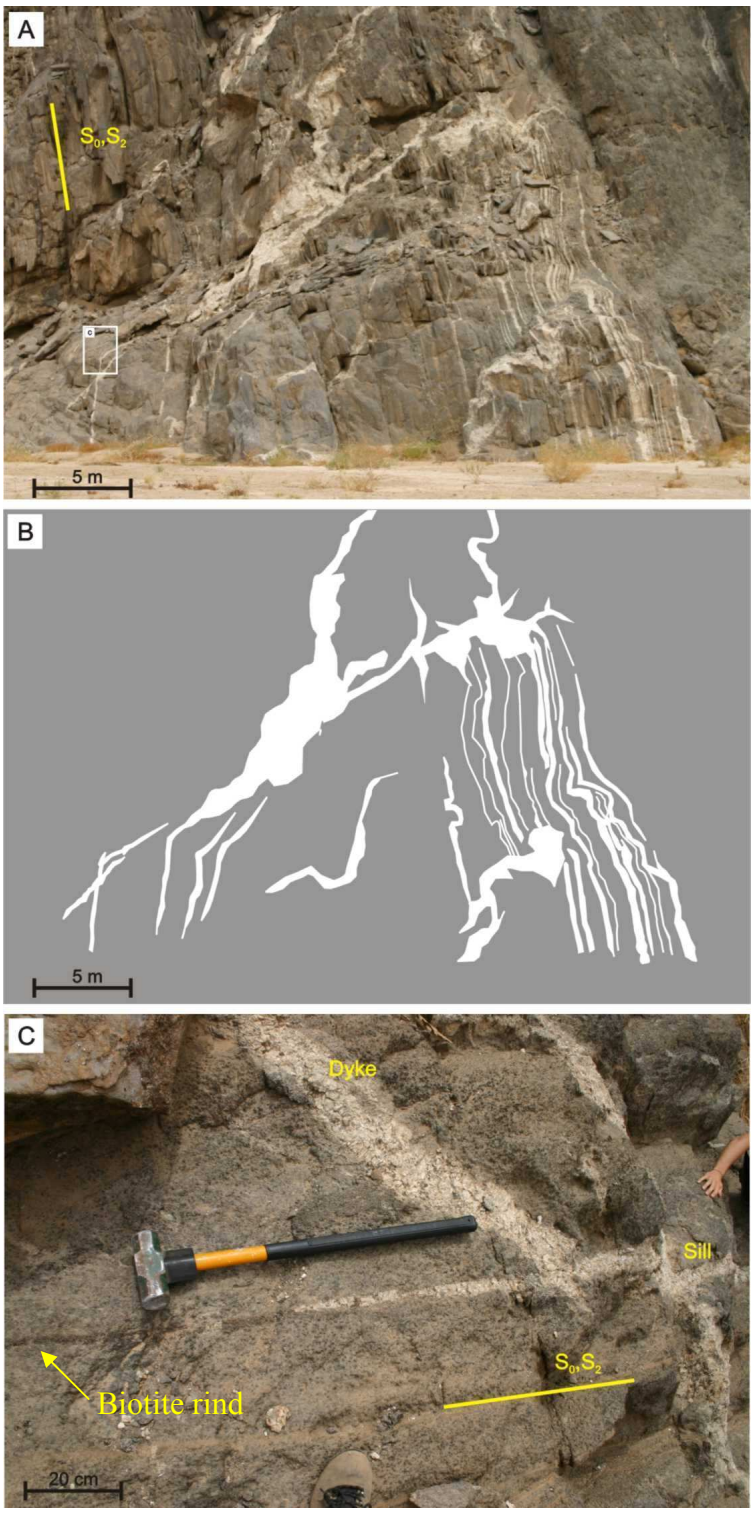

Figure 4.17. (A-C) Interconnectivity of granite sheets in the Kuiseb Formation; A (photo) and B (line drawing) show the focussing of small, closely spaced sills (bottom half of the figure) along the shallowly-dipping, cross-cutting dykes, and self-organisation to fewer, larger sills. C is an enlargement of the block in A that shows a biotite rind where a sill has collapsed after intersection with a dyke.

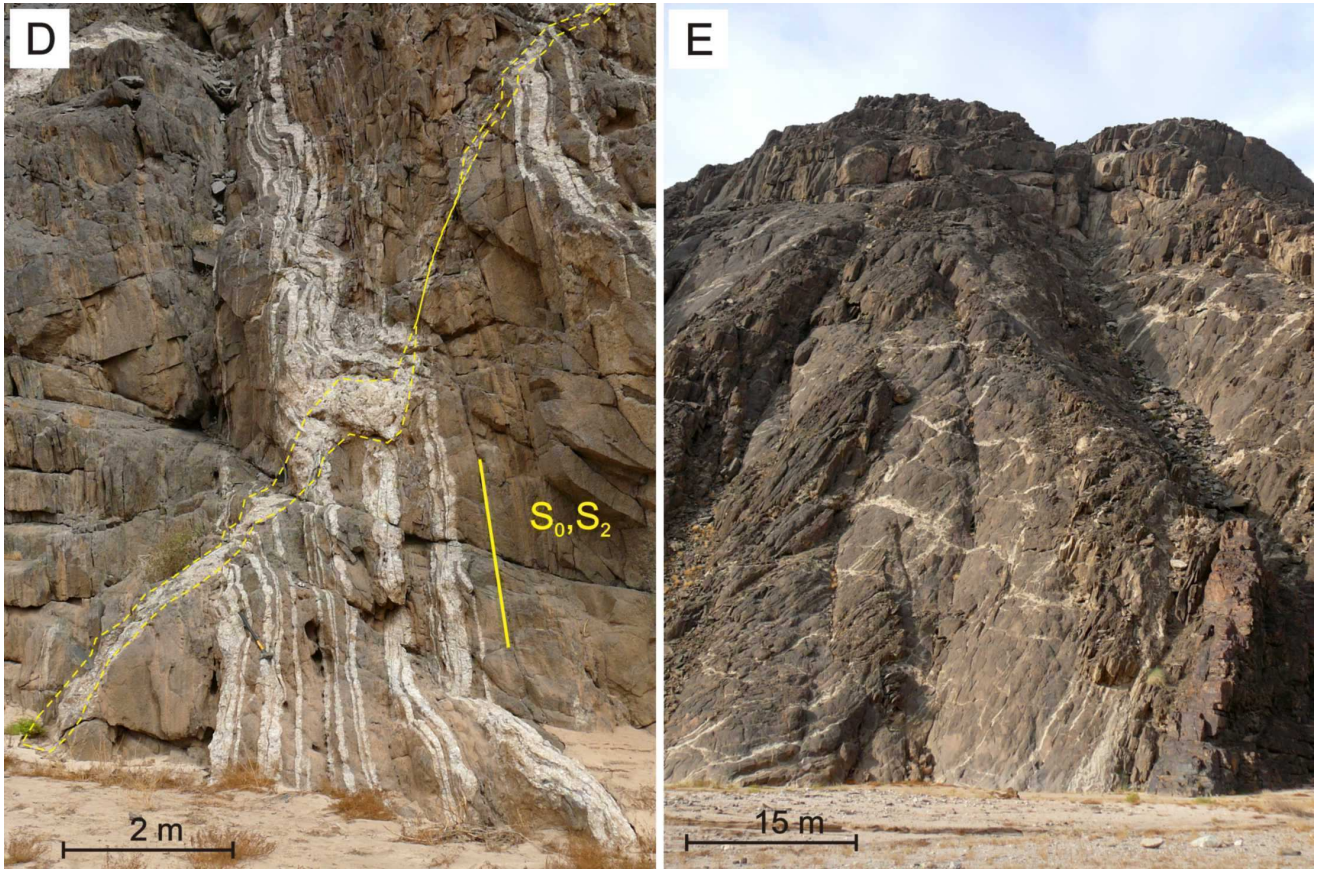

Figure 4.17. (D & E) Interconnectivity between granite sheets in the Kuiseb Formation; D shows the reduction in the number of sills across a dyke, as well as the accompanied increase in size. E shows a large stock-work of sills and dykes and represents one of the few areas where dykes (subhorizontal granite sheets) are volumetrically significant in comparison to sills.

In some particularly large outcrops, a stock-work of sills and dykes has produced a large-scale melt network that is reminiscent of that discussed by Brown (1994) and Weinberg (1999) forming a possible pathway that would be highly efficient if all the conduits were open and active simultaneously and driven by a sufficient supply of magma from below (same authors). The variable cross-cutting relationships of dykes and sills in the BHS demonstrate the importance of both spatial and temporal connectivity for interaction of magmas in melt networks and the requirements for efficient magma movement through this part of the crust.

4.4 Controls of leucosome formation in dilational fractures

The localisation of melting sites largely confined to the dilational fracture arrays underlines the structural controls of the melting reactions. This chapter attempts to describe the role of deformation for melting and the begining of melt segregation. Details of the reactions that led to partial melting and the formation of anatectic leucosomes will be presented in Chapter 11 and the structural and petrographic aspects will be discussed in conjunction in Chapter 12.

The segregation and accumulation of melt in the otherwise largely impermeable mid-crustal rocks is determined by mainly two factors, namely (1) the presence and/or formation and subsequent connectivity of fracture permeabilities that are able to segregate and extract melts, and (2) hydraulic gradients that drive melt flow and any fluid flow (McCaig, 1988, Sibson, 1994, Weinberg, 1999, Bons et al., 2004, Brown, 2007). Fracturing, i.e. brittle deformation, of regionally ductilely deforming mid-crustal rocks is a commonly observed feature of many exhumed high-grade metamorphic terrains and quartz veins, granitic dykes or sills testify to fracturing under high-grade conditions (e.g. Etheridge et al., 1983, Ague, 1995). Brittle deformation is commonly, though not exclusively, related to suprahydrostatic and/or lithostatic pressures at the mid-crustal levels, resulting in effective stresses that allow for the tensile fracturing of rocks:

$$\sigma_{eff} = \sigma_n - P_f$$

where σ_{eff} is the effective stress, σ_n the lithostatic pressure and P_f the fluid pressure (Terzaghi, 1924, Anderson, 1936, Hubbert & Rubey, 1959, Secor, 1965, Jaeger & Cook, 1976, Fyfe et al., 1978, see Figure 4.19 a). In high-grade migmatite terrains the presence of partial melts, means that the fluid pressure may be expressed as the melt pressure. Additionally, temporarily increased strain rates may promote brittle fracturing, assisted by high fluid/melt pressures. Hydraulic gradients form mainly in response to (1) the buoyancy of melt, and (2) variations in mean rock stress (Sawyer, 1994, Brown, 2004). Variations in mean rock stress may occur on a variety of scales such as around shear zones, between adjacent lithological layers of different competencies, or in structural sites such as boudin necks or fold hinges (e.g. Collins & Sawyer, 1996b).

Given that the shallowly-dipping leucosome-filled pockets formed as dilatant fractures the cracks represented, at least temporarily, sites of reduced mean stress. Fracture growth was probably incremental so that each fracture event re-established a hydraulic gradient into the fracture site. Any local (cm- to dm-scale) fluid and/or melt flow would, thus, be directed from the wall rock into the dilatant fracture as long as deformation was ongoing. The envisaged process is similar to the mechanisms of fluid-pressure cycling invoked for the focusing of hydrothermal fluids around brittle-ductile fault zones, where hydraulic gradients are created in response to the formation of transient fracture permeabilities during faulting and associated fracturing (e.g. Sibson, 1994).

Melting reactions in rocks of the Kuiseb Formation are not entirely restricted to the fracture sites and foliation-parallel, mainly subvertical stromatic-type leucosomes illustrate the flow of melt from the wall rocks into the dilational sites (Figure 4.20 b, see also Figure 4.11). The mineralogical and textural continuation between the stromatic leucosomes and those in dilatant fractures suggest that the two were physically interconnected and not merely cross-cutting. As such, stromatic leucosomes resemble the cm-scale melt segregation in compaction bands described for example by Brown (2004).

These features suggest that the dilatant fracture arrays fulfill a dual role. They represent (1) the sites of initial melting, as indicated by the almost ubiquitous presence of large peritectic garnets in the fractures and (2) repeated extensional fracturing has also provided hydraulic gradients that focused melt flow on a cm- to dm-scale from the surrounding wall rocks along the foliation into the dilatant sites. The petrographic details and consequences will be summarised in chapter 11.

4.5 Relative timing of intrusive events

In order to produce a sound model of melt formation, extraction and ascent for the migmatites of the BHS it is necessary to demonstrate that the likely ascent conduits (sills and dykes) could have been active in the period during which melting occurred in the fracture-hosted leucosomes. It is necessary to have both a temporal and a spatial connectivity in the network of melt-bearing features to allow the melt to accumulate and move significant distances.

There is clear evidence that granite sills and dykes were intruded during the D_2 deformation and over an extended period of time. The fact that many intrusive sheets show cross-cutting relationships with F_2 folds, yet are either boudinaged or folded as a result of D_2 deformation indicates that these sills are indeed syn-tectonic. Early sills are commonly tightly folded and occasionally also display boudinage. It can be argued that these sills are pre-tectonic, rather than early syn-tectonic, but the close association of all sills to this phase of deformation and their compositional and textural similarity to other granite sheets suggests they are simply an early generation of these structures that have experienced progressive deformation.

Examples of syn-tectonic intrusions, progressing from early to late are illustrated in Figure 4.18. Figure 4.18 B, in particular shows a bedding-parallel sill that has not only been folded, but has made use of the hinge of a metre-scale F_2 fold to pond and cross-cut bedding where the axial plane affords easier dissection of the bedding.

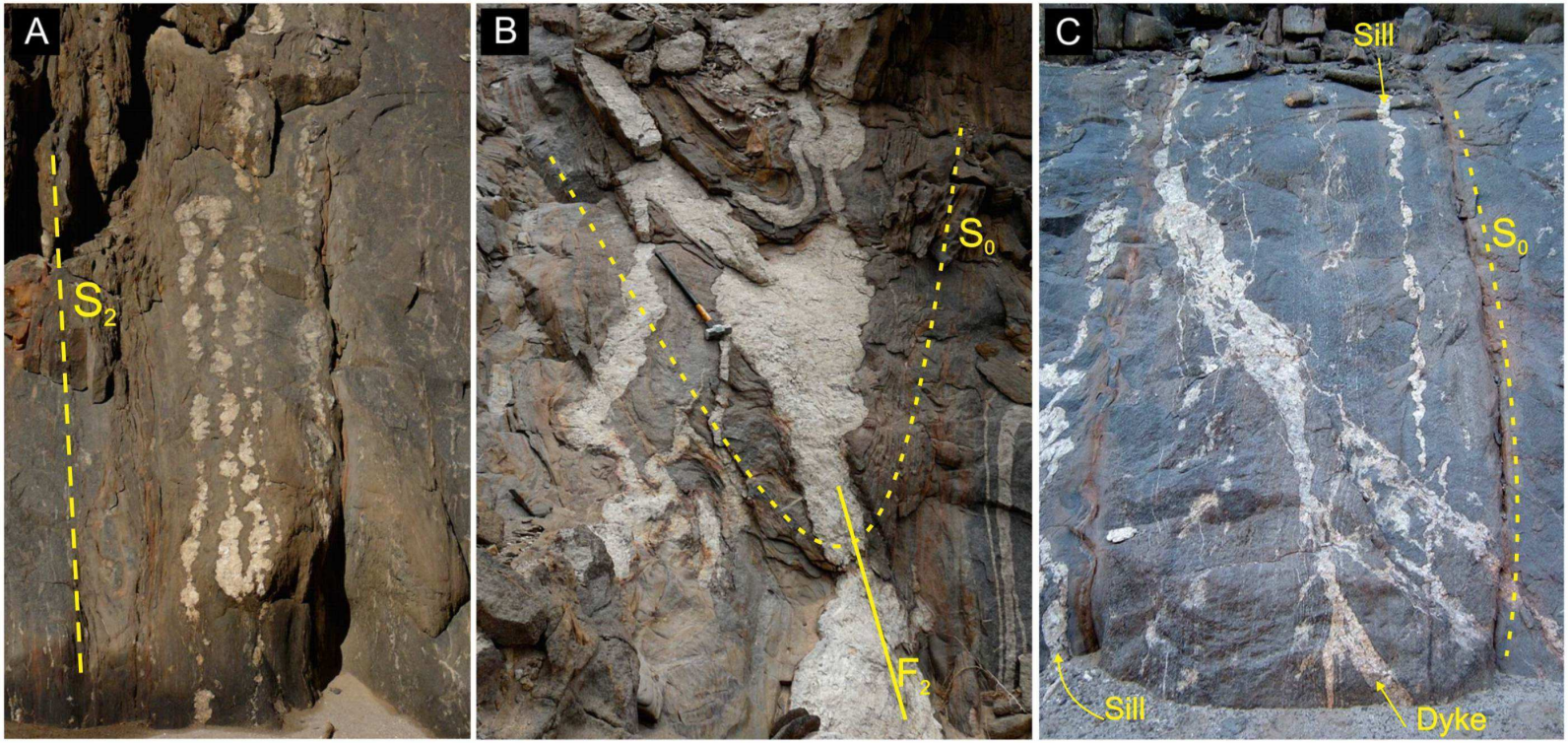

Figure 4.18. Generations of sills from early syn-tectonic, to late syn-tectonic. A) shows an early, isoclinally folded granite sheet that is also boudinaged. B) In this field image, the leucogranite sheet is folded by a 3rd-order F_2 fold (top of the photo), but also cross-cuts the hinge of the fold (leucocratic apophyses in the bottom half of the photo that have an axial-planar orientation with respect to the fold); the image was taken looking approximately down-plunge). This indicates that the fold must have been formed at the time of the intrusion and that deformation continued subsequently. An earlier phase of granite is present in the lower right-hand corner, but the main, coarse-grained granite adjacent to the hammer (1 m in length for scale) is mineralogically continuous with the folded granite sills in the top half of the photo indicating emplacement during a single intrusive event. C) A late, cross-cutting granite sheet (a 'dyke') is undeformed indicating that it formed after the deformation that caused tight folding in the sill on the left and open folding in the sill on the right. Note also how the 'dyke' is only transgressive with respect to bedding for part of its length. At the top of the image it is bedding parallel.

The broadly syn-tectonic nature of the sheeted granites indicates that these structures did indeed form during the same D_2 phase of deformation during which the partial melting of the host rocks also occurred. The relative timing of the sills with respect to the high-grade partial melting is thus consistent with the interpretation that these features may have formed ascent conduits for melt formed during this event.

4.6 Sills versus Dykes

The mechanics of brittle failure of rocks and the propagation of fluid-filled fractures have an important control on the emplacement of dykes and sills in the crust. Lucas and St. Onge (1995) illustrate how syn-tectonic intrusions in the layered mid- and lower-crust may often form at a high angle to the regional shortening direction. The figure below (Figure 4.19) summarises the work of many authors on the concept of "effective stress" (σ^*) (Terzaghi, 1924, Anderson, 1936, Hubbert & Rubey, 1959, Secor, 1965, Jaeger & Cook, 1976, Fyfe et al., 1978). It also illustrates the importance of a fabric in controlling the tensile strength of the rock in different directions. This is the result of the preferred orientation of microscopic flaws (such as grain boundaries or cleavage planes of platy minerals) (e.g. Griffith, 1921, Griffith, 1925).

The rocks of this study are characterised by well-developed anisotropy, S_0, enhanced by S_1 and S_2 on limbs of F_2 folds. Such anisotropy affects the strength of the material in such a way that a rock will have its lowest tensile strength perpendicular to the anisotropy and a maximum tensile strength parallel to any such fabric. This means that the rock will part most easily in the direction perpendicular to the anisotropy, indicating that in a hydrostatic stress regime, where $\sigma1 = \sigma2 = \sigma3$, sheeted intrusions would be most likely to intrude parallel to the anisotropy (Figure 4.19).

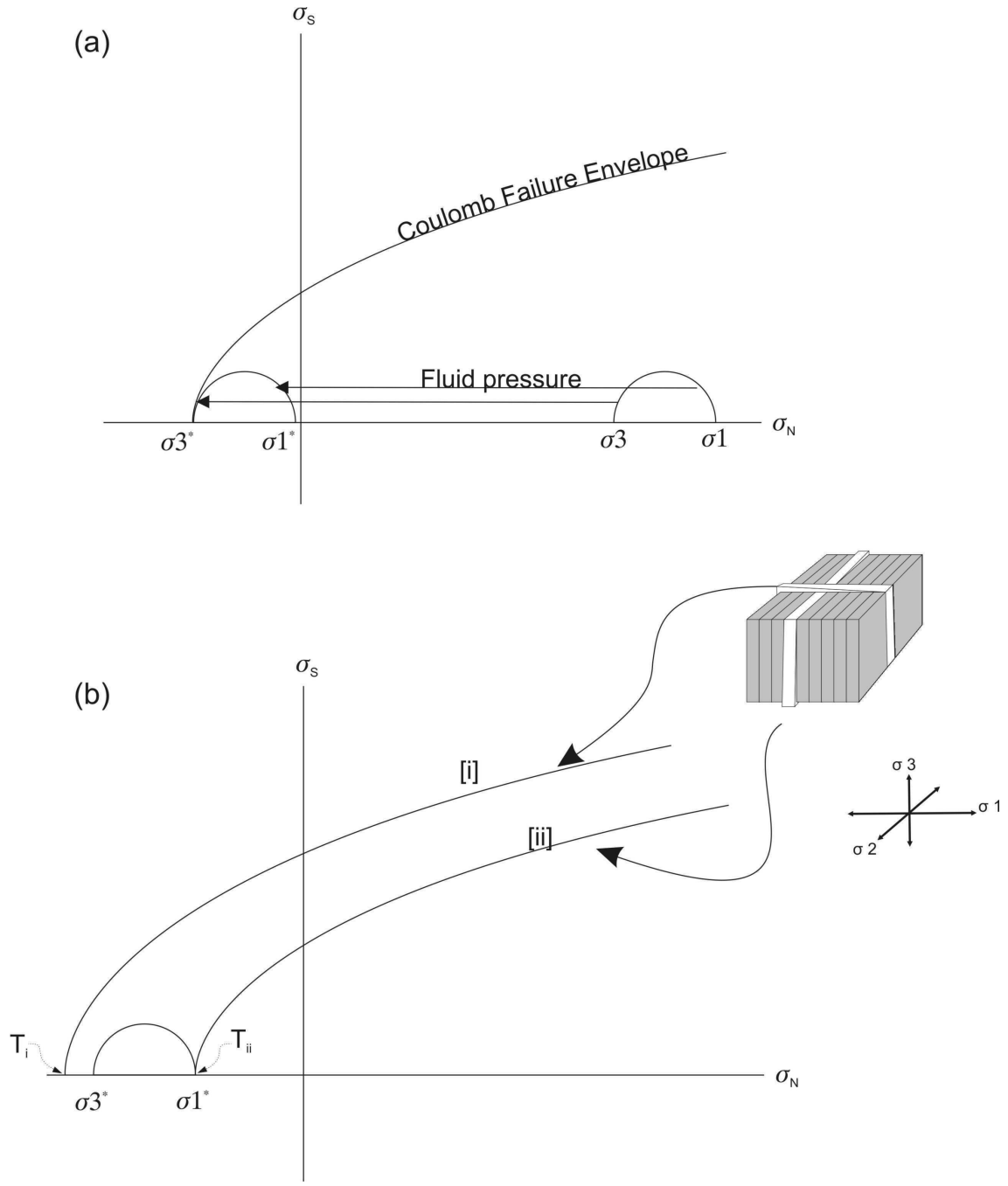

Figure 4.19. Mohr stress circles. (a) The maximum (σ_1) and minimum (σ_3) principle stresses are initially compressional, but with increasing fluid pressure are reduced, by the same amount, until the stress circle encounters the failure envelope and failure of the rock results. The low differential stress (σ_1 - σ_3) ensures that the stress circle will only encounter the failure envelope in the field of tensile failure (at negative normal stress, $-\sigma_N$), resulting in tensile fracture of the rock. (b) The effect of anisotropy in the rock is illustrated in this diagram, with two failure envelopes, one for the failure normal to the fabric (i) and the other for failure of the rock in the plane of the fabric (ii). Failure along the foliation will always occur at lower values of stress, and less negative values, than for fracture across the foliation. [After Lucas and St-Onge (1995)]

Deforming orogens are characterised by the presence of a deviatoric stress and the rocks are commonly bedded and/or foliated and, hence, anisotropic. Unless, in the rare case where σ_3 is normal to the plane of anisotropy, the directions of parting favoured by the pre-existing anisotropy and the principal stress directions will not coincide. When the two are at an angle (i) the magnitude of the differential stress, (ii) the difference in the tensile strengths of the rock parallel and normal to the anisotropy and (iii) the angles of the principal stress directions to the plane of anisotropy, will all play a role in determining the orientation of sheeted intrusions.

As illustrated in Figure 4.19 b, the Mohr stress circle's diameter represents the difference in the tensile strengths of the rock in the plane of the anisotropy and normal to it ($T_{ii} - T_i$). This must be the case such that when the stresses are equally reduced by a hydrostatic fluid pressure it is σ_1* that first encounters the failure envelope of the rock in the direction normal to σ_1 (i.e. in the plane of the anisotropy (envelope [ii])). It is a concept not commonly shown in such stress diagrams as it is difficult to envisage the stress circle passing through the failure envelope without actually causing failure until the trailing edge encounters the envelope. This is because the direction of the anisotropy is not commonly considered in these diagrams. The simultaneous reduction to σ_3* will simply not cause fracture in a direction other than normal to σ_3 and, in this case, normal to the anisotropy.

The dominance of sills over dykes illustrates that the intrinsic properties of the rock are the dominant control on the intrusion of the granite sheets of the BHS. The implications of this are significant because the orientation of the fabric in the rock thus exercised a powerful control on the ascent of magma through this part of the crust.

4.7 The transition from melt segregation to melt ascent

Being hosted in extensional fractures, the leucosomes effectively reside in low-pressure sites, which is consistent with the observation that melt has moved into these sites from the adjacent wall rocks over a distance of several centimetres, upto a few 10's of

centimetres. For melt ascent, these sites of initial melting and melt segregation seem to have an unsuitable orientation. The fractures not only show shallow dips that are likely to inhibit any buoyancy-driven melt ascent, they also form isolated disc-shaped bodies that are, for the most part, not interconnected. The features that indicate transfer of melt and ascent on the outcrop- and regional-scale are the abundant subvertical bedding- and/or foliation- parallel sills. This implies that, in the absence of other melt transfer zones, the sills must have been able to drain melt from the dilational fracture arrays. This, in turn, implies that sills must have provided hydraulic gradients and that mean stresses in the sills were even lower than those in the leucosome-filled dilatant fracture arrays. A prerequisite for any model of melt tapping and melt ascent is that the sites of initial melting and melt storage, in this case the garnet-bearing leucosomes in dilatant fractures, and melt ascent, the subvertical penny-shaped sills, were hydraulically connected. In other words, there must have been a temporal and spatial connectivity between melt storage sites and melt ascent conduits. This connectivity is illustrated in the "ladder-structures" (Figure 4.20 C) of upright sills and horizontal, connecting dilatant fractures that are common in the BHS. Indeed, pucker structures and collapsed wall-rock foliations enveloping large relic garnets suggest melt loss from the fractures and, as such, demonstrate hydraulic connectivity between melting sites and transfer conduits.

The physico-mechanical aspects leading to the collection of intergranular melt from partially molten wall rocks into parallel-sided, tabular dykes has been discussed by e.g. Sleep (1988), following the pioneering work by Weertman (1971) on the propagation of melt pockets in the Earth's crust. Sleep (1988) presented the theoretical background that could account for the formation of sheeted dyke complexes from pervasively distributed melt at mid-ocean ridges. Both the tectonic environment as well as some of the basic assumptions of Sleep's model for melt segregation and migration are different from the present case. However, the theoretical considerations outlined in Sleep (1988) find their manifestation in the field observations presented above. Crucial to the understanding of melt migration in fractures is the understanding of (1) the pressure distribution within the melt-filled fracture, and (2) pressure differences between the melt-filled fracture and the surrounding, partially molten wall rocks.

The subvertical, penny-shaped sills in the BHS represent a discreet volume of granitic magma, corresponding to the hydrofractures described by Bons (2001). The pressure distribution that drives magma ascent in such a melt-filled fracture is illustrated in (Figure 4.20) where it is assumed that at the centre of the subvertical melt-filled fracture (at $z = 0$), the internal magma pressure equals the surrounding lithostatic pressure (P_{lith}) so that the fracture is neither opening nor closing. The melt in the fracture is under the influence of its own buoyancy causing it to be over-pressured with respect to the wall rock at the top of the fracture and under-pressured at the bottom (Sleep, 1988, Bons et al., 2001), as outlined in the fold-out below.

Pressure is a function of the density of the material and the change in depth (ρgh, as shown above). Therefore, for an equal change of depth, there will be a greater change in lithostatic pressure in the wall rocks than in the pressure in the melt-filled volume because of the greater density of the wall-rock compared to that of granitic liquid. Thus, at the top of the intrusion the melt will be over-pressured. The supralithostatic melt pressure is able to part the wall rocks and thereby propagate the fracture. Similarly, the bottom of the intrusion will be under-pressured and the lithostatic pressure will tend to close the fracture. If the length of the intrusion is sufficient, the differences in the pressures at either tip will be large enough to drive the process such that the melt-filled volume is able to propagate upwards independently. This can occur once the magma-filled volume reaches a certain critical length which is in the order of 100 m for granitic magma (Weertman, 1971, Secor & Pollard, 1975).

Melt stored in structurally controlled fracture arrays

At h,

$P_{sill} = P_0 - \rho_{melt}gh$

$P_{lith} = P_0 - \rho_{rock}gh$

Thus, $\mathbf{P_{sill} > P_{lith}}$ by

$(\rho_{rock}-\rho_{melt})gh$

At 0, $\mathbf{P_{sill} = P_{lith} = P_0}$

At -h,

$P_{sill} = P_0 + \rho_{melt}gh$

$P_{lith} = P_0 + \rho_{rock}gh$

Thus, $\mathbf{P_{sill} < P_{lith}}$ by

$(\rho_{rock}-\rho_{melt})gh$

Melt extracted, leaving a residue containing large porphyroblasts of garnet and common 'pucker-structures'

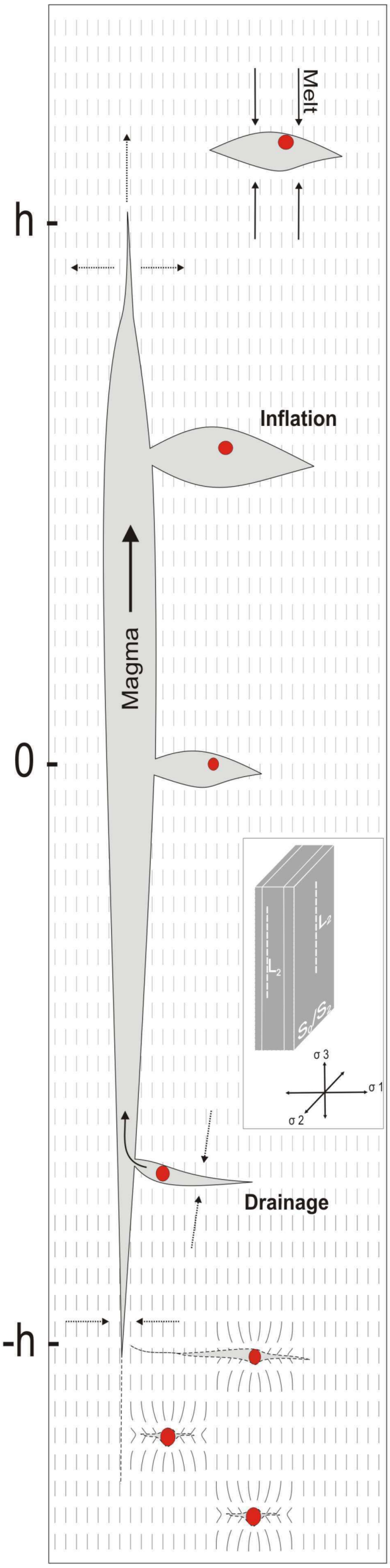

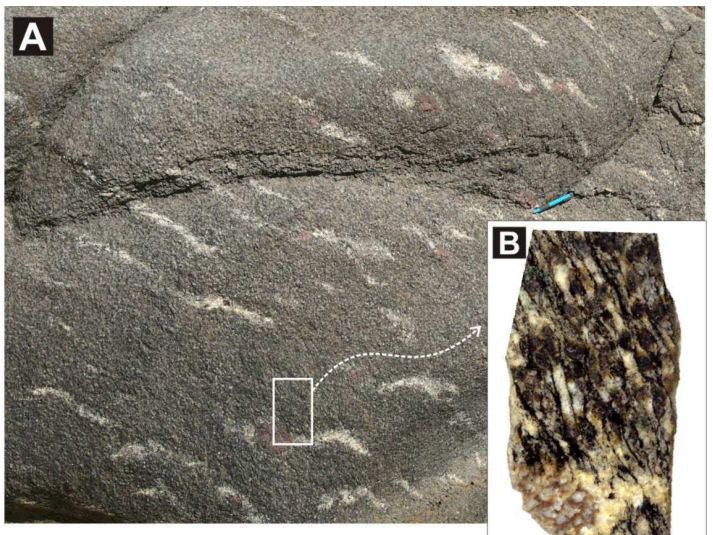

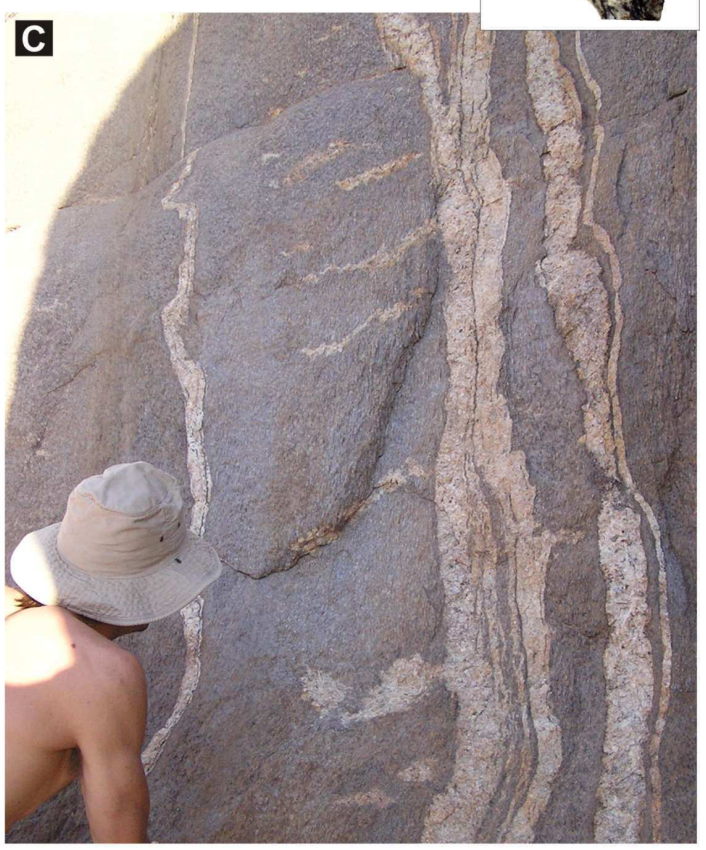

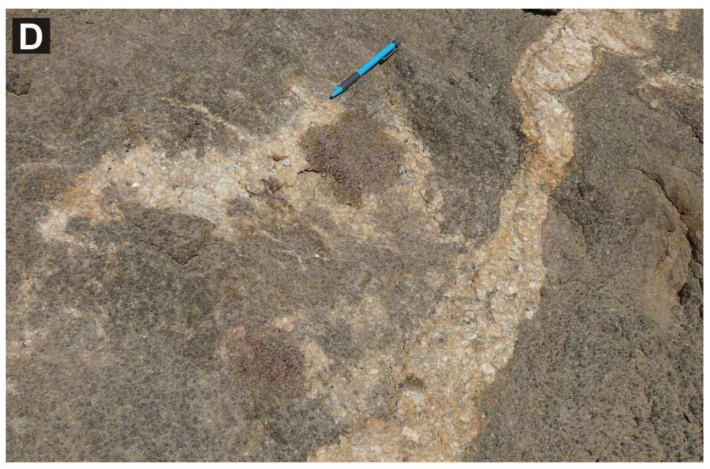

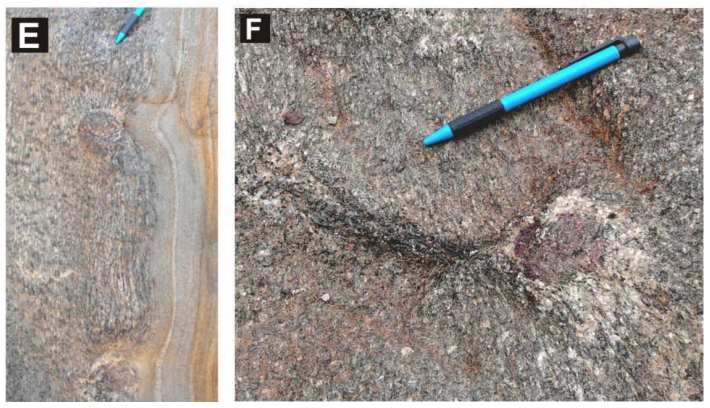

Figure 4.20. A schematic model of melt extraction of melt from the rocks of the Blauer Heinrich Syncline with field examples of several steps in the process (A-F). The model is described by Sleep (1988) for a subvertical σ_1, but still applies to this study where σ_1 is sub-horizontal. σ_3 in defined by the moderately steeply dipping stretching lineation, but this has been rotated to the vertical in this figure for simplicity. A is a typical leucosome array and shows how melt resides in the extensional fractures. The fractures have accumulated the melt by porous flow, evidence of which is preserved in B. C illustrates the typical 'ladder-structures' that show the connectivity of the leucosome arrays and bedding-parallel sills. D shows the connectivity in more detail with a garnet leucosome connected to a sill and a low leucosome-to-garnet ratio being preserved. E and F show the melt-depleted state of many of the rocks of the BHS with evidence of foliation collapse (pucker-structures), biotite selvages and typical peritectic porphyroblasts of garnet in the absence of leucosome.

Since the top half of the sill would be over-pressured with respect to the surrounding wall rock, melt would theoretically inject from the sill into the wall rock upon introduction of the sill. This is not observed in the field and probably reflects the special stress conditions during granitic emplacement outlined in chapter 4.6 (and Figure 4.19). Given that the vertical extent of most sills is in the order of 50 to 200 m, the overpressure developed at the tip of the sill would be too small to fracture the rock. Assuming a difference in density between the granitic melt (ca. 2.4 g/cm^3) and the biotite-cordierite gneisses (ca. 2.7 g/cm^3) of ca. 0.3 g/cm^3, the overpressure at the tip of a sill with a vertical extent of 200 m would be in the order of 0.3 MPa and, hence, below the tensile strength of the rock perpendicular to the bedding plane. Since the difference in tensile strength normal and parallel to the bedding/foliation anisotropy is larger than the regional differential stress, the fracture cannot propagate across the bedding plane and the sill will remain confined to the anisotropy. Thus, unless the sill directly intersects a dilatant fracture hosting the shallowly-dipping leucosome pockets, it is unlikely to inflate such sites as the sill will preferentially propagate along the bedding/foliation plane than cut across it into the rock or a nearby leucosome. However, an example of a propagating fracture tip intersecting and being off-set by a leucosome is shown in Figure 4.21.

When the sill passes through the rock, the tail end of the sill will create a hydraulic gradient from the wall rocks and the close-to-lithostatically pressured leucosomes into the sill. Again, for a sill with a vertical extent of ca. 200 m the hydraulic pressure gradient from the wall rocks into the sill would be approximately 0.3 Mpa. Leucosomes that are intersected by the sill can be drained and melt will flow from leucosome pockets into the sills following the hydraulic gradient. Sills with large vertical extents should be associated with larger hydraulic gradients. It is conceivable that hydraulic gradients could be large enough to drain leucosomes in the near vicinity of such sills. In this case, melt migration is possible since the rock has already fractured. The small leucosome only needs to migrate towards the sill, along the hydraulic gradient, with the stress-concentration at the tip of the leucosome favourable for its propagation towards an intersection with the sill. Such a mechanism could efficiently deplete the rocks of melt hosted in such a storage network, as the melt is freely available to rapid extraction.

Figure 4.21 Oblique view shows the termination of a sill that can be seen as a close analogue of what a propagating sill tip may have looked like. Note the abrupt steps in the otherwise straight propagation path of the sill where the sill intersects shallowly-dipping leucosome pockets.

Leucosomes that are not directly intersected by the sill are likely to remain unaffected. This may explain why large areas in the BHS still contain well-preserved leucosomes. In areas that have not been intruded by bedding parallel sills, the melts were not drained from the sites where they formed. In this model of melt drainage of shallowly-dipping leucosome pockets through vertically inclined ascending sills, the peritectic garnets in the melting sites obviously represent large solid obstacles that are not easily mobilised and incorporated into the ascent conduit. Field observations confirm that the sills are largely free of peritectic minerals and large peritectic garnets are often "trapped" in the wall

rocks without any evidence of surrounding melt. There is abundant evidence for melt extraction (foliation collapse and low leucosome to garnet ratios or, locally, abundant, large peritectic garnets enveloped by the wall-rock foliation without evidence of leucosome) in areas where no sills or ladder-structures occur. Magma must have escaped from these regions, without leaving a trace of their passing and ascent, indicating that sills could have removed magma and subsequently closed allowing the bedding planes to collapse. Evidence for this process is observed at the tail ends of sills. The only indication of the passing of the sill is given by a thin (<0.5 cm wide) biotite rind, which is otherwise easy to be overlooked in the biotite-cordierite gneisses.

Although the hydraulic gradient would be a function of the size of the sill, the gradient would be of a transient nature because of the upward migration of the sill. For this reason it is not clear how large a sill needed to be or how many sills would have needed to pass through a rock to drain it of melt. However, it can be deduced that for efficient draining to have occurred, the time for the migration of a leucosome towards a sill, and the extraction of the melt into the sill must have been significantly less than the residence time of the sill in that particular body of rock. This must have been a minute instant in geological time.

4.8 Emplacement features (Mini-plutons)

The mechanism of melt transfer described above hinges strongly on the pre-existing anisotropy in the rocks of the BHS. The subvertical orientation of the fabric facilitates the upward migration of melt and is a prerequisite for melt ascent as buoyancy-driven penny-shaped hydrofractures. Naturally, this model also predicts that when the orientation of the anisotropy deviates from steep attitudes, then the magma ascent may be arrested. This would favour the localised, perhaps temporary ponding of magma at structural sites where the fabric in the rock is subhorizontal.

The strong control of pre-existing structures on the style of emplacement of the intrusive material is not only evident in the bedding-parallel nature of the majority of the sills, but is also illustrated where granite emplacement is controlled by 2nd- and lower-order F_2 folds. Steeply plunging fold hinges may form favourable conduits for the ascent of magma, whereas shallowly plunging fold hinges may result in structural traps that retard the upward progress of magma along the steep bedding planes. This indicates that such F_2 structures must have been present before the intrusion, indicating that these granites may be late- or even post-tectonic. Small bodies of granite (mini-plutons) are often associated with such structures.

The contacts between mini-plutons and the gneisses are often discordant with respect to bedding and foliation in the gneisses; schlieren of the country rock occasionally occur within the plutons. These mini-plutons typically show a very pronounced compositional and textural layering that is subparallel to the orientation of the sills in the surrounding wall rocks. The magmas seem to have ponded below the subhorizontal bedding in the fold hinges, but narrow leucosomes emanating from the apex of some of the plutons seem to follow and utilize the subvertical S_2 foliation in the fold hinges. This testifies to the transient nature of these plutons, indicating that such features represent temporary accumulation and transfer sites and not the final emplacement site for the magma. This temporary ponding and subsequent focussing of upward migrating magmas could be a reason for the observation that certain zones of the BHS are inundated with sills and adjacent packages of biotite schist have a dearth of intrusive material.

In the far east of the BHS, a 2nd order fold in the southern limb corresponds to an area of extremely abundant granite sheeting. The fold is parasitic to the BHS, but does not have the expected symmetry and forms a synclinal-antiform and an anticlinal-synform pair with shallow plunges and an axial trace parallel to that of the BHS. The inverted stratigraphy (Smith, 1965) puts older Karibib Marbles overlying the Kuiseb Formation (from where the granites are likely to have originated) and thus forming an excellent trap that prevented the upward movement of the granite. The blunting of fracture tips of granite dykes is common along contacts with ductile marbles undergoing high-

temperature metamorphism, inhibiting the propagation of fractures dykes through marble units. The area is inundated with closely-spaced lit-par-lit intrusions of metre-wide sheets. This again shows the strong influence of pre-existing structures in the rocks controlling the location and style of intrusions.

Having established the mechanisms of accumulation and ascent and even local emplacement of magma in the BHS it remains to better understand the mechanical formation of the fracture-hosted leucosomes and gain a better understanding of the anatectic reactions in order to determine if these structural sites are merely accumulation sites, or if the fracturing has a fundamental control on the melting reaction. Melt-loss is a physical process that would change the composition of the rocks in which it occurs towards more restitic compositions. This should result in a noticeable trend in whole rock chemistry.

5. Whole-rock geochemistry

5.1 Introduction

A fortunate consequence of the oblique crustal section of the Damara Belt is that the metamorphic isograds run normal to the Belt in the Central Zone. The Kuiseb Formation metapelites (which are exposed along the length of the Belt) are sensitive to metamorphic grade and are also particularly reactive with respect to partial melting. Their exposure along the length of the Damara makes them useful for comparing the effect of different degrees of metamorphism (assuming that the chemistry of the metapelites did not vary considerably along strike). Previous attempts to compare low- and high-grade metapelites of the Damara Belt (e.g. Schneider, 1983; Haack et al., 1984) indicate that there are certain noticeable compositional trends, such as, increasing FeO and MgO and decreasing K_2O with increasing metamorphic grade. However, despite the apparently ideal situation for the study of metamorphism on a homogeneous lithology that trends normal to the metamorphic isograds, little work has been done in the Damara Belt with respect to the changes in bulk-rock composition with increasing grade and possible melt-loss at the highest grades.

This study seeks to identify and quantify partial melting in the Kuiseb Formation metapelites of the Blauer Heinrich Syncline (BHS). To this end we took a number of samples of these rocks in the study area as well as samples of the interbedded metapsammitic rocks for comparison. Furthermore, amphibolite-facies Kuiseb Formation rocks were sampled near the town of Usakos (some 100 km northeast along strike of the orogen) on the northern limb of the Usakos Dome. These were sampled to compare to the high-grade rocks as they are likely to compare very closely in composition to the protoliths of the BHS metapelites. These lower-grade 'equivalent' rocks display no evidence of partial melting, with temperature estimates of 550-600 °C (Hoffer, 1977, Puhan, 1983) being below the lowest temperature at which partial melting can occur.

Furthermore, because the bulk-composition has an important control on the mineral assemblage together with the pressure and temperature, the rocks were analysed in order to put the mineral assemblage into context. In addition to typical thermobarometry, the rocks were also modelled with pseudosections using THERMOCALC (version 3.21) (Powell et al., 1998). The modelling approach can be used to provide an additional bracket of the PT-estimates of the metamorphism that the study area has experienced (to be discussed in Chapter 10).

5.2 Methodology and apparatus

X-Ray Fluorescence Spectrometry (XRFS): Description of the technique

Samples were crushed with a sledgehammer and jaw crusher and milled in a Siebtechnik tungsten-carbide swing-mill prior to the preparation of a fused disc for major element analysis and a pressed briquette for trace element analysis.

Eleven major elements, Fe, Mn, Ti, Ca, K, S, P, Si, Al, Mg and Na (with Ni and Cr when Ni and Cr concentrations exceed –2000 ppm or 0.2 %) were determined at the University of Cape Town using fused disks prepared with LiT-LiM flux in the proportion 57:43 (Sigma Chemicals) and LiBr as releasing agent, according to the method of Fernand Claisse (April, 1999). The disks are analyzed on a Philips PW1480 wavelength dispersive XRF spectrometer with a dual target Mo/Sc x-ray tube. All measurements are made with the tube at 50 kV, 50 mA. Analytical conditions are given in table 5.1.

Fused disks made up with 100% Johnson Matthey Specpure SiO_2 were used as blanks for all elements except Si. Fused disks made up from mixtures of Johnson Matthey Specpure Fe_2O_3 and $CaCO_3$ were used as blanks for Si. Intensity data were collected using the Philips X40 software. All peaks were corrected for background. Spectral overlap corrections were made for Br on Al, Cr on Mn, Al and Ca on Mg, and Mg and Ca on Na. Matrix corrections were made on all elements using the de Jongh model in the X40

software. Theoretical alpha coefficients, calculated using the Philips on-line ALPHAS programme, were used in the de Jongh model.

Table 5.1. Analytical conditions for determination of major elements using a Philips PW1480 WDXRF spectrometer.

Element /line	Collimator	Crystal	Detector	PHS LWL	PHS UPL	Counting time (s)	Concentration range **	RMS	Lower limits of determination*	No. of standards
NiKα	F	LiF(220)	FS	22	70	100	0 - 0.48	0.003	0.004	11
FeKα	F	LiF(220)	FL	16	68	100	0 - 17	0.069	0.019	20
MnKα	F	LiF(220)	FL	15	66	100	0 - 0.27	0.004	0.014	22
CrKα	F	LiF(220)	FL	14	70	100	0 - 3.5	0.011	0.008	11
TiKα	F	LiF(200)	FL	32	68	100	0 - 3.9	0.022	0.023	22
CaKα	F	LiF(200)	FL	30	76	50	0 - 77	0.102	0.004	21
K Kα	F	LiF(200)	FL	32	74	100	0 - 15.5	0.037	0.003	21
S Kα	C	GE(111)	FL	32	74	100	0 - 53.5	0.112	0.100	11
P Kα	C	GE(111)	FL	34	74	100	0 - 3.4	0.011	0.008	16
SiKα	C	PE(002)	FL	26	80	100	0 - 100	0.215	0.052	20
AlKα	C	PE(002)	FL	26	80	100	0 - 100	0.084	0.074	21
MgKα	F	PX-1	FL	36	68	100	0 - 85	0.141	0.102	20
NaKα	F	PX-1	FL	30	78	100	0 - 9.1	0.065	0.17	12

** all concentrations expressed as wt% oxide; S as SO_3
* = 10 H lower limit of detection, expressed as wt% oxide

5.3 Results

5.3.1 Metapelites

Major and trace element compositions for the high- and low-grade rocks are given in Table 5.2. listed according to SiO_2 values. The rocks of the study area typically have high Mg# and high, but variable total Fe + Mg values. The rocks have low MnO values of less than 0.25 wt%, low P_2O_5 values (< 0.3 wt%) and TiO_2 values of between 0.7 and 1.3 wt%. Compositional trends are also illustrated in Figure 5.1 in comparison to data for aluminous metapelites from the work of Haack et al., (1984).

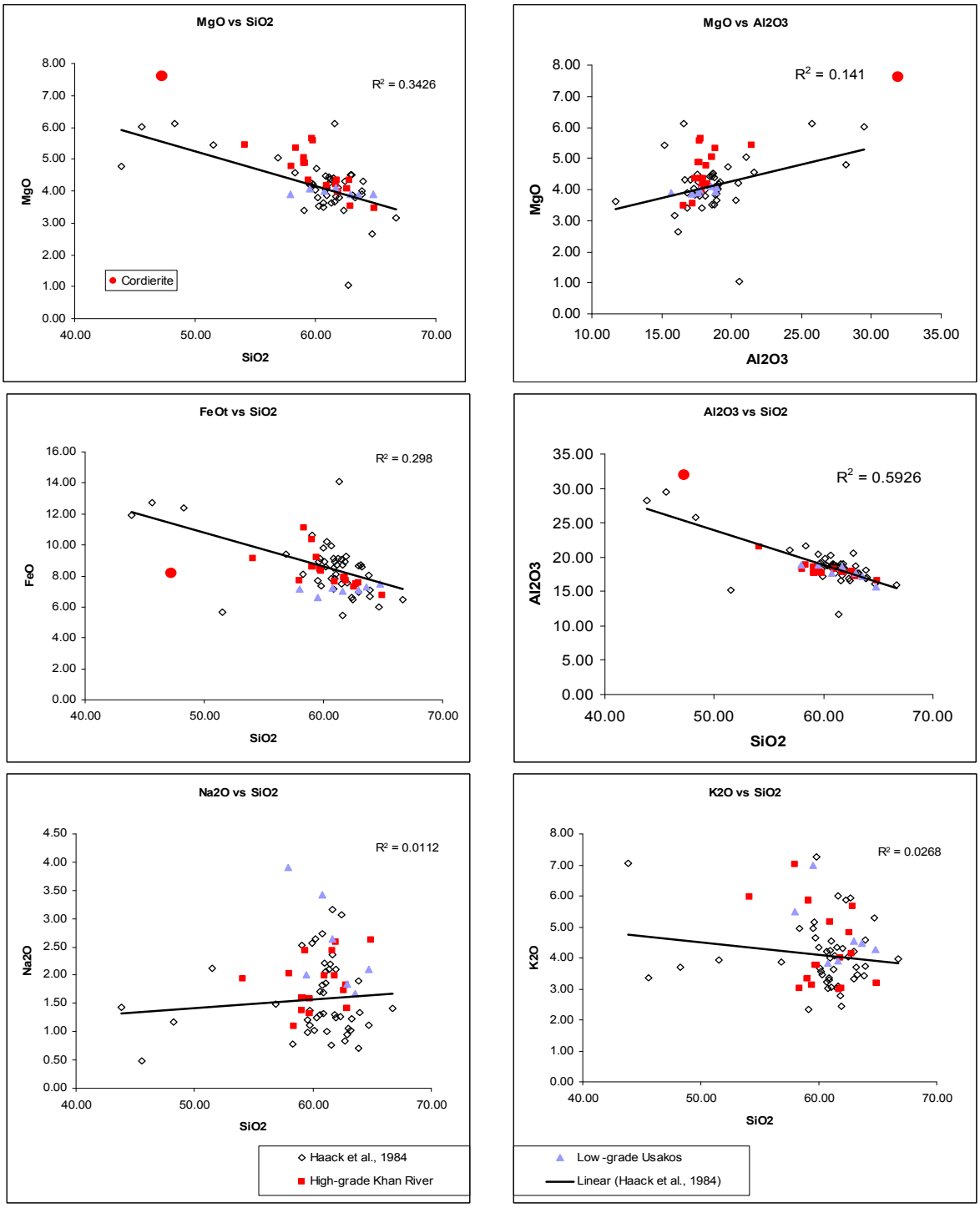

Figure 5.1. The graphs compare the compositions of the low-grade samples of the Kuiseb Formation collected at Usakos, the high-grade Kuiseb Formation rocks from the Blauer Heinrich Syncline and the aluminous metapelite compositional data of Haack et al., (1984) collected from several locations in the Damara Belt. Plotted data was normalised to 100 wt% (anhydrous) with all Fe as FeO. The graphs indicate a trend in MgO content (both versus SiO_2 and versus Al_2O_3) towards the composition of a typical peritectic cordierite from this study (the filled circle) which is consisted with compositional shift caused by melt-loss. The data of Haack et al., (1984) does not define useful compositional trends for most of the data, particularly for Na_2O and K_2O, with poor R^2-values

indicating the poor fit of the trendline to the data. This may be the result of a wide range of sampling, not explicitly restricted to the Kuiseb Formation. The Na_2O content of the high-grade rocks is noticeably shifted to lower values when compared to the samples from Usakos. This is consistent with the loss of a sodium-rich melt.

Plotted in the diagram above are the compositions of 45 aluminous metapelites from various locations in the Damara Belt, studied by Haack et al., (1984) to determine the mobility of metals during regional metamorphism. The aim of the study was to determine if the H_2O produced during metamorphism was capable of mobilising metals in significant amounts to produce mineral deposits. None of the samples were described to show evidence of melt-loss, however a sample collected in the Khan Gorge was not included in the data here, because of the possibility that it may have been from an area very close to the Blauer Heinrich Syncline which is in the Khan Gorge. This data was considered with the aim of defining a compositional baseline trend for unmelted metapelites in the Damara Belt that could be used to quantify melt-loss in the high-grade rocks of this study.

The data of Haack et al., (1984) scatters widely due to the fact that the samples are collected from various locations and metamorphic grades across the Damara Belt. Unfortunately, this data does not show well-defined compositional trends which could be used to determine the degree of melt-loss for the rocks of this study. The data for Na_2O and K_2O, particularly, show a wide scatter. These elements are expected to be most strongly influenced by melt-loss due to the fact that they constitute a large proportion of granitic melt. Unfortunately, no confidence can be placed in the baseline trend defined by these compounds in the dataset of metapelites, as shown by the very low R^2-values. This could be due to the fact that the dataset of Haack et al., (1984) might not have been explicitly restricted to the Kuiseb Formation metapelites, as the stratigraphy of the samples is not given in the article.

Determining the average of the low-grade rocks is a similar approach to determining a trendline by regression analysis. The composition of the high-grade samples can then be compared to this 'average protolith' composition to determine an estimate of melt loss. If each of the high-grade samples is compared to this composition, the degree of melt-loss

can be estimated. As a result of melt-loss, the Al_2O_3, MgO, FeO and Ca contents of the rock would be expected to increase, whereas the SiO_2, Na_2O and K_2O contents would be expected to decrease.

These effects can be conflicting for many of the samples, with some of the elements reflecting apparent melt-loss, and some reflecting apparent addition of melt when compared to the average Usakos sample. For example, KHt2/2 contains significantly more MgO and FeO than the average low-grade composition, pointing to as much as 15% melt-loss. However, the concentrations of CaO and K_2O in this sample contradict this and would suggest that the rock *gained* melt. For this reason, it is difficult to quantify the degree of melt-loss, as the original compositional variations within the rocks leads to a complexity that cannot easily be resolved. Nevertheless, it is possible to make some reasonable estimates of the degree of melt-loss by comparing the average composition of the high-grade rocks to the average of the low-grade rocks. This will decrease the effect of the inherited source-rock heterogeneity and allow a basic estimation of melt-loss. Here, it is important to keep in mind that this would be a total melt-loss, including all possible events of quartz-feldspar-H_2O melting and incongruent melting that may have occurred during the history of these rocks. Furthermore, it can only estimate the amount of melt that has been lost from the rocks, not the total degree of melting at the time, as it is likely that a significant fraction of the melt would have remained in the rock, unable to escape.

The averages with standard deviations of the high- and low-grade rocks are presented for comparison in Table 5.2. The difference between the average high-grade metapelite (cordierite gneiss) and the average low-grade metapelite (schist) indicate that the rocks of the BHS are slightly depleted in the oxides of fusible elements such as Na_2O, K_2O and H_2O and enriched in FeO_t, MgO and CaO. This effect is small and largely within the standard deviations, yet it is systematic and indicative of depletion in the elements found in granitic magma. The average populations do overlap considerably, and the number of samples is not sufficient to produce statistically sound, unambiguous results, but the data do point to melt-loss as a likely candidate for the slight compositional differences.

The diagram below (Figure 5.2) compares the compositions of the high-grade cordierite gneisses and (including the grt-crd-gneisses) and the low-grade equivalent schist. On average, the rocks of the higher-grade area are lower in SiO_2, Na_2O, K_2O and H_2O (inferred from the LOI) and also have a higher FeO_t, MgO, Al_2O_3, TiO_2, MnO, and CaO. Thus, the high grade rocks appear to be depleted in fusible elements and enriched in the refractory components. This effect is slight and somewhat blurred by the natural compositional variation in the rocks. However, the differences between the average compositions from the two areas are consistent with minor melt loss having been important in shaping the compositions of the higher-grade rocks. Thus, the average high grade composition can be reasonably well modelled as the product of 5 to 10% of melt loss from the low grade average composition, using the melt compositions produced in the relatively low-temperature experiments on the amphibolite-facies rocks.

Table 5.2. a: Table of XRF major and trace element compositions for the High-grade metapelitic rocks.

Sample	11/1	11/11C	KH1/3	11/6	KH1/2	14/4	13/4	13/5	KH1/1	KHT2/2	11/4B	12/1C	12/1A	KHt2/1	KH2/1	12/1D	14/5B
SiO_2	51.8	56.2	56.4	57.0	57.1	57.4	57.5	57.5	57.6	59.6	59.7	59.7	60.0	60.2	60.8	60.9	63.4
TiO_2	0.95	0.98	1.10	1.13	1.07	1.15	0.97	0.98	1.01	0.81	0.90	0.93	0.83	0.80	0.82	0.73	0.86
Al_2O_3	20.5	17.6	18.2	17.1	18.0	17.1	17.0	17.2	17.4	17.9	17.1	17.4	17.3	17.2	16.9	16.6	16.2
Fe_2O_3	9.69	8.30	11.94	9.18	11.14	9.25	8.88	9.02	9.90	8.27	8.45	8.50	8.31	7.79	8.05	8.15	7.34
MnO	0.18	0.11	0.15	0.14	0.14	0.14	0.16	0.16	0.18	0.16	0.14	0.17	0.17	0.12	0.14	0.28	0.12
MgO	5.20	4.61	5.16	4.71	4.86	4.74	5.35	5.44	4.21	4.08	4.20	4.07	3.84	3.92	4.21	3.42	3.38
CaO	0.79	1.06	0.92	0.93	0.94	0.94	2.04	2.06	2.26	0.81	1.09	1.59	1.83	0.61	0.95	0.62	1.39
Na_2O	1.86	1.97	1.06	1.54	1.32	1.55	1.52	1.28	2.36	1.95	1.92	2.36	2.49	1.65	1.76	1.38	2.56
K_2O	5.71	6.79	2.90	5.64	3.21	5.67	3.61	3.62	3.04	5.02	3.87	2.89	2.91	4.64	4.02	5.48	3.10
P_2O_5	0.08	0.08	0.08	0.31	0.08	0.31	0.24	0.24	0.10	0.14	0.18	0.21	0.26	0.11	0.15	0.11	0.19
SO_3	0.08	0.02	0.02	0.03	0.04	0.03	0.01	0.03	0.06	0.02	0.04	0.01	0.01	0.04	0.05	0.03	0.04
Cr_2O_3	0.05	0.05	0.05	0.04	0.04	0.04	0.06	0.06	0.04	0.04	0.10	0.07	0.07	0.03	0.04	0.06	0.05
NiO	0.01	0.01	0.02	0.01	0.01	0.01	0.01	0.01	0.01	0.01	0.01	0.01	0.02	0.01	0.01	0.01	0.01
H_2O-	0.17	0.14	0.14	0.14	0.19	0.11	0.10	0.11	0.24	0.12	0.11	0.12	0.14	0.14	0.18	0.19	0.16
LOI	2.43	1.73	1.11	2.04	1.39	1.60	1.68	1.64	1.75	1.24	1.58	1.22	1.20	2.11	1.32	1.48	0.92
Total	**99.6**	**99.7**	**99.3**	**99.9**	**99.5**	**100.1**	**99.1**	**99.3**	**100.2**	**100.2**	**99.4**	**99.2**	**99.4**	**99.4**	**99.3**	**99.5**	**99.7**
Co	36	33	33	46	31	41	47	56	25	20	31	32	24	18	22	34	22
Cu	29	22	44	49	37	15	14	14	29	17	16	11	11	10	17	15	11
Zn	170	28	141	178	134	177	159	149	109	147	136	148	143	135	138	121	114
Ga	27	25	30	50	29	26	22	26	24	24	21	23	22	25	27	17	24
Rb	304	230	163	142	185	235	158	134	171	196	173	174	178	210	172	197	148
Sr	97	83	62	69	73	112	168	141	124	84	122	74	69	60	84	112	116
Y	21	37	36	54	31	30	25	28	30	21	29	38	33	25	30	37	34
Zr	220	197	193	320	192	224	177	182	185	181	180	202	187	159	185	173	198
Nb	25	23	14	28	14	28	18	17	14	14	14	18	23	12	13	23	19
Ba	688	1199	641	2613	644	850	756	583	596	613	799	145	63	628	618	828	247
La	34	40	24	67	61	42	9	14	31	29	47	28	24	22	41	28	24
Ce	96	139	152	199	126	130	119	122	113	101	71	69	79	70	124	127	98
Nd	27	44	31	53	29	32	28	36	27	26	24	28	36	24	36	28	38
Pb	29	4	15	23	23	34	15	14	29	24	22	8	24	28	29	33	23
Th	29	23	42	54	37	55	40	45	26	17	16	31	30	11	11	47	29
U	10	16	6	10	6	9	14	3	7	8	0	5	8	7	17	0	6
Mg#	**51.6**	**52.4**	**46.1**	**50.4**	**46.3**	**50.4**	**54.4**	**54.4**	**45.7**	**49.4**	**49.6**	**48.7**	**47.8**	**49.9**	**50.9**	**45.4**	**47.7**

Table 5.2. b: Table of XRF major and trace element compositions for the lower-grade equivalent rocks (Kuiseb Formation metapelites from the Usakos area) and a comparison of the average compositions for the high- and low-grade rocks with the difference.

Low-grade Schist								Low-grade Schist		High-grade gneiss		
Sample	***USK4***	***USK3***	***USK2***	***USK1***	***USK7***	***USK5***	***USK6***	**Average**	**St Dev**	**Average**	**St Dev**	**Difference**
SiO_2	56.4	57.6	59.2	60.2	60.9	61.3	62.5	59.8	2.14	58.4	2.57	*1.36*
TiO_2	1.02	0.92	0.88	0.81	0.86	0.93	0.86	0.90	0.07	0.94	0.12	*-0.05*
Al_2O_3	18.4	18.3	17.3	18.1	17.1	16.5	15.2	17.3	1.16	17.5	0.93	*-0.19*
Fe_2O_3	7.74	7.13	7.78	7.60	7.64	7.77	8.05	7.67	0.28	8.95	1.19	*-1.28*
MnO	0.09	0.06	0.19	0.12	0.08	0.09	0.09	0.10	0.04	0.16	0.04	*-0.05*
MgO	3.81	3.94	3.88	4.00	3.77	3.73	3.77	3.84	0.10	4.44	0.64	*-0.59*
CaO	1.51	0.88	1.93	1.18	1.01	0.83	0.76	1.16	0.42	1.23	0.53	*-0.07*
Na_2O	3.81	1.95	3.33	2.58	1.77	1.61	2.02	2.44	0.84	1.80	0.45	*0.64*
K_2O	5.35	6.78	3.75	3.81	4.41	4.32	4.12	4.65	1.08	4.24	1.25	*0.40*
P_2O_5	0.21	0.15	0.15	0.23	0.31	0.19	0.20	0.20	0.05	0.17	0.08	*0.04*
SO_3	0.03	0.04	0.01	0.01	0.02	0.02	0.00	0.02	0.01	0.03	0.02	*-0.01*
Cr_2O_3	0.03	0.04	0.03	0.06	0.04	0.04	0.07	0.05	0.01	0.05	0.02	*-0.01*
NiO	0.01	0.01	0.01	0.01	0.01	0.01	0.04	0.01	0.01	0.01	0.00	*0.00*
H_2O-	0.07	0.14	0.20	0.08	0.14	0.20	0.11	0.13	0.05	0.15	0.04	*-0.01*
LOI	1.16	2.09	1.06	1.33	1.90	1.92	1.62	1.58	0.40	1.55	0.39	*0.03*
Total	**99.6**	**100.1**	**99.7**	**100.2**	**100.0**	**99.5**	**99.4**	**99.8**	**0.29**	**99.6**	**0.34**	**0.21**
Co	17	17	25	18	16	20	22	19	3.3	32	10.5	*-13.13*
Cu	17	14	16	10	9	11	17	13	3.4	21	12.1	*-7.81*
Zn	132	147	125	130	135	136	138	135	6.9	137	34.2	*-2.17*
Ga	27	25	26	22	28	27	22	25	2.4	26	6.9	*-0.71*
Rb	180	222	160	149	155	154	153	168	26.1	186	41.3	*-18.90*
Sr	147	140	132	184	133	146	111	142	22.2	97	30.6	*44.80*
Y	38	31	33	27	42	37	32	34	5.0	32	7.8	*2.58*
Zr	225	198	224	184	200	209	186	204	16.5	197	35.4	*6.36*
Nb	14	13	15	11	12	13	13	13	1.3	19	5.4	*-5.65*
Ba	1278	762	695	687	1174	716	678	856	256.2	736	553.9	*119.85*
La	38	14	32	25	42	28	31	30	9.1	33	15.2	*-3.24*
Ce	66	80	60	69	92	97	107	82	17.6	114	33.4	*-32.25*
Nd	22	28	22	21	36	33	29	27	5.9	32	7.7	*-4.89*
Pb	40	22	38	31	25	20	24	29	7.9	22	8.4	*6.39*
Th	18	14	10	9	8	11	14	12	3.5	32	13.9	*-19.94*
U	10	12	18	5	11	17	4	11	5.4	8	4.8	*3.24*
Mg#	**49.4**	**52.3**	**49.7**	**51.0**	**49.4**	**48.7**	**48.1**	**49.8**		**49.5**		*0.27*

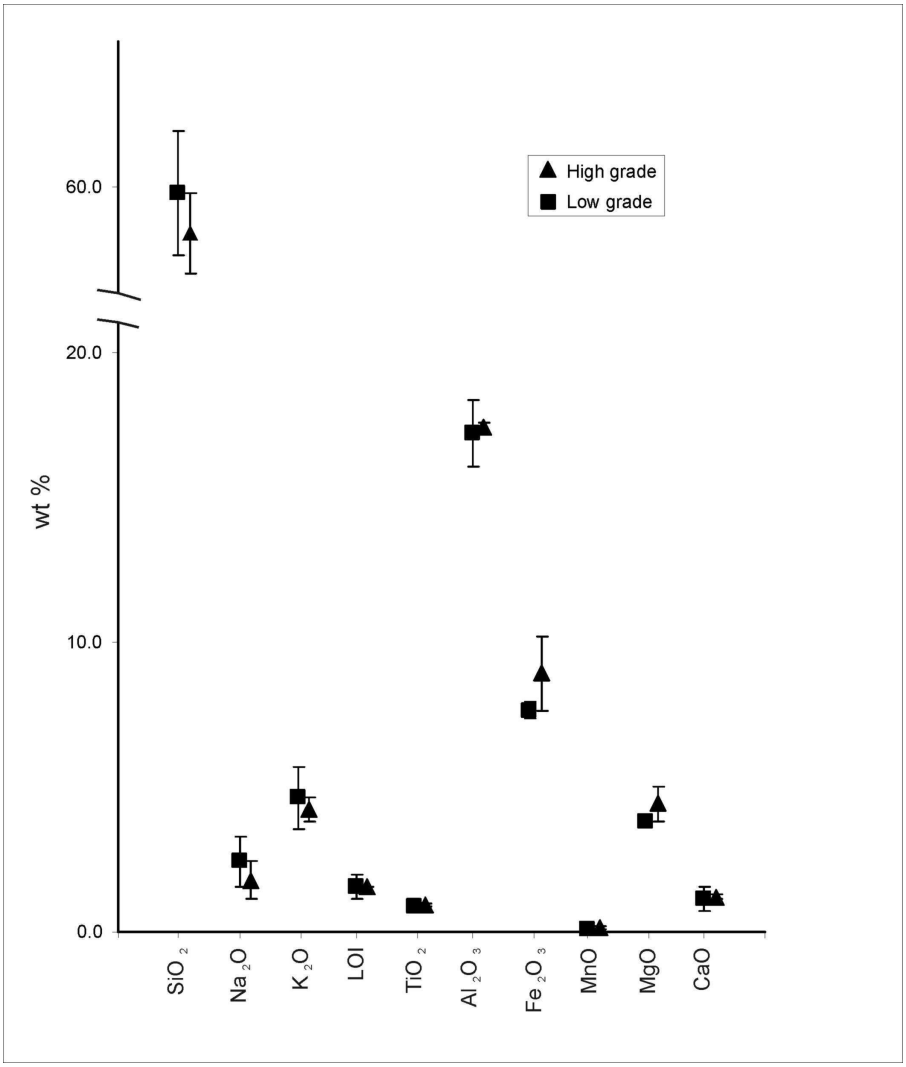

Figure 5.2. A comparison of the average major element compositions of the high-grade Kuiseb Formation metasediments of the Blauer Heinrich Syncline and the lower-grade equivalent rocks from Usakos. Note the depletion of SiO_2, Na_2O, K_2O and the lower value of LOI for the high-grade rocks, and their relative enrichment in the other major elements that are more commonly indicate restitic compositions.

5.3.2 Metapsammites

Metapsammitic rocks were not studied in detail and compositional data is not presented. These rocks are richer in SiO_2, but have lower Mg#'s and are poorer in alkali elements. The rocks rarely display evidence of *in situ* melting and such compositional differences with respect to the metapelites could have influenced their melting behaviour.

5.3.3 Granites

The granites of the study area are generally coarse-grained or pegmatiodal (many contain graphic intergrowths of quartz and feldspar) with variable content of ferro-magnesian phases. This, together with the large sample sizes required for bulk sampling of granites to avoid bias, made a full geochemical investigation of the granites beyond the scope of this study. Furthermore, the structurally controlled leucosomes are the main point of interest of this study, but due to their small size and commonly cumulate character, the composition of the original magma is difficult to establish with confidence, however, the chemistry of a selected group of granites and leucosomes is discussed in Chapter 9 in comparison to the composition of experimental glasses (quenched melts).

6. Mineral chemistry

6.1 Introduction

The Kuiseb Formation metapelites typically have the assemblage, Crd + Bi + qtz + plag ± ksp ± grt. The fairly simple textural associations discussed in the preceding section on lithology and petrography provide little information on the prograde, pre-tectonic history of the rocks as this has been destroyed by recrystallisation of the minerals by deformation at high temperature. However, the rocks may contain complexities in the chemistry of the minerals that are not clearly expressed in their textural appearance. For example, zonation of minerals such as garnet may preserve information on the prograde history or they may host small inclusions of minerals equilibrated with the garnet at different conditions to those at which the rim of the garnet and the matrix equilibrated. For this reason the compositions of the minerals from all the textural associations were investigated using SEM-EDS (described below) and special attention was paid to zonation patterns within the minerals. Finding the compositions of the minerals that form the peak metamorphic assemblage will allow a quantitative estimation of the pressure and temperature conditions of this metamorphism via the application of geothermobarometry.

6.2 Methodology and apparatus

6.2.1 Major elements

SEM-EDS technique

Imaging of the samples and analysis of the phase compositions was accomplished using a Leo® 1430VP Scanning Electron Microscope at Stellenbosch University. Prior to imaging or analysis the polished samples were sputter-coated with carbon. Samples were identified with backscattered electron (BSE) images, and phase compositions quantified by EDS analysis using an Oxford Instruments® 133KeV detector and Oxford INCA software. Beam conditions during the quantitative analyses were 20 KV and approximately 1.5 A, with a working distance of 13 mm and a specimen beam current of -4.00 nA. Despite the relatively low energy of the beam, X-ray counts with the set-up

used were typically ~ 5000 cps. The counting time was 50 seconds live-time. Natural mineral standards were used for standardization and verification of the analyses. Pure Co, as well as Ti and Fe in Ilmenite were used periodically to correct for detector drift.

6.2.2 Trace- and Rare-Earth Elements (REEs)

Laser-ablation ICP-MS

Transition trace element and REE concentrations of one large anatectic garnet were determined by LA-ICP-MS analysis at Stellenbosch University. Data on garnets were obtained using a New Wave 213 nm laser ablation system connected to an Agilent 7500ce ICP-MS. Specifications and parameters of the 213nm laser are listed below:

Laser output:	213 nm flat-top beam
Energy:	~ 6 J/cm^3
Pulse width:	4 ns nominal
Pulse rate:	15 Hz
Spot size:	80 μm
Background counting time:	17 sec
Data acquisition time:	40 sec

ICP-MS parameters were as follows during the analysis:

RF Power:	1350 kW
Plasma gas flow:	15 L/min
Auxiliary gas flow:	0.9 L/min
Carrier gas flow:	0.9 L/min Ar, 0.6 L/min He
Acquisition mode:	Time Resolved Analysis
Integration time:	0.01 sec / isotope

Optimized for oxide levels < 0.6%

6.2.3 Control Standards

Major elements

Actual published major element concentrations of mineral standards were compared with measured values as determined by electron microprobe EDS analysis for other studies using this same equipment (Diener et al., 2005, Moyen et al., 2006) and can be seen in the appendix. The analyses were in good agreement for most elements, but become more unreliable with decreasing concentration in the mineral. Energy dispersive spectroscopy is only suitable for determining major elements of minerals at concentrations over 0.4 wt% for heavy elements, and over 0.6 wt% for light elements.

Trace- and Rare-Earth Elements

Trace elements in the garnet samples were quantified using the NIST 614 and 612 series of standards for calibration and ^{29}Si as internal standard. Standard reference material BHVO-2G was used as quality check standard to establish the level of accuracy of the data set. The data is available in the appendix.

6.3 Results

Major element compositions of the minerals are presented in the appendix. Typical compositions as used for conventional thermobarometry are presented in Table 8.2 according to the assemblages used to constrain the metamorphic conditions in chapter 8. Below, the most significant characteristics of the mineral compositions and variation of compositions are discussed.

6.3.1 Biotite

Three compositionally and texturally distinct generations of biotite are present in the high-grade metapelites. The oriented biotite of the Qtz-Pl-Bi patches in the rocks is chemically indistinguishable from the coarser-grained, strongly-oriented biotite that occurs between the cordierite porphyroblasts and most strongly defines the fabric in the rocks. This biotite typically has high TiO_2 concentrations, but has the lowest Mg# (Mg#

= Mg/[Fe + Mg]) at ~ 42, of the three textural varieties. The presence of garnet in the assemblage rarely affects the Mg# of biotite noticeably as garnet is usually present in very low modal abundance. This biotite can be distinguished texturally and by its chemistry from that preserved as corroded inclusions in metamorphic garnet, but is of the same composition as the biotite inclusions preserved in cordierite. This indicates that the cordierite was probably open to diffusion, allowing the biotite in the cordierite to equilibrate, whereas the biotite caught in the garnet was not able to do so. The biotite inclusions preserved in these metamorphic garnet crystals are very rich in TiO_2, commonly with up to 4.6 wt%. They are also the most magnesian of the biotite generations, with a Mg# of up to 50.

The last type of biotite observed in these rocks occurs in the lens-shaped leucosomes that form in the cordierite gneisses. This generation of biotite is very low in TiO_2 (< 1 wt%) but has a Mg# similar to that of the oriented biotite in the foliation. It is often coarse-grained and randomly oriented, possibly indicating that it formed as a product of the crystallising melt of the leucosome. Interestingly, the coarse poikilitic garnet in the leucosomes does not appear to contain inclusions of high-TiO_2, corroded biotite that can be interpreted as remnants of the anatectic reaction that formed the leucosome.

Biotite of the metapsammitic rocks occurs in two textural and compositional associations. One is as fine-grained crystals oriented to define a fabric in the matrix of the rocks, and the other is as small, corroded inclusions in garnet. The former has fairly high Ti-content of between 2.5 - 3.5 wt% and a Mg# between 44 and 49. Interestingly, the biotite found as inclusions in the garnet has a lower TiO_2 concentrations (1.4 – 2.3 wt%) but a higher Mg# of over 52.

Biotite from the low-grade schists of the Kuiseb Formation near Usakos typically has TiO_2 concentrations of between 2 and 3 wt%, and a fairly high Mg# of between 46 and 50. The high Mg content of the biotite in comparison to that of the biotite in the high-grade rocks is probably the result of the lower modal proportion of cordierite, a phase

which strongly partitions Mg and thus depressed the Mg number of other phases in the assemblage.

6.3.2 Garnet

Garnet is present in two associations; one a finer-grained metamorphic phase, not associated with leucosome and the other coarse, and most commonly poikilitic, variety associated with leucosome. In the case of the metamorphic garnet, crystals are commonly several millimetres in diameter, inclusion poor and are chemically unzoned except for a thin (20 to 50 μm) weakly retrograde zoned rim that is characterised by a lower Mg# and a higher MnO concentration (Figure 6.1). This metamorphic garnet is more common in the metapsammites than in the metapelites. In the metapelites this generation of garnet coexists with oriented matrix biotite, poikiloblastic cordierite, as well as quartz and plagioclase. All of these minerals are unzoned. In the metapsammites garnet coexists with biotite, cordierite, quartz and more rarely plagioclase. The garnet commonly contains small, rounded inclusions of biotite that are interpreted to represent the biotite consumed by the garnet-producing reaction. The biotite inclusions in garnet have lower TiO_2 concentrations and a higher Mg# than the matrix biotite.

Garnet in the stromatic and nebulitic leucosomes commonly forms large crystals up to 2 cm in diameter. These grains are also inclusion-poor and chemically unzoned except for a narrow rim enriched in MnO, similar to that described for the metamorphic garnet. In these rocks the peritectic garnet occurs in association with a new, peritectic generation of cordierite and the coarse quartz and feldspar minerals that have crystallised to produce the leucosome. These garnet crystals contain inclusions of corroded biotite interpreted to be remnants from the anatectic reaction. These biotite inclusions have higher TiO_2 concentrations and higher Mg#'s than the matrix biotite.

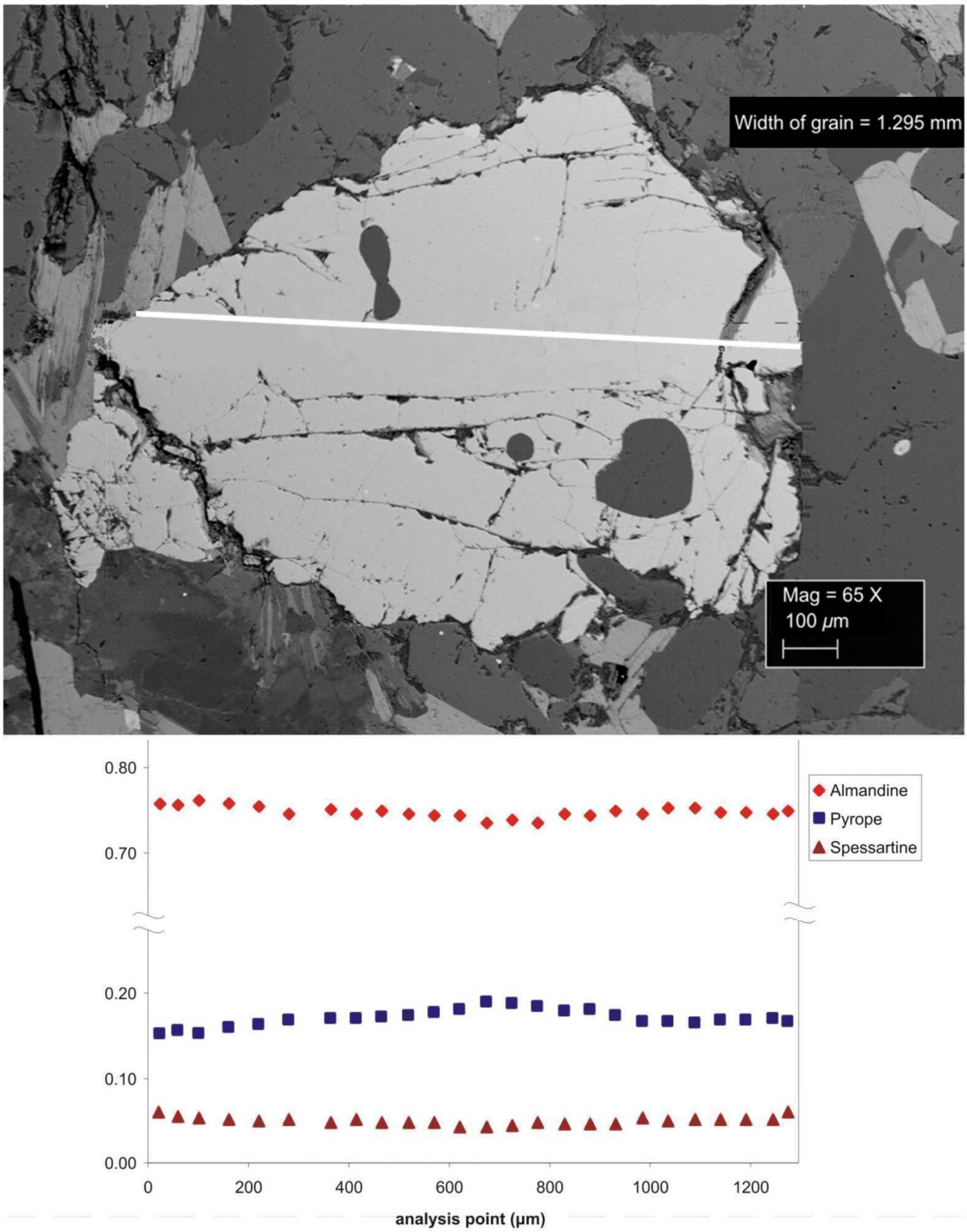

Figure 6.1. Major element chemical profiles of a typical metamorphic garnet in metapelite. The garnet has a retrograde signature with a slight increase in MnO concentration towards the rim and a coupled, slight decrease of MgO from core to rim.

Garnet in the lens-shaped extensional leucosomes occurs as the large, poikiloblastic crystals as described previously. Locally these garnet crystals occur in association with euhedral peritectic cordierite and are always associated with coarse-grained quartz, biotite and feldspar crystallised to form the leucosome. In these leucosomes the garnet is also closely associated with, but not in contact with, the poikiloblastic cordierite in the matrix of the gneisses. This garnet is characterised by an identical lack of zonation and a subordinate retrograde rim to the other leucosome types, but these crystals have not been observed to contain the high-TiO_2, corroded biotite inclusions that can be interpreted as remnants of the anatectic reaction.

A distinction between the two types of garnet can be made on the basis of their composition; the finer-grained metamorphic garnet can be distinguished from the coarser-grained garnet associated with the leucosomes (anatectic garnet) by its lower Mn-content. The Mn-content of garnet can be presented as a percentage of the spessartine molecule ($Mn_3Al_2Si_3O_{12}$) in the garnet (Figure 6.2). The metamorphic garnets generally have a low spessartine content of less than 10 %, whereas the anatectic garnets contain between 8 and 18 % spessartine. Both have further spessartine enrichment towards the rim.

Many of the garnet analyses produced high cation totals after recalculation to mineral stoichiometries. This problem was largely solved by applying Droop's Fe^{3+} recalculation (Droop, 1987), however, applying this technique to several of the samples resulted in an overestimation of the Fe^{3+} cation, such that the M-site (2+) of garnet could no longer be filled. This suggests a slight over-estimation of either Si^{4+} or Al^{3+} in these garnets by the SEM-EDS analytical technique. In this case, Droop's correction was applied until Fe^{2+} could no longer be taken from the M-site and the remaining (small) cation excess could be attributed to analytical overestimation of the Si^{4+} or Al^{3+} cations.

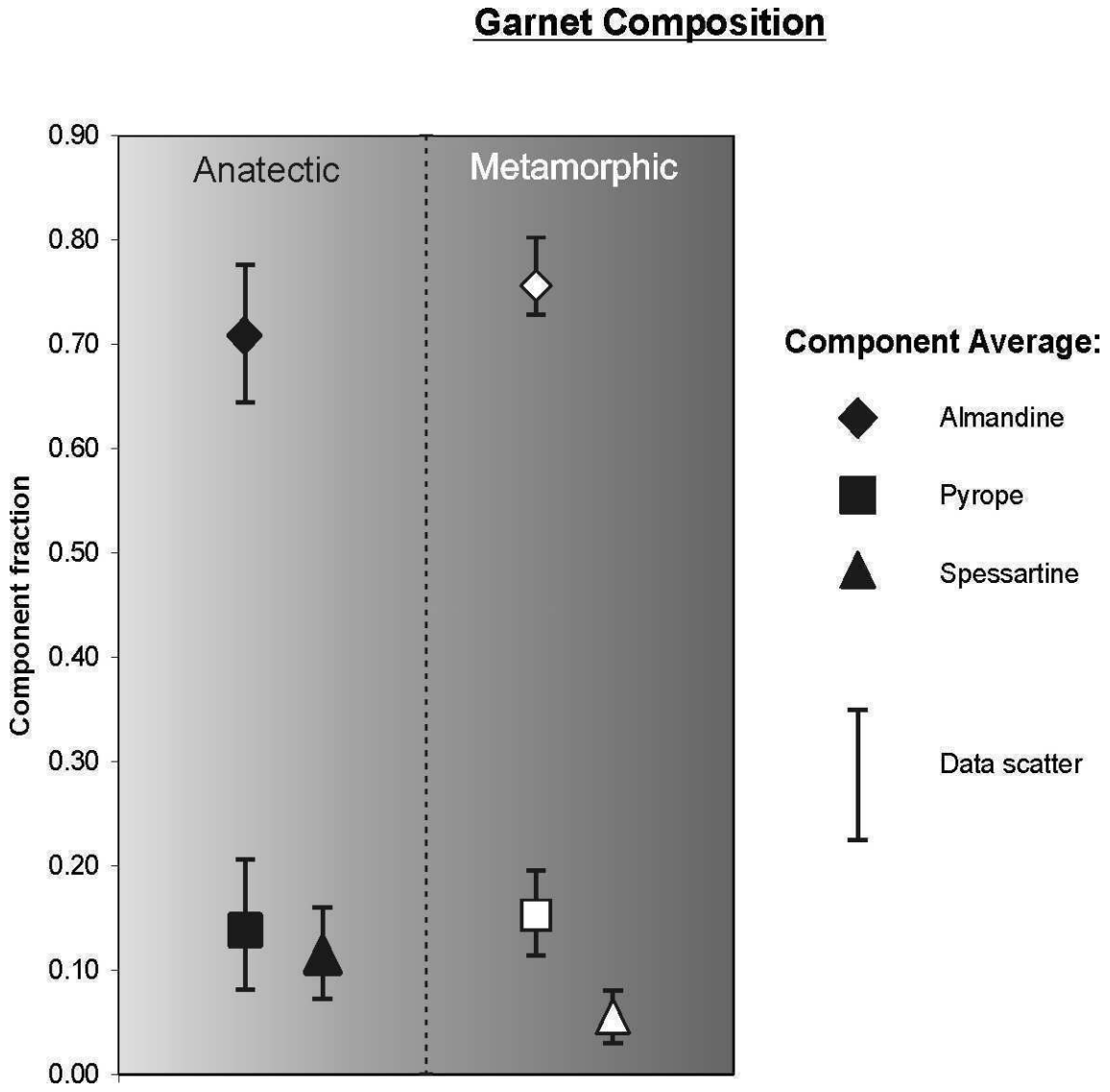

Figure 6.2. Note the significantly higher content of spessartine in the anatectic garnet as opposed to the finer-grained metamorphic garnet.

Trace- and Rare-Earth Element compositions in garnet

The results of LA-ICP-MS analyses of an anatectic garnet from a typical leucosome are presented as a plot of chondrite-normalised (Taylor & McLennan, 1985) REE concentrations for several analyses across the cm-size garnet (Figure 6.3) and in Appendix 3. The diagram illustrates the typical Heavy REE-enriched pattern of garnet. The strong negative Eu anomalies could be interpreted as a result of the coexistence with potassium feldspar as a result of biotite-breakdown in rocks that did not previously contain feldspar other than plagioclase (Harris et al., 1992, Bea & Montero, 1999, Jung &

Hellebrand, 2006). This would be true for many of the rocks, however, not necessarily for those that contained sub-solidus potassium feldspar, as is common in these rocks. The scatter in the light-REEs (LREE) is a result of their low concentrations that are poorly resolved with LA-ICP-MS, although this effect is probably exacerbated by the presence of LREE-rich micro-inclusions such as monazite that could add to the scatter of the data by being incorporated in the analysis.

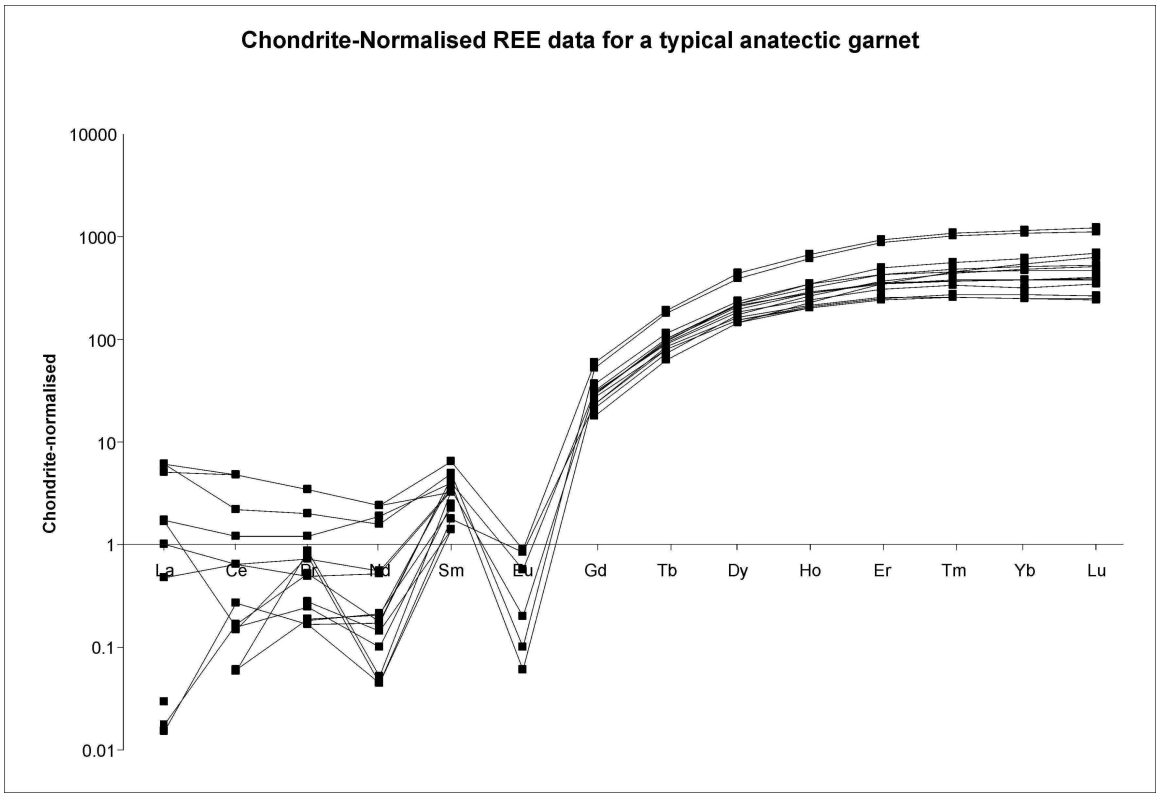

Figure 6.3. The REE- chemistry of a typical anatectic garnet.

6.3.3 Cordierite

This mineral occurs in a number of textural varieties, but shows little compositional variation. Cordierite is the phase with the highest Mg# in the assemblage of both the metapelites and the metapsammites by virtue of its favourable partitioning of Mg over that of minerals such as garnet and biotite. The Mg# of the rock and the coexistence of other ferromagnesian minerals plays a role in determining the composition of the

cordierite, however, within a particular rock, no variation in cordierite composition can be determined between textural varieties, and the cordierite displays no zoning pattern of any sort, despite having texturally distinct rims that have a lower inclusion abundance. In metapelites that host cordierite-bearing leucosomes, the compositions of the cordierite porphyroblasts and the peritectic cordierite in the leucosomes are also indistinguishable. This together with the biotite inclusions in cordierite being of identical composition to those in the matrix strongly suggests that the cordierite was open to diffusion and that its chemistry was reset.

6.3.4 Plagioclase

Plagioclase is present as an important constituent of the matrix of the metapelitic rocks, but is less common in the matrix of the metapsammites. The other important association in which this feldspar is found is within leucocratic segregations of several types. It is present in small Qtz-Fsp segregations within the metapelitic rocks as well as in all leucosomes of the study area, and also occurs in the granitic sheets that are interspersed between the metasedimentary rocks.

No zonation in the plagioclase crystals was observed in this study for any of the textural associations of the mineral. This mineral has limited potassium substitution and generally has a composition of between An_{20} and An_{35}. The plagioclase of the lower-grade equivalent rocks from Usakos is only found as a matrix mineral in these rocks and has a composition of $An_{12} - An_{22}$, this is significantly less calcic than that of the BHS. The plagioclase in both the high- and low-grade rocks does not contain more than ca. 0.2 wt% K.

6.3.5 Potassium Feldspar

The low-grade metapelites contain potassium feldspar porphyroblasts that contain ca. 1.4 wt% Na and ca. 1 wt% Ba in substitution with K. They do not contain any reliably detectable amounts of Ca. The potassium feldspar from the high-grade metapelites has a very similar chemical composition to the low-grade rocks, but it also commonly has

exsolution lamellae of albitic plagioclase, indicating that the potassium feldspar had considerably more Na at the peak of metamorphism, before cooling forced the Na to be exsolved (Figure 6.4).

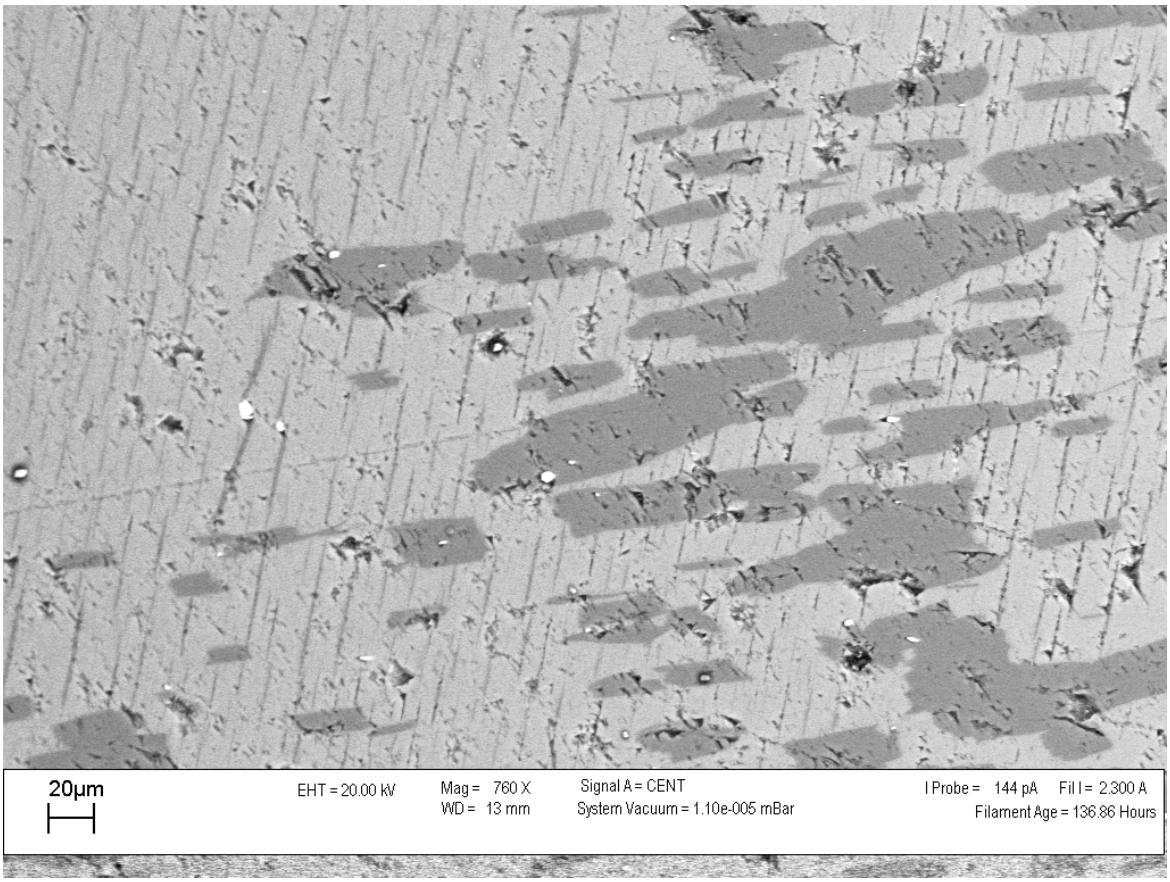

Figure 6.4. Typical exsolution texture of albitic plagioclase from potassium feldspar of a leucocratic segregation in metapelitic gneiss.

7. Estimating the conditions of anatexis

In the Central Zone, metamorphic conditions decrease from west to east. The highest grade metamorphic conditions recorded in the belt correspond to lower granulite-facies grades (0.7 ± 0.05 GPa, and 760 ± 50 °C) and are recorded in coastal outcrops of Grt-Crd-Sil-Spl-Kfs-Qtz bearing metapelites (Masberg, 2000), where metamorphism resulted in extensive partial melting of the rocks. In contrast, mid- to lower amphibolite-facies conditions of 0.3 ± 0.1 GPa and 550-600 °C prevail in the Karibib/Usakos region, some 150 km to the east of the highest grade coastal outcrops (Hoffer, 1977, Puhan, 1983). The shape of the isograds determined by previous work in the Damara Belt (Figure 2.2) indicates that the study area is still below the conditions at which an incongruent biotite melting reaction occurred. These conditions supposedly only existed some 40 km to the West (Masberg, 2000).

As discussed in chapter 2.3 there has been considerable debate with regards to the timing of metamorphism in the CZ of the Damara Belt (see discussion in Jung and Mezger (2003), p. 240-241). Many of the previous authors working in the high-grade part of the belt argue for a post-tectonic thermal peak (e.g. M_2 of Nex et al., (2001), or for a thermal peak during late extensional tectonics (e.g. Jung and Mezger (2003)). However, there is sufficient discrepancy between these assertions of post-tectonic thermal peaks and the observations in this study that the anatexis is associated with deformation, to warrant a detailed investigation of the recorded metamorphic conditions in the anatectic rocks of this study. Hopefully this will also better constrain the pressure-temperature conditions of the metamorphic peak.

7.1 The nature of the anatectic reactions

The production of peritectic garnet and cordierite in conjunction with the leucocratic material indicates that incongruent melting of biotite has produced the anatectic features. This contradicts the previous work in the Damara Belt that indicates that the study area should be below the conditions at which such a reaction could have occurred. The consistent shallow dip of the leucosomes at high angles to the dominant stretching

lineation (Ward et al., 2007) illustrates the strong structural control with the anatectic features confined to dilational sites. Given that the associated peritectic garnet almost exclusively occurs in leucosomes of the shallowly-dipping fracture arrays, it appears that the dilational sites have, in fact, controlled where the anatectic reactions occurred and were not merely transient accumulation or transfer sites during the migration of melt as it is commonly observed in migmatitic terrains (e.g. Collins & Sawyer, 1996b, Kisters et al., 1998). The localisation of anatexis in the structural features creates the possibility that melting was fluid-present and controlled by fluid availability. This would be broadly consistent with the relatively low, for anatectic rocks, estimates of peak metamorphic temperatures from previous studies (Masberg, 2000, Jung & Mezger, 2003).

Alternatively, the previous work in the area may have underestimated the temperature of metamorphism leading to the hypothesis that the observed melting features could have been the result of a high-temperature and fluid-absent incongruent biotite melting reaction. This would bracket the possible conditions at which the melting reaction occurred to between 730 and about 850 °C (Stevens et al., 1997, Spicer et al., 2004). The lower limit is defined by the possible conditions at which fluid-present biotite breakdown can begin. The upper limit could not have been much higher that about 850 °C because there is no evidence for the pervasive melt production which would be expected at these conditions where biotite breakdown would have become significant in all the metapelites.

It could be argued that the pressure drop caused by the fracture formation could have caused the melting reaction to begin by a process of decompression melting. However, the small differential stress that ductile rocks can sustain would result in only a very small and short-lived pressure reduction that would not be likely to trigger a melting reaction.

The commonly observed foliation collapse and characteristic pucker structures around the dilational, leucosome-filled fractures also imply a loss of volume during and subsequent to the melting reactions. Coupled to the fact that peritectic products have grown both in the leucosomes, in the case of garnet, and in the bounding gneisses, in the case of cordierite, the stoichiometry of the melting reaction is difficult to constrain on the basis of

field or petrographic observations. Knowledge of these parameters, i.e. the temperature of anatexis, the fluid regime of melting and the stoichiometry of the melting reaction are required in order to be able to make an accurate assessment of melt loss from the cordierite-biotite gneisses.

8. Metamorphic conditions from this study

8.1 Introduction

As all the metapelitic rocks in the study contain cordierite and biotite, both the garnet bearing anatectic domains and unmelted garnet bearing rocks present an opportunity to calculate peak metamorphic conditions. Metamorphic garnet is more common in the metapsammites than in the metapelites, but the feldspar-poor mineralogy of the metapsammites often makes thermobarometry difficult on these rocks due to the high-variance of the assemblage. In the metapelites this generation of garnet coexists with foliated matrix biotite, poikiloblastic cordierite porphyroblasts, quartz, plagioclase and occasionally potassium feldspar. All of these minerals are unzoned. In the metapsammites garnet coexists with biotite, cordierite, quartz and more rarely plagioclase.

8.2 Implication of mineral zoning patterns

Garnet is the only mineral observed in this study to display mineral zonation of the major elements (trace element zonation was not investigated). The pattern of zonation, described above, is referred to as retrograde. This is because the spessartine component of the garnet, which is the more stable end member of garnet at low temperatures, increases towards the rims of the mineral. This indicates that the core of the garnet equilibrated at higher temperature than did the rim. This is consistent with down-temperature diffusional re-equilibration of the garnet with the matrix or a fluid (on the retrograde path). The cores of garnet crystals of the study area, irrespective of grain size, have a flat zonation profile, with no growth zonation preserved. This indicates that the mineral was largely open to diffusion until the closure temperature for garnet was encountered on the retrograde path (producing the Mn-enriched rim). This is typical of garnets that have grown at, or experienced, granulite-facies conditions (Frost & Chacko, 1989, Perchuk et al., 2006). Amphibolite-facies garnets commonly retain distinct growth-zoning patterns as a result of systematic depletion of the elements available for garnet growth. If any of the metamorphic garnets formed at lower-temperature conditions, then the zoning pattern was erased during the high-temperature part of the history of the metamorphism. The

anatectic garnets, believed to only have formed at the peak of metamorphism, grew in the presence of a melt, which would have further helped to increase the rate of diffusion to destroy any chemical gradients that might have produced zoning during the growth of these porphyroblasts (For an empirical study of diffusion in garnet see Yardley, 1977).

The interpretation that the garnet, and thus almost any other mineral, was open to diffusion is important for the application of geothermobarometry. The techniques used to calculate the conditions at which the minerals in the assemblage are compositionally in equilibrium. If the minerals were open to diffusion at temperatures significantly below the peak of metamorphism then they would have continued to equilibrate on the retrograde path until the minerals encountered their so-called blocking temperatures. Thus any calculated temperatures will represent the point at which the minerals were no longer able to exchange elements freely. This is complicated by the fact that minerals such as cordierite and biotite are open to diffusion to lower temperatures than garnet. Frost and Chacko (1989) discussed this problem which results in the majority of granulite-facies peak assemblages being calculated in the interval between 780 °C and 820 °C, namely around the closure temperature of minerals such as garnet. They refer to this problem as the "granulite-facies uncertainty principle".

However, the lack of zonation in minerals such as cordierite and the retrograde zonation pattern of minerals such as garnet are already significant indicators towards determining the conditions of metamorphism. The rocks must have experienced high-temperature conditions in order to produce these chemical characteristics in the minerals. This together with the evidence presented for incongruent melting of biotite suggests that these rocks must have experienced upper amphibolite-facies or lower granulite-facies conditions.

8.3 Calculating the conditions of anatexis

P–T conditions were estimated using the program THERMOCALC (Version 3.21) of Powell *et al.* (1998) in conjunction with the internally consistent dataset of Holland and

Powell (1998) as well as subsequent upgrades. All calculations were performed in 'Average *P–T*' mode and assumed fluid-absent conditions and a water activity of 0.5. This is justified by the fact that quartz and plagioclase account for a substantial portion of the matrix of the gneisses and that the PT conditions calculated by previous workers are generally above the conditions of the reaction Qtz + Pl $_{(An20-30)}$ + H_2O = Melt (Holtz & Johannes, 1994, Holtz *et al.*, 2001). Thus, the rocks could not have generally coexisted with a water-rich fluid at the peak of metamorphism and if such a fluid was involved in initiating melting at the sites of anatexis, the melting reaction must have resulted in a resumption of fluid-absent conditions. Biotite incongruent melting under these relatively low temperature conditions would most likely buffer water activity to a value in the range of 0.3 to 0.6 (Clemens & Watkins, 2001; Figures 1 & 4). Mineral end-member activities were calculated at 0.5 GPa and 650 °C with the program AX (Powell et al., 1998) and an example of this information for sample KHt2/2 is shown in Table 8.1. In general, *P–T* estimates in the gneisses and psammites that combine the garnet rim composition with the matrix mineral compositions produce the lowest PT estimates of 630 °C and 0.35 GPa (Table 8.2 (a-c)).

Table 8.1. *The following table shows the endmember activities calculated for sample KHt2/2 (Table 8.2 c) as well as the incomplete set of independent reactions determined by the Thermocalc software. Without a complete set of reactions the results of the thermobarometry must be treated with caution. Only sample 14/5A had a complete set of independent reactions on which its PT results were based. The table does show that the statistical parameters are within reasonable limits (this is the case for all samples and calculations). The fit value is below what is stipulated for all the calculations and the e* value (a measure of the degree to which the endmember activities were shifted) is between the accepted values of -1 and 1. Larger values would indicate that the activities would have been shifted beyond their uncertainties.*

	py	gr	alm	spss	phl	ann	east	Crd
A	0.0032	2.10E-05	0.34	0.00089	0.018	0.038	0.034	0.31
sd(a)/a	0.65429	1.08738	0.15	0.73519	0.4498	0.39657	0.39913	0.14283

	fcrd	mncrd	an	ab	san	ab	q	H2O
A	0.22	0.00048	0.32	0.79	0.86	0.61	1	0.5
sd(a)/a	0.16915	20.8333	0.13872	0.05	0.05	0.05	0	

INCOMPLETE independent set of reactions

1) py + east + 3q = phl + crd
2) py + 2gr + 3east + 6q = 3phl + 6an
3) 6phl + 21an = 7gr + 4east + 5crd + 2san + 2H2O
4) gr + 2ann + 3fcrd = 4alm + 3an + 2san + 2H2O
5) py + 2alm + 3east + 9q = 3phl + 3fcrd

For 95% confidence, fit (= sd(fit)) < 1.61
(for a(H2O) = 0.5)

	P	sd(P)	T	sd(T)	cor	fit	e*	Hat
Py	3.86	0.98	703	71	0.179	0.6	0.17	0.51
Gr	3.88	0.96	709	55	0.06	0.49	0.7	0.01
Alm	4.10	1.13	714	55	0.109	0.58	-0.22	0.17
Phl	3.98	1.05	712	55	0.03	0.6	0.15	0.16
Ann	3.80	1.18	710	58	0.23	0.61	-0.12	0.4
East	3.66	1.08	734	70	-0.242	0.54	0.39	0.58
Crd	3.89	0.96	711	55	0.059	0.57	-0.27	0
Fcrd	4.13	1.04	710	55	0.029	0.51	0.45	0.1
An	3.89	0.96	711	55	0.058	0.57	-0.27	0
San	3.91	0.97	713	56	0.076	0.61	-0.05	0.01
Q	3.90	0.96	712	55	0.057	0.61	0	0
H2O	3.90	0.96	712	55	0.057	0.61	0	0

However, the assemblage from the anatectic rocks, combining garnet core compositions with compositions of biotite inclusions in matrix cordierite (as no inclusions of biotite occur in the garnet) and the peritectic cordierite compositions produce intermediate temperatures and pressures of 730 °C and 0.41 GPa (Table 8.2. a). This is interesting because these biotite compositions are very similar to those of matrix biotite (as explained, the cordierite was open to diffusion).

The highest temperatures recorded in this study come from restitic garnet-cordierite-biotite metapelites. Garnet in these rocks retains TiO_2-rich biotite inclusions which together with the garnet core compositions produce PT estimates of 750 °C and 0.45 GPa. There is a strong correlation between the calculated peak temperature and the TiO_2

content of the biotite generation involved in the assemblage (Table 8.2. b). These results suggests that the biotite in the matrix has been compositionally re-equilibrated during cooling and that the anatectic mineral generations, particularly from domains that appear to have lost significant amounts of melt, provide the best record of peak metamorphic conditions, which appear to be in excess of 750 °C and 0.45 GPa.

Table 8.2. (On the following pages) The following tables show representative mineral compositions for metapsammite (a), restitic metapelite (b) and metapelite hosting a structurally controlled leucosome (c) with PT estimates for various choices of assemblage at certain a_{H2O} *conditions.*

Table 8.2. a:

14/5A metapsammite									
	Garnet			Biotite			Cordierite		Plagioclase
	Core	Rim		Inclusion	Matrix				
SiO_2	36.29	36.15		35.62	35.76		48.67		62.13
TiO_2				1.58	2.65		0.00		
Al_2O_3	20.17	20.22		19.63	19.42		33.06		23.54
Fe_2O_3							0.00		
FeO	33.90	34.02		18.15	20.47		9.85		0.12
MnO	6.08	6.55		0.08	0.10		0.46		
MgO	3.18	2.84		11.35	9.57		8.31		
CaO	0.90	0.86					0.00		5.21
Na_2O				0.3	0.36		0.35		8.47
K_2O				9.12	9.26		0.00		0.09
Total	**100.53**	**100.63**		**95.83**	**97.60**		**100.70**		**99.56**
Si	2.92	2.92	**Si (5-6)**	5.35	5.33	**Si**	4.93	**Si**	2.76
Al^{IV}	0.08	0.08	**Al^{IV} (3-2)**	2.65	2.67	**AlIV**	1.07	**Al**	1.23
Σ T-site	**3.00**	**3.00**	**Σ T-site**	**8.00**	**8.00**	**Σ T-site**	**6.00**	**Fe3+**	0.00
								Σ T-site	**4.00**
Al^{VI}	1.84	1.84	**Al^{VI}**	0.82	0.74	**AlVI**	2.87		
Fe^{3+}	0.23	0.24	**Ti**	0.18	0.30	**Ti**	0.00	**Ca**	0.25
Σ M-site	**2.08**	**2.08**	**Σ XX-site (0-2)**	**1.00**	**1.04**	**Fe3+**	0.20	**Na**	0.73
						Σ M-site	**3.07**	**K**	0.01
Fe^{2+}	2.05	2.05	**Fe^{2+}**	2.28	2.55			**Σ A-site**	**0.98**
Mn	0.41	0.45	**Mn**	0.01	0.01	**Mg**	1.25		
Mg	0.38	0.34	**Mg**	2.54	2.13	**Fe2+**	0.63		
Ca	0.08	0.07	**Σ M-site (6-4)**	**4.83**	**4.69**	**Mn**	0.04		
Σ A-site	**2.92**	**2.92**				**Σ A-site**	**1.93**	**An**	25.65
			Na	0.09	0.10			**Ab**	75.47
XAnd	0.11	0.11	**K**	1.75	1.76	**Ca**	0.00	**Or**	0.53
XAlm	0.70	0.70	**Σ A-site (2)**	**1.83**	**1.86**	**Na**	0.07		
XPyr	0.13	0.12				**K**	0.00		
XSps	0.14	0.15	**Cation Σ**	**15.66**	**15.60**	**Σ Channel cations**	**0.07**		
Total	**1.08**	**1.09**							
Mg*	15.72	14.25	**Mg***	52.72	45.47	**Mg***	66.43		

	Thermobarometry of Assemblage (fluid absent):											
	grt (rim) matrix bt				grt (core), matrix bt				grt (core) bt inclusion			
a_{H2O}	**T**	**st dev**	**P**	**st dev**	**T**	**st dev**	**P**	**st dev**	**T**	**st dev**	**P**	**st dev**
0.5	590	74	3.1	1.0	621	77	3.3	1.1	641	97	3.9	1.3
0.6	591	74	3.3	1.1	622	78	3.5	1.1	642	96	4.1	1.3
0.7	591	74	3.4	1.1	622	78	3.6	1.1	643	97	4.2	1.3

Table 8.2. b:

KH 1/2 restitic metapelite										
	Garnet			Biotite			Cordierite		Plag	KSp
	Core	Rim		Inclusion	Matrix					
SiO_2	37.41	37.6		35.42	34.94		50.90		61.85	63.91
TiO_2				4.56	3.58		0.00			
Al_2O_3	20.91	20.87		18.25	18.74		32.41		24.67	18.40
Fe_2O_3									0.11	0.85
FeO	35.31	36.7		19.16	21.91		9.49			
MnO	1.62	2.12		0.00	0.00		0.03			
MgO	4.31	3.23		10.16	8.83		7.63			
CaO	1.07	1.00					0.05		5.85	0.02
Na_2O				0.00	0.00		0.00		8.39	1.63
K_2O				9.05	9.42		0.00		0.12	14.62
Total	**100.63**	**101.52**		**96.6**	**97.42**		**100.50**		**101.00**	**99.43**
Si	2.98	2.99	**Si (5-6)**	5.30	5.27	**Si**	5.16	**Si**	2.72	2.97
Al^{IV}	0.02	0.01	**Al^{IV} (3-2)**	2.70	2.73	**AlIV**	0.84	**Al**	1.28	1.01
Σ T-site	**3.00**	**3.00**	**Σ T-site**	**8.00**	**8.00**	**Σ T-site**	**6.00**	**Fe3+**	0.00	0.03
								Σ T-site	**4.00**	**4.01**
Al^{VI}	1.94	1.95	**Al^{VI}**	0.52	0.60	**AlVI**	3.04			
Fe^{3+}	0.08	0.06	**Ti**	0.51	0.41	**Ti**	0.00	**Ca**	0.28	0.00
Σ M-site	**2.02**	**2.01**	**Σ XX-site (0-2)**	**1.04**	**1.00**	**Fe3+**	0.00	**Na**	0.72	0.15
						Σ M-site	**3.04**	**K**	0.01	0.87
								Σ A-site	**1.00**	**1.01**
Fe^{2+}	2.27	2.38	**Fe^{2+}**	2.40	2.76					
Mn	0.11	0.14	**Mn**	0.00	0.00	**Mg**	1.15			
Mg	0.51	0.38	**Mg**	2.27	1.99	**Fe2+**	0.80			
Ca	0.09	0.09	**Σ M-site (6-4)**	**4.67**	**4.75**	**Mn**	0.00			
Σ A-site	**2.98**	**2.99**				**Σ A-site**	**1.96**	**An**	27.63	0.10
			Na	0.00	0.00			**Ab**	71.7	14.48
XAnd	0.04	0.03	**K**	1.73	1.81	**Ca**	0.01	**Or**	0.7	85.43
XAlm	0.76	0.80	**Σ A-site (2)**	**1.73**	**1.81**	**Na**	0.00			
XPyr	0.17	0.13				**K**	0.00			
XSps	0.04	0.05	**Cation Σ**	**15.44**	**15.57**	**Σ Channel cations**	**0.01**			
Total	**1.01**	**1.00**								
Mg*	18.42	13.86	**Mg***	48.59	41.81	**Mg***	58.91			

	Thermobarometry of Assemblage (fluid absent):											
	grt (rim) matrix bt				grt (core), matrix bt				grt (core) bt inclusion			
a_{H2O}	**T**	**st dev**	**P**	**st dev**	**T**	**st dev**	**P**	**st dev**	**T**	**st dev**	**P**	**st dev**
0.5	690	54	4.0	0.9	748	56	3.7	1.0	753	57	4.4	1.0
0.6	709	57	4.5	0.9	770	59	4.1	1.0	775	60	4.9	1.1
0.7	725	59	4.9	1.0	788	62	4.5	1.1	793	63	5.3	1.1

Table 8.2. c: Structurally controlled leucosomes:

KHt2/2 Grt-bearing leucosome												
	Garnet			Biotite				Cordierite			Feldspar	
	Core	Rim		Leuco-some	Matrix	Inclusion in crd		Leuco-some	Matrix		Plag	Ksp
SiO_2	35.38	35.67		36.69	35.53	35.31		47.81	47.52		62.75	65.22
TiO_2				0.00	2.99	2.60		0.00	0.00			
Al_2O_3	20.41	20.43		19.64	19.62	19.74		32.37	32.02		23.34	18.60
Fe_2O_3								0.00	0.00			
FeO	35.02	35.03		22.00	20.78	20.09		10.47	10.82			
MnO	4.30	5.77		0.20	0.20	0.15		0.31	0.50			
MgO	3.22	2.11		9.62	8.71	8.69		7.73	7.40			
CaO	0.84	0.83						0.00	0.00		4.47	0.02
Na_2O				0.00	0.32	0.34		0.32	0.00		9.00	1.81
K_2O				8.75	9.29	9.12		0.00	0.00			14.38
Total	**99.177**	**99.84**		**96.90**	**97.44**	**96.05**		**98.99**	**98.25**		**99.57**	**100.03**
Si	2.89	2.91	**Si (5-6)**	5.51	5.32	5.34	**Si**	4.94	4.94	**Si**	2.78	2.99
Al^{IV}	0.11	**0.09**	**Al^{IV} (3-2)**	2.49	2.68	2.66	**AlIV**	1.06	1.06	**Al**	1.22	1.01
Σ T-site	**3.00**	**3.00**	**Σ T-site**	**8.00**	**8.00**	**8.00**	**Σ T-site**	**6.00**	**6.00**	**Σ T-site**	**4.01**	**4.00**
Al^{VI}	1.85	1.88	**Al^{VI}**	0.98	0.78	0.86	**AlVI**	2.88	2.87			
Fe^{3+}	0.26	0.21	**Ti**	0.00	0.34	0.30	**Ti**	0.00	0.00	**Ca**	0.21	0.00
Σ M-site	**2.11**	**2.09**	**Σ XX-site (0-2)**	**0.98**	**1.11**	**1.16**	**Fe3+**	0.18	0.19	**Na**	0.77	0.16
							Σ M-site	**3.06**	**3.06**	**K**	0.00	0.84
Fe^{2+}	2.12	2.18	**Fe^{2+}**	2.76	2.60	2.54				**Σ A-site**	**0.99**	**1.00**
Mn	0.30	0.40	**Mn**	0.03	0.03	0.02	**Mg**	1.19	1.15			
Mg	0.39	0.26	**Mg**	2.15	1.94	1.96	**Fe2+**	0.72	0.75			
Ca	0.07	0.07	**Σ M-site (6-4)**	**4.94**	**4.57**	**4.52**	**Mn**	0.03	0.04			
Σ A-site	**2.89**	**2.91**					**Σ A-site**	**1.94**	**1.94**	**An**	21.54	0.10
			Na	0.00	0.09	0.10				**Ab**	78.46	16.06
XAnd	0.12	0.10	**K**	1.67	1.77	1.76	**Ca**	0.00	0.00	**Or**	0.00	83.84
XAlm	0.74	0.75	**Σ A-site (2)**	**1.67**	**1.87**	**1.86**	**Na**	0.06	0.00			
XPyr	0.14	0.09					**K**	0.00	0.00			
XSps	0.10	0.14	**Cation Σ**	**15.59**	**15.55**	**15.53**	**Σ Channel cations**	**0.06**	**0.00**			
Total	**1.09**	**1.07**										
Mg*	15.56	10.52	**Mg***	43.81	42.77	43.53	**Mg***	62.26	60.40			

Thermobarometry of Assemblage (fluid absent):

	grt (core), leucosome bt, leucosome crd				grt (core), matrix bt, leucosome crd				grt (core), matrix crd, bt inclusion in crd			
a_{H2O}	**T**	**st dev**	**P**	**st dev**	**T**	**St dev**	**P**	**st dev**	**T**	**st dev**	**P**	**st dev**
0.5	689	50	3.2	0.9	715	55	3.8	1.0	712	55	3.9	1.0
0.6	710	53	3.5	0.9	736	58	4.2	1.0	734	58	4.3	1.0
0.7	729	55	3.9	1.0	755	61	4.6	1.1	752	60	4.7	1.1

An excellent example of this exists in sample 12/1D; this rock displays evidence for partial melting, but retained leucocratic material as nebulitic leucosomes associated with garnet and cordierite. There is no evidence for melt loss and the rock is still considerably K-rich (Table 5.2. a). This argues that there could have been the opportunity for significant back reaction of biotite with the liquid. Indeed, this rock has a significant difference between the composition of matrix biotite and that of biotite inclusions in garnet formed during the melting reaction. The latter is considerably richer in TiO_2 and has a higher Mg#. This trend is opposite to the trend of biotite composition as found in the matrix and as inclusions in garnet of the metapsammitic rocks. In these rocks, there was no partial melting and the inclusions of biotite in garnet seem to retain a lower-temperature chemistry compared to that of the matrix biotite (they are poorer in TiO_2). The biotite inclusions appear to retain part of the prograde history, whereas the biotite in the garnet of metapelitic rocks records the peak metamorphic conditions with the matrix biotite of both rocks retaining a retrograde signature. This indicates that the garnet in these rocks could have formed at different times during the metamorphism, forming inclusions of a prograde assemblage in the metapsammites and of a peak (anatectic) assemblage in the metapelite. PT conditions of 741 ± 58 °C and 0.41 ± 0.1 GPa were obtained for the assemblage preserved in the garnet core of the metapelite. In comparison, the assemblage that considers the garnet to be in equilibrium with the biotite, which defines a foliation that wraps around the garnet, gives PT estimates over 100 °C and 0.1 GPa lower.

It is important to question the validity of the thermobarometry because, as discussed in Section 8.2, the minerals in high-grade metamorphic environments might only record the retrograde path (Spear & Florence, 1992). The results of the thermobarometry are unfortunately not very robust due to the lack of complete sets of independent reactions however, fairly good 'fit criteria' exist for the PT estimates (see Table 8.1). The fit criteria is a measure of the statistical validity of the result determined by taking into account the uncertainties of the calculations and for sample 14/5A was in the order of 0.5, for sample KHt2/2 was 0.61 and for sample KH1/2 was around 0.4. The Thermocalc output suggests that for a confidence of 95% the fit criterion should be less than 1.61 (for

another example see Proyer et al., 2004). Although, the parameters shown in Table 8.1 inicate that the calculations may be statistically plausible it cannot determine whether the mineral assemblage equilibrated at temperatures far below the metamorphic peak as commonly happens in high-grade metamorphic environments (Frost and Chacko, 1989). The large standard deviations of the results together with the possible underestimation of the peak of metamorphism means that significantly more work is required to constrain the conditions of metamorphism and thus also the mechanism of melting in the study area.

Despite the uncertainties, some useful indications can be drawn from the thermobarometry. The PT conditions determined here for the peak of metamorphism must be a minimum, but suggest that the conditions are at the low end of the 730 – 850 °C range where the likely biotite breakdown reactions that could account for the field evidence lie. The conditions determined are at least consistent with the field observations that melting is in the insipient phases, seemingly controlled by deformation and not pervasive in the metapelites as could be expected at higher temperatures. Furthermore, the dearth of garnet in the metapelites, except in the local melting sites is an argument for conditions near the boundary between the amphibolite- and the granulite-facies.

The peak conditions calculated are the highest yet recorded for the study area and are similar to the temperatures determined by Jung and Mezger (2003). The temperatures determined fall close to the lowest temperature conditions under which biotite is believed to undergo fluid-absent melting and definitely within the range of fluid-present melting of biotite. The lowest temperatures documented for biotite fluid-absent melting in experimental studies are approximately 800 °C (e.g. Vielzeuf & Holloway, 1988). However, such low temperatures are normally only reported in studies where a natural rock starting material was used that contained some minor proportion of lower grade hydrous minerals (chlorite and staurolite in the Vielzeuf and Holloway example). More commonly biotite only begins to melt by fluid-absent processes in the temperature interval 850 to 900 °C (Clemens & Vielzeuf, 1987; Patino-Douce & Johnston, 1991; Patiño Douce & Beard, 1995; Stevens et al., 1997).

This, lower than expected, temperature recorded for the peak metamorphism and the anatexis of the Kuiseb Formation metapelites in this part of the Damara Belt, together with the close link between structural sites and melting suggests that the anatectic process includes some variable that cannot be tested with conventional thermobarometry. For this reason an independent test on the PT conditions and fluid-regime of the biotite melting must be conducted. In this study partial melting experiments have been conducted on Damara metasedimentary protoliths in order to better constrain the fluid conditions during anatexis as well as the stoichiometry of the melting reaction with the aim of understanding the possibly low-temperature melting and any possible structural influences.

9. Experimental anatexis of the Kuiseb metasediments

9.1 Introduction

Representative examples of both the cordierite-biotite gneiss from the study area that displays none of the features interpreted to be the result of partial melting and a chemically similar, but more hydrous, lower grade rock from the Usakos region were selected as starting materials for the experimental study (comparison in Table 9.2). In general, the lower grade rock is more "fertile" containing more potassium, a higher Na/Ca ratio and a higher proportion of water (Table 9.2). This rock will be used to test the possibility that, although the higher grade rock used in the experiments displays no evidence for incongruent melting of biotite, there is a possibility that the rock may have lost a small amount of melt due to quartz + feldspar + H_2O melting. Experiments were conducted at 0.7 GPa, which is slightly higher than any published estimate of pressure in the Damara, but within error of the highest P estimate from this study. The highest reasonable pressure for the experimental study was chosen to encourage garnet growth without greatly affecting the position of the incongruent melting reactions. Greater pressure favours garnet stability over that of cordierite (Hensen, 1971, Hensen & Green, 1973), but has little effect on the melting reactions due to their steep slope in P-T space (Vielzeuf & Holloway, 1988, Clemens et al., 1997, Stevens et al., 1997). Three types of experiments were performed. ***Type 1*** experiments were fluid-absent and were conducted at 0.7 GPa over the temperature range of 800 – 1000 °C. ***Type 1a*** experiments used the high-grade starting material (12/1A) and ***Type 1b*** used the lower-grade starting material (USK-7). These experiments effectively test the fluid-absent anatectic processes relevant to the Kuiseb schists in the Blauer Heinrich Syncline, from the maximum metamorphic temperatures in the study area to a temperature in excess of the highest grades estimated for the Damara belt. The inclusion of the amphibolite-facies starting material aims to test the dependence of melting, at temperatures below the fluid-absent solidus of the high-grade rock, on the minor amount of water that will be released as a result of "prograde metamorphism" of this starting material. ***Type 2*** experiments were performed on the high-grade starting material at the same pressure at 800, 750 and 700 °C with sufficient

water added, that water would remain in excess (details of each experiment are presented in Table 9.1). ***Type 3*** experiments used the same starting material, but had less water added, such that the experiments were initially water-saturated experiments, but became fluid-absent as melting progressed. Both the Type 2 and 3 experiments were designed to test the reaction of the rocks to fluid ingress under high-grade metamorphic conditions.

The experiments used an early Holloway-design, non-end-loaded piston-cylinder apparatus. Lead-jacketed NaCl-MgO pressure cells were used for all experiments. Experiments were performed using a 1.27 cm pressure vessel, accommodating a single sample. Pressure assemblies comprised an outer, molybdenite lubricated, NaCl sleeve surrounding the graphite furnace and a crushable magnesia rod filling the lower half of the furnace. The sample packet was placed on top of this and embedded in a small amount of MgO powder. The sample was covered by a 0.5 mm thick synthetic ruby disc. The top half of the furnace was filled by a hollow crushable magnesia rod, with the ceramic (recrystallised alumina) sheathed thermocouple support down the centre and the measuring tip abutting the ruby disc. The tip of the thermocouple was thus placed within 1 mm of the top of the capsule. In other studies using a similar arrangement (e.g. Vielzeuf and Montel 1994), the temperature deference between the sample and the thermocouple was found to be less than 5 °C. In all experiments, full pressure was applied before heating. We used the hot piston-out technique to approach the run pressure and pressure measurement was by a HEISE gauge. Temperature was controlled to 1 °C by a "Depths of the Earth" temperature controller and measured by means of a type-K thermocouple. Total temperature uncertainties are believed to be ± 4 °C.

Table 9.1: The table lists the experimental conditions and parameters with variations for all experiments. Garnet seeds were added for all experiments at 800 °C and below to avoid nucleation problems. Garnet from the field area were used where possible, but garnet from Limpopo Belt metasediments was used when image analysis was required for the run products; the higher Ca-content made these seeds more easily distinguishable from new garnet, ensuring that only new garnet was considered in the calculations.

Exp no	Temp (°C)	Max Temp Variation	Pressure (Gpa)	Max pressure variation	Duration (h)	Exp type	Garnet seeds	% H_2O added	Fluid regime
1	*1000*	*993-997*	*0.7*	*0.66-0.74*	*122*	*1a*	*no*	*0.0*	*Fluid-absent*
2	*1000*	*993-997*	*0.7*	*0.60-0.74*	*120*	*1b*	*no*	*0.0*	*Fluid-absent*
3	*950*	*947-952*	*0.7*	*0.65-0.74*	*121*	*1a*	*no*	*0.0*	*Fluid-absent*
4	*950*	*948-952*	*0.7*	*0.64-0.73*	*123*	*1b*	*no*	*0.0*	*Fluid-absent*
5	-	*Failed*	-	-	-	*1a&b*	*no*	*0.0*	*Fluid-absent*
6	*900*	*898-901*	*0.7*	*0.67-0.73*	*165*	*1a*	*no*	*0.0*	*Fluid-absent*
7	*900*	*898-901*	*0.7*	*0.64-0.72*	*168*	*1b*	*no*	*0.0*	*Fluid-absent*
8	-	*(>850)*	*0.7*	-		*Failed Type 1a*	*no*	*0.0*	*Fluid-absent*
9	*850*	*848-851*	*0.7*	*0.65-0.72*	*240*	*1a*	*no*	*0.0*	*Fluid-absent*
10	*850*	*849-851*	*0.7*	*0.66-0.75*	*246*	*1b*	*no*	*0.0*	*Fluid-absent*
11	*800*	*798-801*	*0.7*	*0.64-0.73*	*312*	*1a*	*yes (Damara)*	*0.0*	*Fluid-absent*
12	*800*	*798-801*	*0.7*	*0.68-0.75*	*351*	*1b*	*yes (Damara)*	*0.0*	*Fluid-absent*
13	*800*	*799-802*	*0.7*	*0.65-0.72*	*330*	*Failed Type 2, but duplicates Exp 11*	*yes (Damara)*	*effectively zero*	*Undersaturated*
14	*800*	*799-801*	*0.7*	*0.63-0.72*	*307*	*Failed Type 2, but duplicates Exp 11*	*yes (Damara)*	*effectively zero*	*Undersaturated*
15	*800*	*799-802*	*0.7*	*0.64-0.72*	*183*	*2*	*yes (Damara)*	*27.4*	*Saturated*
16	*750*	*749-751*	*0.7*	*0.63-0.71*	*169*	*2*	*yes (Damara)*	*20.0*	*Saturated*
17	*700*	*699-701*	*0.7*	*0.66-0.75*	*180*	*2*	*yes (Damara)*	*15.0*	*Saturated*
18	*750*	*750-751*	*0.7*	*0.68-0.71*	*223*	*3*	*yes (Limpopo)*	*5.7*	*Undersaturated*
19	*800*	*799-801*	*0.7*	*0.69-0.72*	*241*	*3*	*yes (Limpopo)*	*5.1*	*Undersaturated*
				total hours	3601				

9.2 Experimental Results

9.2.1 Experimental run products

The experimental results are summarised in Table 9.3 and SEM-BSE images of the textures in the run products are presented in Figures 9.1, 9.2 and 9.3.

9.2.1.a Type 1 Experiments

In the Type 1 Experiments using the granulite-facies starting material (12/1A), there was no noticeable change in the mineralogy of the mineral assemblage at 800 °C, despite the experiment being performed in duplicate. No glass was found and the chemistry of the minerals was the same as the composition of the minerals in the starting material. Melt was produced in all the other experiments at higher temperatures with the melt fraction increasing with temperature. At 850 °C the melt fraction was very small (possibly as little as 1%), but paired with the presence of new garnet and recrystallised biotite it suggests that this melt is not the result of quartz + feldspar + H_2O melting, but rather of incongruent breakdown of biotite. There is no evidence of cordierite participating in this reaction at 850 °C. The amount of glass produced in the 900 °C run is more pronounced (± 10 %) and both peritectic garnet and cordierite were also present in greater amounts. Cordierite has formed euhedral crystals in the melt patches as shown in Figure 9.1, C. Biotite was present in two textural associations in this run product, namely with the 'matted' texture of the starting material biotite and as tabular crystals that occur within the melt. These probably formed in response to breakdown of the initial biotite to yield melt + garnet + biotite (ii) + cordierite.

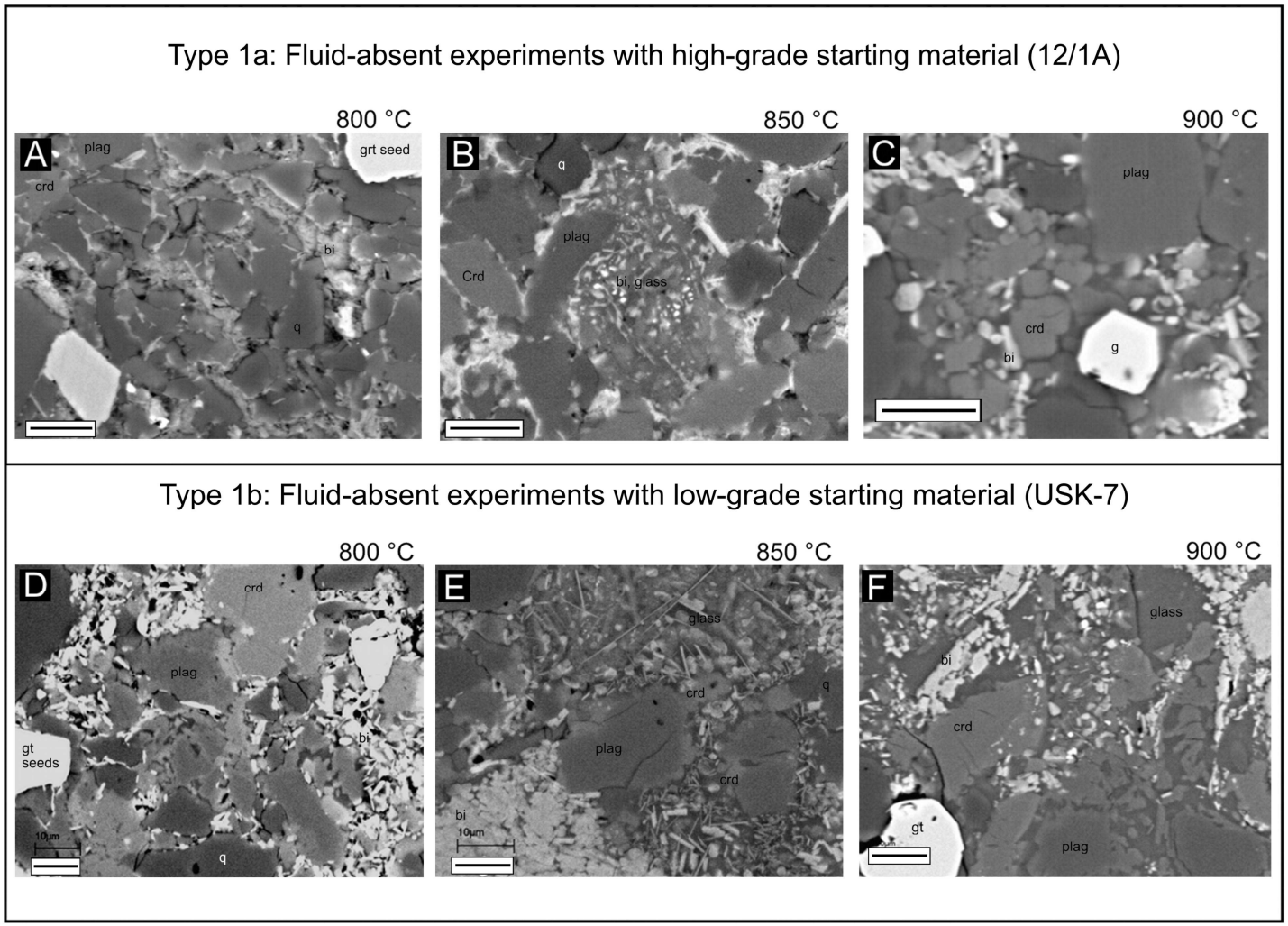

Figure 9.1. Summary diagram showing an annotated backscattered electron image for each of the fluid-absent experimental run products. A-C are images of Type 1a experiments performed on the high-grade starting material and D-F are images of Type 1b experiments using the low-grade starting material. The scale bars represent 10 µm in each case. Glass represents quenched melt and is the darkest grey-scale phase in the images.

In the Type 1 experiments using the amphibolite-facies starting material (USK-7) minor melting (< 1 %) had occurred in the lowest temperature experiment at 800 ºC. However, despite the presence of garnet seed crystals, no new, euhedral garnet was produced, but neither were the seeds dissolved (Figure 9.1, D), possibly indicating that the conditions of the experiment were very close to those of a garnet-in reaction in this composition. The melt in this experiment is interpreted to have formed by wet melting of quartz + plagioclase made possible by the release of water from muscovite on heating; this phase was present in the low-grade starting material in modal amounts of < 1 %.

The 850 °C run product is characterised by the presence of garnet and melt in addition to the two textural varieties of biotite discussed above. The volume of melt produced in this experiment is significantly larger than that in the equivalent experiment using the granulite-facies starting material. The melt fraction increases further in the 900 °C experiment with large, euhedral garnet having formed as a result together with abundant blocky cordierite. The minerals and the textural associations are similar to those of the granulite-facies starting material experiments at the same temperature, except for the greater proportion of melt.

At 950 °C both starting materials produced significant quantities of melt with peritectic orthopyroxene, but only the experiment using the high-grade starting material produced garnet. Garnet is again present in both Type 1a and 1b experiments at 1000 °C (Figure 9.2). This suggests the experiments define an isobaric section through the divariant field of garnet and orthopyroxene co-existence. The composition used in the Type 1b experiments results in slight differences in the positions of these reaction lines (the divariant field) and in this case the isobaric section must be very close to the Opx-in line. These reaction lines are probably very flat in PT space, accounting for the variability in the garnet stability, with garnet going out between 900 and 950 °C and then reappearing at 1000 °C. This garnet at 1000 °C in the Type 1b experiment was, however, formed in a low proportion and consisted of very fine crystals that could not be analysed accurately.

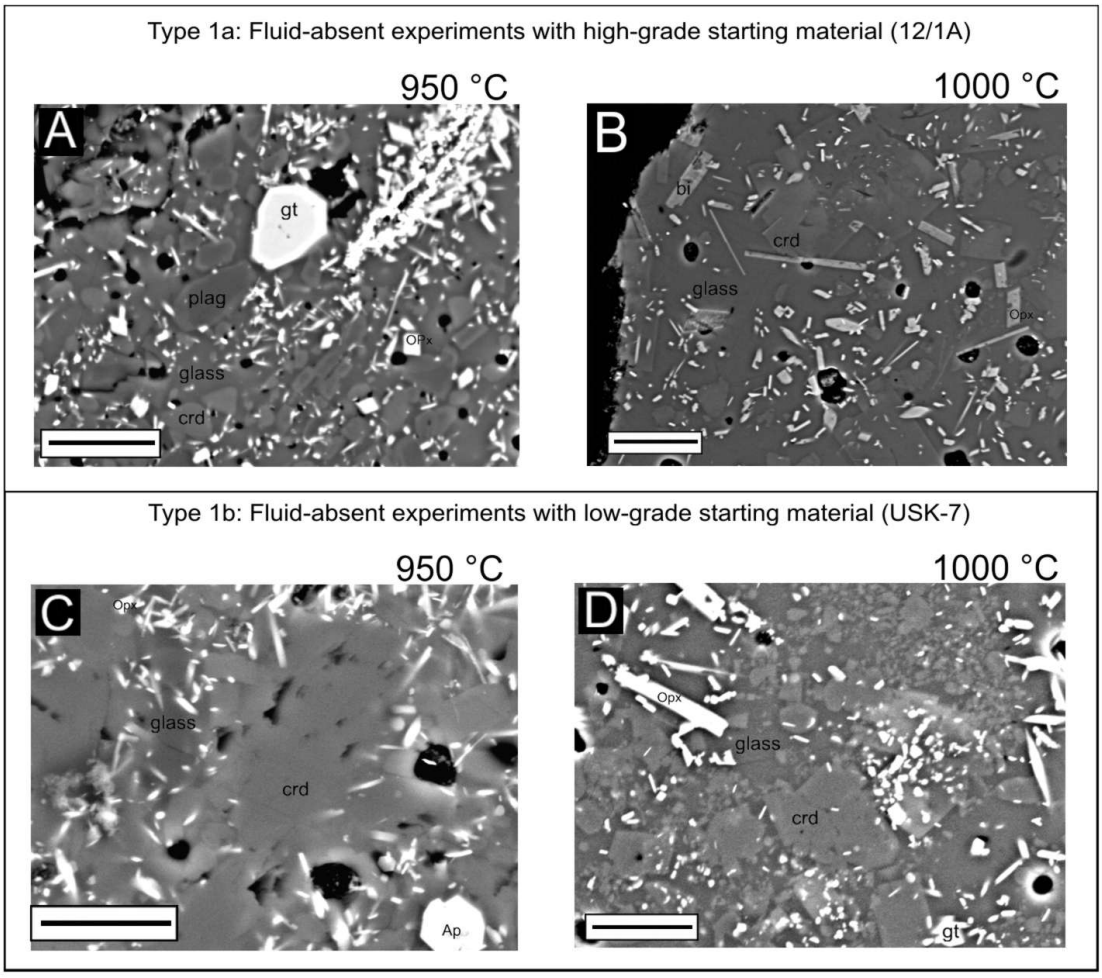

Figure 9.2. Summary diagram showing an annotated backscattered electron image for each of the fluid-absent, high-temperature experimental run products. A and B are images of Type 1a experiments performed on the high-grade starting material and C and D are images of Type 1b experiments using the low-grade starting material. The scale bars represent 10 µm in each case. Glass represents quenched melt and is the darkest grey-scale phase in the images.

It is interesting to note that biotite is still present in the 1000 °C Type 1b experiment. This extreme thermally-stable biotite is probably present as a result of the rock becoming quartz deficient, and thereby stabilising the hydrous silicate far beyond the conditions at which it would incongruently breakdown (to completion) to form melt in a quartz-saturated system.

9.2.1.b Type 2 experiments

In the Type 2 experiments water remained in excess in the experiments, with a discernable loss of mass upon piercing the capsule and drying under vacuum. In the 700 °C Type 2 experiment the run product remained partially friable on removal from the capsule. No glass could be found in the product assemblage and no new garnet had formed on the seed crystals. No cordierite remained in the product assemblage, having been replaced by gedrite. Biotite had recrystallised and reequilibrated with the new, cordierite-free assemblage. Plagioclase had become slightly more calcic, indicating that it had also reequilibrated at the experimental conditions, possibly losing Na to the amphibole, although small cores with the composition of the initial plagioclase do remain.

Melting had clearly occurred in the 750 °C experiment, with the products emerging from the capsule as a fused glassy pellet. New garnet and cordierite had formed in the run products and had nucleated on the garnet seeds and pre-existing cordierite crystals and can be both texturally and chemically distinguished from the relict cores. This, together with the large volume (± 40 %) of relatively potassic melt, indicates that the charge had melted predominantly by the water-present biotite incongruent melting reaction Bt + Pl_1 + Q + H_2O = Melt + Grt + Crd + Pl_2. Biotite remained in the assemblage, possibly because quartz was exhausted by the melting reaction. Very large (> 100 μm) crystals of plagioclase were formed in the run product, indicating the participation of plagioclase in the melting reaction. Gedrite was absent from the product assemblage.

Abundant melt was produced (± 60 %) in the 800 °C experiment, in conjunction with peritectic garnet, cordierite, orthopyroxene and spinel. In addition to the emergence of orthopyroxene in the product assemblage, a greater proportion of garnet relative to cordierite was produced in this experiment when compared to the 750 °C result (Figure 9.3). Biotite remains in the product assemblage and quartz has been completely consumed by the melting reaction. Spinel is a very minor phase in the run product, occurring as approximately 1 μm crystals in association with garnet.

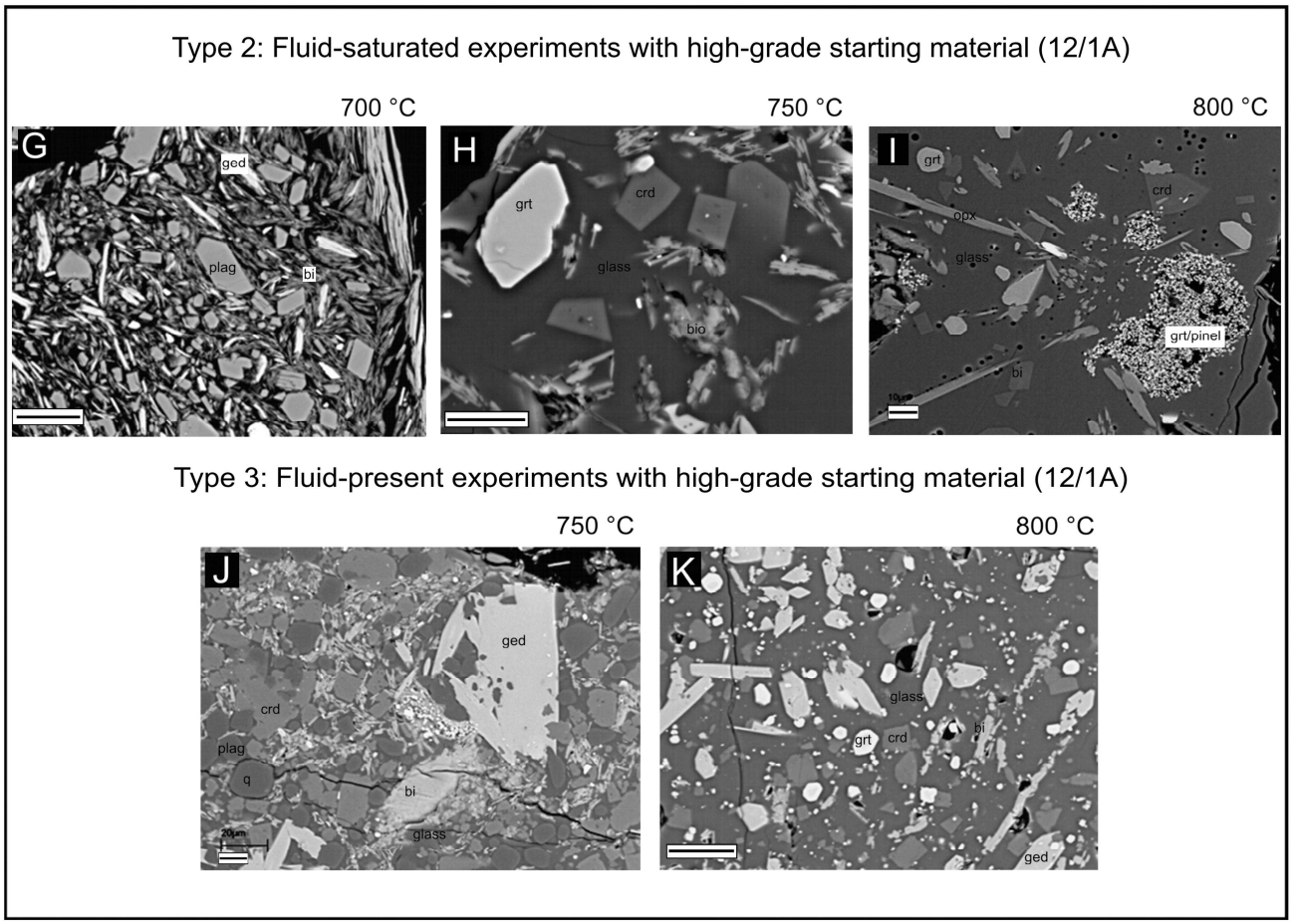

Figure 9.3. Summary diagram showing an annotated backscattered electron image for each of the fluid-present experimental run products. G-I are images of Type 2 experiments performed on the high-grade starting material that remained water-saturated during the experiment and J and K are images of Type 3 experiments also using the high-grade starting material but became water-undersaturated as melting progressed in the capsule. The scale bars represent 10 µm in each case. Glass represents quenched melt and is the darkest grey-scale phase in the images.

9.2.1.c Type 3 experiments

The principal difference between the Type 2 (~ 15 wt% H_2O) and 3 (~ 5.5 wt% H_2O) experimental results are that in the Type 3 experiment products quartz remains as an abundant phase in the product assemblage at 750 °C, garnet appears only at 800 °C and at 750 °C biotite, melt and cordierite coexist with gedrite instead of garnet. The gedrite has formed large euhedral crystals with inclusions of quartz and glass (Figure 9.3, J). Cordierite has formed euhedral overgrowths on the crushed cordierite from the starting material. Thus, in this case the melting reaction appears to be Bt + Pl_1 + Qtz + H_2O = Melt + Ged + Crd + Pl_2. Quartz and plagioclase are still abundant and are in contact with the glass indicating that the melting reaction was limited by the availability of water. This was confirmed by the fact that the post-experiment pierced capsule did not loose weight on drying under vacuum. Biotite is present as abundant small, euhedral crystals and rare mats of biotite of a similar texture to the starting material. The two textural varieties of biotite are chemically identical and different from that in the starting material.

At 800 °C, the charge contained the assemblage cordierite, gedrite, garnet, biotite and glass. The sample was determined to be water-undersaturated by means of gravimetric analysis, however, quartz and plagioclase were completely consumed in the melting. The difference between this run-product compared to that of the 800 °C water-saturated run is, most significantly, the presence of gedrite and the absence of orthopyroxene.

9.2.2 Determining Experimental phase compositions

The same analytical technique described in Chapter 6, used to determine the mineral compositions of the natural rocks, was used to determine the compositions of the minerals in the experiments. The one phase that was analysed with a modification to this technique was the glass that is formed as the liquid melt quenches to a solid on termination of the run.

It is difficult to constrain the composition of glasses, as they often contain the light compounds and elements CO_2, H_2O, B, Na, Si, K and Li (Luth, 1967, Eggler &

Holloway, 1977, Burnham, 1979, Clemens & Vielzeuf, 1987, London et al., 1988) in significant abundances, which are notoriously difficult to analyze accurately in non-crystalline solids. In the experiments of this study, CO_2, B and Li concentrations will be in the range of trace elements as no phases were present in the starting materials that contain these as major elements. Analysis of Si and K in the glasses is relatively straightforward, given the low-energy electron beam (made possible by the inherent efficiency of energy dispersive x-ray detection systems). This leaves H and Na as the problematic elements that are present in the glass in significant quantities.

In determining the quantity of Na_2O in silicate glasses via electron beam techniques, a common problem manifests itself as a decrease in the Na X-ray count rate with time during analysis. Counteracting this problem involves standardizing on an appropriate glass standard i.e. ideally one with the same Na count-rate decrease as the unknown, and/or choosing an analytical setup to reduce the problem and/or determining a correction factor for Na (Pichavant, 1987, London et al., 1988, Holtz et al., 1992, Preston et al., 2003). These are all problems in a study such as this. It is known that the rate of Na count decrease is a function of the 1/ASI, the Na_2O concentration and the H_2O concentration in the glass. In these experiments glass compositions, H_2O concentrations particularly vary strongly as a function of both starting material and temperature. Thus, in effect, a different standard, or correction factor, would be needed in each case. A normal, low beam-energy analytical setup for analyzing melts with the Electron Microprobe involves dropping the beam current to 2 nA, using a defocused beam of 20 μm diameter, an accelerating voltage of 15 kV and counting times of as low as 2 to 5 seconds to counter the effect of Na-loss. This analytical approach uses less aggressive beam conditions and, therefore, tries to reduce the Na losses during analysis. It is accepted that there is generally no need for corrections of the electron microprobe data for dry glasses, whereas for H_2O-bearing glasses, Na_2O has to be corrected upward by significant factors because of the migration of Na from under the electron beam (Holtz et al., 1992). The problem with correction factors is that the abundance of H_2O and Na_2O varies across the melting interval. Underestimations of 3-4 wt% Na_2O in hydrous glasses have been noted (Preston et al., 2003) and lead to shifts in many of the petrologic classification systems, for example the Aluminium Saturation Index which incorporates Na_2O in its calculation, and

therefore has an influence on the classification and interpretation of the system. Defocusing the beam is very problematic in studies, such as this, that investigate the beginning of anatexis. Melt volumes close to the solidus are simply too small to allow for anything other than a tightly focussed beam. In addition, the short counting times deliver poor statistics making it very difficult to distinguish glass analyses that are slightly contaminated by minerals. This is made particularly difficult by the fact that the glass has no set stoichiometry.

Another technique used to analyze silicate glasses is by means of a Scanning Electron Microscope fitted with an EDS system and a freezing- or cryo-stage (Vielzeuf & Clemens, 1992). This involves using a setup of 15 kV accelerating voltage and a probe current of 1.5 nA. We used a 4 nA beam setup (Spicer & Stevens, in prep). The sample is then cooled down to below -190 $^{\circ}$C to counteract the migration-related counting losses on the light elements, especially Na_2O. Counting times of 50 seconds were used. A large-diameter Be window was fitted to the detector and good count rates were obtained, similar to analyses from normal minerals. Standardization used natural mineral standards analysed at the same conditions.

A problem with the technique of Vielzeuf and Clemens (1992) is that it requires normalization of the results to 100 wt% because of the instability of the electron-beam, compared to that of an electron microprobe, and compositions can thus be slightly shifted from their true values. Calculations involving mass-balance reactions might be influenced when normalised and therefore affect interpretation of the results. To counteract this normalisation problem we used a Faraday cup to monitor the beam stability and therefore did not have to normalize results. Simultaneously, analyses of minerals in the run products were also made as a check on the beam stability. Quartz was used whenever it was present in the run product to correct the beam energy conditions to give 100 wt% totals. This check to determine if the beam conditions were the same as those of the standard analyses conditions validates the assigning of the difference between the total of a glass analysis and 100 wt% to the content of compounds that cannot be analysed with SEM-EDS (H_2O in the case of this study).

In this study the effect was briefly investigated to illustrate the loss of sodium with an intensely focussed beam, as well as investigating the effect of temperature on the mobility of sodium with certain techniques. The results of a qualitative comparison of the different techniques are presented here. The glass produced in the 800 °C Type 2 experiment was used in this study due to the large proportion of glass produced, giving large, homogeneous volumes of glass to analyse. The glass was analysed at room temperature (21 °C) with both a focussed beam counting for 50 seconds live time as well as a focussed beam rapidly rastered over a 50 by 50 μm area for the same duration. It was also tested with the two beam states at low temperature (ca. -190 °C).

The results of the investigation are presented in Figure 9.4, which illustrates the trend of Na as a function of the SiO_2 content of the glass. It is important to remember that in representing the data as wt% amounts, the amounts of all the other elements present in the glass will increase with a decrease in any one element. Thus a Na-loss will be coupled with an increase in SiO_2 content – it is most noticeable in this compound as it is the major constituent of the glass. This is exactly what the diagram illustrates with the negative trend. The K_2O content of the glass is also displayed for the sake of comparison. It does not decrease with the increasing SiO_2 (which increases as a function of the Na-loss). The data was normalised to 92 wt%, which is the average total of the cold analyses.

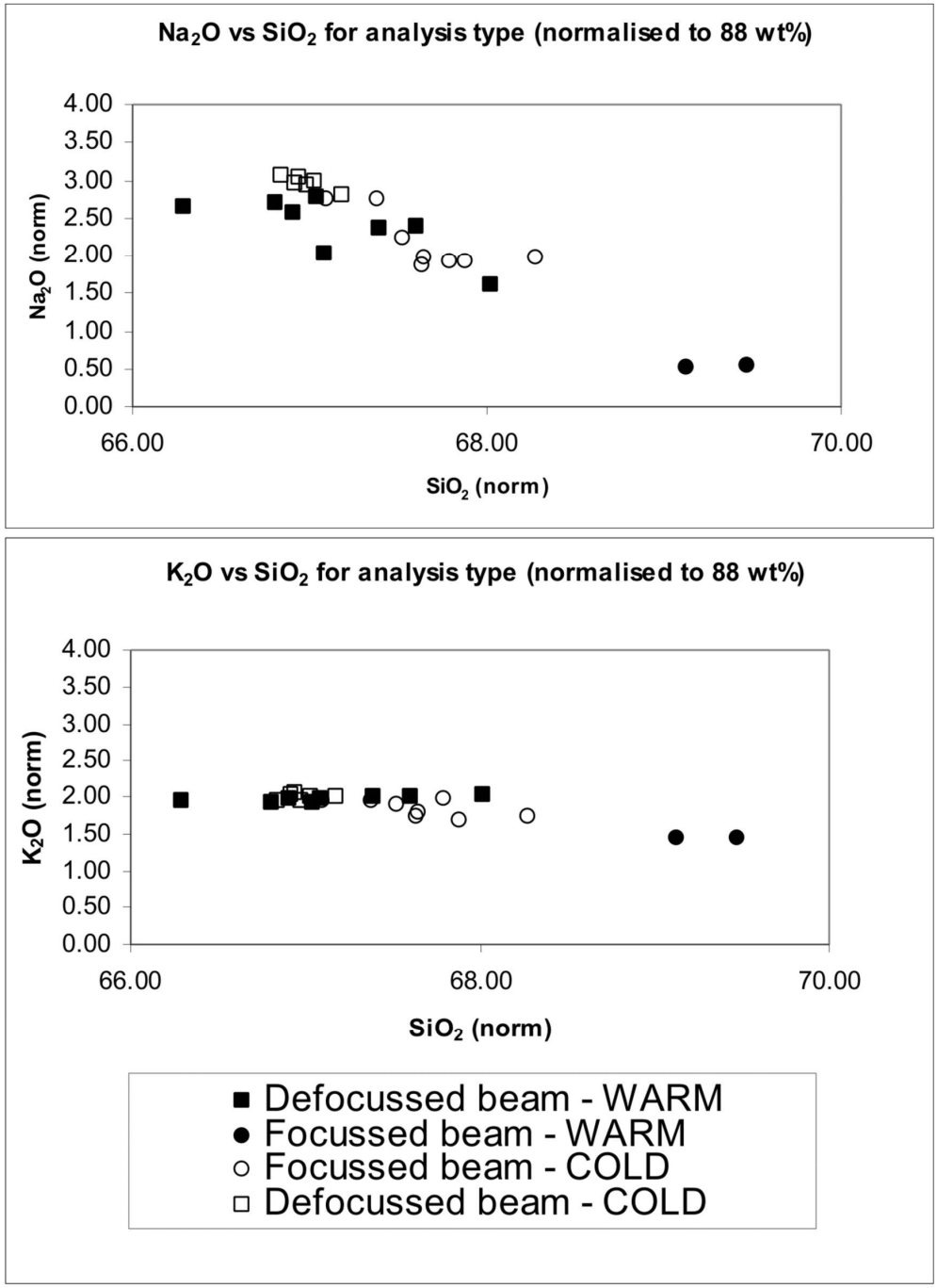

Figure 9.4. Graphs showing the variability in the determined composition of silicate glass according to different analytical techniques. The diagram shows that the loss of sodium during the duration of the analysis was minimized using the freezing-stage technique together with rastering the beam over the 50 µm spot (open squares). Using a focussed beam at -190 °C (open circles) did result in some Na-loss, however, this method was slightly better than rastering the beam on the glass at room temperature (filled squares). Using a focused beam at room temperature (filled circles) resulted in large decreases in the analysed Na-content of the glass, despite the relatively low beam energy deployed.

Despite being the most precise method, using the defocused beam at cold conditions was not always practical, due to the very small volumes of glass formed at low proportions of melting in most of the experiments and the greater risk of contaminations by adjacent phases. Given this practical consideration and together with the fact that the standard materials were analysed with a focused beam, it was decided to use the spot analysis technique in combination with the freezing-stage to acquire all glass compositions. Special care was taken to identify Na-loss during analysis and to discard data that showed a decrease in Na X-ray counts. Nevertheless, reported glass compositions may underestimate Na-content by almost 1 wt%. This could also influence the water content determined for the glasses. Despite this the freezing stage technique represents an improvement on other techniques regularly reporting glass compositional data in the literature.

9.2.3 Experimental Phase Chemistry - results

Details of the mineral and melt compositions produced in this study are provided in the tables of Appendix 2.3 and are summarised in Table 9.3. The evolution of the cordierite, plagioclase, garnet and melt compositions produced in the experiments using starting material 12/1A as a function of temperature and water content of the experiments are illustrated in (Figure 9.5). The following key phase composition changes occurred in the experiments:

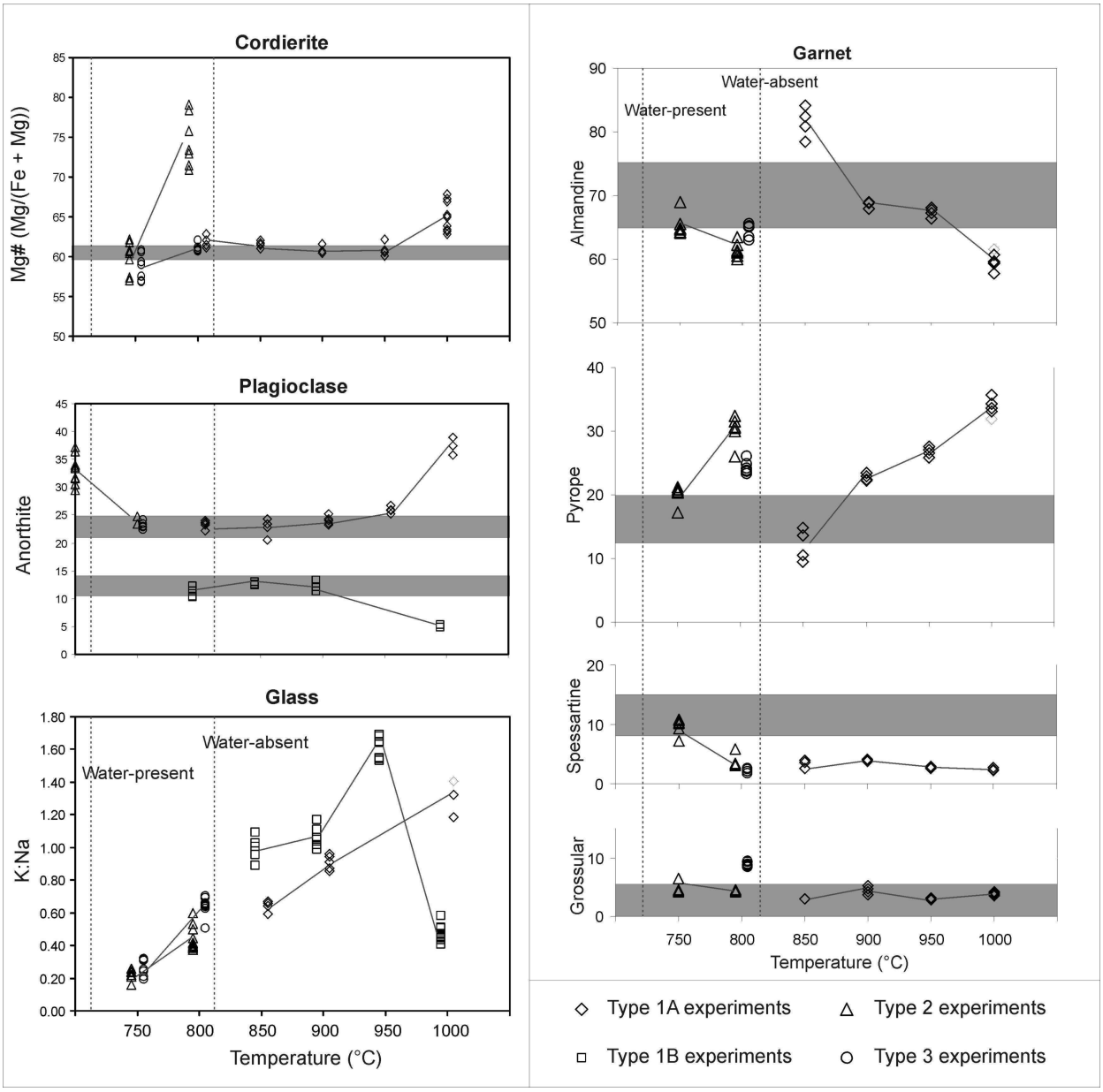

Figure 9.5. Summary diagram of the phase chemistry of the experimental run-products. Data from these experiments are available in the tables of appendix 2.3. The shaded boxes across the diagrams indicate the range of compositions found in typical metapelites of the study area for comparison with the chemical composition of the run-products. Vertical broken lines indicate the approximate positions of the 'water-absent' and the 'water-present' biotite breakdown reactions as determined from the experiments. Where different experiment types were conducted at the same temperature, the results have been artificially listed at slightly higher (Type 1a) or slightly lower (Type 1b, Type 2) temperatures for clarity on the graphs. The Mg# of new cordierite remains similar to that of the starting material in the Type 1 experiments (Mg# of cordierite from the low-grade starting material is shifted to slightly lower values than illustrated by the shaded block. Cordierite in the Type 2 and Type 3 experiments has a composition most similar to that in the field at the conditions of the 750 °C experiments. The scatter in the data is attributed to analytical difficulties such as analysing a portion of the core together with new cordierite at the rim. Plagioclase composition remains similar to the starting materials until high temperature in the Type 1 experiments. In the Type 3 subsolidus experiment the plagioclase composition is shifted due to partitioning of Na into the newly produced

gedrite. Glass compositions vary with temperature, and the K:Na ratio illustrates the greater role of biotite breakdown as the volume of melt increases with temperature in comparison to the melt produced by qtz + pl melting. At right is a graph of garnet composition listing the almandine, pyrope and spessartine components of garnet produced in experiments (only Type 1a, Type 2 and Type 3 experiments shown), plotted versus the temperature of the experiment. The compositional range of naturally occurring anatectic garnets from the field area are drawn as shaded bands across the diagram. The water-present and water-absent solidi are also given. The Type 3 b garnet composition is plotted at slightly higher temperature for clarity on the diagram. From the diagram it is clear that the garnet produced in the 750 °C experiment most closely matches that of the natural garnets produced by biotite breakdown in structural sites.

Table 9.2 Table of experimental starting materials, including modal amounts of minerals in the starting rocks.

Experimental starting materials		
	12/1A	***USK7***
SiO_2	59.969	60.924
TiO_2	0.831	0.861
Al_2O_3	17.311	17.089
Fe_2O_3	8.311	7.639
MnO	0.173	0.081
MgO	3.843	3.768
CaO	1.825	1.015
Na_2O	2.495	1.774
K_2O	2.911	4.408
P_2O_5	0.259	0.306
SO_3	0.013	0.016
Cr_2O_3	0.070	0.038
NiO	0.022	0.007
H2O-	0.140	0.140
LOI	1.204	1.901
Total	99.377	99.968
Mg#	47.8	49.4
Modal proportions		
Qtz	22	25
Plag	32 (An23)	24 (An12)
Bt	33 (Mg#=47)	41 (Mg#=47)
Crd	12 (Mg#=61)	9 (Mg#=64)
Mu	0	1
Ksp	1	0

Table 9.3. *Table of experimental run products and compositional information, as well as modal amounts of phases in parenthesis*:

	Type 1a (12/1A)	Type 1b (USK-7)		Type 2 (12/1A)	Type 3 (12/1A)
			700	Qtz **(25)** Plag core **(17)** An22.7, Or0.0 Plag rim **(13)** An36.4, Or0.0 Bt **(35)** Mg# = 48 Ged **(10)** Mg# = 61	
800	Qtz **(22)** Plag **(30)** An23.6, Or0.6 Bt **(33)** Mg# = 43 Crd **(15)** Mg# = 62	Glass **(3)** Glass volume too small to analyse Qtz **(24)** Plag **(22)** An10.3, Or0.0 Bt **(41)** Mg# = 47 Crd **(9)** Mg# = 64 Tern fsp **(1)** Or20.9, An12.6	750	Glass **(46)** ASI = 1.56, K:Na = 0.22, FeO + MgO = 2.01 Grt **(2)** Mg# = 24, spes = 10.3 Plag **(9)** An24.8, Or0.6 Bt **(19)** Mg# = 45 Crd core **(9)** Mg# = 62 Crd rim **(14)** Mg# = 57 Ilm **(1)**	Glass **(20)** ASI = 1.45, K:Na = 0.28, FeO + MgO = 1.94 Qtz **(3)** Plag **(19)** An24.1, Or0.7 Bt **(22)** Mg# = 47 Crd core **(10)** Mg# = 61 Crd rim **(19)** Mg# = 57 Ged **(7)** Mg# = 48
850	Glass **(6)** ASI = 1.36, K:Na = 0.58, FeO + MgO= 2.48 Grt **(1)** Mg# = 10, spes = 3.6 Qtz **(17)** Plag **(27)** An22.9, Or0.9 Bt **(30)** Mg# = 45 Crd **(19)** Mg# = 61	Glass **(14)** ASI = 1.34, K:Na = 0.99, FeO + MgO= 1.30 Grt **(1)** Mg# = 13, spes = 1.2 Qtz **(16)** Plag **(17)** An12.6, Or0.6 Bt **(33)** Mg# = 48 Crd **(19)** Mg# = 64	800	Glass **(76)** ASI = 1.47, K:Na = 0.43, FeO + MgO = 2.99 Grt **(2)** Mg# = 34, spes = 3.5 Bt **(11)** Mg# = 61 Crd core **(1)** Mg# = 65 Crd rim **(6)** Mg# = 78 Opx **(3)** Mg# = 52, total Al = 0.64 (6 O) Spinel **(1)**	Glass **(67)** ASI = 1.34, K:Na = 0.64, FeO + MgO = 2.50 Grt **(4)** Mg# = 27, spes = 2.5 Bt **(8)** Mg# = 52 Crd **(13)** Mg# = 61 Ged **(7)** Mg# = 48 Ilm **(1)**
900	Glass **(14)** ASI = 1.31, K:Na = 0.91, FeO + MgO= 2.01 Grt **(3)** Mg# = 25, spes = 4.1 Qtz **(12)** Plag **(23)** An24.3, Or2.2 Bt **(25)** Mg# = 49 Crd **(23)** Mg# = 62	Glass **(19)** ASI = 1.36, K:Na = 1.08, FeO + MgO= 1.71 Grt **(3)** Mg# = 26, spes = 2.6 Qtz **(14)** Plag **(11)** An13.3, Or0.6 Bt **(28)** Mg# = 49 Crd **(23)** Mg# = 64 Tern fsp **(2)** Or68.2, An3.8			

In the Type 1 experiments, cordierite composition does not vary significantly from that of the starting material over the temperature range investigated. In contrast, in the Type 2 and 3 experiments, cordierite in the 750 °C runs has a Mg# of 58. This is slightly lower than those of cordierite in the Kuiseb gneisses (Mg# = 62). However, these evolve rapidly to higher Mg#s with increasing temperature (up to Mg# = 80 and 63 in the type 2 and 3 experiments respectively at 800 °C). This is a function of the greater degree of biotite breakdown that has occurred in these experiments and the significantly larger proportion of garnet in the product assemblage.

In all three series of experiments biotite evolves towards higher magnesium numbers with temperature and increasing degree of melting. In the Type 1 experiments TiO_2 in biotite increases as a function of temperature. In the Type 2 and 3 experiments this is not the case, possibly due to the fact that the temperature range of the experiments is much less. Ilmenite was a trace mineral in the product assemblage of all the experiments with a significant degree of melting.

Plagioclase in the Type 1 experiments evolves towards slightly higher orthoclase component contents with increasing temperature. A maximum Or proportion of approximately 6.5 % being attained in the 900 °C experiment using the 12/1A starting material. This starting material contained plagioclase of composition An_{23} and this value increased slightly to An_{25} in the 900 °C run. Type 1 experiments on the Usakos starting material produced plagioclase of similar composition to the relatively albitic plagioclase of the starting material (An_{12}) in conjunction with a ternary feldspar at 900 °C. The K-rich feldspar occurred as narrow rims on new plagioclase. Plagioclase was completely consumed in the 800 °C experiments of the Type 2 and 3 experiments. In the 750 °C experiments the composition of the new plagioclase is only slightly enriched in K and Ca over that of the starting material. In the subsolidus 700 °C experiment, however, the composition of the new plagioclase is considerably more calcic (An_{36}). This is due to the presence of gedrite which has completely replaced cordierite and which hosts up to 4 wt% Na_2O.

The peritectic garnet in the Kuiseb gneisses has a consistent composition that is characterised by a low Mg# and a significant (~10%) spessartine component (Figure 9.5). In all three types of experiments, garnet evolves to lower almandine and spessartine concentrations and higher pyrope concentrations as a function of temperature. The trends for pyrope and almandine are displaced to markedly lower temperature in the water-saturated experiments (Figure 9.5). As a result, the trends defined by pyrope and almandine intersect with the natural peritectic garnet compositions at a temperature of approximately 900 °C in the fluid-absent experiments and at 750 °C in the water-saturated experiment. The spessartine content of the garnet in all the Type 1 experiments is less than half that of the natural peritectic garnet. The garnet produced in the 750 °C Type 2 experiment matches very well with the peritectic garnet compositions in the natural rocks. In the 800 °C Type 2 experiment (where there was significantly more garnet produced) the spessartine content of the garnet was significantly lower than in the natural garnet.

During the analysis of the glasses special care was taken to ensure analytical accuracy. This was done by cooling the samples to -190 °C via a liquid nitrogen cryostage prior to analysis. The difference of the analysis totals from 100 wt% is interpreted to represent the amount of H_2O in the glass. Quartz, analysed routinely in the sequence of glass analyses typically gave totals between 99.8 and 100.1 wt%, as discussed in the preceding section. All the glass (quenched melt) compositions produced in this study are strongly peraluminous and leucocratic with A/CNK values between 1.35 and 1.6 and FeO + MgO concentration of < 2.5 wt% (Table 9.3). The most significant major element compositional variation occurs as variations in the melt are in the concentrations of Na_2O and K_2O. The K/Na ratio of the glasses formed in the Type 1 experiments is considerably higher than that in the Type 2 and 3 experiments where melting occurred at lower temperature. This reflects the more important role of plagioclase in the fluid-present over the fluid-absent melting reaction of biotite.

Here it is important to try to understand the relationship between the melt compositions in the experiments and those that can be found in the natural rocks. The small dataset of

compositional information of the BHS granites and leucosomes from this study is presented below as a first order comparison of the experimental glass composition to natural granites. Furthermore, the work of Jung et al., (2000) on the Oetmoed Granite-Migmatite Complex of the Damara Belt can also be used to compare the experimental compositions to natural melts, which according to the authors were also generated by water-present melting.

Table 9.4. *Whole-rock chemistry of a few granitite sills and leucosomes of the Blauer Heinrich Syncline.*

Sample	11/8A	11/8C	12/1B	13/2	13/3
Rock type	Leucosome	Leucosome	Granite	Granite	Garnet granite
SiO_2	*73.8*	*68.1*	*73.1*	*81.5*	*73.9*
TiO_2	*0.09*	*0.12*	*0.12*	*0.09*	*0.09*
Al_2O_3	*12.5*	*14.0*	*13.9*	*8.78*	*15.4*
FeO	*0.37*	*0.95*	*0.71*	*0.84*	*0.61*
MnO	*0.05*	*0.08*	*0.09*	*0.03*	*0.17*
MgO	*0.50*	*1.62*	*0.46*	*0.37*	*1.06*
CaO	*1.20*	*3.24*	*2.09*	*0.91*	*3.54*
Na_2O	*2.44*	*2.46*	*4.51*	*2.02*	*3.57*
K_2O	*7.42*	*6.56*	*4.07*	*2.93*	*1.40*
Total	*98.4*	*97.1*	*99.1*	*97.4*	*99.7*

The following diagram (Figure 9.6) shows the K/Na ratio versus the SiO_2 content of the experimental glasses (quenched melts) of this study (empty squares) in comparison to the natural granites of the study area (filled triangles) and the leucosomes in the Oetmoed Complex (filled circles). The cross represents the composition of the water-saturated 750 °C experiment (Exp 16) that most closely mimics the assemblage and mineral compositions of the natural rocks of the BHS.

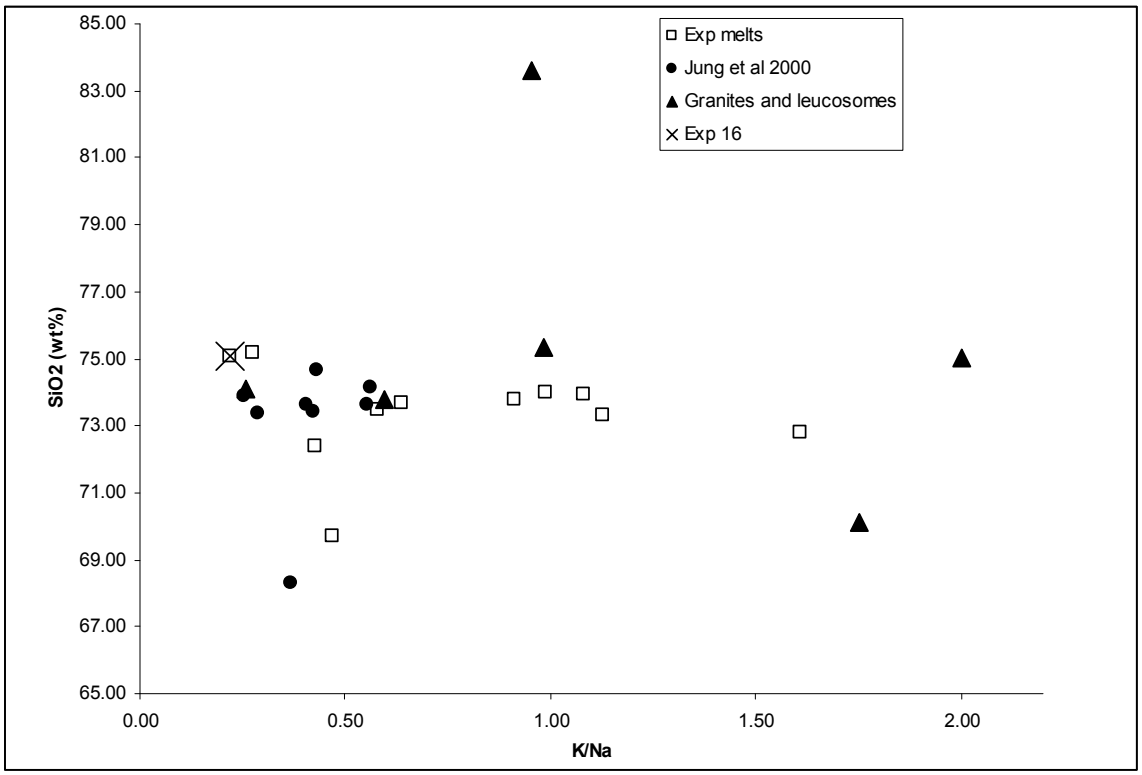

Figure 9.6. A comparison of the composition of quenched melts from the experiments to some granite and migmatite samples from the study area. The work of Jung et al., (2000) allows further comparison with natural migmatites from the Damara Belt which formed as a result of water present melting. The cross indicates the composition of the experiment that was determined to be most comparable to the natural rocks with respect to mineral chemistry and modal abundances. This melt composition is at the extreme end of the series of natural rocks that tend towards higher K/Na ratios, which is discussed in the text. The K/Na ratio was used as the compositional parameter because it is a good indication of the contribution of biotite-breakdown melting versus that of quartz-plagioclase melting to the melt composition.

The diagram shows that the experimental compositions tend towards higher K/Na values from that produced in the low-temperature water-saturated experiment. This is the result of larger contributions of biotite with increasing temperature and less water (which encourages plagioclase to participate). The difference in the trends of the natural rock compositions of the BHS could be the result of several factors:

1) The leucosomes and granite sills are cumulates that have selectively lost Na-rich melt during their crystallisation. Sawyer and Barnes (1988) indicate that anatectic leucosomes in migmatite terranes can comprise primary, unfractionated bodies as well as strongly fractionated leucosomes that would have a composition far removed that of the original melt composition. This effect could have played a

major role in the BHS as the ongoing deformation and fracturing was likely to remove a significant fraction of melt as described by Figure 4.20.

2) Too much plagioclase melted in the experiments due to too much water being added (a constraint of the experimental technique).
3) The way water equilibrated with the rock powders in the experiments could have differed from the way water reacted with the natural rocks due to kinetic factors.
4) The melting reactions may evolve to more biotite-dominated melting as water is consumed. This would drive the melt composition from that formed in experiment 16 to that of the water-undersaturated experiments and the water-absent runs.

The datapoints from the work of Jung et al., (2000) cluster quite well towards the composition of the glass in the water-saturated melting experiment. There is a slight deviation to higher K/Na ratio, but this could be the result of the presence of K-feldspar in the metapelites that were interpreted to have melted. Nevertheless, it is possible to envisage a process whereby the similarly potassic leucosomes and sills of the BHS could have formed as a result of initial water-saturated biotite melting triggered by fracturing and subsequent evolution towards the fluid-absent melting reaction as the water was consumed. This would result in leucosome and granite sill compositions bracketed by the compositions of these two types of experimental glasses.

The high-temperature, fluid-absent reactions did not match the field evidence for the modal proportions of minerals, nor did they approach the compositions of the peritectic minerals preserved in the field (Figure 9.5). There is no evidence to support a hypothesis that the rocks of the BHS underwent very high temperature metamorphism or anatexis (~ 900). This would have been evidenced by the pervasive breakdown of biotite with likely production of large amounts of garnet in the rocks.

10. Pseudosection analysis of the effect of water on the metamorphic assemblage and anatexis

An alternative to determining the metamorphic conditions from the phase chemistry of the natural rocks is to thermodynamically model a rock of known whole-rock composition in a suitable system of components over a range of pressures and temperatures. This approach predicts the stable assemblages of phases at a given P and T allowing the assemblage of minerals in the field to be compared to those predicted by the model. The most suitable modeling technique for this study is pseudosection analysis. Pseudosections determine the most stable assemblage of minerals for a given set of parameters (P, T and X (composition)) by using either a range of pseudocompounds, whose thermodynamic properties can then be tested at each point on the diagram for the set of compounds with the lowest Gibb's free energy (such as Perplex (Connolly, 1990, Connolly, 2005)) or by directly calculating invariant and univariant mineral equilibria (such as Thermocalc, Powell & Holland, 1990; Powell et al., 1998). Quantitative mineral equilibria modeling of natural rock systems is a powerful way to constrain both the P–T evolution of rocks and the effects of a range of metamorphic crustal processes. The modeling undertaken here is in the chemical system Na_2O–CaO–K_2O–FeO–MgO–Al_2O_3–SiO_2–H_2O–TiO_2–Fe_2O_3 (NCKFMASHTO), which is a near-comprehensive compositional analogue of natural metapelitic rock systems (White et al., 2007). The omission of MnO from the calculations (the MnNCKFMASHTO datafile was not available at the time of production) is likely to result in the garnet-in boundary on the diagrams being at temperatures 15–25 °C higher than that calculated for a MnO-bearing system. The calculations were undertaken using THERMOCALC 3.2 (Powell et al., 1998) and an updated internally consistent dataset of Holland & Powell (1998). The a–X relationships for minerals with solid solution are those adopted by White et al. (2003). Simple application of this technique will not take into account the effects of disequilibrium processes and is limited by the accuracy of the thermodynamic models of the composition of mineral solutions. This is a mathematically difficult approach as minerals such as amphiboles have several sites in the crystal lattice in which varying degrees of exchange between elements can occur. Furthermore, our understanding of

these models is also limited by the data (and the accuracy thereof) produced from experimental petrology and is further complicated by being affected by which phases are in equilibrium with the given mineral.

Despite some of these difficulties and limitations, the approach can be used to produce very usable results as long as these results are related carefully to the natural rocks and considered as supplementary to the evidence recorded in them.

In the metapelites of the BHS, the most significant field relationship must be the association of poikilitic garnet in structurally controlled sites of biotite breakdown. PT estimates produced from these anatectic assemblages indicate that the temperatures may have been slightly low to produce these associations via fluid-absent biotite breakdown. The rocks of the study area that have recorded the highest PT conditions are cordierite- and garnet-rich rocks that show evidence of melt-loss (less chance of back reaction). Using these rocks for the pseudosection modeling may skew the results and increase the melting reaction conditions because the rock composition is more refractory than the rock that initially underwent partial melting. For this reason and for the sake of easy comparison to the experimental results, the same sample (12/1A) as was used as the high-grade starting material for the experiments was used for the modeling. This rock was chosen on the basis of its representative composition and the absence of evidence for *in situ* biotite melting reactions.

It is important at this point to keep in mind the limitations of the system and the end-member mixing models used to construct the diagram. Firstly, it is important to reduce the natural system to a compositional space with a manageable number of components. This can be done by removing components that do not participate in the reactions, or that do not exercise a significant control on mineral stabilities or reactions. This must be done with care so as not to exclude certain phases from the assemblage. For example reducing the component list to KFMASH will preclude the stability of plagioclase, whereas as it is possible to form that mineral in the system, NCKFMASH.

Here, the most comprehensive system available at the time of production was the NCKFMASHTO system, which includes TiO_2 (T) and Fe_2O_3 (O) (White et al., 2007). This system does not include manganese as the mineral end-member models of THERMOCALC (Powell & Holland, 1990) do not allocate this element to any other mineral than garnet, hence forcing the (meta-)stability of this mineral beyond what is reasonable in order to accommodate the Mn somewhere. This is slightly problematic as, given the field-relationship discussed above, anatectic garnet is slightly enriched in Mn in comparison to metamorphic garnet. However, with this in mind, the fact that spessartine is generally the garnet end-member favoured by low temperature, would tend to give maximum estimates of the conditions at which garnet will enter the assemblage on the prograde path.

The diagram below, (Figure 10.1), is a T-X pseudosection in NCKFMASHTO as calculated at 0.5 GPa which was the pressure determined by conventional thermobarometry.

The diagram illustrates the effect of the concentration of water on the metamorphic assemblage and the reduction of the temperature at which melting can initiate. This is true up to about x = 0.25, beyond which water can exist as a free phase at temperatures below the solidus (just over 650 °C in this example) and will cause quartz + feldspar melting at higher temperatures. Beyond x = 0.25, the field boundaries become relatively flat indicating that the addition of more water will not greatly affect the minerals that may be present, and will only have an effect on the phase proportions. At high temperature and high water content, the degree of melting is very large and the assemblage becomes deficient in quartz.

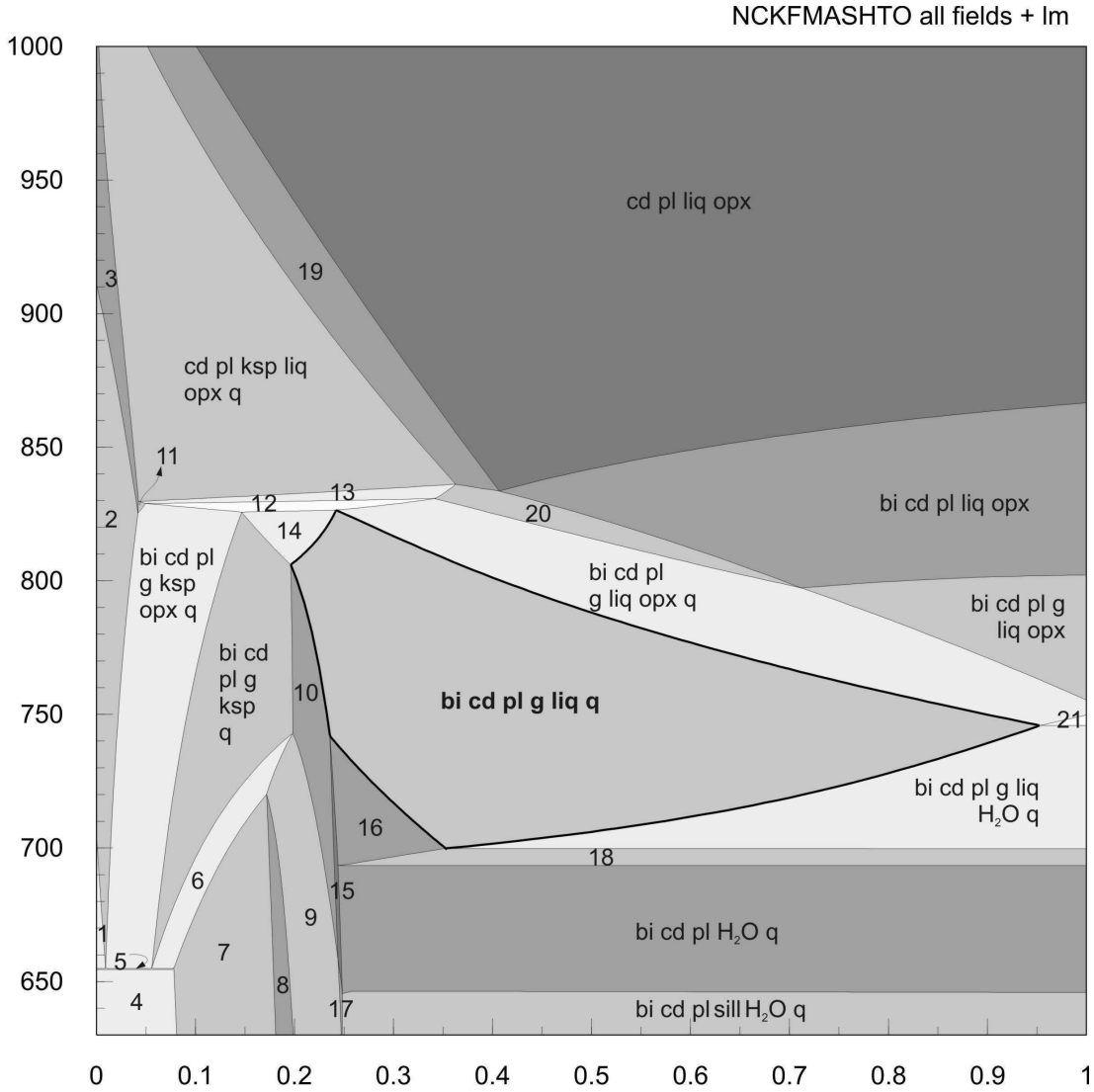

1	cd pl g sill ksp opx q	8	bi pl g sill q	15	bi cd pl q
2	cd pl g ksp opx q	9	bi cd pl g sill q	16	bi cd pl liq q
3	cd pl ksp opx q	10	bi cd pl g q	17	bi cd pl sill q
4	bi pl g sill ksp opx q	11	bi cd pl ksp opx q	18	bi cd pl liq H_2O q
5	bi cd pl g sill ksp opx q	12	bi cd pl g ksp liq opx q	19	cd pl liq opx q
6	bi cd pl g sill ksp q	13	bi cd pl ksp liq opx q	20	bi cd pl liq opx q
7	bi pl g sill ksp q	14	bi cd pl g ksp liq q	21	bi cd pl g liq opx H_2O q

Figure 10.1. The temperature versus composition (T-X) pseudosection of sample 12/1A (the high grade experimental starting material) modelled in the system NCKFMASHTO at 0.5 GPa. The composition varies from the anhydrous composition of the sample (see also table 2) at zero on the x-axis, to the same composition with 6 wt% (18 molar %) H_2O at 1 on the x-axis. The model extends over the temperature range of 650 °C to 1000 °C and thus covers the range of experimental temperatures and also the low-grade equivalent rocks of the study area. The lightest shading represents fields that have a variance of 3, with shading becoming darker with increasing variance, up to the darkest shading for the field with a variance of 7. The field that represents the most common anatectic assemblage in the rocks of the BHS is highlighted in bold.

The typical anatectic assemblage found in the study area is highlighted by the bold lines and consists of **bi cd pl g liq q lm** (in Thermocalc notation). Ksp is fairly rare in the rocks, but this could be as a result of most of the rocks having experienced a small degree of melting that is likely to have consumed this mineral and segregated part of those components into leucosomes or leucocratic segregations. Ksp stability is rapidly reduced with an increase in the content of H_2O at any given temperature as K^+ is taken up in melt (liq) or in biotite.

Sample 12/1A has the assemblage **bi cd pl q lm** which occurs on the diagram in the very small field labelled 15. Thus, for a pressure 0.5 GPa this rock should have contained about 1.5 wt% H_2O if the assemblage preserved in the rock represents the ± 750 °C peak assemblage. There is a significant change in the assemblage from this field with the addition of more water. The appearance of melt (liq) and then garnet is significant with only a small addition of H_2O of just over 1 wt% between 700 and 750 °C. It is important to remember that this would actually be a significant volume of water in the natural system due to the large molar volume of supercritical water in comparison to rock.

The predicted presence of sillimanite at low temperature in favour of cordierite in the diagram suggests that the rock did not fully equilibrate on the retrograde path as cordierite is a dominant phase in the rocks of the study area, whereas sillimanite is rare. However, the large-scale resetting of biotite can be demonstrated in the study area by the low PT estimates obtained using matrix assemblages in conventional thermobarometry. This is an important consideration for the metamorphic evolution of the study area as it is likely to have been synchronous with the waning stages of deformation, because the minerals did not recrystallise to form a late generation of minerals that cross-cut the foliation (even late biotite lies in the foliation). This suggests that the retrograde re-equilibration may have been effective until a temperature of about 700 °C (cordierite-out on the diagram). This could be the result of diffusion rates and closure temperatures of the minerals involved, however, the fact that deformation is a powerful mechanism to drive recrystallisation and thereby facilitate compositional re-equilibration could also

suggest that the deformation ceased at significantly high temperatures. It also suggests that the idea of a post-tectonic peak of metamorphism (e.g. Nex et al., 2001) is not correct, as the Biotite that defines the foliation, formed during the deformation, has already been demonstrated to be part of the retrograde assemblage.

Figure 10.2 shows the field of typical anatectic assemblages in the BHS. Plotted within this field are isopleths of garnet composition (x(g) = Fe/(Fe+Mg)) as well as modal amounts of garnet and melt (liq). The typical anatectic garnets of the study area have x(g) contents of between 0.8 and 0.85 and the rocks of the study area rarely contain more than a few percent of garnet. Furthermore, the chemistry of the rocks of the BHS and lower-grade equivalents are not inconsistent with the composition of the high-grade gneisses being modified by melt-loss in the order of 10 %. Therefore, using these modal amounts and the phase chemistry the large stability field of the anatectic assemblage can be dissected to better constrain the amount of water that is likely to have been introduced into a rock to cause melting. On the diagram, at the conditions predicted by thermobarometry, the likely composition (X) from which the anatectic assemblage could have evolved probably lies between 0.3 and 0.4. This corresponds to between 2 and 2.5 wt% of H_2O and this is less than 1 wt% of additional water to that predicted for the composition of the unmelted assemblage (ca. 1.5 wt%).

As a check on the thermobarometry and to better understand the conditions under which such reactions could occur, the PT pseudosection for sample 12/1A with 2.7 wt% H_2O was constructed (Figure 10.3). It is presented below, again with the dominant anatectic assemblage of the BHS highlighted by bold lines. The following diagram again shows the same mineral modes and isopleths of garnet composition to better constrain the assemblage (Figure 10.4).

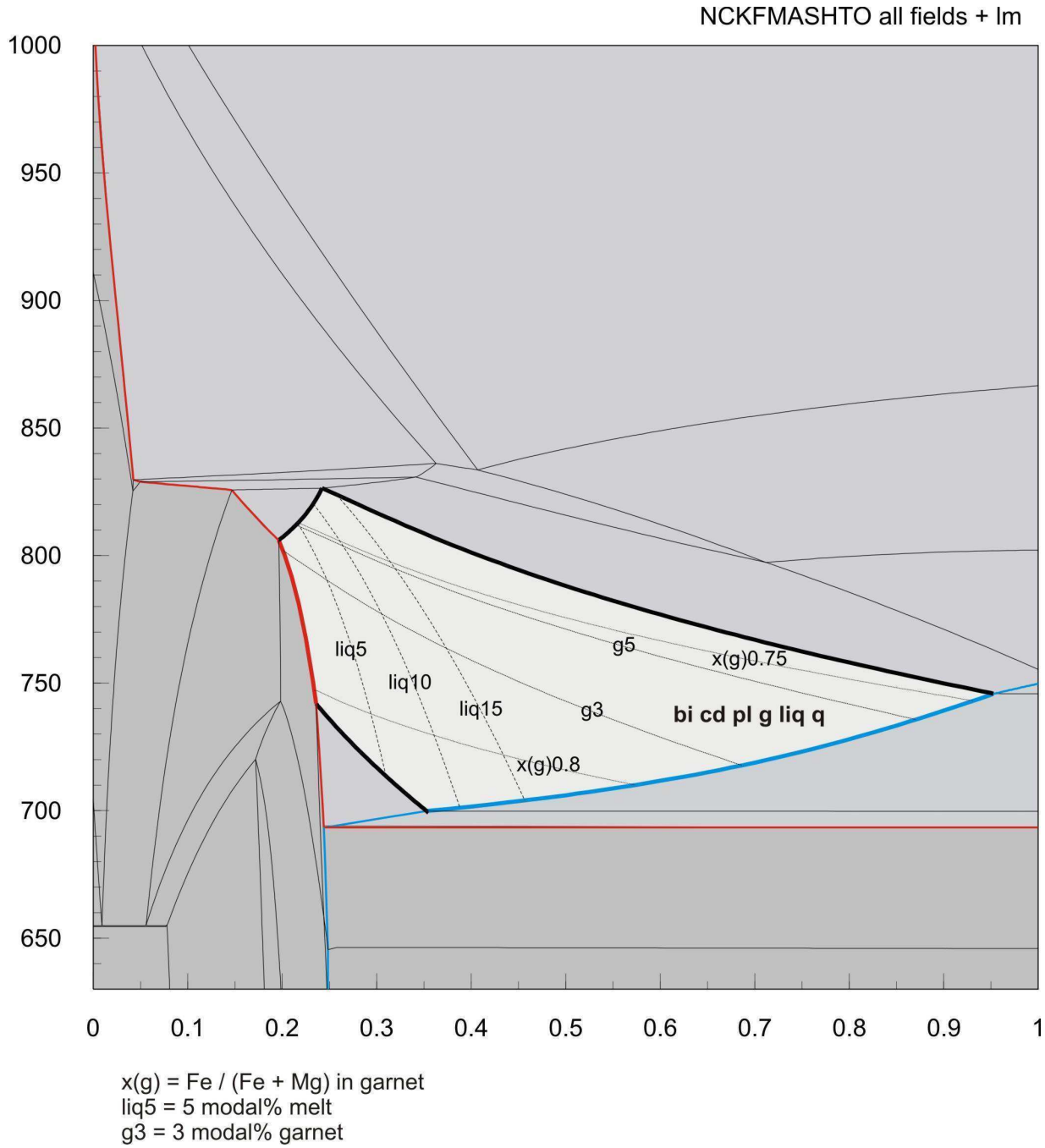

Figure 10.2. The T-X pseudosection of sample 12/1A modelled in the system NCKFMASHTO at 0.5 GPa and showing only the portion representing the anatectic assemblage observed in the field. Superimposed on this are the isopleths of garnet composition (x(g) = Fe/(Fe+Mg)) as well as modal amounts of melt (liq) and garnet (g). Typical values of x(g) in anatectic garnets are between 0.8 and 0.85 and from the field evidence and whole-rock geochemistry, the typical modal amounts expected in such an assemblage would be about 3 % garnet and no more than 15 % melt. The bold red line represents the melt (liq)-in line and the bold blue line represents the H2O-out line with respect to increasing T.

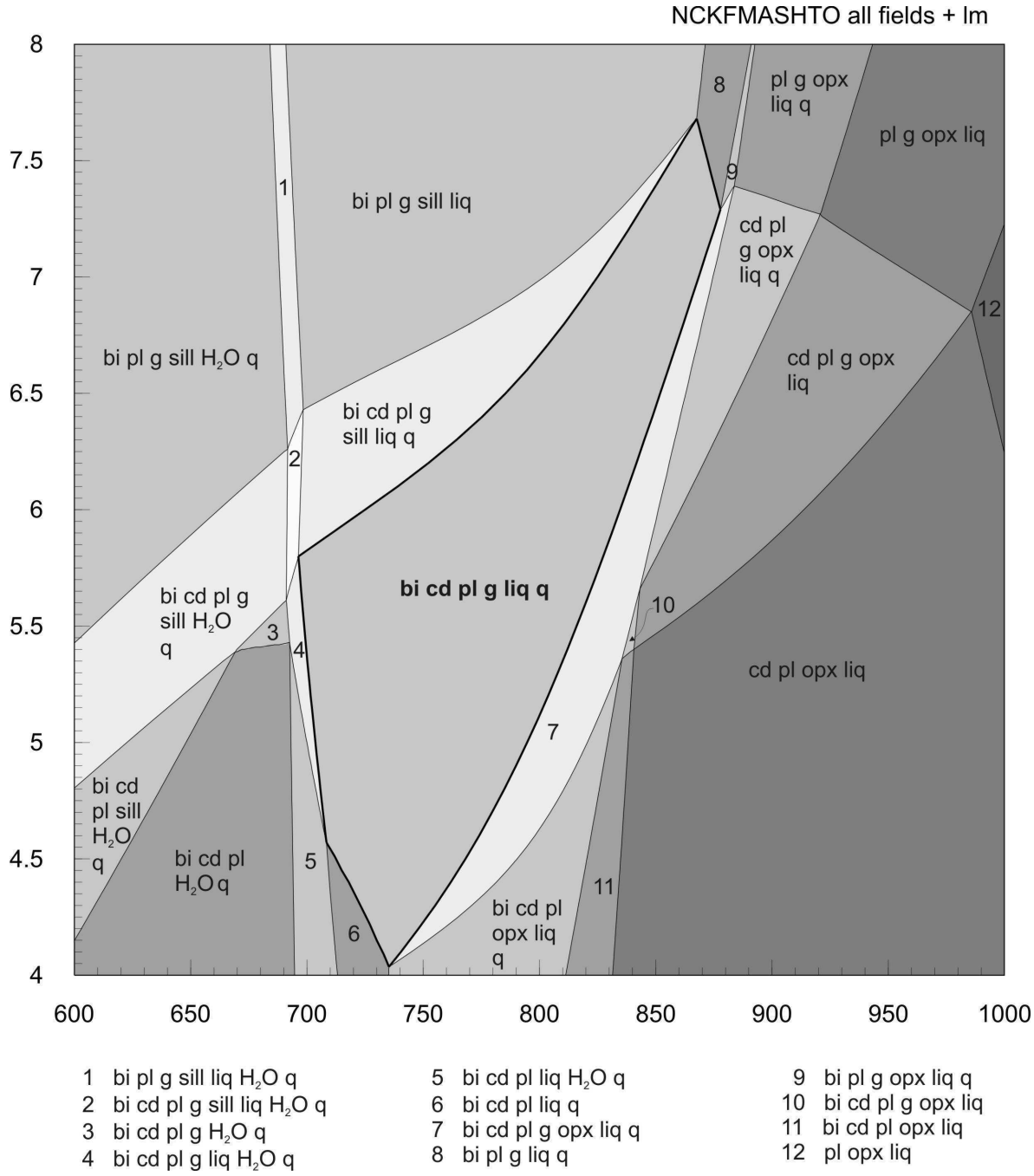

1 bi pl g sill liq H_2O q
2 bi cd pl g sill liq H_2O q
3 bi cd pl g H_2O q
4 bi cd pl g liq H_2O q
5 bi cd pl liq H_2O q
6 bi cd pl liq q
7 bi cd pl g opx liq q
8 bi pl g liq q
9 bi pl g opx liq q
10 bi cd pl g opx liq
11 bi cd pl opx liq
12 pl opx liq

Figure 10.3. The pressure versus temperature (P-T) pseudosection of sample 12/1A (the high grade experimental starting material) modelled in the system NCKFMASHTO. The composition used in the model is that of sample 12/1A with the amount of additional H_2O as indicated by the anatectic assemblage and mineral modes and compositions modelled by the T-X pseudosection. The modelled composition includes 2.7 wt% H_2O which is less than double the amount of water contained in a subsolidus, garnet absent rock as predicted by the T-X pseudosection. The model extends over the temperature range of 600 °C to 1000 °C and 0.4 to 0.8 GPa (4 - 8 kbar) and thus also covers some of the experiments conducted at 0.7 GPa with water added (Type 3). The lightest shading represents fields that have a variance of 3, with shading becoming darker with increasing variance, up to the darkest shading for the field with a variance of 8. The field that represents the most common anatectic assemblage in the rocks of the BHS is highlighted in bold.

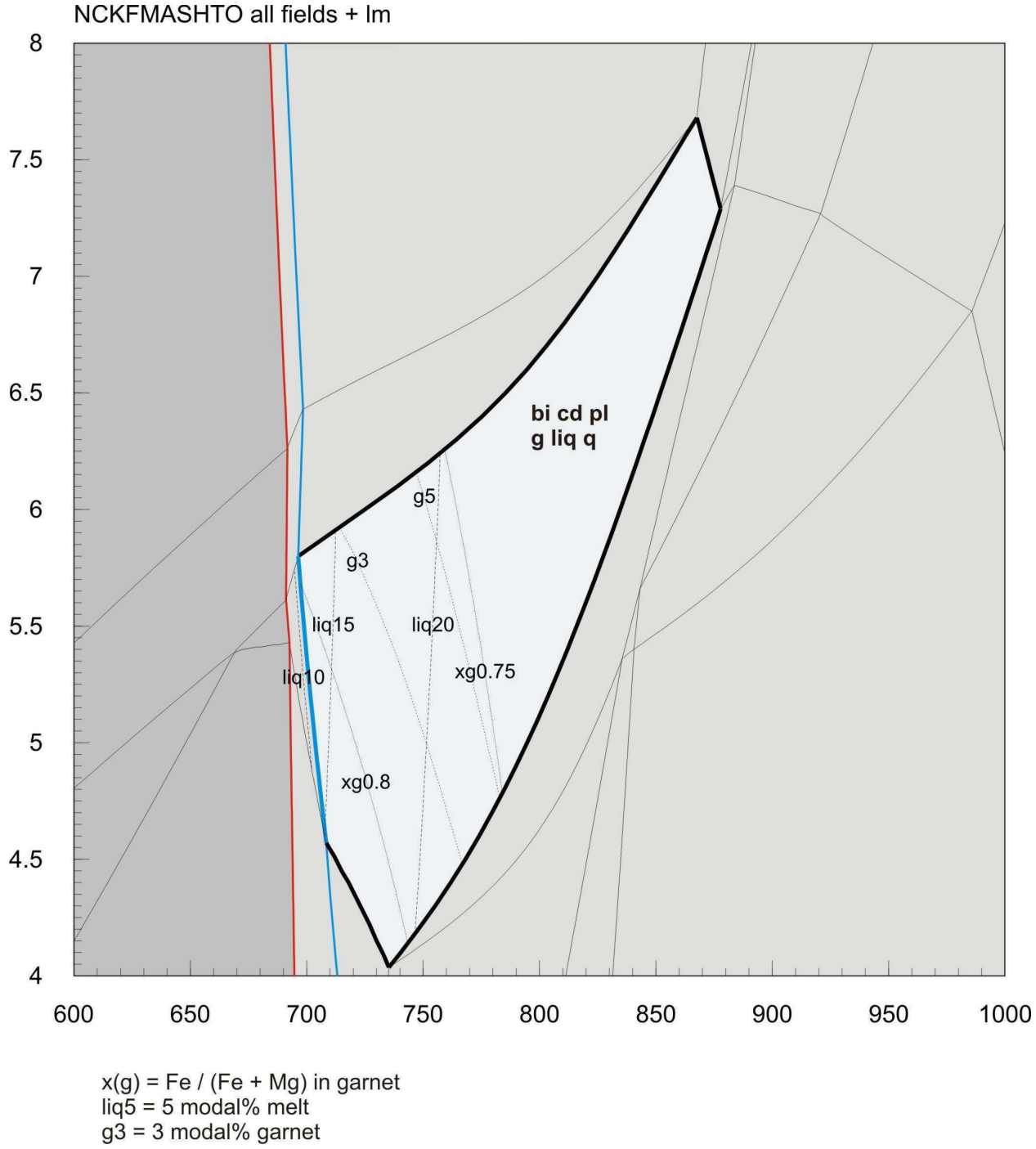

Figure 10.4. The P-T pseudosection of sample 12/1A modelled in the system NCKFMASHTO showing only the field representing the anatectic assemblage in the field. Superimposed on this field are isopleths of garnet composition (x(g) = Fe/(Fe+Mg)) as well as modal amounts of melt (liq) and garnet (g). Typical values of x(g) in anatectic garnets are between 0.8 and 0.85 and from the field evidence and whole-rock geochemistry, the typical modal amounts expected in such an assemblage would be about 3 % garnet and no more than 15 % melt. The bold red line represents the melt (liq)-in line and the bold blue line represents the H_2O-out line with respect to increasing T. The diagram indicates that this typical assemblage with the additional compositional and modal constraints would occur at slightly lower pressure and temperature than predicted by the conventional thermobarometry.

The P-T pseudosection extends to the conditions at which the experiments were conducted (0.7 GPa) and in a way attempts to model the fluid present Type 3 experiments where water was added but did not remain in excess as melting progressed. However, it does not replicate the results of these experiments exactly. Gedrite is, for example, not predicted in any of the diagrams. Although not predicted at the fluid-absent conditions in Figure 10.1, the coexistence of garnet and orthopyroxene is predicted at high temperature as was found in the Type 1 and Type 2 experiments. Furthermore, the diagrams show that the stability of cordierite is reduced at low temperatures (subsolidus conditions), although, the coupled stability of gedrite is not predicted. Importantly, the TX pseudosection (Figure 10.1) does also indicate that melting in a rock of this composition will not occur until well over 800 °C without the addition of water as seen in the Type 1 experiments.

The models seem to indicate that the anatectic assemblage in the BHS was stable at slightly lower PT conditions than predicted by conventional thermobarometry. However, it is important to remember that the effect of Mn in garnet is not considered (although this would be expected to lower the conditions even further). More significantly perhaps, is the important proviso that this modeling technique always assumes a complete equilibration of the phases. The proposed mechanism of the introduction of water to trigger an over-stepped melting reaction is inherently a disequilibrium process and would thus require careful consideration of the modeling results. Namely, at the point of initial water saturation, the local composition is likely to be strongly skewed towards H_2O, here melting would be triggered and would lead to a rapid reduction in the water activity. Depending on the rates of magma extraction, the rocks may or may not be able to equilibrate with all of the melt formed. Thus, although the amount of melt formed in the model is too large when compared to the field evidence; within the fracture sites the amount of melting would out of necessity be larger than that of the rock as a whole.

This highlights the fact that such modelling should be carefully interpreted as it necessitates the assumption of perfect equilibration for all points on the diagram whereas

equilibrium processes in natural systems are in fact very rare. Nevertheless, the diagram does provide useful insight into the evolution of the rocks of the study area as well as providing a valuable comparison to the experimental investigation of melting processes in the Kuiseb Formation metasediments.

11. The “best fit” melting scenario for the Kuiseb Formation cordierite-biotite gneisses

Field evidence indicates that anatexis of the Kuiseb Formation metapelites occurred through the incongruent melting of biotite to produce leucosomes that are associated with peritectic garnet and cordierite. Peak metamorphic PT estimates (from this study and others) indicate a peak temperature lower than would be considered typical for the onset of fluid-absent melting of biotite (Figure 11.1). The Type 1 experiments confirm this and fluid-absent solidus for the 12/1A starting material was determined to be located between 800 and 850 °C. At 900 °C this rock had produced less than 10 % melt. To determine the degree to which this behaviour was dependant on the fact that these rocks may have lost a melt fraction, thereby becoming more refractory, the melting behaviour of the more “fertile” amphibolite-facies USK-7 composition was also investigated. This rock melted at 800 °C, to produce a trace of melt. No ferromagnesian peritectic minerals were produced. These were present in the 850 °C experiment, indicating that in this rock fluid-absent incongruent melting of biotite also lies between 800 and 850 °C. At 850 °C the volume of melt produced from USK-7 was approximately 10 %. Granulite-facies assemblages typically deliver minimum estimates of peak PT conditions (Frost & Chacko, 1989, Pattison et al., 2003). Consequently, it could be argued that Kuiseb Formation peak metamorphic estimates are an underestimate for temperature and that anatexis has occurred through fluid-absent melting of biotite. However, two important features seem to be at odds with this. The cation exchange reactions that are the basis of the geothermometry applied to these rocks have “closure” temperatures close to 800 °C. Consequently, calculated granulite-facies peak temperatures are focussed on the 820 to 780 ºC interval (Frost & Chacko, 1989). In the Kuiseb gneisses, such temperatures are never calculated, with 750 °C being the highest temperature estimates that are routinely attained from the anatectic assemblages. In addition to this, the spessartine contents of the anatectic garnets appear to be a powerful discriminator of the fluid regime of melting. Significant fluid-absent melting of these rocks appears to start at 850 °C, at this temperature and higher the concentration of the spessartine molecule in garnet is low. In contrast, at the lowest temperatures of water-present biotite melting the spessartine

content of the peritectic garnet rises to approximately 10 %, within the range of the natural peritectic garnet. Under these conditions there is also good agreement between the pyrope, almandine and grossular contents of the experimental and natural peritectic garnets. The presence of gedrite in the Type 3 experiments as a ferromagnesian product of the melting reaction suggests a subtle water-activity control on the peritectic assemblage formed. There is some textural evidence in the natural anatectic rocks (in close spatial association with peritectic garnet) of the replacement of orthopyroxene or gedrite by crystallisation-hydration reactions (Figure 3.3). This is in the form of coarse intergrowths of quartz and biotite, such as are often found partially replacing orthopyroxene in anatectic granulites. Given the experimental results, the replaced mineral is interpreted to have been gedrite.

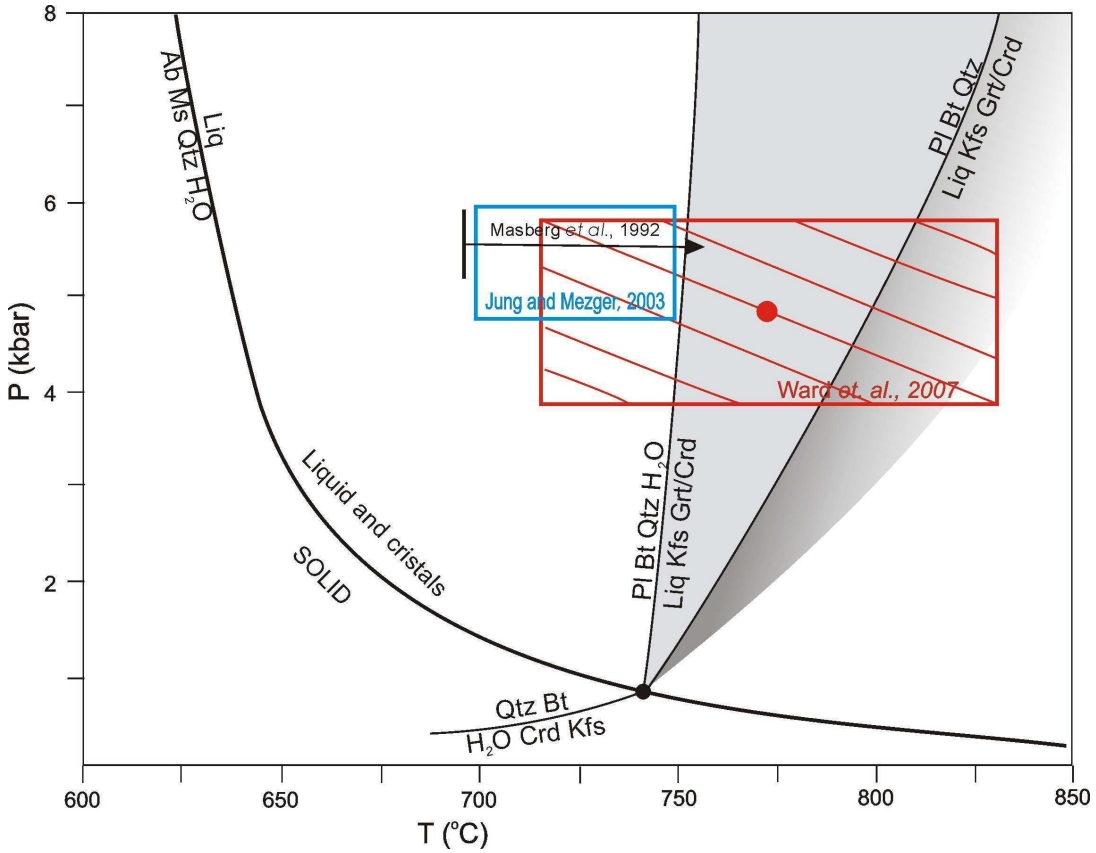

Figure 11.1. PT diagram illustrating the estimates of peak metamorphism of Jung and Mezger (2003) and Masberg et. al. (1992) and the conditions determined in this study (in red) in relation to the positions of the fluid absent and fluid present biotite melting reactions (Spicer et al., 2004).

Collectively the field data on the migmatites, the thermobarometry on the anatectic assemblages and the experimental results indicate that the Kuiseb gneisses are unusually low temperature granulites where the granulite-facies assemblage (garnet + cordierite) in the anatectic domains has been produced through water-induced biotite incongruent melting. In this scenario, the focussing of anatexis in the extensional sites is likely to be the result of the availability of water within these sites as a consequence of the lower effective pressure achieved in these domains on fracturing. Thus, it is proposed that anatexis of the Kuiseb Formation in the study area occurred via the reaction Bt + Pl + Qtz + H_2O = Grt + Crd + Melt and that this reaction only occurred where fracturing during extensional tectonics resulted in local water present conditions. The availability of water would have been the limiting factor in melting.

12. Mechanism of melting

The anatexis of the metapelites of the Blauer Heinrich Syncline appears to be controlled by an interplay between extensional deformation and the attainment of a transient water-present state. This is indicated by the following features: Leucosomes in dilational features are ubiquitous throughout the BHS and peritectic garnet (which indicates biotite melting) is almost exclusively hosted in these leucosomes; evidence for incongruent melting of biotite is rare away from dilational features; experiments indicate that fluid presence is required to cause biotite melting at the conditions that prevailed in the BHS; experiments also show that fluid absent biotite melting cannot account for the field evidence. Thus, as no significant temperature or pressure gradients can be sustained across tension gashes, the fluid conditions must be responsible for making the sites of fracture favourable for anatexis while the rest of the host rock mass was not. Below, a mechanism of fracture formation, melt initiation, followed by initial migration and extraction of the melt is described that best explains the field observations combined with the results of the petrological and experimental investigation.

12.1 A conceptual model for the structurally controlled formation of granitic magma, via fluid-present biotite melting in dilational sites in the BHS

The mechanism of formation of the garnet-bearing leucosomes, considering the evidence presented for melt loss and the fluid regime from the field associations and experimental results, is presented below. Each stage is discussed separately.

a) During prograde metamorphism rocks lose water progressively with reactions such as those that increase the mode of the cordierite at the expense of biotite in the Kuiseb Formation rocks. Whether or not fluid saturation occurs depends on the rate of water production in relation to the rate of migration of the molecules away from the sites of production (Thompson, 1983). The rates of accumulation and migration are strongly

influenced by deformation and the hydraulic gradients produced during fracturing. In rocks that are above the wet granite solidus and that also contain quartz and feldspar this balance is further influenced by the consumption of any free water by melting at the wet granite solidus. This ensures that it is impossible to sustain pervasive water-rich fluids in much of the silicate crust above approximately 650 °C (Stevens et al., 1995). Nevertheless, a transient fluid-saturated state must have existed in association with fracturing in the metapelites of the BHS to account for the melting that is evidenced in the dilational sites.

The constrictional strain during D_2 resulted in the formation of tension gashes and extensional shear bands in the fertile Kuiseb Formation metasediments. The brittle cracking of the metapelites was preceded by ductile necking of the rocks (an incipient boudinage perhaps). Such deformation may produce a drop in pressure due to the extension. This could have resulted in the ingress of water to give a sufficiently large fluid pressure, required to cause the brittle failure of the rocks which is shown in Figure 12.1. Decompression has been suggested as a way to encourage the initiation of biotite breakdown (Brown, 2007). However, this drop in pressure would have been very small (Chapter 4) and insufficient to trigger fluid-absent biotite breakdown due to the steep gradient of this reaction in PT-space and the high temperature predicted for this reaction from the experimental investigation (over 850 °C). Furthermore, the experimental phase relations and compositions of this study indicate that biotite breakdown was indeed in the presence of water in the BHS. Similar results are obtained from pseudosection modelling.

Figure 12.1. This image illustrates the significance of ductile necking occurring as a precursor to fracturing and melt initiation. Boudinage preceded fracturing and melting before the boudin at centre was surrounded by the more ductile metapsammite.

The inferred mechanism for the formation of the melt in the dilational sites involves an initial, brief saturation of water on the boundaries of the fractures at the instant of failure to trigger a water-present biotite melting reaction. The momentary decrease in pressure upon fracturing resulted in the ingress of water along the hydraulic gradients that would have been generated in the surrounding rock volume. In order to create such fractures in the Earth's crust a fluid pressure that can counter-act the lithostatic load is required before rocks can undergo brittle failure (as discussed in section 4.4). This demands that a

fluid phase was present in the rocks before failure. This fluid could not have been a melt formed by biotite breakdown, as the rocks do not display any evidence of melting prior to the described event. Figure 12.2 shows melt-filled fractures at a high angle to the lineation; these structures are interpreted to be the sites of the initiation of melting.

Figure 12.2. Melting is initiated on fractures formed at a high angle to the dominant stretching lineation (plunge of L2 is parallel to the pencil). The reddish-brown spots in the matrix of the rock are weathered cordierite porphyroblasts.

Thus it appears that water must exist in the rock in a finely balanced state, possibly as a water-rich grain-boundary fluid that co-exists with the minerals in the rock, but that does not allow melting despite being substantially above the fluid-present melting reaction temperatures. This fine balance is upset by extensional deformation, leading to a concentration of water on certain sites, subsequently triggering melting in suitable mineral assemblages.

b) Biotite incongruent melting in a fluid-present environment resulted in the formation of a granitic liquid and the initial growth of peritectic garnet and cordierite. The melting

front must have propagated out into the volume of the rock, because of the formation of peritectic cordierite rims nucleated on the pre-existing metamorphic cordierite, up to 15 cm away from the fracture sites within which the garnet nucleated (Figure 4.11, c iii). Subsequently, the melt that was formed away from the fracture would have migrated towards the fracture if ongoing deformation maintained the hydraulic gradient. Garnet was not present in the rocks before the melting event and, once nucleated in the fracture, continued to grow there due to its sluggish nucleation kinetics. Melting was triggered by water saturation, however, water made available by biotite breakdown also contributed to the water available for melting. Thus, the amount of melting that occurred was determined by the amount of water that gained ingress to the fracture sites as well as the amount of biotite induced to break down by the presence of this water. Water was clearly the factor limiting the reaction as all the other reactants continued to coexist within the matrix surrounding the leucosomes.

As the melting occurred through an overstepped fluid-present reaction, the rate of the reaction would be greatly increased (Rubie & Brearley, 1990, Acosta-Vigil et al., 2006) because the reaction would not be limited by the supply of heat. The presence of water and, subsequent to the reaction, a melt phase, would greatly improve diffusion, such that the reaction kinetics of the melting reaction(s) would be the rate controlling factor.

c) Further constriction leads to continued dilation and inflation of the fractures with melt. The peritectic garnet continued to grow rapidly, forming a poikiloblastic intergrowth with quartz, probably as a result of the reaction being overstepped in temperature and subsequently having cascaded upon the introduction of water. The formation of the strongly rodded leucosomes is the extreme end-member scenario of this part of the process. With further constriction, the initially small, thick lens-shaped leucosomes would be extruded into the long, cigar/pencil-shaped objects we see in the parts of the study area where L>>S.

d) The deformation would have occurred in incremental steps, resulting in a dilatency pumping mechanism. Although there is no mineral chemical record of this, such as

oscillatory zoning, such evidence could have been destroyed by post anatectic recrystallisation. Intermissions between the dilational events could have resulted in the periodic compression of the leucosomes, encouraging lateral growth at the fracture tips. If the fracture tips encountered adjacent weaker lithologies, these anisotropies in the rocks could be utilised as a plane of weakness for sill formation. The swap in orientation of the body that bears the melt volume indicates a change in the driving forces on melt segregation into the fracture site and subsequent migration out of these sites into steeply orientated, bedding parallel sills capable of transporting the magma to higher structural levels.

e) Once the sills had grown to above the critical length (see discussion in section 4.7) they would have been able to move upwards and extract melt from the overlying fracture arrays by the mechanism described in detail in Figure 4.20. Some sills can be seen to connect with a number of fractures of a particular array (Figure 12.3). Further dilation will still result in water-ingress and melting in the fracture sites until the volume of the rock becomes depleted in one of the reactant phases (probably water). The reaction front, displayed in the diagram below as the outer rim of a darker volume around the fracture, indicates the volume that is no longer fertile to this type of melting. The volume of rock determined for melt production from the mass balance calculations and the volume of garnet in the fractures in this study corresponds very well to the fracture spacing in the rocks. At this point garnet production in the fracture site was the result of spatially far-removed melting reactions. The very large equilibration volumes implied can probably only exist in environments where diffusion is vastly enhanced by the presence of a liquid, such as a water-rich volatile phase or a water-rich granitic melt.

Figure 12.3. A typical 'ladder-structure' showing the interconnection between lineation-normal leucosomes and a bedding parallel sill. Andrea Dini is studying the factors that control the orientation and emplacement style of the melt segregation features and the swap that must occur to the factors that control the melt transfer features.

f) Extraction of melt resulted in a loss of volume that is evidenced by the characteristic 'pucker-structures' as well as the typically lower leucosome to garnet ratios than expected from the experiments. Bedding-parallel sills may contain some granitic material to indicate their involvement as transfer structures, but it is believed that many were efficiently emptied of melt and would simply have closed upon themselves to leave little or no evidence of their existence/passing.

Below, the mechanism of melting is schematically illustrated with block diagrams numbered with respect to the discussion above (Figure 12.4).

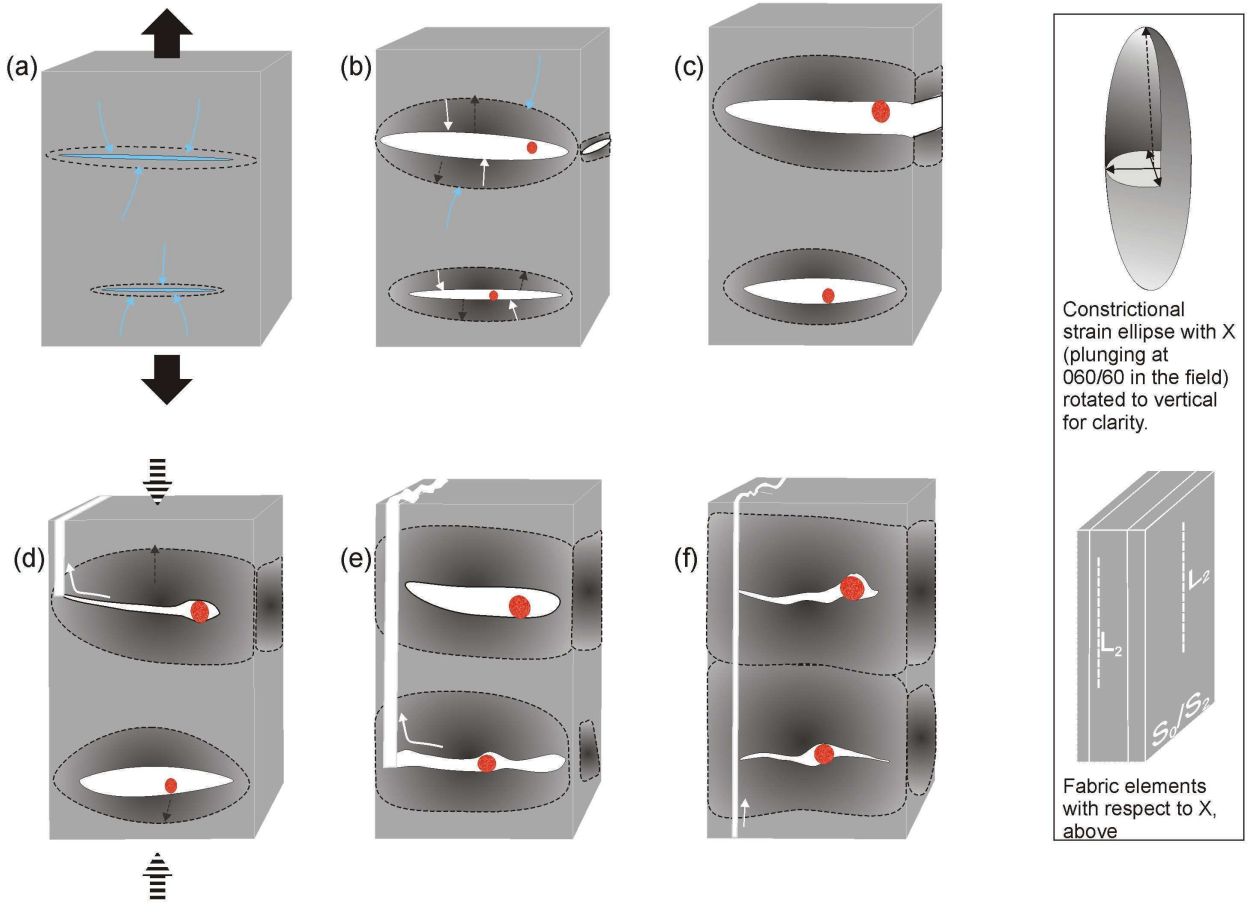

Figure 12.4. A schematic cartoon of the melting mechanism inferred for the structurally-controlled, fluid-induced breakdown of biotite in the Kuiseb Formation metapelites of the Blauer Heinrich Syncline.

12.2 Garnet texture

A problem persists with the comparison between the field relations and the experiments that best mimicked these. Most significantly, none of the experiments have product assemblages that resemble the large garnet-quartz intergrowths in the field. In fact, quartz is always consumed by the melting experiments and never forms part of the product assemblage, whereas this is clearly the case in the field.

The different texture of the mineral assemblage in the field from that produced in the experiments is partly the result of such chemical gradients that can exist in the natural system. In the laboratory, a fine powder is used in the experiments to try to encourage the rapid attainment of equilibrium by making the material as homogeneous as possible. Furthermore, the introduction of water is also via a different mechanism in the field to that in the experiments. Initially, the rocks were able to evolve to high temperatures (above the water-present solidus) in the absence of water; the introduction of water, or its initial accumulation to high-enough concentration, was along discrete plains (the fractures) in the rock. In the experiments water is present from the start of the run, and the "rock" is rapidly brought to the desired high pressure, high temperature conditions. Such kinetic factors and their effects on reactions achieving equilibrium must be considered in interpreting the results of experiments. However, the similarity between the chemistry of the run products and of the minerals of the natural rocks in the anatectic domains is striking and gives good confidence in the interpretations of the anatectic processes derived from the experiments that best match the natural rocks.

No suitable metamorphic or anatectic reactions involving the pre-existing cordierite and biotite produce product assemblages with sufficient quartz, with respect to the amount of garnet produced, to explain the presence of the intergrowths of approximately equal amounts of garnet and quartz in association with melt. Garnet is only present as infrequent, large porphyroblasts which indicates that the mineral struggled to nucleate

during the melting episode. The necessary large equilibration volumes required to form garnet as a product of reactions up to 15 cm away at least (as evidenced by anatectic cordierite distal to the leucosome), could implement kinetic restraints on garnet growth. Furthermore, the reaction was probably overstepped in temperature, such that when the reaction occurred it was only limited by the availability of reactants.

Although rarely as large as in the migmatites of the BHS, such garnet-quartz intergrowths are common in migmatites and granulites (Waters, 2001), and Barbey (2007) has described mechanisms of diffusion-controlled biotite breakdown in the presence of a melt phase interpreted to be responsible for the formation of such structures. This must be slightly adapted, taking into account the work of Morgan et al., (2008) on diffusion rates of cations in granitic liquids, to apply to the migmatites of the BHS of this study. The greater equilibration volumes and the distance of the intergrowths from the reaction sites would suggest that the melt is the reactant (see below) as opposed to the incongruent breakdown of feldspars being the source of Si and Al as suggested by Barbey (2007).

Fe^{2+} and Mg^{2+} are mobile in granitic magma compared to Al^{3+} and Si^{4+} which form polymer chains in the liquid (Baker, 1990 See table 2 and figure 2). This allows the ferromagnesian component to migrate through the interconnected melt network from the sites of biotite breakdown, however the Al and Si required to form garnet can be sourced from the initially formed magma surrounding the garnet. The rate of replacement of the consumed elements is faster for Fe and Mg (and Mn) than it is for Al and Si. This results in the coarse poikilitic garnet-quartz intergrowths of the typical leucosome assemblage as the melt in the vicinity of garnet growth will rapidly become over-saturated in quartz as the growth of garnet consumes Al (or at least consumes Al and Si at a higher Al:Si ratio than is in the melt). The reaction,

$$\mathbf{3\ FeO + 2\ KAlSi_3O_8}\ \textit{(melt)}\ \rightarrow\ \mathbf{Fe_3Al_2Si_3O_{12}}\ \textit{(Almandine)} + \mathbf{3\ SiO_2 + K_2O}$$

would serve to produce quartz and garnet via the addition of iron to the melt in order to produce the garnet required to accommodate the peritectic product of biotite breakdown. The melt would become enriched in potassium and possibly quartz and would tend to make the melt more alkaline in the vicinity of the garnet if the excess K was not consumed by an ancillary reaction. This is difficult to test due to the fact that most migmatite leucosomes do not represent the initial melt composition and the subtle effect of this reaction would be obscured by the formation of cumulates, partial melt escape or even melt flow within the leucosome (which would result in homogenisation).

12.3 Comparison to other types of spatially-focussed melting mechanisms

The mechanism proposed in this study is different from the spatially-focussed melt formation as described for rocks of similar appearance by White et al., (2004). They attribute garnet porphyroblast and leucosome associations in the metapelitic gneisses of Broken Hill to have formed as a result of limited/sluggish garnet nucleation and subsequent focussing of melting reactions on these sites of garnet growth. The elongated shape of stromatic leucosomes is interpreted to have formed as a result of the improved diffusion parallel to bedding/foliation as opposed to normal to these heterogeneities. In the BHS, the lens-shaped leucosomes are most commonly developed at a high angle to lineation and thus cross-cut the bedding and bedding-parallel foliation that contains the lineation. Had these leucosomes formed via a similar mechanism they would have had a different orientation and would probably also have occurred as stromatic leucosomes. For this reason, the most significant effect of focussed melting on these sites must have been the structural control exercised via the formation of fractures. The fractures initiated melting via a temporary water-saturation at these dilational sites (the temporarily low pressure would have resulted in hydraulic gradients into the fractures). The initial formation of garnet may have subsequently, in addition to the repeated fracturing at these planes of weakness, focussed the formation of peritectic products of the reaction at these sites. In this mechanism the presence of melt in the system produces the large equilibration volumes (as much as 15 cm across) as the melting front propagates further

into the rock (having been triggered on the fracture plane). This is different from the interpretation that the melting reactions were purely controlled by the limited nucleation of garnet (White et al., 2004).

13. Estimating melt loss and water ingress

Peritectic garnet porphyroblasts hosted in rocks that retain very little leucosome material, as shown in Figure 13.1 are very common in the study area, suggesting significant melt loss from the sites of anatexis. Comparison between average compositions of the Kuiseb Formation metasediments in the amphibolite-facies domain near Usakos and in the study area (Table 2.1), allow for a 1st order constraint on how much melt has been lost from the high grade rocks. On average, the rocks of the higher-grade area are lower in SiO_2, Na_2O, K_2O and H_2O (inferred from the LOI) and also have a higher FeO_t, MgO, Al_2O_3, TiO_2, MnO and CaO. Thus, the high-grade rocks appear to be depleted in fusible elements and enriched in the refractory components. This effect is slight, but sufficient to suggest that minor melt loss has been important in shaping the compositions of the higher-grade rocks. The difference in the averages of the two rock compositions is consistent with the extraction of 5 to 10% of the melts generated from the relatively low temperature water-present experiments.

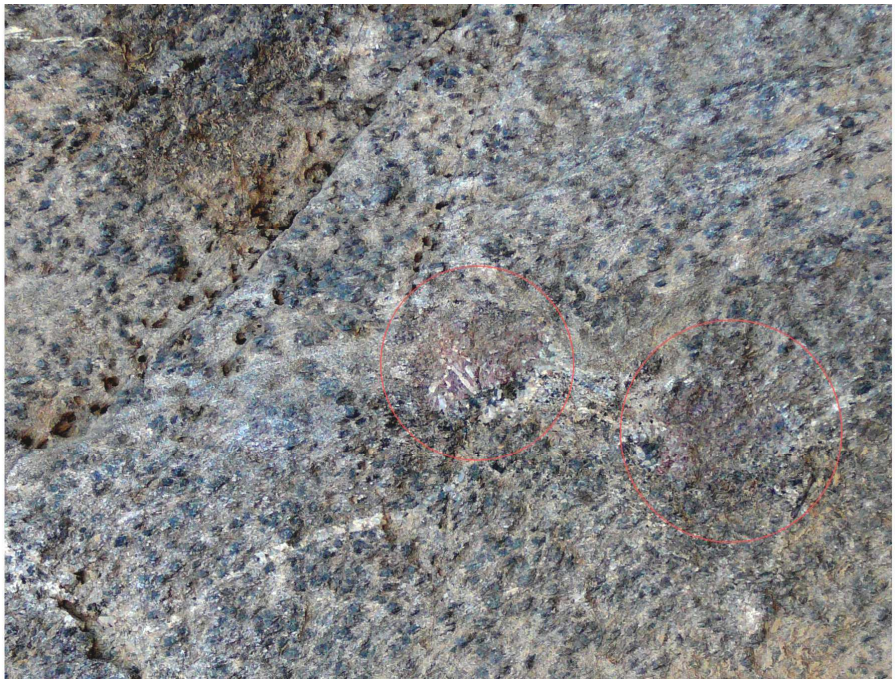

Figure 13.1. Typical example of melt-loss features. Here two large garnet porphyroblasts (indicated by red circles) are not associated with any significant amount of leucosome. These structures indicate that complete melt extraction occurred.

As discussed in Chapter 9, the 750 °C water-saturated experiment appears to best simulate the melting process in the natural rocks. Phase proportions of the product assemblage of this experiment were determined by image analysis to be 73% melt, 24% cordierite and 3% garnet. As the experiments were performed at a maximum pressure feasible for these rocks, considering this and previous metamorphic studies, the melt to garnet ratio determined in the experiments is likely to be a minimum estimate of that produced during anatexis of the natural rocks. A unique feature of the structurally controlled melting in these rocks is that the anatectic rocks only contain the peritectic generation of garnet and that this garnet usually forms as a single, large poikiloblastic crystal within the leucosome. This allows the volume of the garnet formed during the melting of the natural rocks to be easily determined by removing the garnet porphyroblasts from the rock and preparing multiple slices through the crystals for image analysis. This has been done for several garnets and despite the fact that there is a reasonable scatter in the values determined for individual slices (up to 20% between sections of the same garnet) the garnet poikiloblasts can be conservatively estimated to consist of at least 50% garnet Figure 13.2. Thus, the volume of garnet found in a typical, large anatectic poikiloblast (diameter = 10 cm) from these rocks is about 250 cm^3. Extrapolation from the experimental melt proportions implies that growth of this volume of garnet by the melting reaction would also have produced approximately 6 litres of melt. Coupled to the bulk rock chemical argument for limited melt loss from the chemically homogenous biotite-cordierite gneisses of the Kuiseb Formation, approximate limits can be placed on the volume of rock from which the melt has been generated. Thus, the 5 to 10% of melt loss from the rocks of the study area equates with melt being tapped from a 0.08 to 0.16 m^3 volume of rock. During the melting event the equilibration volume of the rock would have expanded to approximately the size of the domain from which melt was extracted, as illustrated by the growth of the peritectic garnet in a single site within this volume. Assuming an isotropic form to symplify the calculations, this volume is typically larger than the thickness of individual beds within the lower grade portions of the Kuiseb Formation. In reality the equilibration volume would probably have been elongated in the direction of the foliation but it would be difficult to establish

the aspect ratio of such a volume. Nevertheless, melting and effective diffusion within the melt-connected volume may be an important mechanism in the homogenisation of the metasediments that appears to have occurred in the high-grade domain. High-temperature fracture spacing and thus leucosome distribution during extensional deformation appears to have been such that the calculated melt depleted volumes would form an interlocking network, such that much of the metapelitic volume of the schists has been effectively drained of melt. The structures and mechanisms of melt ascent are discussed in detail in Chapter 4 (see particularly Figure 4.20)

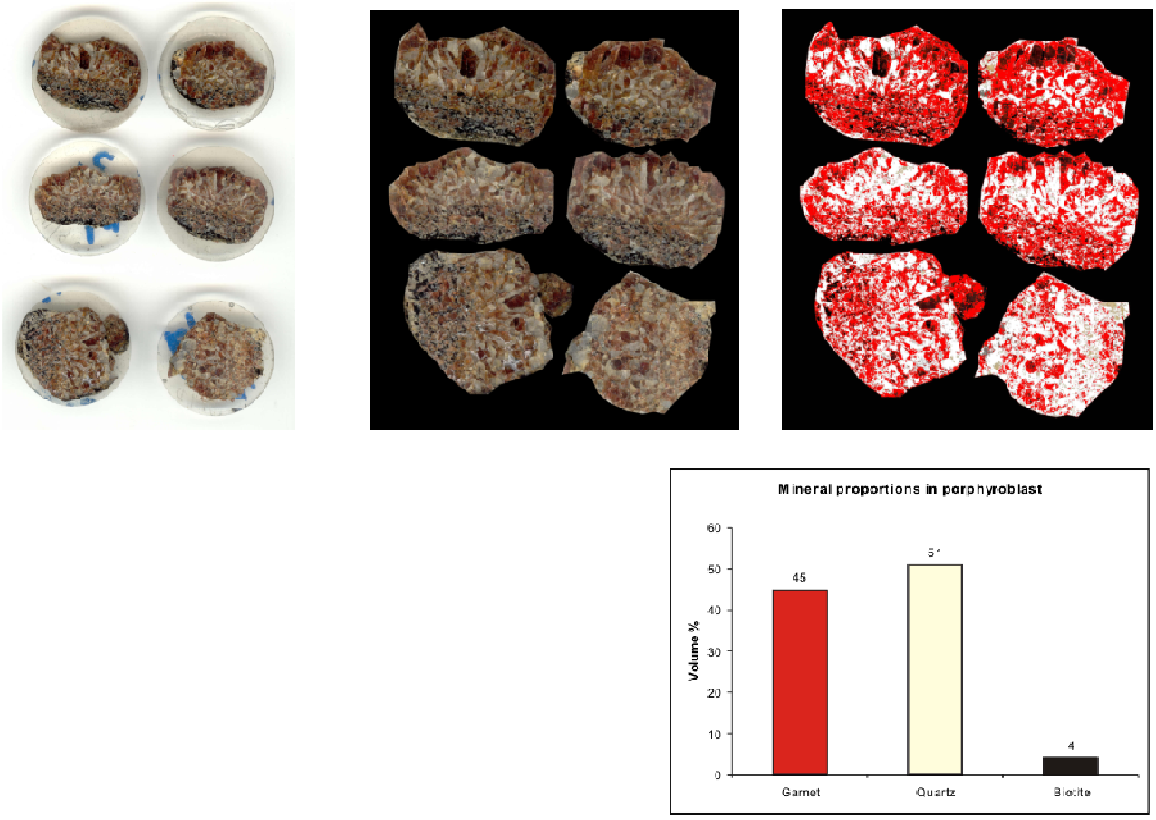

Figure 13.2. Image analysis of slices through a typical garnet porphyroblasts from dilational sites. Top left shows the prepared sections, top centre shows the scanned, trimmed image and the image at the top right shows the false-colour image produced with quartz highlighted in pale yellow, garnet in red and the small amounts of biotite in black. Typically, garnet and quartz are present in the porphyroblast in equal amounts except rarely where some subsequent recrystallisation has removed quartz to leave subhedral garnet crystals with few quartz inclusions.

In addition to this, the volume of water required to trigger the melting in such a typical fracture hosted leucosome can be estimated, after making certain assumptions. Firstly, the melting can be regarded as being fluid saturated as the fluid-absent melting of the rock has been constrained to occur at temperatures that were not attained by the study area. The water content of the melt can be determined in two ways; by calculation and by experiment. The Type 2 experiments of this study were performed with water in excess and this phase was indeed still present in the run products. This indicates that the glasses (crystallised melts) formed in these experiments were saturated in water. The water content of these glasses was estimated indirectly using SEM-EDS as presented in the appendix, but the water content determined for the glasses has a significant uncertainty (6.95 ± 3.08 wt% for the 750 °C Type 2 experiment). Alternatively, the content of water in a saturated melt can be calculated. The program VolatileCalc1.1 (Newman & Lowenstern, 2002) was used to determine the model H_2O content of a water-saturated leucogranitic liquid (13 wt% as shown in Figure 13.3). This gives a fairly broad bracket for the possible water content of the granitic liquid formed in the natural rocks. Conservatively, the calculated water content would require the largest volume of water to account for the phenomenon we see in the field. In other words, this would show to what degree external fluids would need to contribute to the water-budget required for the degree of melting.

Furthermore, using the water content of a saturated melt will give a maximum value of the amount of water consumed by the melting reaction in the field, which includes the contribution from the fluid that triggered melting as well as the water made available from the crystal structure of biotite as it breaks down. The contribution of biotite breakdown to the water budget can be estimated by relating the amount of potassium in the experimental melt to the amount of biotite that has contributed to the melting. This is possible because biotite is the only source of potassium as no potassium feldspar is present in the assemblage of the starting material

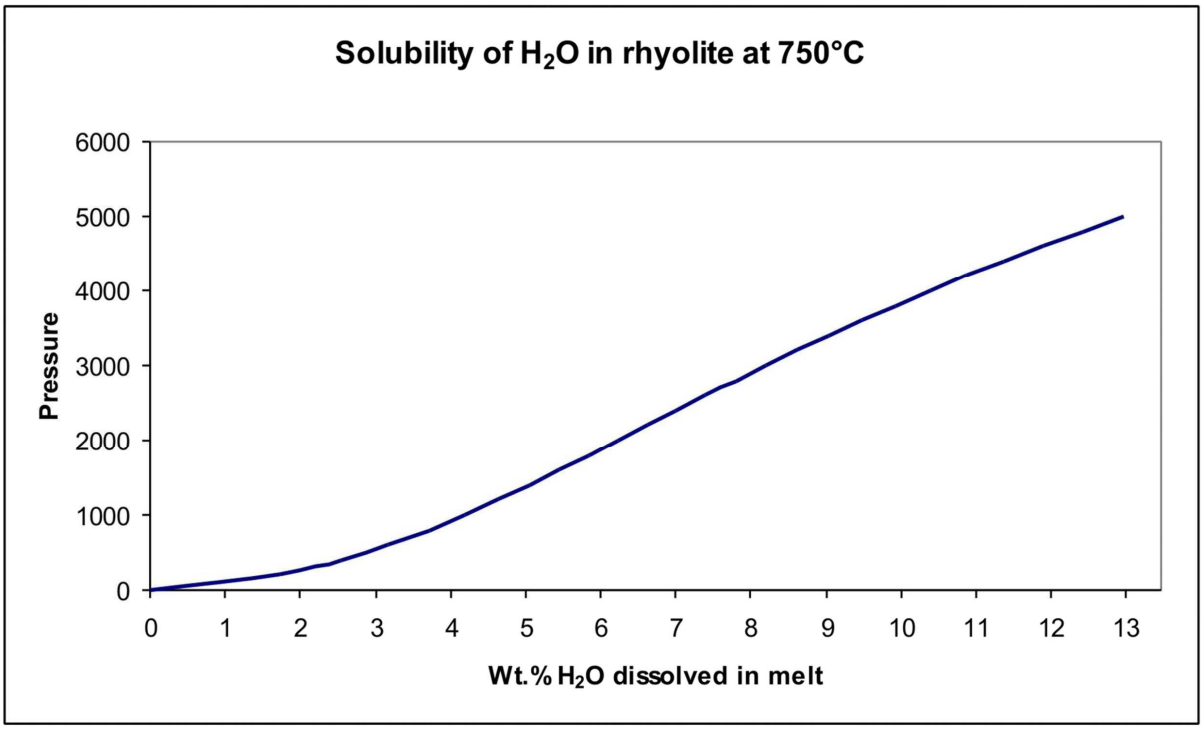

Figure 13.3. The output from VolatileCalc shows that a rhyolitic liquid at 750 °C and 0.5 GPa can dissolve up to 13 wt% H_2O before it is saturated.

This value was then further used to determine the density of the granitic liquid (Using Dense2.0 Stormer, Unpubl.); which was calculated to be 2.02 g/cm^3 at 750 °C and 0.5 GPa. Simple calculations then allow the determination of the amount of water dissolved in the 6 litres of melt formed in a typical garnet-bearing leucosome. This was found to be 1.56 kg. Data tables can be found to determine the density and volume relationships of supercritical water under these conditions. The National Institute of Standards and Technology (Lemmon et al., 2005) gives the isobaric properties of supercritical water to be 40 mol/l at 750 °C and 0.5 GPa. This is the same as 0.72 g/cm^3. Given these values, the 6 litres of granitic melt in a typical leucosome would have consumed about 2.17 litres of water. This volume is only a visualisation of all the water consumed as if it were a free phase and does not consider the contribution to the water budget from biotite breakdown.

It is important to keep in mind that this volume of water is a maximum estimate. SEM-EDS data for the experimental phases suggests that the glasses contained substantially less than 13 wt% H_2O for most of the experiments. The 750 °C runs contained just less than 10 wt% despite having significant amounts of water added to the capsule. The water was added in excess in the 750 °C Type 2 experiment, yet the determined glass composition was not saturated in water according to the value calculated with "VolatileCalc" and was in fact lower than that determined for the water present Type 3 experiments at 750 °C which contained less added water. This probably represents an underestimation of the analysed water content of the glasses. The model values are consistently higher than the values analysed with SEM-EDS, even using the cryostage. For this reason the value for the water content of saturated granite magma are used. This ensures that the volumes of water calculated to participate in the reaction are maximum values.

The assemblage and the mineral chemistries of the run product in the 750 °C Type 2 experiment best mimicked the natural anatectic rocks of the BHS. The melt composition is poor in K, suggesting that the contribution to melting of biotite breakdown is fairly small. It is important to remember that this experiment (Exp 16) had a large melt volume, compared to that produced in the natural anatectic event. This was probably the result of adding too much water and the reaction not being arrested by the absence of water as would have occurred in nature. Instead, the experiment became quartz deficient as a result of the high degree of melting. Plagioclase and biotite remained stable in coexistence with water at these conditions as a result of the melting reaction being limited by the absence of quartz in the reactant assemblage.

The degree of melting in the 750 °C Type 2 experiment is thus more than would have occurred in the natural rocks because these did not become quartz deficient and must thus have been limited by the availability of water. This, together with the possibility that kinetic factors may have favoured biotite breakdown over congruent quartz-feldspar melting (such as water availability being favoured along the foliation planes defined by

biotite) suggest that the natural melts would have been richer in K, as a result of a greater contribution of biotite melting. A greater contribution from biotite to the melt would also liberate more water from its crystal structure for consumption by the melt. Thus this would lower the amount of water ingress required to account for the inferred melt volume produced at a typical anatectic site. For these reasons, using the experimental results to constrain the contribution of biotite to melt production and water availability will give a *minimum* estimate for biotite involvement and a *maximum* estimate for the amount of free water required to account for the melting.

With the assumption that all the potassium in the melt is from biotite (there is no potassium feldspar in the starting material), calculations based on the concentration of K in the experimentally produced melt and a ratio of K to H in the natural biotite of just less than 1:2 show that the contribution of water from biotite breakdown is only 3 - 4 % of the water in a saturated melt (~ 0.5 wt% of H_2O from biotite and ~12.5 wt% from H_2O ingress make the 13 wt% total). This fraction will increase significantly if the melt was not saturated in H_2O (as analyses of run products suggest), if the reaction was water limited, not quartz limited (thus biotite melting would contribute a greater fraction to the melt) and if biotite participation in the melting reaction was somehow kinetically favoured over quartz-feldspar melting.

14. Implications for granite magma production

This finding that the Kuiseb Formation metasediments have undergone some 10 % partial melting with the subsequent, highly efficient, extraction of magma at relatively low temperatures is significant to our understanding of granite genesis. It shows a mechanism through which deformation, by controlling the water availability, can initiate melting in structural sites and facilitate the segregation and migration of low proportions of melt. In doing so it adds to the argument that mobile granitic magma need not be hot, dry and produced at a high degree of melting (Brown, 1979). The study reveals there are circumstances that can produce, at least locally, small bodies of granite that may have been able to feed into larger plutons, from partial melting of metasediments at low temperature and low degrees of melting.

Collisional orogens routinely reach temperatures of 800 °C at times of active deformation. This would be coupled with the production of large volumes of water from prograde metamorphic dehydration reactions in the crust. If imbrication of the crust resulted in cool rocks being thrust below hotter, drier rocks of a composition fertile to melt production, then such water would migrate upwards and possible cause melting in the hot rocks above. This may have occurred in the rocks of the Blauer Heinrich Syncline with the abundant structurally controlled leucosomes could record the attempted movement of large amounts of water through the crust. When this water encountered rocks that were above their water-present melting reaction, they would have reacted quickly (White et al., 2005 give an example of rocks that melted as a result of fluid-transfer from adjacent rocks that had a higher solidus).

However, the occurrence of biotite fluid-present melting reactions in rocks that are also above their quartz-feldspar-water melting reactions indicates that this water ingress is a process that is poorly explained by our present understanding of the state of water-rich fluids in the silica-rich crust above the conditions of possible melting. Current beliefs hold that water cannot exist as a free phase in a rock that also contains quartz and feldspar above the solidus temperature for the rock. This makes it very difficult to suggest a

model for water ingress into rocks that have demonstrably undergone water-present melting without the uncomfortableness of the dogma that all water should be consumed before biotite melting could occur.

Perhaps, the reaction rates for the different types of melting (biotite breakdown vs congruent melting) are a controlling factor in allowing one to progress in a meta-stable way in favour of the other. The kinetics of melting reactions should receive more attention in future studies. Experimental studies could be a fruitful source of information in this regard.

Given the success of this and previous experimental investigations into understanding the role of fluids in partial melting, this method, coupled with modelling of rocks via thermodynamic calculation software such as ThermoCalc and Perplex gives the metamorphic petrologist a powerful set of tools to investigate anatexis in the crust. The results of this study hinged heavily on the results of the experimental investigation; and together with the image analysis and mass balance calculations allowed a quantification of melt loss by the amount of preserved peritectic phase in the rock. Such quantification, together with the estimation of the amount of water required to sustain the melting reaction is rarely possible in geology, but the excellent outcrop and the style of melting that occurred in the BHS provides this unique opportunity (see Guernina and Sawyer, 2003 for another example).

Beyond the description of the melting reaction and the quantification of melt loss and water ingress, the excellent outcrop also allowed the physical mechanism of melt migration to be studied, from the initiation of melting in fractures as a result of water ingress, right through to the emplacement style of small plutonic granite bodies. The role of the regional stress fields vs local effects such as the intrinsic properties of a rock (such as anisotropies) were investigated qualitatively. Results indicate that the sites of initial melting were formed under the major influence of the regional stress field as their orientation is strictly perpendicular to the stretching lineation. The sills, however, are almost always bedding parallel, indicating that the predominant control in their formation

is the anisotropy of the host rocks. This has led to an understanding of the local stress directions as well as semi-quantitatively estimated the magnitude of maximum deviatoric stress in the study area, which could be typical for any high-grade part of an orogenic belt. The value is very low and yet exercises a strong control in the case of leucosomes, but is heavily outweighed by the tensile strength contrasts of the bedded sedimentary rocks as the controlling factor of sill formation and orientation.

An important implication of the work may be to highlight the importance of 'melt-avalanches' in the deforming orogenic crust. The study has demonstrated that the leucosomes form an effective melt reservoir that can be quickly and efficiently tapped by migrating sills. The significance of sills to a sudden and rapid injection of melt into higher crustal levels is due to their dependence on suitable pathways, such as favourably oriented anisotropies. The sills of the BHS would not have been efficient in moving magma upwards had the bedding and foliation not been oriented sub-vertically. This is illustrated in areas where the magma has ponded below a fold hinge; the pathway being effectively choked or blocked off. The corollary of this suggests that if magma had been present before the bedding was folded into the subvertical by progressive deformation, then such steepening could have caused a sudden flux of melt upwards along the newly oriented anisotropy; a melt avalanche could have ensued with a rapid emplacement of granite at higher structural levels. This could have a similar effect to the melt avalanches discussed by Bons et al., (2004) that they believed to be caused by a random perturbation in melt batches coalescing to form such sudden, large magma pulses within a system of self-organised criticality.

Conclusions

Within the study area, granulite-facies anatectic assemblages are preserved in the Kuiseb metapelites in leucosome-filled dilation sites developed as shallowly-dipping fracture sets. Thermobarometry on these assemblages indicates a temperature of equilibration below that of the experimentally-determined fluid-absent solidus for these rocks, but within the temperature range for fluid-present melting. In addition, water-present melting is confirmed by experimental peritectic garnet compositions that only match those of the natural peritectic garnet in water-present experiments. Thus, water saturation was achieved in the dilational sites at a temperature in excess of the water-present biotite melting reaction. This triggered melting at approximately 750 °C and produced melt in conjunction with large, peritectic garnet in the leucosomes, as well as a peritectic generation of cordierite that nucleated on existing cordierite in the gneisses adjacent to the leucosomes. The fact that the reaction was overstepped, coupled to nucleation difficulties probably produced the characteristic, sometimes single, large poikilitic garnets. Field evidence, such as the collapse of the foliation to form 'pucker-structures' and low leucosome to garnet ratios clearly indicate melt loss from the sites of anatexis. The compositions of the high-grade rocks relative to those of their likely amphibolite-facies protoliths, appear to have lost approximately 10% melt on average. Melt escape most likely occurred via what we called ‘ladder-structures’ that can be observed to link leucosome-filled fracture arrays with subvertical leucosome sills. The amount of peritectic garnet produced at the sites of anatexis, together with experimental data on the ratio of garnet, cordierite and melt produced by low temperature fluid-saturated melting in these compositions, allows the amount of melt and the volume of source rock initially involved in producing the peritectic garnet to be estimated. A rock volume of at least 80 litres melted to produce 6 litres of melt and a typical large garnet of 250 cm^3, in addition to the peritectic cordierite. This leads to the implication that at the time of anatexis the equilibration volume in the partially melted domains was as large as 80 litres. This must have been responsible for producing the unusual garnet textures and was achieved by melt migration through the extensional fracture and sill network. This melt streaming kept the garnet chemically connected with the increasingly distant sites of melt

generation. Collectively, these findings indicate that mobile granitic magma can be produced and effectively extracted from the relatively low-temperature crust, even at small degrees of melting.

References

Acosta-Vigil, A., London, D. & Morgan, G., 2006. Experiments on the kinetics of partial melting of a leucogranite at 200 MPa H2O and 690–800°C: compositional variability of melts during the onset of H2O-saturated crustal anatexis. Contributions to Mineralogy and Petrology 151, 539-557.

Ague, J. J., 1995. Deep crustal growth of quartz, kyanite and garnet into large-aperture, fluid-filled fractures, north-eastern Connecticut, USA. Journal of Metamorphic Geology 13, 299–314.

Anderson, E. M., 1936. The dynamics of the formation of cone-sheets, ring-dykes, and cauldron subsidences. Royal Soc. Edinburgh Proc. 56, 128-163.

Anderson, H. & Nash, C., 1997. Integrated lithostructural mapping of the Rössing area, Namibia using high resolution aeromagnetic, radiometric, Landsat data and aerial photographs. Exploration Geophysics 28, 185-191.

Anhaeusser, C. R., 1973. The Evolution of the early Precambrian crust of Southern Africa. Philosophical Transactions of the Royal Society of London. Series A, Mathematical and Physical Sciences 273, 359-388.

Arzi, A. A., 1978. Critical phenomena in the rheology of partially melted rocks. Tectonophysics 44, 173-184.

Ashworth, J. R., 1985: *Migmatites*. Ashworth, J.R. (Ed.). Blackie, Glasgow. 302 pp.

Baker, D. R., 1990. Chemical interdiffusion of dacite and rhyolite: anhydrous measurements at 1 atm and 10 kbar, application of transition state theory, and diffusion in zoned magma chambers. Contributions to Mineralogy and Petrology 104, 407-423.

Barbey, P., 2007. Diffusion-controlled biotite breakdown reaction textures at the solid/liquid transition in the continental crust. Contributions to Mineralogy and Petrology 154, 707-716.

Barnes, J. F. H., 1981. Some aspects of the Tectonic history of the Khan-Swakop region of the Damara Belt, Namibia. Geology. Leeds: University of Leeds, 348.

Barnes, J. F. H. & Downing, K. N., 1979. Origin of domes in the central Damaran belt, Namibia. Revue de Geologie Dynamique et de Geographie Physique 21, 383-386.

Barraud, J., Gardien, V., Allemand, P. & Grandjean, P., 2001. Analogue modelling of melt segregation and migration during deformation. Physics and Chemistry of the Earth 26, 317-323.

Barraud, J., Gardien, V., Allemand, P. & Grandjean, P., 2004. Analogue models of melt flow networks in folding migmatites. Journal of Structural Geology 26, 307-324.

Barrow, D., 2007. BSc Honours Dissertation: The geometry and regional controls of melt transfer zones of leucogranites in mid-crustal rocks of the Blauer Heinrich Syncline in the South Central Zone of the Damara Belt in Namibia: A GIS approach. Department of Geology, Geography and Environmental Studies. Stellenbosch: Stellenbosch University, 85.

Basson, I. J. & Greenway, G., 2004. The Rössing Uranium Deposit: a product of late-kinematic localization of uraniferous granites in the Central Zone of the Damara Orogen, Namibia. Journal of African Earth Sciences 38, 413-435.

Bea, F. & Montero, P., 1999. Behavior of accessory phases and redistribution of Zr, REE, Y, Th, and U during metamorphism and partial melting of metapelites in the lower crust: an example from the Kinzigite Formation of Ivrea-Verbano, NW Italy. Geochimica et Cosmochimica Acta 63, 1133-1153.

Bons, P. D., Arnold, J., Elburg, M. A., Kalda, J., Soesoo, A. & van Milligen, B. P., 2004. Melt extraction and accumulation from partially molten rocks. Lithos 78, 25-42.

Bons, P. D., Dougherty-Page, J. & Elburg, M. A., 2001. Stepwise accumulation and ascent of magmas. Journal of Metamorphic Geology 19, 627-633.

Briqueu, L., Lancelot, J. R., Valois, J.-P. & Walgenwitz, F., 1980. Geochronologie U-Pb et genese d'un type de mineralisation uranifere: Les alaskites de Goanikontes (Namibie) et leur encaissant. Bulletin Centres Recherches Exploration Production Elf Aquitaine 4, 759-811.

Brown, M., 1979. The petrogenesis of the St-Malo migmatite belt, Armorican Massif, France, with particular reference to the diatexites. Neues Jahrbuch Fur Mineralogie, Abhandlungen, 135, 48–74.

Brown, M., 1994. The generation, segregation, ascent and emplacement of granite magma: the migmatite-to-crustally-derived granite connection in thickened orogens. Earth-Science Reviews 36, 83-130.

Brown, M., 2004. The mechanism of melt extraction from lower continental crust of orogens. Transactions of the Royal Society of Edinburgh, Earth Sciences 95, 35-48.

Brown, M., 2007. Crustal melting and melt extraction, ascent and emplacement in orogens: mechanisms and consequences. Journal of the Geological Society 164, 709-730.

Brown, M. & Rushmer, T., 1997. The role of deformation in the movement of granitic melt: views from the laboratory and the field. In: Holness, M. B. (Ed.) Deformation-enhanced Fluid Transport in the Earth's Crust and Mantle. London: Chapman & Hall.

Brown, M. & Solar, G. S., 1998. Shear-zone systems and melts: Feedback relations and self-organization in orogenic belts. Journal of structural geology 20, 211-227.

Brown, M. & Solar, G. S., 1999. The mechanism of ascent and emplacement of granite magma during transpression: a syntectonic granite paradigm. Tectonophysics 312, 1-33.

Bühn, B., Stanistreet, I. G. & Charlesworth, E. G., 1993. Fold shape variation controlling interference mechanisms and patterns during oblique fold superpositions in the Damara Orogen, eastern Namibia. Annales Tectonicae 7, 113-128.

Buick, I. S., Stevens, G. & Gibson, R. L., 2004. The role of water retention in the anatexis of metapelites in the Bushveld Complex Aureole, South Africa: an experimental study. Journal of Petrology 45, 1777-1797.

Burnham, C. W., 1979. The importance of volatile constituents. In: Yoder, H. S. (Ed.) The evolution of the igneous rocks (Fiftieth anniversary perspectives). New Jersey: Princeton University Press, 439-482.

Chapman, D. S., 1986. Thermal gradients in the continental crust. Geological Society, London, Special Publications 24, 63-70.

Clemens, J. D., 1990. The granulite-granite connection. In: Vielzeuf, D. & Vidal, P. (Eds.) Granulites and Crustal Evolution. Dordrecht: Kluwer, 25-36.

Clemens, J. D., 2003. S-type granitic magmas-petrogenetic issues, models and evidence. Earth Science Reviews 61, 1-18.

Clemens, J. D. & Droop, G. T. R., 1998. Fluids, P-T paths and the fates of anatectic melts in the Earth's crust. Lithos 44, 21-36.

Clemens, J. D., Droop, G. T. R. & Stevens, G., 1997. High Grade metamorphism, dehydration and crustal melting: a reinvestigation based on new experiments in the silica-saturated portion of the system $KAlO_2$-MgO-SiO_2-H_2O-CO_2 at P<1.5GPa. Contributions to Mineralogy and Petrology 129, 308-325.

Clemens, J. D. & Vielzeuf, D., 1987. Constraints on melting and magma production in the crust. Earth and Planetary Science Letters 86, 287-306.

Clemens, J. D. & Watkins, J., 2001. The fluid regime of high-temperature metamorphism during granitoid magma genesis. Contributions to Mineralogy and Petrology 140, 600-606.

Collins, W. J. & Sawyer, E. W., 1996. Pervasive granitoid magma transfer through the lower middle crust during non-coaxial compressional deformation. Journal of Metamorphic Geology 14, 565-579.

Connolly, J. A. D., 1990. Multivariable Phase Diagrams: An algorythm based on generalized thermodynamics. American Journal of Science 290, 666-718.

Connolly, J. A. D., 2005. Computation of phase equilibria by linear programming: a tool for geodynamic modeling and its application to subduction zone decarbonation. Earth and Planetary Sciences Letters 236, 534-541.

Connolly, J. A. D. & Petrini, K., 2002. An automated strategy for calculation of phase diagram sections and retrieval of rock properties as a function of physical conditions. Journal of Metamorphic Geology 20, 697-708.

Coward, M. P., 1981. The junction between Pan African Mobile Belts in Namibia: its structural history. Tectonophysics 76, 59–73.

Coward, M. P., 1983. The tectonic history of the Damara belt. In: Miller, R. M. (Ed.) Evolution of the Damara Orogen of South West Africa/Namibia. Geological Society of South Africa Special Publication, 409-421.

Davidson, C., Schmid, S. M. & Hollister, L. S., 1994. Role of melt during deformation in the deep crust. Terra Nova 6, 133-142.

Diener, J. F. A., Stevens, G., Kisters, A. F. M. & Poujol, M., 2005. Metamorphism and exhumation of the basal parts of the Barberton greenstone belt, South Africa: Constraining the rates of the Mesoarchean tectonism. Precambrian Research 143, 87-112.

Droop, G. T. R., 1987. A general equation for estimating Fe^{3+} concentrations in ferromagnesian silicates and oxides from microprobe analyses, using stoichiometric criteria. Mineralogical Magazine 51, 431-435.

Eggler, D. H. & Holloway, J. R., 1977. Partial melting of peridotite in the presence of H_2O and CO_2: Principles and review. Magma Genesis, Oregon Department of Geology and Mineral Industries Bulletin 96, 15-36.

Eskola, P. E., 1948. The problem of mantled gneiss domes. Quarterly Journal of the Geological Society of London 104, 461-476.

Etheridge, M. A., Wall, V. J. & Vernon, R. H., 1983. The role of the fluid phase during regional metamorphism and deformation. Journal of Metamorphic Geology 1, 205-226.

Fossen, H. & Tikoff, B., 1997. Extended models of transpression and transtension and application to tectonic settings. In: Holdsworth, R. E., Strachan, R. A. & Dewey, J. F. (Eds.) Continental Transpressional and Transtentional Tectonics. Geological Society Special Publication 135, 187-196.

Frost, B. R. & Chacko, T., 1989. The Granulite Uncertainty Principle - Limitations on Thermobarometry in Granulites. Journal of Geology 97, 435-450.

Fyfe, W. S., 1973. The granulite-facies, partial melting and the Archaean crust. Philosophical Transactions of the Royal Society of London. Series A, Mathematical and Physical Sciences 273, 457-461.

Fyfe, W. S., Price, N. J. & Thompson, A. B., 1978. *Fluids in the Earth's Crust*. Amsterdam: Elsevier. 383.

Ghosh, S. K., 1970. A theoretical study of intersecting fold patterns. Tectonophysics 9, 559-569.

Gray, D. R., Foster, D. A., Goscombe, B., Passchier, C. W. & Trouw, R. A. J., 2006. $^{40}Ar/^{39}Ar$ thermochronology of the Pan-African Damara Orogen, Namibia, with implications for tectonothermal and geodynamic evolution. Precambrian research 150, 49-72.

Griffith, A. A., 1921. The phenomenon of rupture and flow in solids. Philosophical Transactions of the Royal Society of London. A221, 163-198.

Griffith, A. A., 1925. The theory of rupture. Proc. 1st Internat. Cong. Appl. Mech. Delft, 1924, 55-63.

Haack, U., Hoefs, J. & Gohn, E., 1982. Constraints on the origin of Damaran granites by rubidium/strontium and δ18O data. Contributions to Mineralogy and Petrology 79, 279-289.

Haack, U., Heinrichs, H., Boneß, M. and Schneider, A., 1984. Loss of metals from pelites during regional metamorphism. Contributions to Mineralogy and Petrology, 85, p 116-132

Hand, M. & Dirks, P. H. G. M., 1992. The influence of deformation on the formation of axial-planar leucosomes and the segregation of small melt bodies within the migmatitic Napperby Gneiss, central Australia. Journal of Structural Geology 14, 591-604.

Harris, N. B. W., Gravestock, P. & Inger, S., 1992. Ion-microprobe determinations of trace-element concentrations in garnets from anatectic assemblages. Chemical Geology 100, 41-49.

Hartmann, O., Hoffer, E. & Haack, U., 1983. Regional metamorphism in the Damara orogen: interaction of crustal motion and heat transfer. Special Publication of the Geological Society of South Africa 11, 233-241.

Hensen, B. J., 1971. Theoretical phase relations involving cordierite and garnet in the system MgO-FeO-Al_2O_3-SiO_2. Contributions to Mineralogy and Petrology 33, 191-214.

Hensen, B. J. & Green, D. H., 1973. Experimental study of the stability of cordierite and garnet in pelitic compositions at high pressures and temperatures. III. Synthesis of experimental data and geological applications. Contributions to Mineralogy and Petrology 38, 151-166.

Hoernes, S. & Hoffer, E., 1985. Stable isotope evidence for fluid-present and fluid-absent metamorphism in metapelites from the Damara Orogen, Namibia. Contributions to Mineralogy and Petrology 90, 322-330.

Hoffer, E., 1977. Petrologische Untersuchungen zur Regionalmetamorphose Al-reicher Metapelite im südlichen Damara-Orogen (Südwest-Afrika). Habilitationsschrift, Göttingen, 130pp.

Hoffmann, C., 1976. Granites and migmatites of the Damara belt, South West Africa. Petrography and melting experiments. International Journal of Earth Sciences 65, 939-966.

Hoffmann, K. H., 1983. Lithostratigraphy and Facies of the Swakop Group of the Southern Damara Belt, Namibia. Special Publication of the Geological Society of South Africa 11, 43-64.

Hoffmann, K. H., 1994. New constraints on the timing of continental breakup and collision in the Damara Belt. In: Niall, M. and McManus, C. (Eds), Proterozoic Crustal and Metallogenic Evolution. Abstracts of Geological Society and Geological Survey of Namibia Conference 30. Windhoek.

Hoffmann, K. H., Condon, D. J., Bowring, S. A. & Crowley, J. L., 2004. U-Pb zircon date from the Neoproterozoic Ghaub Formation, Namibia: Constraints on Marinoan glaciation. Geology 32, no. 9, p. 817-820.

Hoffmann, K. H., Hawkins, D. P., Isachsen, C. E. & Bowring, S. A., 1996. Precise U-Pb zircon ages for early Damaran magmatism in the Summas Mountains and Welwitschia inlier, northern Damara belt, Namibia. Communications - Geological Survey of Namibia 11, 47-52.

Holland, T. J. B. & Powell, R., 1998. An internally consistent thermodynamic data set for phases of petrological interest. Journal of Metamorphic Geology 16, 309-343.

Holtz, F. & Johannes, W., 1994. Maximum and minimum water contents of granitic melts - Implications for chemical and physical-properties of ascending magmas. Lithos 32, 149-159.

Holtz, F., Johannes, W., Tamic, N. & Behrens, H., 2001. Maximum and minimum water contents of granitic melts generated in the crust: A reevaluation and implications. Lithos 56, 1-14.

Holtz, F., Pichavant, M., Barbey, P. & Johannes, W., 1992. Effect of H_2O on liquidus phase relations in the haplogranite system at 2 and 5 kbar. American Mineralogist 77, 1223-1241.

Hubbert, M. K. & Rubey, W. W., 1959. Role of fluid pressure in mechanics of overthrust faulting. Bull. Geol. Soc. Am. 70, 115-166.

Jacob, R. E., 1974. Geology and metamorphic petrology of part of the Damara orogen along the lower Swakop River, South West Africa. Precambrian Research Unit Bulletin 17, 185.

Jacob, R. E., Kröner, A. & Burger, A. J., 1978. Areal extent and first U-Pb age of the Pre-Damaran Abbabis Complex in the central Damara belt of South West Africa (Namibia). Geol. Rdschau. 67, 706-718.

Jacob, R. E., Moore, J. M. & Armstrong, R. A., 2000. Zircon and titanite age determinations from igneous rocks in the Karibib district, Namibia: Implications for Navachab vein-style gold mineralization. Geological Survey of Namibia Communications 12, 157-166.

Jacob, R. E., Snowden, P. A. & Bunting, F. J. L., 1983. Geology and structural development of the Tumas basement dome and its cover rocks. In: Miller, R. M. (Ed.) Evolution of the Damara Orogen of South West Africa/Namibia. Geol. Soc. S. Afr. Special Publ., vol. 11,, 157–172.

Jaeger, J. C. & Cook, N. G. W., 1976. *Fundamentals of rock mechanics* (second edition). London: Chapman and Hall. 585.

Johnson, S. D., Poujol, M. & Kisters, A. F. M., 2006. Constraining the timing and migration of collisional tectonics in the Damara Belt, Namibia: U-Pb zircon ages for the syntectonic Salem-type Stinkbank granite. 611-624.

Jung, S., Hoernes, S. & Mezger, K., 2000. Geochronology and petrology of migmatites from the Proterozoic Damara Belt - importance of episodic fluid-present disequilibrium melting and consequences for granite petology. Lithos 51, 153-179.

Jung, S., Hoernes, S. & Mezger, K., 2002. Synorogenic melting of mafic lower crust: constraints from geochronology, petrology and Sr, Nd, Pb and O isotope geochemistry of quartz diorites (Damara orogen, Namibia). Contributions to Mineralogy and Petrology 143, 551-566.

Jung, S., 2005. Isotopic equilibrium/disequilibrium in granites, metasedimentary rocks and migmatites (Damara orogen, Namibia)--a consequence of polymetamorphism and melting. Lithos 84, 168-184.

Jung, S. & Hellebrand, E., 2006. Trace element fractionation during high-grade metamorphism and crustal melting--constraints from ion microprobe data of metapelitic, migmatitic and igneous garnets and implications for Sm-Nd garnet chronology. Lithos 87, 193-213.

Jung, S., Hoernes, S. & Hoffer, E., 2005. Petrogenesis of cogenetic nepheline and quartz syenites and granites (northern Damara Orogen, Namibia): enriched mantle versus crustal contamination. Journal of Geology 113, 651-672.

Jung, S., Hoernes, S., Masberg, P. & Hoffer, E., 1999. The petrogenesis of some migmatites and granites (central Damara Orogen, Namibia): Evidence for disequilibrium melting, wall-rock contamination and crystal fractionation. Journal of Petrology 40, 1241-1269.

Jung, S., Hoernes, S. & Mezger, K., 2000. Geochronology and petrogenesis of Pan-African, syn-tectonic, S-type and post-tectonic A-type granite (Namibia): products of melting of crustal sources, fractional crystallization and wall rock entrainment. Lithos 50, 259-287.

Jung, S., Hoernes, S. & Mezger, K., 2001. Trace element and isotopic (Sr, Nd, Pb, O) arguments for a mid-crustal origin of Pan-African garnet-bearing S-type granites from the Damara orogen (Namibia). Precambrian Research 110, 325-355.

Jung, S., Hoffer, E. and Hoernes, S., 2007. Neo-Proterozoic rift-related syenites (Northern Damara Belt, Namibia): Geochemical and Nd–Sr–Pb–O isotope constraints for mantle sources and petrogenesis. Lithos 96, 415 - 435.

Jung, S. & Mezger, K., 2001. Geochronology in migmatites - a Sm-Nd, U-Pb and Rb-Sr study from the Proterozoic Damara belt (Namibia): implications for polyphase development of migmatites in high-grade terranes. Journal of Metamorphic Geology 19, 77-97.

Jung, S. & Mezger, K., 2003. Petrology of basement-dominated terranes: I. Regional metamorphic T-t path from U-Pb monazite and Sm-Nd garnet geochronology (Central Damara orogen, Namibia). Chemical Geology 198, 223-247.

Kasch, K. W., 1983. Tectonothermal evolution of the Southern Damara Orogen. In: Miller, R. M. (Ed.) Evolution of the Damara Orogen of South West Africa/Namibia: Geological Society of South Africa Special Publication, 255-265.

Kisters, A. F. M., Gibson, R. L., Charlesworth, E. G. & Anhaeusser, C. R., 1998. The role of strain localization in the segregation and ascent of anatectic melts, Namaqualand, South Africa. Journal of Structural Geology 20, 229-242.

Kisters, A. F. M., Hoffmann, K. H., Ward, R. A. & Stevens, G., 2007. *FT1 Pre-conference field trip to the Pan-African Granites of the Damara Belt, Namibia*. 6th International Hutton Symposium on the origin of granites and related rocks. Stellenbosch. p. 51.

Kisters, A. F. M., Jordaan, L. S. & Neumaier, K., 2004. Thrust-related dome structures in the Karibib district and the origin of orthogonal fabric domains in the south Central Zone of the Pan-African Damara belt, Namibia. Precambrian Research 133, 283-303.

Kretz, R., 1983. Symbols for rock-forming minerals. American Mineralogist 68, 277-279.

Kriegsman, L. M., 2001. Quantitative field methods for estimating melt production and melt loss. Physics and Chemistry of the Earth, Part A: Solid Earth and Geodesy 26, 247-253.

Kröner, A., 1984. Dome structures and basement reactivation in the Pan-African Damara belt of Namibia/South West Africa. In: Kröner, A. & Greiling, R. O. (Eds.) Precambrian Tectonics Illustrated. Stuttgart, Germany: Naegele and Obermiller, 191-206.

Kröner, A., Retief, E. A., Compston, W., Jacob, R. E. & Burger, A. J., 1991. Single-grain and convertional zircon dating of remobilized basement gneisses in the central Damara belt of Namibia. South African Journal of Geology 94, 379-387.

Kusky, T. M. & Polat, A., 1999. Growth of granite-greenstone terranes at convergent margins, and stabilization of Archean cratons. Tectonophysics 305, 43-73.

LeBreton, N. & Thompson, A. B., 1988. Fluid-absent (dehydration) melting of biotite in metapelites in the early stages of crustal anatexis. Contributions to Mineralogy and Petrology 99, 226-237.

Lemmon, E. W., McLinden, M. O. & Friend, D. G., 2005. Thermophysical Properties of Fluid Systems. In: Linstrom, P. J. & Mallard, W. G. (Eds.) NIST Chemistry WebBook, NIST Standard Reference Database Number 69. Gaithersburg MD, 20899: National Institute of Standards and Technology, (http://webbook.nist.gov).

London, D., Hervig, R. L. & Morgan, G. B., 1988. Melt-vapor solubilities and elemental partitioning in peraluminous granite-pegmatite systems: experimental results with Macusani glass at 200 MPa. Contributions to Mineralogy and Petrology 99, 360-373.

Lucas, S. B. & St-Onge, M. R., 1995. Syn-tectonic magmatism and the development of compositional layering, Ungava Orogen (northern Quebec, Canada). Journal of Structural Geology 17, 475-491.

Luth, W. C., 1967. Studies in the system $KAlSiO_4$-Mg_2SiO_4-SiO_2-H_2O: I, Inferred phase relations and petrologic application. Journal of Petrology 8, 372-416.

Masberg, H. P., 2000. Garnet growth in medium pressure granulite-facies metapelites from the central Damara Orogen: igneous versus metamorphic history. Communications - Geological Survey of Namibia 12, 115-124.

Masberg, H. P., Hoffer, E. & Hoernes, S., 1992. Microfabrics indicating granulite-facies metamorphism in the low-pressure central Damara Orogen, Namibia. Precambrian research 55, 243-257.

Masberg, P., 1996. Multiple migmatization in the HT/LP Central Damara Orogen, Namibia. Neues Jahrbuch Fur Mineralogie-Abhandlungen 170, 257-289.

McCaig, A. M., 1988. Deep fluid circulation in fault zones. Geology 16, 867-870.

McDermott, F., Harris, N. B. W. & Hawkesworth, C. J., 1996. Geochemical constraints on crustal anatexis: a case study from the Pan-African Damara granitoids of Namibia. Contributions to Mineralogy and Petrology 123, 406-423.

Miller, R. M., 1983. The Pan-African Damara orogen of south west Africa/Namibia. In: Miller, R. M. (Ed.) Evolution of the Damara Orogen of South West Africa/Namibia: Geological Society of South Africa Special Publication, 431-515.

Miller, R. M. & Hoffmann, K. H., 1981. Guide to the excursion through the Damara Orogen. Geocongress 81, Geological Society South Africa, Windhoek, South West Africa, 103p.

Morgan, G. B., Acosta-Vigil, A. & London, D., 2008. Diffusive equilibration between hydrous metaluminous-peraluminous haplogranite liquid couples at 200 MPa (H_2O) and alkali transport in granitic liquids. Contributions to Mineralogy and Petrology 155, 257-269.

Moyen, J.-F., Stevens, G. & Kisters, A., 2006. Record of mid-Archaean subduction from metamorphism in the Barberton terrain, South Africa. Nature 442, 559-562.

Newman, S. & Lowenstern, J. B., 2002. VolatileCalc: a silicate melt-H_2O-CO_2 solution model written in Visual Basic for Excel. Computers and Geosciences 28, 597-604.

Nex, P. A. M., Oliver, G. J. H. & Kinnaird, J. A., 2001. Spinel-bearing assemblages and P-T-t evolution of the Central Zone of the Damara Orogen, Namibia. Journal of African Earth Sciences 32, 471-489.

Oliver, G. J. H., 1994. Mid-crustal detachment and domes in the central zone of the Damaran orogen, Namibia. Journal of African Earth Sciences 19, 331-344.

Oliver, G. J. H., 1995. The central zone of the Damara Orogen, Namibia, as a deep metamorphic core complex. Communications - Geological Survey of Namibia 10, 33-41.

Patiño Douce, A. E. & Johnston, A. D., 1991. Phase equilibria and melt productivity in the pelitic system: implications for the origin of peraluminous granitoids and aluminous granulites. Contributions to Mineralogy and Petrology 107, 202-218.

Patiño Douce, A. E. & Beard, J. S., 1995. Dehydration-melting of biotite gneiss and quartz amphibolite from 3 to 15 kbar. Journal of Petrology 36, 707-738.

Pattison, D. R. M., Chacko, T., Farquhar, J. & McFarlane, C. R. M., 2003. Temperatures of granulite-facies metamorphism: constraints from experimental phase equilibria and thermobarometry corrected for retrograde exchange. Journal of Petrology 44, 867-900.

Perchuk, L., Gerya, T., van Reenen, D. & Smit, C., 2006. P-T paths and problems of high-temperature polymetamorphism. Journal of Petrology 14, 117-153.

Pichavant, M., 1987. Effect of B and H_2O on liquidus phase relations in the haplogranite system at 1 kbar. American Mineralogist 72, 1056-1070.

Poli, L. C. & Oliver, G. J. H., 2001. Constrictional deformation in the Central Zone of the Damara Orogen Namibia. Journal of African Earth Sciences 33, 303-312.

Powell, R. & Holland, T., 1990. Calculated mineral equilibria in the pelite system, KFMASH. American Mineralogist 75, 367-380.

Powell, R., Holland, T. & Worley, B., 1998. Calculating phase diagrams involving solid solutions via non-linear equations, with examples using THERMOCALC. Journal of Metamorphic Geology 16, 577-588.

Preston, R. F., Stevens, G. & McCarthy, T. S., 2003. Fluid compositions in equilibrium with silica-undersaturated magmas in the system Na_2O-Al_2O_3-SiO_2-H_2O: clues to the composition of fenitizing fluids. Contributions to Mineralogy and Petrology 144, 559-569.

Proyer, A., Dachs, E. and McCammon, C., 2004. Pitfalls in geothermobarometry of eclogites: Fe^{3+} and changes in the mineral chemistry of omphacite at ultrahigh pressures. Contributions to mineralogy and petrology, 147. 305 - 318.

Puhan, D., 1983. Temperature and pressure of metamorphism in the central Damara orogen. In: Miller, R. M. (Ed.) Evolution of the Damara Orogen of South West Africa/Namibia.: Geological Society of South Africa Special Publication, 219-223.

Ramsay, J. G., 1967. *Folding and Fracturing of Rocks*. New York: McGraw-Hill. 521.

Rosenberg, C. L. & Handy, M. R., 2000. Syntectonic melt pathways during simple shearing of a partially molten rock analogue (Norcamphor-Benzamide). Journal of Geophysical Research 105, 3135-3150

Rosenberg, C. L. & Handy, M. R., 2005. Experimental deformation of partially melted granite revisited: implications for the continental crust. Journal of Metamorphic Geology 23, 19-28.

Rubie, D. C. & Brearley, A. J., 1990. A model for rates of disequilibrium melting during metamorphism. In: Ashworth, J. R. & Brown, M. (Eds.) High-temperature metamorphism and crustal anatexis. London: Unwin Hyman, 57–86.

Rushmer, T., 1995. An experimental deformation study of partially molten amphibolite: Application to low-melt fraction segregation. Journal of Geophysical Research 100, 15681-15696.

Rutter, E. H. & Neumann, D. H. K., 1995. Experimental deformation of partially molten Westerly granite under fluid-absent conditions, with implications for the extraction of granitic magmas. Journal of Geophysical Research 100, 15697-15716

Sawyer, E. W., 1981. Damaran structural and metamorphic geology of an area south-east of Walvis Bay, SWA/Namibia. Memoir Geol. Survey, S.W. Afr./Namibia 7, 94.

Sawyer, E. W., 1994. Melt segregation in the continental crust. Geology 22, 1019-1022.

Sawyer, E. W. and Barnes, S. -J., 1988. Temporal and compositional differences between subsolidus and anatectic migmatite leucosomes from the Quetico metasedimentary belt, Canada. Journal of Metamorphic Geology, 6, 437 - 450.

Schneider, A., 1983. The Chemical Composition of the Common Metamorphic Sediments of the Damara Orogen. In: Martin, H. & Eder, F. W. (Eds.) Intracontinental Fold Belts. Berlin: Springer-Verlag, 655-677.

Secor, D. T., 1965. Role of fluid pressure in jointing. Americal Journal of Science 263, 633-646.

Secor, D. T. & Pollard, D. D., 1975. On the stability of open hydrofractures in the Earth's crust. Geophysical Research Letters 2, 510-513.

Sibson, R. H., 1994. Crustal stress, faulting and fluid flow. Geological Society, London, Special Publications 78, 69-84.

Sleep, N. H., 1988. Tapping of Melt by Veins and Dikes. Journal of Geophysical Research 93, 10,255-210,272.

Smith, D. A. M., 1965. The geology around the Khan and Swakop Rivers in South West Africa. Memoirs of the Geological Survey of South Africa, S.W. Afr. Series 3, 113.

Spear, F. S. & Florence, F. P., 1992. Thermobarometry in granulites: pitfalls and new approaches. In: van Reenan, D. D., Roering, C., Ashwal, L. D. & de Wit, M. J. (eds) *The Archean Limpopo Granulite Belt: Tectonics and Deep Crustal Processes. Precambrian Research* **55**, 209–241.

Spicer, E. M., Stevens, G. and Buick, I. S., 2004. The low-pressure partial-melting behaviour of natural boron-bearing metapelites from the Mt. Stafford area, central Australia. Contributions to Mineralogy and Petrology 148, 160-179.

Spicer, E. M. & Stevens, G., in prep. A summary of the quantitative determination of Na_2O in hydrous silicate melts by electron microprobe and scanning electron microscope.

Srogi, L., Wagner, M. E. & Lutz, T. M., 1993. Dehydration partial melting and disequilibrium in the granulite-facies Wilmington Complex, Pennsylvania-Delaware Piedmont. American Journal of Science 293, 405-462.

Stanistreet, I. G., Kukla, P. A. & Henry, G., 1991. Sedimentary basinal responses to a Late Precambrian Wilson Cycle: the Damara Orogen and Nama Foreland, Namibia. Journal of African Earth Sciences 13, 141-156.

Stevens, G., Clemens, J. D. & Droop, G. T. R., 1995. Hydrous cordierite in granulites and crustal magma production. Geology 23, 925-928.

Stevens, G., Clemens, J. D. & Droop, G. T. R., 1997. Melt production during granulite-facies anatexis: experimental data from primitive metasedimentary protoliths. Contributions to Mineralogy and Petrology 128, 352-370.

Stevens, G. & Van Reenen, D., 1992. Partial melting and the origin of metapelitic granulites in the Southern Marginal Zone of the Limpopo Belt, South Africa. Precambrian research 55, 303-319.

Stormer, J. C., Unpubl. Dense 2.0, A macro for Excel to determine the density of silicic magma.

Tack, L., Williams, I. & Bowden, P., 2002. SHRIMP constraints on early post-collisional granitoids in the Ida dome, Central Damara (Pan-African) belt, western Namibia. 11th IAGOD Quadrennial Symposium and Geocongress. Windhoek, Namibia: Geol. Survey Nambia, 1–5.

Taylor, S. R. & McLennan, S. M., 1985. The continental crust: Its composition and evolution. United States: Blackwell Scientific Pub.,Palo Alto, CA. Pages: 328.

Terzaghi, K., 1924. Die Theorie der hydrodynamischen Spannungserscheinungen und ihr bautechnisches Anwendungsgebiet. Proc. Int. Cong. Appl. Mech. Delft, 288-294.

Thompson, A. B., 1983. Fluid-absent metamorphism. Journal of the Geological Society 140, 533-547.

Thompson, A. B., 1990. Heat, fluids and melting in the granulite-facies. In: Vielzeuf, D. & Vidal, P. (Eds.) Granulites and crustal differentiation. Dordrecht: Kluwer, 37-58.

Vanderhaeghe, O., 1999. Pervasive melt migration from migmatites to leucogranites in the Shuswap metamorphic core complex, Canada: control of regional deformation. Tectonophysics 312, 35-55.

Vielzeuf, D. & Clemens, J. D., 1992. The fluid-absent melting of phlogopite+quartz: Experiments and models. American Mineralogist 77S, 1206-1222.

Vielzeuf, D. & Holloway, J. R., 1988. Experimental determination of the fluid-absent melting relations in the pelitic system. Contributions to Mineralogy and Petrology 98, 257-276.

Vielzeuf, D. & Montel, J.-M., 1994. Partial melting of metagreywackes. Part I. Fluid-absent experiment and phase relationship. Contributions to Mineralogy and Petrology 117, 375-393.

Vigneresse, J.-L., Barbey, P. & Cuney, M., 1996. Rheological transitions during partial melting and crystallization with application to felsic magma segregation and transfer. Journal of Petrology 37, 1579-1600.

Vigneresse, J. L., 2004. A new paradigm for granite generation. Transactions of the Royal Society of Edinburgh: Earth Sciences 95, 11-22.

Ward, R. A., Kisters, A. F. M. & Stevens, G., 2007. Structural controls of melt formation, melt extraction and transfer in mid-crustal metapsammites of the Damara belt, Namibia. Hutton Symposium on Granites. Stellenbosch, South Africa.

Warren, R. G. & Ellis, D. J., 1996. Mantle underplating, granite tectonics, and metamorphic P-T-t paths. Geology 24, 663-666.

Waters, D. J., 2001. The significance of prograde and retrograde quartz-bearing intergrowth microstructures in partially melted granulite-facies rocks. Lithos 56, 97–110.

Weertman, S. M., 1971. Theory of water-filled crevasses in glaciers applied to vertical magma transport beneath oceanic ridges. Journal of Geophysical Research 76, 1171-1183.

Weinberg, R. F., 1999. Mesoscale pervasive felsic magma migration: alternatives to dyking. Lithos 46, 393-410.

White, R. W., Pomroy, N. E. & Powell, R., 1995. An *in situ* metatexite-diatexite transition in upper amphibolite-facies rocks from Broken Hill, Australia. Journal of Metamorphic Geology, 23, no. 7. 579 - 602.

White, R. W., Powell, R. & Halpin, J. A., 2004. Spatially-focussed melt formation in aluminous metapelites from Broken Hill, Australia. Journal of Metamorphic Geology 22, 825-845.

White, R. W., Powell, R. & Holland, T. J. B., 2007. Progress relating to calculation of partial melting equilibria for metapelites. Journal of Metamorphic Geology 25, 511-527.

White, R. W., Powell, R. & Phillips, G. N., 2003. A mineral equilibria study of the hydrothermal alteration in mafic greenschist facies rocks at Kalgoorlie, Western Australia. Journal of Metamorphic Geology 21, 455-468.

Winkler, H. G. F., 1983. A survey of granitic rocks of the Damara Orogen and considerations on their origin. In: Martin, H. & Eder, F. W. (eds.) Intracontinental fold belts. Berlin: Springer, 817-837.

Winkler, H. G. F., Boese, M. & Marcopoulos, T., 1975. Low temperature granitic melts. Neues Jahrbuch fur Mineralogie Monatshefte 1975, 245-268.

Winkler, H. G. F. & Breitbart, R., 1978. New aspects of granitic magmas. Neues Jahrbuch fur Mineralogie Monatshefte 1978, 463-480.

Winkler, H. G. F., Das, B. K. & Breitbart, R., 1977. Further data of low temperature melts existing on the quartz + plagioclase + liq. + vap. isobaric cotectic surface within the system Qz-Ab-Or-An-H_2O. Neues Jahrbuch fur Mineralogie Monatshefte 1977, 241-247.

Yardley, B. W. D., 1977. An empirical study of diffusion in garnet. American Mineralogist, 62, 793 - 800.

Appendix

Appendix 1: XRF

Appendix 1.1: UCT data from a recent international proficiency test (60 laboratories, Thompson *et al.*, 1997) comparing assigned values with major oxide data obtained using the Norrish and Hutton (1969) fusion method, and trace element data obtained using MACs. * = > 2 from assigned value.

Oxide	Assigned value in wt%	Value found using Norrish and Hutton fusion disks in wt%	RSD (%)
SiO2	58.247	57.99	0.44
TiO2	0.44	0.433	1.59
Al2O3	15.136	14.9	1.56
Fe2O3	8.987	8.89	1.08
MnO	0.129	0.125	3.10
MgO	4.727	4.65	1.63
CaO	6.488	6.56	1.11
Na2O	2.463	2.4	2.56
K2O	0.215	0.22	2.33
P2O5	0.05	0.049	2.00
LOI	3.058	3.09	1.05

Appendix 2: SEM-EDS

Appendix 2.1: Comparison of actual published major element concentrations of mineral standards and measured values as determined by Scanning Electron Microprobe EDS analysis at Stellenbosch University.

plagioclase				garnet				biotite				chlorite				hornblende			
	actual	measured	Dev		actual	measured	Dev		actual*	measured	Dev		actual*	measured	Dev		actual	measured	Dev
SiO2	54.21	53.07	2.10	**SiO2**	39.19	39.43	0.61	**SiO2**	40.38	40.8	1.04	**SiO2**	34.84	36.74	5.45	**SiO2**	40.37	42.21	4.56
TiO2	0.07	-	-	**TiO2**	0	-	-	**TiO2**	1.85	1.61	12.97	**TiO2**	0.00	-	-	**TiO2**	4.72	4.99	5.72
Al2O3	28.53	29.93	4.91	**Al2O3**	22.05	22.15	0.45	**Al2O3**	15.78	15.42	2.28	**Al2O3**	20.97	21.77	3.81	**Al2O3**	14.90	14.15	5.03
Cr2O3	0.00	-	-	**Cr2O3**	0	-	-	**Cr2O3**	0.00	-	-	**Cr2O3**	1.14	1.25	9.65	**Cr2O3**	0.00	-	-
FeO	0.37	-	-	**FeO**	23.27	23.41	0.60	**FeO**	11.18	11.76	5.19	**FeO**	3.84	4.11	7.03	**FeO**	11.25	11.96	6.31
MnO	0.00	-	-	**MnO**	0.59	0.34	42.37	**MnO**	0.04	0.21	425.00	**MnO**	0.00	-	-	**MnO**	0.09	-	-
MgO	0.13	-	-	**MgO**	10.7	10.74	0.37	**MgO**	20.36	20.07	1.42	**MgO**	38.86	36.06	7.21	**MgO**	12.80	12.16	5.00
CaO	11.80	12.01	1.78	**CaO**	4.2	3.95	5.95	**CaO**	0.10	-	-	**CaO**	0.03	-	-	**CaO**	10.30	10.22	0.78
Na2O	4.35	4.53	4.14	**Na2O**	0	-	-	**Na2O**	0.00	-	-	**Na2O**	0.00	-	-	**Na2O**	2.60	1.86	28.46
K2O	0.41	0.47	14.63	**K2O**	0	-	-	**K2O**	10.33	11.46	10.94	**K2O**	0.00	-	-	**K2O**	2.05	2.35	14.63
Total	99.87	100.01		**Total**	100	100.02		**Total**	100.02	101.33		**Total**	99.67	99.93		**Total**	99.08	99.9	
Anions	8	8		**Anions**	12	12		**Anions**	11	11		**Anions**	14	14		**Anions**	23	23	
Si	2.46	2.40		Si	2.98	2.99		Si	2.81	2.83		Si	2.88	3.01		Si	5.89	6.09	
Al	1.52	1.60						Al	1.19	1.17		Al	1.11	0.99		Ti	0.52	0.54	
Σ	3.98	4.00		Al	1.98	1.98		Σ	4.00	4.00		Σ	4.00	4.00		Al	2.56	2.41	
																Fe	1.37	1.44	
Ca	0.57	0.58		Fe	1.48	1.49		Al	0.11	0.09		Al	0.93	1.12		Mn	0.01	0.00	
Na	0.38	0.40		Mn	0.03	0.02		Ti	0.10	0.08		Cr	0.07	0.08		Mg	2.78	2.62	
K	0.02	0.03		Mg	1.21	1.22		Fe	0.65	0.68		Fe	0.27	0.28		Ca	1.61	1.58	
Σ	0.98	1.01		Ca	0.34	0.32		Mn	0.00	0.01		Mg	4.79	4.41		Na	0.74	0.52	
								Mg	2.11	2.08		Σ	6.06	5.89		K	0.38	0.43	
				Σ	8.03	8.02		Σ	2.97	2.94									
Σ	4.98	5.01																	
				XPy	0.40	0.40		K	0.92	1.01		Σ	10.06	9.89		Σ	15.87	15.64	
XAn	0.60	0.59		XAlm	0.48	0.49													
XAb	0.40	0.41		XSpss	0.01	0.01		Σ	7.89	7.96		Mg#	94.75	93.99		Mg#	66.97	64.44	
				XGrss	0.11	0.11													
				Fe/Fe+Mg	0.55	0.55		Mg#	76.44	75.25									

Note: XPy, XAlm, XSpss and XGrss as defined by Spear (1993). XAn = Ca/(Ca+Na), XAb = Na/(Ca+Na), Mg# = 100 x Mg/(Mg+Fe)
* Recalculated as water-free equivalent
n/d = not determined

Appendix 2.2.1 a: Major element composition and mineral formulae for Anatectic Garnet from metapelites.

Sample No.	Misc B1	Misc B1	Misc B1	Misc B1	Misc C1	Misc C1	Misc C1	Misc C1	Misc C1	Misc C1	Misc C1	Misc C1	Misc C1	Misc C1
Analysis	gt	gt	gt-rim	gt	gt	gt-rim	gt-near rim	gt	gt	gt	gt near to core	gt (core)	gt core but retrgrade	gt
SiO2	37.38	37.67	37.50	38.04	37.05	37.65	36.77	37.95	37.95	37.23	37.85	38.03	37.26	37.61
Al2O3	20.69	20.79	20.74	21.04	20.54	21.07	20.46	20.91	21.09	20.53	20.95	21.05	20.61	20.95
Fe2O3	1.03	0.83	1.06	0.62	0.88	1.37	1.55	0.56	0.85	1.74	0.93	1.04	1.33	1.08
FeO	32.03	32.43	33.02	33.40	32.30	33.20	32.39	33.32	33.25	32.91	33.05	32.71	33.03	31.82
MnO	4.23	4.61	4.01	4.82	4.12	4.41	4.40	4.26	4.13	3.96	3.70	3.72	5.23	4.61
MgO	4.24	3.85	3.86	3.48	3.91	3.80	3.73	3.79	3.94	3.93	4.16	4.51	3.10	4.35
CaO	0.78	0.85	0.83	0.78	0.77	0.88	0.80	0.78	0.83	0.84	0.91	0.88	0.81	0.81
Total	**100.37**	**101.02**	**101.02**	**102.18**	**99.57**	**102.39**	**100.10**	**101.57**	**102.05**	**101.13**	**101.54**	**101.94**	**101.35**	**101.22**
Si	*2.99*	*3.00*	*2.99*	*3.00*	*2.99*	*2.96*	*2.96*	*3.01*	*2.99*	*2.97*	*2.99*	*2.99*	*2.98*	*2.98*
Al^{IV}	*0.01*	*0.00*	*0.01*	*0.00*	*0.01*	*0.04*	*0.04*	*0.00*	*0.01*	*0.03*	*0.01*	*0.01*	*0.02*	*0.02*
Σ T-site	***3.00***	***3.00***	***3.00***	***3.00***	***3.00***	***3.00***	***3.00***	***3.01***	***3.00***	***3.00***	***3.00***	***3.00***	***3.00***	***3.00***
Al^{VI}	*1.94*	*1.95*	*1.94*	*1.96*	*1.95*	*1.92*	*1.91*	*1.95*	*1.95*	*1.90*	*1.94*	*1.94*	*1.92*	*1.94*
Fe^{3+}	*0.06*	*0.05*	*0.06*	*0.04*	*0.05*	*0.08*	*0.09*	*0.03*	*0.05*	*0.10*	*0.06*	*0.06*	*0.08*	*0.06*
Σ M-site	***2.00***	***2.00***	***2.00***	***1.99***	***2.00***	***2.00***	***2.00***	***1.99***	***2.00***	***2.00***	***2.00***	***2.00***	***2.00***	***2.00***
Fe^{2+}	*2.14*	*2.16*	*2.20*	*2.20*	*2.18*	*2.19*	*2.18*	*2.21*	*2.19*	*2.19*	*2.18*	*2.15*	*2.21*	*2.11*
Mn	*0.29*	*0.31*	*0.27*	*0.32*	*0.28*	*0.29*	*0.30*	*0.29*	*0.28*	*0.27*	*0.25*	*0.25*	*0.35*	*0.31*
Mg	*0.51*	*0.46*	*0.46*	*0.41*	*0.47*	*0.45*	*0.45*	*0.45*	*0.46*	*0.47*	*0.49*	*0.53*	*0.37*	*0.51*
Ca	*0.07*	*0.07*	*0.07*	*0.07*	*0.07*	*0.07*	*0.07*	*0.07*	*0.07*	*0.07*	*0.08*	*0.07*	*0.07*	*0.07*
Σ A-site	***3.00***	***3.00***	***3.00***	***3.00***	***3.00***	***3.00***	***3.00***	***3.01***	***3.00***	***3.00***	***3.00***	***3.00***	***3.00***	***3.00***
XAlm	*0.71*	*0.72*	*0.73*	*0.73*	*0.73*	*0.73*	*0.73*	*0.73*	*0.73*	*0.73*	*0.73*	*0.72*	*0.74*	*0.70*
XPyr	*0.10*	*0.10*	*0.09*	*0.11*	*0.09*	*0.10*	*0.10*	*0.10*	*0.09*	*0.09*	*0.08*	*0.08*	*0.12*	*0.10*
XSps	*0.17*	*0.15*	*0.15*	*0.14*	*0.16*	*0.15*	*0.15*	*0.15*	*0.15*	*0.16*	*0.16*	*0.18*	*0.12*	*0.17*
XGrs	*0.02*	*0.02*	*0.02*	*0.02*	*0.02*	*0.02*	*0.02*	*0.02*	*0.02*	*0.02*	*0.03*	*0.02*	*0.02*	*0.02*
Total	***1.00***	***1.00***	***1.00***	***1.00***	***1.00***	***1.00***	***1.00***	***1.00***	***1.00***	***1.00***	***1.00***	***1.00***	***1.00***	***1.00***
Mg #	19	17	17	16	18	17	17	17	17	18	18	20	14	20

Appendix 2.2.1 a: Major element composition and mineral formulae for Anatectic Garnet from metapelites (*continued*).

Sample No.	14_3_b Gt profile	14_3_b Gt profile	14_3_b Gt profile	14_3_b Gt profile	14_3_b Gt profile	14_3_b Gt profile	14_3_b Gt profile	14_3_b Gt profile	14_3_b Gt profile	14_3_b Gt profile	14_3_b Gt profile	14_3_b Gt profile	14_3_b Gt profile	14_3_b Gt profile
Analysis	1	2	3	4	5	6	7	8	9	10	11	12	13	14
SiO2	36.05	36.46	36.64	36.25	35.98	36.34	36.34	36.62	36.45	36.57	36.39	36.69	36.66	36.38
Al2O3	20.87	20.83	21.13	20.84	20.49	20.84	20.86	21.01	20.96	20.73	20.59	20.76	21.14	20.84
Fe2O3	2.49	2.24	2.08	2.33	2.49	2.28	2.35	2.07	2.42	2.37	2.32	2.24	1.90	2.17
FeO	33.46	33.46	33.59	33.46	33.38	33.48	33.42	33.55	33.64	33.27	33.38	33.52	33.73	33.33
MnO	4.95	5.03	5.02	4.99	4.92	4.92	5.08	5.11	5.00	5.06	5.05	4.95	4.91	4.93
MgO	2.89	2.95	2.97	2.86	2.80	2.91	2.92	2.93	2.94	2.96	2.84	2.99	2.95	3.02
CaO	0.96	0.92	1.04	1.00	0.90	1.00	0.95	0.95	0.97	1.08	0.96	0.96	0.98	0.93
Total	**101.67**	**101.90**	**102.46**	**101.73**	**100.94**	**101.77**	**101.91**	**102.23**	**102.38**	**102.04**	**101.53**	**102.10**	**102.27**	**101.60**
Si	*2.88*	*2.91*	*2.90*	*2.90*	*2.90*	*2.90*	*2.90*	*2.91*	*2.89*	*2.91*	*2.92*	*2.92*	*2.91*	*2.91*
Al^{IV}	*0.12*	*0.09*	*0.10*	*0.10*	*0.10*	*0.10*	*0.10*	*0.09*	*0.11*	*0.09*	*0.08*	*0.08*	*0.09*	*0.09*
Σ T-site	***3.00***	***3.00***	***3.00***	***3.00***	***3.00***	***3.00***	***3.00***	***3.00***	***3.00***	***3.00***	***3.00***	***3.00***	***3.00***	***3.00***
Al^{VI}	*1.85*	*1.87*	*1.88*	*1.86*	*1.85*	*1.86*	*1.86*	*1.88*	*1.86*	*1.86*	*1.86*	*1.87*	*1.89*	*1.87*
Fe^{3+}	*0.15*	*0.13*	*0.12*	*0.14*	*0.15*	*0.14*	*0.14*	*0.12*	*0.14*	*0.14*	*0.14*	*0.13*	*0.11*	*0.13*
Σ M-site	***2.00***	***2.00***	***2.00***	***2.00***	***2.00***	***2.00***	***2.00***	***2.00***	***2.00***	***2.00***	***2.00***	***2.00***	***2.00***	***2.00***
Fe^{2+}	*2.24*	*2.23*	*2.23*	*2.24*	*2.25*	*2.24*	*2.23*	*2.23*	*2.23*	*2.22*	*2.24*	*2.23*	*2.24*	*2.23*
Mn	*0.34*	*0.34*	*0.34*	*0.34*	*0.34*	*0.33*	*0.34*	*0.34*	*0.34*	*0.34*	*0.34*	*0.33*	*0.33*	*0.33*
Mg	*0.34*	*0.35*	*0.35*	*0.34*	*0.34*	*0.35*	*0.35*	*0.35*	*0.35*	*0.35*	*0.34*	*0.35*	*0.35*	*0.36*
Ca	*0.08*	*0.08*	*0.09*	*0.09*	*0.08*	*0.09*	*0.08*	*0.08*	*0.08*	*0.09*	*0.08*	*0.08*	*0.08*	*0.08*
Σ A-site	***3.00***	***3.00***	***3.00***	***3.00***	***3.00***	***3.00***	***3.00***	***3.00***	***3.00***	***3.00***	***3.00***	***3.00***	***3.00***	***3.00***
XAlm	*0.75*	*0.74*	*0.74*	*0.75*	*0.75*	*0.75*	*0.74*	*0.74*	*0.74*	*0.74*	*0.75*	*0.74*	*0.75*	*0.74*
XPyr	*0.11*	*0.11*	*0.11*	*0.11*	*0.11*	*0.11*	*0.11*	*0.11*	*0.11*	*0.11*	*0.11*	*0.11*	*0.11*	*0.11*
XSps	*0.11*	*0.12*	*0.12*	*0.11*	*0.11*	*0.12*	*0.12*	*0.12*	*0.12*	*0.12*	*0.11*	*0.12*	*0.12*	*0.12*
XGrs	*0.03*	*0.03*	*0.03*	*0.03*	*0.03*	*0.03*	*0.03*	*0.03*	*0.03*	*0.03*	*0.03*	*0.03*	*0.03*	*0.03*
Total	***1.00***	***1.00***	***1.00***	***1.00***	***1.00***	***1.00***	***1.00***	***1.00***	***1.00***	***1.00***	***1.00***	***1.00***	***1.00***	***1.00***
Mg #	13	14	14	13	13	13	13	13	13	14	13	14	13	14

Appendix 2.2.1 a: Major element composition and mineral formulae for Anatectic Garnet from metapelites (*continued*).

Sample No.	14_3_b Gt profile	14_3_b Gt profile	14_3_b Gt profile	14_3_b Gt profile	GL-1	GL-1	GL-1	GL-1	11/7 D	11/7 D	11/7 D	11/7 D	11/7 D	**11/7 D**
Analysis	15	16	17	18	garnet	gb-gr	gb2-gr	gb3-gr	gt rim	gt rim	gt core	gt core	gt core adjacent bi	**gt core**
SiO2	36.05	36.54	36.28	36.93	37.67	37.49	37.01	36.86	36.46	36.54	36.66	37.28	36.00	36.40
Al2O3	20.78	20.96	20.74	21.27	20.92	21.03	20.63	20.49	20.03	20.31	20.21	20.48	19.98	20.04
Fe2O3	2.26	2.24	2.32	1.89	1.47	1.14	1.51	1.07	2.74	2.76	2.86	2.83	3.08	2.97
FeO	33.23	33.61	33.43	33.82	32.83	33.90	34.63	33.57	30.10	30.75	29.98	30.04	30.72	30.14
MnO	4.94	4.50	4.72	3.65	4.25	4.70	5.18	5.57	6.39	6.50	5.08	5.02	5.28	5.21
MgO	2.89	3.22	3.00	3.76	4.13	3.17	2.17	2.38	3.63	3.38	4.66	4.98	3.82	4.31
CaO	0.99	0.97	0.99	1.00	0.79	0.77	0.84	0.70	1.20	1.18	1.17	1.24	1.18	1.21
Total	**101.16**	**102.03**	**101.48**	**102.32**	**102.06**	**102.19**	**101.96**	**100.64**	**100.54**	**101.41**	**100.64**	**101.88**	**100.06**	**100.28**
Si	*2.90*	*2.90*	*2.90*	*2.91*	*2.97*	*2.97*	*2.96*	*2.98*	*2.93*	*2.92*	*2.93*	*2.93*	*2.91*	*2.92*
Al^{IV}	*0.10*	*0.10*	*0.10*	*0.09*	*0.03*	*0.03*	*0.04*	*0.02*	*0.07*	*0.08*	*0.07*	*0.07*	*0.09*	*0.08*
Σ T-site	***3.00***	***3.00***	***3.00***	***3.00***	***3.00***	***3.00***	***3.00***	***3.00***	***3.00***	***3.00***	***3.00***	***3.00***	***3.00***	***3.00***
Al^{VI}	*1.86*	*1.87*	*1.86*	*1.89*	*1.91*	*1.93*	*1.91*	*1.94*	*1.83*	*1.83*	*1.83*	*1.83*	*1.81*	*1.82*
Fe^{3+}	*0.14*	*0.13*	*0.14*	*0.11*	*0.09*	*0.07*	*0.09*	*0.06*	*0.17*	*0.17*	*0.17*	*0.17*	*0.19*	*0.18*
Σ M-site	***2.00***	***2.00***	***2.00***	***2.00***	***2.00***	***2.00***	***2.00***	***2.00***	***2.00***	***2.00***	***2.00***	***2.00***	***2.00***	***2.00***
Fe^{2+}	*2.23*	*2.23*	*2.24*	*2.23*	*2.16*	*2.25*	*2.32*	*2.27*	*2.03*	*2.06*	*2.00*	*1.98*	*2.08*	*2.02*
Mn	*0.34*	*0.30*	*0.32*	*0.24*	*0.28*	*0.32*	*0.35*	*0.38*	*0.44*	*0.44*	*0.34*	*0.33*	*0.36*	*0.35*
Mg	*0.35*	*0.38*	*0.36*	*0.44*	*0.49*	*0.37*	*0.26*	*0.29*	*0.44*	*0.40*	*0.55*	*0.58*	*0.46*	*0.52*
Ca	*0.09*	*0.08*	*0.08*	*0.08*	*0.07*	*0.07*	*0.07*	*0.06*	*0.10*	*0.10*	*0.10*	*0.10*	*0.10*	*0.10*
Σ A-site	***3.00***	***3.00***	***3.00***	***3.00***	***3.00***	***3.00***	***3.00***	***3.00***	***3.00***	***3.00***	***3.00***	***3.00***	***3.00***	***3.00***
XAlm	*0.74*	*0.74*	*0.75*	*0.74*	*0.72*	*0.75*	*0.77*	*0.76*	*0.68*	*0.69*	*0.67*	*0.66*	*0.69*	*0.67*
XPyr	*0.11*	*0.10*	*0.11*	*0.08*	*0.09*	*0.11*	*0.12*	*0.13*	*0.15*	*0.15*	*0.11*	*0.11*	*0.12*	*0.12*
XSps	*0.12*	*0.13*	*0.12*	*0.15*	*0.16*	*0.12*	*0.09*	*0.10*	*0.15*	*0.13*	*0.18*	*0.19*	*0.15*	*0.17*
XGrs	*0.03*	*0.03*	*0.03*	*0.03*	*0.02*	*0.02*	*0.02*	*0.02*	*0.03*	*0.03*	*0.03*	*0.03*	*0.03*	*0.03*
Total	***1.00***	***1.00***	***1.00***	***1.00***	***1.00***	***1.00***	***1.00***	***1.00***	***1.00***	***1.00***	***1.00***	***1.00***	***1.00***	***1.00***
Mg #	13	15	14	17	18	14	10	11	18	16	22	23	18	20

Appendix 2.2.1 a: Major element composition and mineral formulae for Anatectic Garnet from metapelites (*continued*).

Sample No.	11/7 D	11/7 D	11/7 D	11_9 C stub	11_9 C stub	11_9 C stub	11_9 C stub	11_9 C stub	11_9 C stub	11_9 C stub	11_9 C stub	11_9 C stub	11_9 C stub	11_9 C stub
Analysis	gt rim	gt rim	gt	gt	gt	gt	gt rim	gt rim	gt	gt	gt	margin gt	margin gt	margin gt
SiO2	36.74	36.23	36.34	36.59	36.44	36.71	36.57	35.99	36.33	36.54	36.13	36.26	35.94	36.29
Al2O3	20.51	19.97	20.20	20.75	20.83	20.74	20.72	20.59	20.79	20.93	20.61	20.72	20.67	20.61
Fe2O3	2.97	3.09	2.92	2.41	1.98	1.95	2.05	2.71	2.19	2.21	2.81	2.20	2.27	2.35
FeO	30.30	29.55	29.71	32.83	32.63	32.74	32.61	32.36	32.46	32.74	34.03	33.45	33.46	33.36
MnO	6.61	6.55	5.68	1.60	1.64	1.76	1.74	1.80	1.88	2.00	2.21	2.04	2.47	2.06
MgO	3.79	3.83	4.32	5.37	5.31	5.23	5.31	5.23	5.23	5.15	4.15	4.54	4.13	4.57
CaO	1.22	1.21	1.21	0.84	0.84	0.85	0.81	0.92	0.89	0.91	0.93	0.87	0.91	0.89
Total	**102.14**	**100.42**	**100.38**	**100.38**	**99.68**	**99.97**	**99.82**	**99.61**	**99.78**	**100.47**	**100.88**	**100.08**	**99.85**	**100.13**
Si	*2.91*	*2.92*	*2.91*	*2.91*	*2.92*	*2.93*	*2.92*	*2.89*	*2.91*	*2.91*	*2.89*	*2.91*	*2.90*	*2.91*
Al^{IV}	*0.09*	*0.08*	*0.09*	*0.09*	*0.08*	*0.07*	*0.08*	*0.11*	*0.09*	*0.09*	*0.11*	*0.09*	*0.10*	*0.09*
Σ T-site	***3.00***	***3.00***	***3.00***	***3.00***	***3.00***	***3.00***	***3.00***	***3.00***	***3.00***	***3.00***	***3.00***	***3.00***	***3.00***	***3.00***
Al^{VI}	*1.82*	*1.81*	*1.82*	*1.86*	*1.88*	*1.88*	*1.88*	*1.84*	*1.87*	*1.87*	*1.83*	*1.87*	*1.86*	*1.86*
Fe^{3+}	*0.18*	*0.19*	*0.18*	*0.14*	*0.12*	*0.12*	*0.12*	*0.16*	*0.13*	*0.13*	*0.17*	*0.13*	*0.14*	*0.14*
Σ M-site	***2.00***	***2.00***	***2.00***	***2.00***	***2.00***	***2.00***	***2.00***	***2.00***	***2.00***	***2.00***	***2.00***	***2.00***	***2.00***	***2.00***
Fe^{2+}	*2.01*	*1.99*	*1.99*	*2.18*	*2.18*	*2.19*	*2.18*	*2.17*	*2.17*	*2.18*	*2.28*	*2.24*	*2.26*	*2.24*
Mn	*0.44*	*0.45*	*0.39*	*0.11*	*0.11*	*0.12*	*0.12*	*0.12*	*0.13*	*0.13*	*0.15*	*0.14*	*0.17*	*0.14*
Mg	*0.45*	*0.46*	*0.52*	*0.64*	*0.63*	*0.62*	*0.63*	*0.63*	*0.62*	*0.61*	*0.50*	*0.54*	*0.50*	*0.55*
Ca	*0.10*	*0.10*	*0.10*	*0.07*	*0.07*	*0.07*	*0.07*	*0.08*	*0.08*	*0.08*	*0.08*	*0.07*	*0.08*	*0.08*
Σ A-site	***3.00***	***3.00***	***3.00***	***3.00***	***3.00***	***3.00***	***3.00***	***3.00***	***3.00***	***3.00***	***3.00***	***3.00***	***3.00***	***3.00***
XAlm	*0.67*	*0.66*	*0.66*	*0.73*	*0.73*	*0.73*	*0.73*	*0.72*	*0.72*	*0.73*	*0.76*	*0.75*	*0.75*	*0.75*
XPyr	*0.15*	*0.15*	*0.13*	*0.04*	*0.04*	*0.04*	*0.04*	*0.04*	*0.04*	*0.04*	*0.05*	*0.05*	*0.06*	*0.05*
XSps	*0.15*	*0.15*	*0.17*	*0.21*	*0.21*	*0.21*	*0.21*	*0.21*	*0.21*	*0.20*	*0.17*	*0.18*	*0.17*	*0.18*
XGrs	*0.03*	*0.03*	*0.03*	*0.02*	*0.02*	*0.02*	*0.02*	*0.03*	*0.03*	*0.03*	*0.03*	*0.02*	*0.03*	*0.03*
Total	***1.00***	***1.00***	***1.00***	***1.00***	***1.00***	***1.00***	***1.00***	***1.00***	***1.00***	***1.00***	***1.00***	***1.00***	***1.00***	***1.00***
Mg #	18	19	21	23	22	22	22	22	22	22	18	19	18	20

Appendix 2.2.1 a: Major element composition and mineral formulae for Anatectic Garnet from metapelites (*continued*).

Sample No.	11_9 C stub	11_9 C stub	11_1 stub	11_1 stub	11_1 stub	11_1 stub	11_1 stub	11_1 stub	11_1 stub	11_1 stub	11_1 stub	KHt2_2 c	KHt2_2 c	KHt2_2 c	KHt2_2 c
Analysis	margin gt	margin gt	gt core	gt core	gt core	gt adjacent bio	gt in fissure	gt adjcent bi	gt rim	gt rim	gt rim	leucosome Gt	leucosome Gt	leucosome gt rim	leucosome gt core
SiO2	37.70	36.05	37.04	36.84	36.48	35.80	35.66	35.59	36.40	36.14	36.57	36.93	36.77	35.67	35.38
Al2O3	21.45	20.63	21.11	21.11	20.99	20.58	20.53	20.41	20.63	20.73	21.02	21.00	20.88	20.43	20.41
Fe2O3	1.05	2.56	1.31	1.52	1.65	1.76	2.19	2.06	1.08	1.45	1.20	2.02	1.80	1.96	2.46
FeO	33.90	33.03	32.23	32.23	31.74	33.36	33.24	33.32	33.05	32.92	33.22	33.63	33.72	33.27	32.80
MnO	2.05	2.14	3.58	3.45	3.60	5.41	5.52	5.43	4.84	5.01	6.36	4.30	4.27	5.77	4.30
MgO	4.90	4.70	4.55	4.66	4.67	2.36	2.42	2.21	2.87	2.90	2.18	3.54	3.36	2.11	3.22
CaO	0.81	0.87	0.91	0.83	0.86	0.77	0.77	0.89	0.84	0.85	0.86	0.82	0.76	0.83	0.84
Total	**101.86**	**99.99**	**100.73**	**100.65**	**100.00**	**100.03**	**100.33**	**99.91**	**99.72**	**100.00**	**101.41**	**102.23**	**101.56**	**100.03**	**99.42**
Si	*2.96*	*2.89*	*2.94*	*2.93*	*2.92*	*2.92*	*2.90*	*2.91*	*2.96*	*2.93*	*2.94*	*2.92*	*2.93*	*2.91*	*2.89*
Al^{IV}	*0.04*	*0.11*	*0.06*	*0.07*	*0.08*	*0.08*	*0.10*	*0.09*	*0.04*	*0.07*	*0.06*	*0.08*	*0.07*	*0.09*	*0.11*
Σ T-site	***3.00***	***3.00***	***3.00***	***3.00***	***3.00***	***3.00***	***3.00***	***3.00***	***3.00***	***3.00***	***3.00***	***3.00***	***3.00***	***3.00***	***3.00***
Al^{VI}	*1.94*	*1.85*	*1.92*	*1.91*	*1.90*	*1.89*	*1.87*	*1.87*	*1.93*	*1.91*	*1.93*	*1.88*	*1.89*	*1.88*	*1.85*
Fe^{3+}	*0.06*	*0.15*	*0.08*	*0.09*	*0.10*	*0.11*	*0.13*	*0.13*	*0.07*	*0.09*	*0.07*	*0.12*	*0.11*	*0.12*	*0.15*
Σ M-site	***2.00***	***2.00***	***2.00***	***2.00***	***2.00***	***2.00***	***2.00***	***2.00***	***2.00***	***2.00***	***2.00***	***2.00***	***2.00***	***2.00***	***2.00***
Fe^{2+}	*2.22*	*2.22*	*2.14*	*2.14*	*2.12*	*2.27*	*2.26*	*2.28*	*2.25*	*2.23*	*2.23*	*2.23*	*2.25*	*2.27*	*2.24*
Mn	*0.14*	*0.15*	*0.24*	*0.23*	*0.24*	*0.37*	*0.38*	*0.38*	*0.33*	*0.34*	*0.43*	*0.29*	*0.29*	*0.40*	*0.30*
Mg	*0.57*	*0.56*	*0.54*	*0.55*	*0.56*	*0.29*	*0.29*	*0.27*	*0.35*	*0.35*	*0.26*	*0.42*	*0.40*	*0.26*	*0.39*
Ca	*0.07*	*0.07*	*0.08*	*0.07*	*0.07*	*0.07*	*0.07*	*0.08*	*0.07*	*0.07*	*0.07*	*0.07*	*0.06*	*0.07*	*0.07*
Σ A-site	***3.00***	***3.00***	***3.00***	***3.00***	***3.00***	***3.00***	***3.00***	***3.00***	***3.00***	***3.00***	***3.00***	***3.00***	***3.00***	***3.00***	***3.00***
XAlm	*0.74*	*0.74*	*0.71*	*0.71*	*0.71*	*0.76*	*0.75*	*0.76*	*0.75*	*0.74*	*0.74*	*0.74*	*0.75*	*0.76*	*0.75*
XPyr	*0.05*	*0.05*	*0.08*	*0.08*	*0.08*	*0.12*	*0.13*	*0.13*	*0.11*	*0.11*	*0.14*	*0.10*	*0.10*	*0.13*	*0.10*
XSps	*0.19*	*0.19*	*0.18*	*0.18*	*0.19*	*0.10*	*0.10*	*0.09*	*0.12*	*0.12*	*0.09*	*0.14*	*0.13*	*0.09*	*0.13*
XGrs	*0.02*	*0.02*	*0.03*	*0.02*	*0.02*	*0.02*	*0.02*	*0.03*	*0.02*	*0.02*	*0.02*	*0.02*	*0.02*	*0.02*	*0.02*
Total	***1.00***	***1.00***	***1.00***	***1.00***	***1.00***	***1.00***	***1.00***	***1.00***	***1.00***	***1.00***	***1.00***	***1.00***	***1.00***	***1.00***	***1.00***
Mg #	21	20	20	21	21	11	11	11	13	14	10	16	15	10	15

Appendix 2.2.1 b: Major element composition and mineral formulae for Metamorphic Garnet from metapelites.

Sample No.	KH1-2	KH1-2	KH1-2	KH1-2	KH1_1 B gt Profile	KH1_1 B gt Profile	KH1_1 B gt Profile	KH1_1 B gt Profile	KH1_1 B gt Profile	KH1_1 B gt Profile	KH1_1 B gt Profile	KH1_1 B gt Profile	KH1_1 B gt Profile	KH1_1 B gt Profile
Analysis					1	2	3	4	5	6	7	8	9	10
SiO2	37.60	37.68	37.41	37.58	37.83	37.63	37.87	38.34	37.82	37.80	38.05	38.13	37.48	37.37
Al2O3	20.87	20.92	20.91	20.53	20.98	20.76	21.15	21.12	20.93	21.16	21.04	21.02	20.95	20.79
Fe2O3	0.87	1.11	1.03	0.26	0.00	0.00	0.00	0.23	0.38	0.88	0.16	0.63	0.43	0.75
FeO	35.91	35.08	34.38	35.01	33.57	33.69	34.22	34.74	34.12	34.01	34.11	33.99	33.55	33.40
MnO	2.12	2.11	1.62	2.34	2.58	2.42	2.35	2.31	2.20	2.32	2.13	2.28	2.09	2.11
MgO	3.23	3.81	4.31	3.45	3.67	3.87	3.84	4.10	4.15	4.27	4.34	4.36	4.33	4.34
CaO	1.00	1.03	1.07	1.10	1.15	1.17	1.15	1.14	1.16	1.19	1.17	1.19	1.15	1.19
Total	**101.61**	**101.73**	**100.73**	**100.28**	**99.78**	**99.54**	**100.59**	**101.98**	**100.76**	**101.62**	**101.00**	**101.60**	**99.97**	**99.94**
Si	*2.99*	*2.98*	*2.98*	*3.02*	*3.04*	*3.03*	*3.02*	*3.01*	*3.01*	*2.98*	*3.01*	*3.01*	*3.00*	*2.99*
Al^{IV}	*0.01*	*0.02*	*0.02*	*0.00*	*0.00*	*0.00*	*0.00*	*0.00*	*0.00*	*0.02*	*0.00*	*0.00*	*0.00*	*0.01*
Σ T-site	***3.00***	***3.00***	***3.00***	***3.02***	***3.04***	***3.03***	***3.02***	***3.01***	***3.01***	***3.00***	***3.01***	***3.01***	***3.00***	***3.00***
Al^{VI}	*1.95*	*1.93*	*1.94*	*1.94*	*1.99*	*1.97*	*1.99*	*1.96*	*1.96*	*1.95*	*1.96*	*1.95*	*1.97*	*1.96*
Fe^{3+}	*0.05*	*0.07*	*0.06*	*0.02*	*0.00*	*0.00*	*0.00*	*0.01*	*0.02*	*0.05*	*0.01*	*0.04*	*0.03*	*0.04*
Σ M-site	***2.00***	***2.00***	***2.00***	***1.96***	***1.99***	***1.97***	***1.99***	***1.97***	***1.98***	***2.00***	***1.97***	***1.99***	***2.00***	***2.00***
Fe^{2+}	*2.39*	*2.32*	*2.29*	*2.35*	*2.26*	*2.27*	*2.28*	*2.28*	*2.27*	*2.24*	*2.26*	*2.24*	*2.24*	*2.24*
Mn	*0.14*	*0.14*	*0.11*	*0.16*	*0.18*	*0.17*	*0.16*	*0.15*	*0.15*	*0.15*	*0.14*	*0.15*	*0.14*	*0.14*
Mg	*0.38*	*0.45*	*0.51*	*0.41*	*0.44*	*0.46*	*0.46*	*0.48*	*0.49*	*0.50*	*0.51*	*0.51*	*0.52*	*0.52*
Ca	*0.09*	*0.09*	*0.09*	*0.09*	*0.10*	*0.10*	*0.10*	*0.10*	*0.10*	*0.10*	*0.10*	*0.10*	*0.10*	*0.10*
Σ A-site	***3.00***	***3.00***	***3.00***	***3.02***	***2.97***	***3.00***	***2.99***	***3.01***	***3.01***	***3.00***	***3.01***	***3.01***	***3.00***	***3.00***
XAlm	*0.80*	*0.77*	*0.76*	*0.78*	*0.76*	*0.76*	*0.76*	*0.76*	*0.75*	*0.75*	*0.75*	*0.75*	*0.75*	*0.75*
XPyr	*0.05*	*0.05*	*0.04*	*0.05*	*0.06*	*0.06*	*0.05*	*0.05*	*0.05*	*0.05*	*0.05*	*0.05*	*0.05*	*0.05*
XSps	*0.13*	*0.15*	*0.17*	*0.14*	*0.15*	*0.15*	*0.15*	*0.16*	*0.16*	*0.17*	*0.17*	*0.17*	*0.17*	*0.17*
XGrs	*0.03*	*0.03*	*0.03*	*0.03*	*0.03*	*0.03*	*0.03*	*0.03*	*0.03*	*0.03*	*0.03*	*0.03*	*0.03*	*0.03*
Total	***1.00***	***1.00***	***1.00***	***1.00***	***1.00***	***1.00***	***1.00***	***1.00***	***1.00***	***1.00***	***1.00***	***1.00***	***1.00***	***1.00***
Mg #	14	16	18	15	16	17	17	17	18	18	18	19	19	19

Appendix 2.2.1 b: Major element composition and mineral formulae for Metamorphic Garnet from metapelites (*continued*).

Sample No.	KH1_1 B gt Profile	KH1_1 B gt Profile	KH1_1 B gt Profile	KH1_1 B gt Profile	KH1_1 B gt Profile	KH1_1 B gt Profile	KH1_1 B gt Profile	KH1_1 B gt Profile	KH1_1 B gt Profile	KH1_1 B gt Profile	KH1_1 B gt Profile	KH1_1 B gt Profile	KH1_1 B gt Profile	KH1_1 B gt Profile
Analysis	11	12	13	14	15	16	17	18	19	20	21	22	23	24
SiO2	37.81	38.40	38.33	37.96	37.54	38.09	38.14	38.25	36.67	38.41	37.42	37.59	37.55	37.49
Al2O3	20.84	21.37	21.14	21.20	20.57	21.07	21.06	20.92	20.42	21.50	20.78	20.75	20.80	20.81
Fe2O3	0.38	0.60	0.94	0.80	1.37	0.85	0.74	0.42	1.67	0.00	0.69	0.70	0.84	0.84
FeO	33.61	34.17	33.74	33.70	33.17	33.96	33.88	34.22	33.30	34.26	33.71	33.61	33.60	33.55
MnO	2.14	1.93	1.96	1.97	2.12	2.05	2.06	2.12	2.29	2.20	2.23	2.27	2.26	2.24
MgO	4.49	4.66	4.86	4.76	4.64	4.58	4.60	4.44	4.11	4.25	4.13	4.22	4.23	4.29
CaO	1.11	1.18	1.18	1.10	1.16	1.10	1.13	1.15	1.20	1.14	1.14	1.19	1.21	1.16
Total	**100.39**	**102.30**	**102.15**	**101.49**	**100.56**	**101.68**	**101.61**	**101.52**	**99.66**	**101.76**	**100.10**	**100.33**	**100.49**	**100.38**
Si	*3.01*	*3.00*	*3.00*	*2.99*	*2.99*	*3.00*	*3.00*	*3.02*	*2.96*	*3.02*	*3.00*	*3.00*	*2.99*	*2.99*
Al^{IV}	*0.00*	*0.00*	*0.00*	*0.01*	*0.01*	*0.00*	*0.00*	*0.00*	*0.04*	*0.00*	*0.00*	*0.00*	*0.01*	*0.01*
Σ T-site	***3.01***	***3.00***	***3.00***	***3.00***	***3.00***	***3.00***	***3.00***	***3.02***	***3.00***	***3.02***	***3.00***	***3.00***	***3.00***	***3.00***
Al^{VI}	*1.96*	*1.96*	*1.94*	*1.95*	*1.92*	*1.95*	*1.95*	*1.94*	*1.90*	*1.99*	*1.96*	*1.95*	*1.95*	*1.95*
Fe^{3+}	*0.02*	*0.04*	*0.06*	*0.05*	*0.08*	*0.05*	*0.04*	*0.02*	*0.10*	*0.00*	*0.04*	*0.04*	*0.05*	*0.05*
Σ M-site	***1.98***	***2.00***	***2.00***	***2.00***	***2.00***	***2.00***	***2.00***	***1.97***	***2.00***	***1.99***	***2.00***	***2.00***	***2.00***	***2.00***
Fe^{2+}	*2.24*	*2.23*	*2.21*	*2.22*	*2.21*	*2.23*	*2.23*	*2.26*	*2.25*	*2.25*	*2.26*	*2.24*	*2.24*	*2.24*
Mn	*0.14*	*0.13*	*0.13*	*0.13*	*0.14*	*0.14*	*0.14*	*0.14*	*0.16*	*0.15*	*0.15*	*0.15*	*0.15*	*0.15*
Mg	*0.53*	*0.54*	*0.57*	*0.56*	*0.55*	*0.54*	*0.54*	*0.52*	*0.49*	*0.50*	*0.49*	*0.50*	*0.50*	*0.51*
Ca	*0.10*	*0.10*	*0.10*	*0.09*	*0.10*	*0.09*	*0.09*	*0.10*	*0.10*	*0.10*	*0.10*	*0.10*	*0.10*	*0.10*
Σ A-site	***3.01***	***3.00***	***3.00***	***3.00***	***3.00***	***3.00***	***3.00***	***3.02***	***3.00***	***2.99***	***3.00***	***3.00***	***3.00***	***3.00***
XAlm	*0.74*	*0.74*	*0.74*	*0.74*	*0.74*	*0.74*	*0.74*	*0.75*	*0.75*	*0.75*	*0.75*	*0.75*	*0.75*	*0.75*
XPyr	*0.05*	*0.04*	*0.04*	*0.04*	*0.05*	*0.05*	*0.05*	*0.05*	*0.05*	*0.05*	*0.05*	*0.05*	*0.05*	*0.05*
XSps	*0.18*	*0.18*	*0.19*	*0.19*	*0.18*	*0.18*	*0.18*	*0.17*	*0.16*	*0.17*	*0.16*	*0.17*	*0.17*	*0.17*
XGrs	*0.03*	*0.03*	*0.03*	*0.03*	*0.03*	*0.03*	*0.03*	*0.03*	*0.03*	*0.03*	*0.03*	*0.03*	*0.03*	*0.03*
Total	***1.00***	***1.00***	***1.00***	***1.00***	***1.00***	***1.00***	***1.00***	***1.00***	***1.00***	***1.00***	***1.00***	***1.00***	***1.00***	***1.00***
Mg #	19	20	20	20	20	19	20	19	18	18	18	18	18	19

Appendix 2.2.1 b: Major element composition and mineral formulae for Metamorphic Garnet from metapelites (*continued*).

Sample No.	KH1_1 B gt Profile	KH 1_3 B1	KH 1_3 B1	KH 1_3 B3	KH 1_3 B3	KH 1/1 B	KH 1/1 B	KH 1/1 B	12/1 D a	12/1 D a	12/1 D a	12/1 D a gt near	12/1 D a	12/1 D a
Analysis	25					Rim	Core	Core	garnet	gt rim	gt	core	gt core	gt core
SiO2	37.51	37.28	38.13	37.63	37.87	38.17	37.32	37.45	35.41	35.65	35.82	35.88	35.94	35.94
Al2O3	20.85	20.81	21.25	20.97	20.95	21.53	20.75	20.84	19.75	19.90	19.59	20.00	20.05	20.09
Fe2O3	0.00	0.73	0.54	0.83	0.82	-0.25	0.92	1.03	3.04	2.71	3.01	3.10	3.14	3.09
FeO	33.47	33.62	34.50	35.29	35.00	34.70	34.71	34.96	29.85	30.29	30.63	31.96	32.05	32.70
MnO	2.23	1.55	1.65	2.12	2.11	4.82	3.06	3.26	9.23	8.36	7.40	5.29	4.40	4.35
MgO	4.16	4.68	4.62	3.61	3.88	2.03	3.05	3.03	1.92	2.26	2.59	3.26	3.78	3.47
CaO	1.22	0.95	0.95	1.02	1.00	1.18	1.23	1.08	0.89	0.85	0.90	0.94	0.93	0.90
Total	**99.44**	**99.61**	**101.63**	**101.47**	**101.63**	**102.19**	**101.03**	**101.65**	**100.09**	**100.02**	**99.94**	**100.42**	**100.28**	**100.53**
Si	*3.02*	*2.99*	*3.00*	*2.99*	*3.00*	*3.03*	*2.99*	*2.98*	*2.90*	*2.92*	*2.93*	*2.90*	*2.90*	*2.90*
Al^{IV}	*0.00*	*0.01*	*0.00*	*0.01*	*0.00*	*0.00*	*0.01*	*0.02*	*0.10*	*0.08*	*0.07*	*0.10*	*0.10*	*0.10*
Σ T-site	***3.02***	***3.00***	***3.00***	***3.00***	***3.00***	***3.03***	***3.00***	***3.00***	***3.00***	***3.00***	***3.00***	***3.00***	***3.00***	***3.00***
Al^{VI}	*1.98*	*1.96*	*1.97*	*1.95*	*1.95*	*2.01*	*1.94*	*1.94*	*1.81*	*1.83*	*1.81*	*1.81*	*1.81*	*1.81*
Fe^{3+}	*0.00*	*0.04*	*0.03*	*0.05*	*0.05*	*0.01*	*0.06*	*0.06*	*0.19*	*0.17*	*0.19*	*0.19*	*0.19*	*0.19*
Σ M-site	***1.98***	***2.00***	***2.00***	***2.00***	***2.00***	***2.00***	***2.00***	***2.00***	***2.00***	***2.00***	***2.00***	***2.00***	***2.00***	***2.00***
Fe^{2+}	*2.25*	*2.25*	*2.27*	*2.34*	*2.32*	*2.30*	*2.32*	*2.33*	*2.05*	*2.07*	*2.09*	*2.16*	*2.16*	*2.21*
Mn	*0.15*	*0.11*	*0.11*	*0.14*	*0.14*	*0.32*	*0.21*	*0.22*	*0.64*	*0.58*	*0.51*	*0.36*	*0.30*	*0.30*
Mg	*0.50*	*0.56*	*0.54*	*0.43*	*0.46*	*0.24*	*0.36*	*0.36*	*0.23*	*0.28*	*0.32*	*0.39*	*0.45*	*0.42*
Ca	*0.11*	*0.08*	*0.08*	*0.09*	*0.08*	*0.10*	*0.11*	*0.09*	*0.08*	*0.07*	*0.08*	*0.08*	*0.08*	*0.08*
Σ A-site	***3.01***	***3.00***	***3.00***	***3.00***	***3.00***	***2.97***	***3.00***	***3.00***	***3.00***	***3.00***	***3.00***	***3.00***	***3.00***	***3.00***
XAlm	*0.75*	*0.75*	*0.76*	*0.78*	*0.77*	*0.78*	*0.77*	*0.78*	*0.68*	*0.69*	*0.70*	*0.72*	*0.72*	*0.74*
XPyr	*0.05*	*0.04*	*0.04*	*0.05*	*0.05*	*0.11*	*0.07*	*0.07*	*0.21*	*0.19*	*0.17*	*0.12*	*0.10*	*0.10*
XSps	*0.17*	*0.19*	*0.18*	*0.14*	*0.15*	*0.08*	*0.12*	*0.12*	*0.08*	*0.09*	*0.11*	*0.13*	*0.15*	*0.14*
XGrs	*0.03*	*0.03*	*0.03*	*0.03*	*0.03*	*0.03*	*0.04*	*0.03*	*0.03*	*0.02*	*0.03*	*0.03*	*0.03*	*0.03*
Total	***1.00***	***1.00***	***1.00***	***1.00***	***1.00***	***1.00***	***1.00***	***1.00***	***1.00***	***1.00***	***1.00***	***1.00***	***1.00***	***1.00***
Mg #	18	20	19	15	17	9	14	13	10	12	13	15	17	16

Appendix 2.2.1 b: Major element composition and mineral formulae for Metamorphic Garnet from metapelites (*continued*).

Sample No.	12/1 D a	12/1 D a	12/1 D a	12_1Da test	12_1Da test	12_1Da test	12_1Da test	12_1Da test	12_1Da test
Analysis	gt rim	gt 2	gt 2	gt	gt	gt	gt	gt in crd	gt
SiO2	36.10	36.04	36.08	35.52	35.60	34.91	35.92	36.33	36.65
Al2O3	19.92	20.27	19.99	19.48	19.56	19.14	19.65	19.85	20.24
Fe2O3	3.30	3.26	3.28	2.81	3.06	2.78	2.84	2.84	2.70
FeO	30.44	30.57	30.71	30.32	30.47	29.88	30.45	30.95	32.78
MnO	9.56	9.71	8.95	8.06	8.03	8.29	8.68	9.12	5.51
MgO	1.82	1.76	2.03	2.19	2.21	1.86	1.93	1.68	3.00
CaO	0.91	0.95	0.92	0.85	0.94	0.89	0.96	0.94	0.90
Total	**102.05**	**102.57**	**101.96**	**99.23**	**99.87**	**97.75**	**100.43**	**101.71**	**101.79**
Si	*2.91*	*2.89*	*2.90*	*2.93*	*2.92*	*2.93*	*2.93*	*2.94*	*2.93*
Al^{IV}	*0.09*	*0.11*	*0.10*	*0.07*	*0.08*	*0.07*	*0.07*	*0.06*	*0.07*
Σ T-site	***3.00***	***3.00***	***3.00***	***3.00***	***3.00***	***3.00***	***3.00***	***3.00***	***3.00***
Al^{VI}	*1.80*	*1.80*	*1.80*	*1.83*	*1.81*	*1.82*	*1.83*	*1.83*	*1.84*
Fe^{3+}	*0.20*	*0.20*	*0.20*	*0.17*	*0.19*	*0.18*	*0.17*	*0.17*	*0.16*
Σ M-site	***2.00***	***2.00***	***2.00***	***2.00***	***2.00***	***2.00***	***2.00***	***2.00***	***2.00***
Fe^{2+}	*2.05*	*2.05*	*2.07*	*2.09*	*2.09*	*2.10*	*2.08*	*2.09*	*2.19*
Mn	*0.65*	*0.66*	*0.61*	*0.56*	*0.56*	*0.59*	*0.60*	*0.62*	*0.37*
Mg	*0.22*	*0.21*	*0.24*	*0.27*	*0.27*	*0.23*	*0.24*	*0.20*	*0.36*
Ca	*0.08*	*0.08*	*0.08*	*0.08*	*0.08*	*0.08*	*0.08*	*0.08*	*0.08*
Σ A-site	***3.00***	***3.00***	***3.00***	***3.00***	***3.00***	***3.00***	***3.00***	***3.00***	***3.00***
XAlm	*0.68*	*0.68*	*0.69*	*0.70*	*0.70*	*0.70*	*0.69*	*0.70*	*0.73*
XPyr	*0.22*	*0.22*	*0.20*	*0.19*	*0.19*	*0.20*	*0.20*	*0.21*	*0.12*
XSps	*0.07*	*0.07*	*0.08*	*0.09*	*0.09*	*0.08*	*0.08*	*0.07*	*0.12*
XGrs	*0.03*	*0.03*	*0.03*	*0.03*	*0.03*	*0.03*	*0.03*	*0.03*	*0.03*
Total	***1.00***	***1.00***	***1.00***	***1.00***	***1.00***	***1.00***	***1.00***	***1.00***	***1.00***
Mg #	10	9	11	11	11	10	10	9	14

Appendix 2.2.1 c: Major element composition and mineral formulae for Metamorphic Garnet from metapsammites.

Sample No.	14/5 A	14/5 A	14/5 A	14/5 A	14/5 A	14/5 A	14/5 A
Analysis	gt	gt rim	gt	gt core	gt core	gt core	gt rim
SiO2	36.15	37.19	36.70	36.29	36.29	36.27	36.37
Al2O3	20.22	20.06	20.01	20.17	20.07	19.97	20.11
Fe2O3	2.63	2.69	2.54	2.63	2.83	2.90	2.56
FeO	31.66	32.19	31.84	31.54	32.25	31.40	32.25
MnO	6.55	6.71	6.16	6.08	6.23	6.02	6.65
MgO	2.84	2.82	3.04	3.18	2.78	3.29	2.48
CaO	0.86	0.86	0.89	0.90	0.80	0.87	0.85
Total	**100.90**	**102.52**	**101.17**	**100.79**	**101.25**	**100.73**	**101.26**
Si	*2.92*	*2.96*	*2.95*	*2.92*	*2.92*	*2.93*	*2.93*
Al^{IV}	*0.08*	*0.04*	*0.05*	*0.08*	*0.08*	*0.07*	*0.07*
Σ T-site	***3.00***	***3.00***	***3.00***	***3.00***	***3.00***	***3.00***	***3.00***
Al^{VI}	*1.84*	*1.84*	*1.85*	*1.84*	*1.83*	*1.82*	*1.84*
Fe^{3+}	*0.16*	*0.16*	*0.15*	*0.16*	*0.17*	*0.18*	*0.16*
Σ M-site	***2.00***	***2.00***	***2.00***	***2.00***	***2.00***	***2.00***	***2.00***
Fe^{2+}	*2.14*	*2.14*	*2.14*	*2.13*	*2.17*	*2.12*	*2.17*
Mn	*0.45*	*0.45*	*0.42*	*0.41*	*0.42*	*0.41*	*0.45*
Mg	*0.34*	*0.33*	*0.36*	*0.38*	*0.33*	*0.40*	*0.30*
Ca	*0.07*	*0.07*	*0.08*	*0.08*	*0.07*	*0.08*	*0.07*
Σ A-site	***3.00***	***3.00***	***3.00***	***3.00***	***3.00***	***3.00***	***3.00***
XAlm	*0.71*	*0.71*	*0.71*	*0.71*	*0.72*	*0.71*	*0.72*
XPyr	*0.15*	*0.15*	*0.14*	*0.14*	*0.14*	*0.14*	*0.15*
XSps	*0.11*	*0.11*	*0.12*	*0.13*	*0.11*	*0.13*	*0.10*
XGrs	*0.02*	*0.02*	*0.03*	*0.03*	*0.02*	*0.03*	*0.02*
Total	***1.00***	***1.00***	***1.00***	***1.00***	***1.00***	***1.00***	***1.00***
Mg #	14	14	15	15	13	16	12

Appendix 2.2.2. a: Major element composition and mineral formulae for Feldspar from the low-grade equivalent rocks.

Sample no.	USK-1 D	USK-1 D	USK-1 D	USK-1 D	USK-2B	USK-2B	USK-2B	USK-3D	USK-3D	USK-3D	USK-3D	USK-3D	USK-4A Bottom Bed	USK-4A Bottom Bed
Analysis	spec 4	plag	plag	plag	Spec 3	plag	plag	plag	plag	ksp	ksp	ksp	ksp poik	plag
SiO2	65.24	65.11	64.22	65.44	62.40	62.25	63.47	64.51	64.08	65.46	65.00	65.21	64.31	64.62
Al2O3	22.51	22.30	22.03	22.32	23.11	23.09	23.41	23.06	23.16	18.68	18.59	18.88	18.75	22.34
Fe2O3	0.26	0.16	0.12	0.01	0.13	0.16	0.10	0.02	0.09	0.08	0.00	0.03	0.05	0.06
CaO	3.21	3.14	3.09	3.17	4.50	4.59	4.56	4.14	4.10	0.00	0.00	0.00	0.00	3.39
Na2O	9.81	9.84	9.79	9.83	8.90	8.86	8.97	9.22	9.23	1.26	1.09	1.72	1.43	9.63
K2O	0.11	0.02	0.05	0.03	0.13	0.12	0.16	0.10	0.10	14.80	14.77	13.89	14.36	0.10
BaO	0.05	0.09	0.02	0.06	0.03	0.03	0.00	0.02	0.06	0.73	0.93	0.79	1.05	0.04
Total	**101.19**	**100.66**	**99.33**	**100.86**	**99.20**	**99.12**	**100.67**	**101.07**	**100.82**	**101.01**	**100.38**	**100.52**	**99.96**	**100.18**
Si	*2.84*	*2.85*	*2.85*	*2.86*	*2.78*	*2.78*	*2.79*	*2.82*	*2.81*	*2.99*	*2.99*	*2.99*	*2.98*	*2.84*
Al	*1.16*	*1.15*	*1.15*	*1.15*	*1.21*	*1.22*	*1.21*	*1.19*	*1.20*	*1.01*	*1.01*	*1.02*	*1.02*	*1.16*
Fe3+	*0.01*	*0.01*	*0.00*	*0.00*	*0.00*	*0.01*	*0.00*	*0.00*	*0.00*	*0.00*	*0.00*	*0.00*	*0.00*	*0.00*
Σ T-site	*4.01*	*4.01*	*4.00*	*4.00*	*4.00*	*4.00*	*4.00*	*4.00*	*4.01*	*4.00*	*4.00*	*4.01*	*4.00*	*4.00*
Ca	*0.15*	*0.15*	*0.15*	*0.15*	*0.22*	*0.22*	*0.21*	*0.19*	*0.19*	*0.00*	*0.00*	*0.00*	*0.00*	*0.16*
Na	*0.83*	*0.84*	*0.84*	*0.83*	*0.77*	*0.77*	*0.76*	*0.78*	*0.78*	*0.11*	*0.10*	*0.15*	*0.13*	*0.82*
K	*0.01*	*0.00*	*0.00*	*0.00*	*0.01*	*0.01*	*0.01*	*0.01*	*0.01*	*0.86*	*0.87*	*0.81*	*0.85*	*0.01*
Ba	*0.00*	*0.00*	*0.00*	*0.00*	*0.00*	*0.00*	*0.00*	*0.00*	*0.00*	*0.01*	*0.02*	*0.01*	*0.02*	*0.00*
Σ A-site	*0.99*	*0.98*	*0.99*	*0.98*	*0.99*	*0.99*	*0.99*	*0.98*	*0.98*	*0.99*	*0.98*	*0.98*	*1.00*	*0.99*
An (Ca)	15.2	15.0	14.8	15.1	21.7	22.1	21.7	19.8	19.6	0.0	0.0	0.0	0.0	16.2
Ab (Na)	84.2	84.9	84.9	84.7	77.6	77.2	77.4	79.7	79.8	11.5	10.1	15.8	13.2	83.2
Or (K)	0.6	0.1	0.3	0.2	0.7	0.7	0.9	0.6	0.6	88.5	89.9	84.2	86.8	0.6

Appendix 2.2.2. a: Major element composition and mineral formulae for Feldspar from the low-grade equivalent rocks (*continued)*.

Sample no.	USK-4A Bottom Bed	USK-4A Middle Bed	USK-4A Middle Bed	USK-4A Middle Bed	USK-4A Middle Bed	USK-4A Top Bed	USK-4A Top Bed	USK-4A Top Bed	USK-4A Top Bed	USK-4A Top Bed	USK-4A Top Bed	USK-4A Top Bed	USK-5C	USK-5C
Analysis	Spect 6	plag	plag	ksp poik	plag	Spect 1	plag	kspar poik	kspar poik	ksp	plag	plag	plag	plag
SiO2	64.82	64.24	64.52	64.23	64.76	64.49	65.61	64.55	65.25	65.23	65.42	64.09	65.08	65.29
Al2O3	19.02	22.43	22.50	18.81	21.79	21.65	22.01	18.68	19.01	19.03	22.46	22.07	22.15	21.88
Fe2O3	0.00	0.05	0.14	0.06	0.20	0.07	0.06	0.06	0.00	0.03	0.11	0.15	0.21	0.10
CaO	0.00	3.54	3.47	0.00	3.00	2.60	3.00	0.00	0.00	0.00	2.99	3.29	3.10	3.09
Na2O	1.86	9.59	9.70	1.27	9.68	10.05	9.89	1.30	1.54	1.44	10.05	9.66	9.76	9.94
K2O	14.33	0.13	0.07	14.40	0.07	0.13	0.06	14.41	14.41	14.40	0.04	0.10	0.02	0.03
BaO	0.84	0.04	0.04	1.21	0.00	0.04	0.05	1.08	0.72	0.95	0.00	0.01	0.04	0.00
Total	**100.87**	**100.01**	**100.44**	**99.98**	**99.48**	**99.03**	**100.68**	**100.08**	**100.93**	**101.08**	**101.07**	**99.36**	**100.36**	**100.33**
Si	*2.97*	*2.83*	*2.83*	*2.98*	*2.86*	*2.87*	*2.87*	*2.98*	*2.98*	*2.98*	*2.85*	*2.84*	*2.86*	*2.86*
Al	*1.03*	*1.17*	*1.16*	*1.03*	*1.14*	*1.13*	*1.13*	*1.02*	*1.02*	*1.02*	*1.15*	*1.15*	*1.15*	*1.13*
Fe3+	*0.00*	*0.00*	*0.00*	*0.00*	*0.01*	*0.00*	*0.00*	*0.00*	*0.00*	*0.00*	*0.00*	*0.01*	*0.01*	*0.00*
Σ T-site	*4.00*	*4.00*	*4.00*	*4.01*	*4.01*	*4.00*	*4.00*	*4.00*	*4.01*	*4.01*	*4.01*	*4.00*	*4.01*	*4.00*
Ca	*0.00*	*0.17*	*0.16*	*0.00*	*0.14*	*0.12*	*0.14*	*0.00*	*0.00*	*0.00*	*0.14*	*0.16*	*0.15*	*0.15*
Na	*0.17*	*0.82*	*0.83*	*0.11*	*0.83*	*0.87*	*0.84*	*0.12*	*0.14*	*0.13*	*0.85*	*0.83*	*0.83*	*0.85*
K	*0.84*	*0.01*	*0.00*	*0.85*	*0.00*	*0.01*	*0.00*	*0.85*	*0.84*	*0.84*	*0.00*	*0.01*	*0.00*	*0.00*
Ba	*0.02*	*0.00*	*0.00*	*0.02*	*0.00*	*0.00*	*0.00*	*0.02*	*0.01*	*0.02*	*0.00*	*0.00*	*0.00*	*0.00*
Σ A-site	*1.02*	*1.00*	*0.99*	*0.99*	*0.98*	*1.00*	*0.98*	*0.99*	*0.99*	*0.98*	*0.99*	*0.99*	*0.98*	*0.99*
An (Ca)	0.0	16.8	16.4	0.0	14.6	12.4	14.3	0.0	0.0	0.0	14.1	15.7	14.9	14.6
Ab (Na)	16.5	82.4	83.2	11.8	85.1	86.8	85.3	12.1	14.0	13.2	85.7	83.7	85.0	85.2
Or (K)	83.5	0.7	0.4	88.2	0.4	0.7	0.4	87.9	86.0	86.8	0.2	0.5	0.1	0.2

Appendix 2.2.2. a: Major element composition and mineral formulae for Feldspar from the low-grade equivalent rocks (*continued)*.

Sample no.	USK_6A	USK_6A	USK_6A	USK-7B	USK-7B
Analysis	plag	plag	plag	plag	plag
SiO2	65.62	65.51	64.72	65.31	65.35
Al2O3	21.90	22.09	21.58	21.76	21.82
Fe2O3	0.11	0.16	0.11	0.11	0.13
CaO	2.73	2.61	2.57	2.49	2.55
Na2O	10.12	10.35	10.03	9.95	10.41
K2O	0.00	0.03	0.05	0.02	0.03
BaO	0.07	0.04	0.00	0.03	0.06
Total	**100.56**	**100.79**	**99.06**	**99.67**	**100.35**
Si	*2.87*	*2.86*	*2.87*	*2.88*	*2.87*
Al	*1.13*	*1.14*	*1.13*	*1.13*	*1.13*
Fe3+	*0.00*	*0.01*	*0.00*	*0.00*	*0.00*
Σ T-site	*4.00*	*4.00*	*4.01*	*4.01*	*4.00*
Ca	*0.13*	*0.12*	*0.12*	*0.12*	*0.12*
Na	*0.86*	*0.88*	*0.86*	*0.85*	*0.89*
K	*0.00*	*0.00*	*0.00*	*0.00*	*0.00*
Ba	*0.00*	*0.00*	*0.00*	*0.00*	*0.00*
Σ A-site	*0.99*	*1.00*	*0.99*	*0.97*	*1.01*
An (Ca)	13.0	12.2	12.4	12.1	11.9
Ab (Na)	87.0	87.6	87.3	87.7	87.9
Or (K)	0.0	0.2	0.3	0.1	0.2

Appendix 2.2.2. b: Major element composition and mineral formulae for Feldspar from rocks of the high-grade study area.

Sample no.	KH3_ts	Kh-3	Kh-3 Spectrum	KH_1-2	KH_1-2	KH_1-2	KH_1-2 Spectrum	KH_1-2 hydrous	KH_1-2 Spectrum	14/5 A	14/5 A	14/5 A	14/5 A	12/1 D a
Analysis	k--sp	k-spar	11	plag	plag2	plag again	16	albitic?	19	plag	plag	plag	plag	plag
SiO2	65.74	65.00	63.89	61.85	61.75	61.54	61.42	66.77	63.61	62.13	61.75	63.12	61.94	61.82
Al2O3	19.05	18.96	18.39	24.67	24.84	24.67	24.91	19.28	18.37	23.54	23.39	23.57	23.27	23.65
Fe2O3	0.00	0.00	0.02	0.11	0.01	0.00	0.24	0.15	0.94	0.12	0.15	0.06	0.05	0.08
CaO	0.00	0.00	0.00	5.85	6.13	6.19	5.99	0.52	0.00	5.21	5.28	5.00	5.07	5.22
Na2O	1.56	0.82	1.06	8.39	8.00	7.99	7.88	11.22	1.14	8.47	8.39	8.64	8.49	8.38
K2O	14.71	16.02	15.54	0.12	0.17	0.09	0.10	0.47	14.32	0.09	0.12	0.14	0.14	0.17
BaO	0.00	0.02	0.00	0.01	0.00	0.04	0.00	0.00	1.09	0.00	0.05	0.11	0.08	0.00
Total	**101.06**	**100.82**	**98.90**	**101.00**	**100.90**	**100.52**	**100.54**	**98.42**	**99.47**	**99.56**	**99.12**	**100.64**	**99.02**	**99.32**
Si	*2.99*	*2.98*	*2.98*	*2.72*	*2.72*	*2.72*	*2.71*	*2.98*	*2.97*	*2.76*	*2.76*	*2.78*	*2.77*	*2.76*
Al	*1.02*	*1.02*	*1.01*	*1.28*	*1.29*	*1.28*	*1.30*	*1.01*	*1.01*	*1.23*	*1.23*	*1.22*	*1.23*	*1.24*
Fe3+	*0.00*	*0.00*	*0.00*	*0.00*	*0.00*	*0.00*	*0.01*	*0.00*	*0.03*	*0.00*	*0.01*	*0.00*	*0.00*	*0.00*
Σ T-site	*4.01*	*4.00*	*4.00*	*4.00*	*4.00*	*4.00*	*4.01*	*3.99*	*4.01*	*4.00*	*4.00*	*4.00*	*4.00*	*4.00*
Ca	*0.00*	*0.00*	*0.00*	*0.28*	*0.29*	*0.29*	*0.28*	*0.02*	*0.00*	*0.25*	*0.25*	*0.24*	*0.24*	*0.25*
Na	*0.14*	*0.07*	*0.10*	*0.72*	*0.68*	*0.68*	*0.67*	*0.97*	*0.10*	*0.73*	*0.73*	*0.74*	*0.74*	*0.72*
K	*0.85*	*0.94*	*0.93*	*0.01*	*0.01*	*0.01*	*0.01*	*0.03*	*0.85*	*0.01*	*0.01*	*0.01*	*0.01*	*0.01*
Ba	*0.00*	*0.00*	*0.00*	*0.00*	*0.00*	*0.00*	*0.00*	*0.00*	*0.02*	*0.00*	*0.00*	*0.00*	*0.00*	*0.00*
Σ A-site	*0.99*	*1.01*	*1.02*	*1.00*	*0.98*	*0.98*	*0.96*	*1.02*	*0.98*	*0.98*	*0.99*	*0.98*	*0.99*	*0.98*
An (Ca)	0.0	0.0	0.0	27.6	29.5	29.8	29.4	2.4	0.0	25.2	25.6	24.0	24.6	25.4
Ab (Na)	13.9	7.2	9.4	71.7	69.6	69.7	70.0	94.9	10.8	74.2	73.7	75.2	74.6	73.7
Or (K)	86.1	92.8	90.6	0.7	1.0	0.5	0.6	2.6	89.2	0.5	0.7	0.8	0.8	1.0

Appendix 2.2.2. b: Major element composition and mineral formulae for Feldspar from rocks of the high-grade study area (*continued*).

Sample no.	12/1 D a	12/1 D a	12/1 D a	12/1 D a	12/1 D a	12/1 D a	11/7 D	11/7 D	11/7 D matrix	11/7 D plag in qtz	11/7 D matrix	11/7 D	12_1A c	12_1A c
Analysis	kspar	kspar	kspar	plag	plag	fspar poik	plag in crd	plag in crd	plag	in gt	plag	large plag	plag	plag
SiO2	65.30	73.15	64.80	61.81	59.03	64.73	60.66	59.75	60.23	60.04	61.06	61.05	62.06	62.31
Al2O3	18.64	21.08	18.61	23.68	22.42	18.43	24.93	24.99	25.17	24.77	25.14	24.82	23.84	23.46
Fe2O3	0.04	0.04	0.00	0.06	0.01	0.08	0.11	0.15	0.12	0.14	0.12	0.07	0.00	0.00
CaO	0.00	0.00	0.00	5.26	4.99	0.00	6.92	7.03	7.05	6.86	6.80	6.93	5.30	5.37
Na2O	2.45	1.29	1.15	8.27	8.05	1.14	7.42	7.31	7.45	7.27	7.68	7.65	8.29	8.24
K2O	13.12	17.23	15.10	0.12	0.21	15.25	0.12	0.16	0.15	0.08	0.28	0.21	0.12	0.00
BaO	0.25	0.55	0.24	0.07	0.02	0.39	0.05	0.00	0.09	0.03	0.04	0.07	0.00	0.00
Total	**99.80**	**113.34**	**99.90**	**99.27**	**94.72**	**100.02**	**100.21**	**99.39**	**100.25**	**99.19**	**101.11**	**100.79**	**99.61**	**99.39**
Si	*2.99*	*2.98*	*2.99*	*2.76*	*2.76*	*2.99*	*2.69*	*2.68*	*2.68*	*2.69*	*2.69*	*2.70*	*2.76*	*2.77*
Al	*1.01*	*1.01*	*1.01*	*1.25*	*1.24*	*1.00*	*1.30*	*1.32*	*1.32*	*1.31*	*1.31*	*1.29*	*1.25*	*1.23*
Fe3+	*0.00*	*0.00*	*0.00*	*0.00*	*0.00*	*0.00*	*0.00*	*0.01*	*0.00*	*0.00*	*0.00*	*0.00*	*0.00*	*0.00*
Σ T-site	*4.00*	*4.00*	*4.00*	*4.00*	*4.00*	*4.00*	*4.00*	*4.00*	*4.00*	*4.00*	*4.00*	*3.99*	*4.01*	*4.00*
Ca	*0.00*	*0.00*	*0.00*	*0.25*	*0.25*	*0.00*	*0.33*	*0.34*	*0.34*	*0.33*	*0.32*	*0.33*	*0.25*	*0.26*
Na	*0.22*	*0.10*	*0.10*	*0.72*	*0.73*	*0.10*	*0.64*	*0.63*	*0.64*	*0.63*	*0.66*	*0.66*	*0.71*	*0.71*
K	*0.77*	*0.90*	*0.89*	*0.01*	*0.01*	*0.90*	*0.01*	*0.01*	*0.01*	*0.00*	*0.02*	*0.01*	*0.01*	*0.00*
Ba	*0.00*	*0.01*	*0.00*	*0.00*	*0.00*	*0.01*	*0.00*	*0.00*	*0.00*	*0.00*	*0.00*	*0.00*	*0.00*	*0.00*
Σ A-site	*0.99*	*1.01*	*1.00*	*0.97*	*0.99*	*1.01*	*0.98*	*0.98*	*0.99*	*0.97*	*0.99*	*1.00*	*0.97*	*0.97*
An (Ca)	0.0	0.0	0.0	25.8	25.2	0.0	33.8	34.4	34.0	34.1	32.3	33.0	25.9	26.5
Ab (Na)	22.1	10.2	10.4	73.5	73.5	10.2	65.5	64.7	65.1	65.4	66.1	65.8	73.4	73.5
Or (K)	77.9	89.8	89.6	0.7	1.3	89.8	0.7	0.9	0.9	0.5	1.6	1.2	0.7	0.0

Appendix 2.2.2. b: Major element composition and mineral formulae for Feldspar from rocks of the high-grade study area (*continued*).

Sample no.	12_1A c	KH1_1B	KH1_1B	KH1_1B	KH1_1B	KH1_1B	KH1_1B	KH1_1B	KHt2_2 c	KHt2_2 c	KHt2_2 c	KHt2_2 c	KHt2_2 c	KHt2_2 c
Analysis	plag	plag	plag	plag inclusion	plag	plag large	plag	plag	leucosome kspar	ternary feld	kspar	plag in ksp	leucosome plag	matrix kspar
SiO2	62.67	58.98	59.75	63.24	62.99	62.85	61.52	60.57	64.55	64.97	65.09	62.78	63.63	65.24
Al2O3	23.86	24.77	24.60	26.78	26.61	25.94	26.17	25.43	18.35	18.37	18.73	22.68	23.32	18.58
Fe2O3	0.00	0.00	0.00	0.00	0.00	0.00	0.19	0.00	0.00	0.00	0.00	0.00	0.00	0.00
CaO	5.30	6.61	5.73	7.26	7.24	6.72	7.07	6.88	0.00	0.00	0.00	4.49	4.51	0.00
Na2O	8.54	7.57	7.60	7.77	7.59	8.21	7.87	7.72	1.39	2.10	1.27	8.60	8.77	1.82
K2O	0.00	0.00	0.36	0.00	0.00	0.14	0.00	0.14	14.83	13.86	15.08	0.22	0.21	14.20
BaO	0.00	0.00	0.00	0.00	0.00	0.00	0.00	0.00	0.33	0.33	0.26	0.00	0.00	0.00
Total	**100.37**	**97.93**	**98.04**	**105.06**	**104.43**	**103.87**	**102.81**	**100.73**	**99.44**	**99.63**	**100.44**	**98.77**	**100.43**	**99.83**
Si	*2.76*	*2.68*	*2.71*	*2.68*	*2.68*	*2.69*	*2.66*	*2.68*	*2.99*	*3.00*	*2.99*	*2.81*	*2.80*	*3.00*
Al	*1.24*	*1.33*	*1.31*	*1.33*	*1.33*	*1.31*	*1.34*	*1.32*	*1.00*	*1.00*	*1.01*	*1.19*	*1.21*	*1.01*
Fe3+	*0.00*	*0.00*	*0.00*	*0.00*	*0.00*	*0.00*	*0.01*	*0.00*	*0.00*	*0.00*	*0.00*	*0.00*	*0.00*	*0.00*
Σ T-site	*4.00*	*4.00*	*4.02*	*4.01*	*4.01*	*4.00*	*4.01*	*4.00*	*4.00*	*4.00*	*4.00*	*4.00*	*4.01*	*4.00*
Ca	*0.25*	*0.32*	*0.28*	*0.33*	*0.33*	*0.31*	*0.33*	*0.33*	*0.00*	*0.00*	*0.00*	*0.21*	*0.21*	*0.00*
Na	*0.73*	*0.67*	*0.67*	*0.64*	*0.63*	*0.68*	*0.66*	*0.66*	*0.12*	*0.19*	*0.11*	*0.75*	*0.75*	*0.16*
K	*0.00*	*0.00*	*0.02*	*0.00*	*0.00*	*0.01*	*0.00*	*0.01*	*0.88*	*0.82*	*0.88*	*0.01*	*0.01*	*0.83*
Ba	*0.00*	*0.00*	*0.00*	*0.00*	*0.00*	*0.00*	*0.00*	*0.00*	*0.01*	*0.01*	*0.00*	*0.00*	*0.00*	*0.00*
Σ A-site	*0.98*	*0.99*	*0.97*	*0.97*	*0.96*	*1.00*	*0.99*	*0.99*	*1.01*	*1.01*	*1.00*	*0.97*	*0.97*	*0.99*
An (Ca)	25.5	32.5	28.8	34.0	34.5	30.9	33.2	32.7	0.0	0.0	0.0	22.1	21.9	0.0
Ab (Na)	74.5	67.5	69.1	66.0	65.5	68.3	66.8	66.5	12.5	18.7	11.3	76.6	76.9	16.3
Or (K)	0.0	0.0	2.2	0.0	0.0	0.8	0.0	0.8	87.5	81.3	88.7	1.3	1.2	83.7

Appendix 2.2.2. b: Major element composition and mineral formulae for Feldspar from rocks of the high-grade study area (*continued*).

Sample no.	KHt2_2 c	KHt2_2 c matrix	KHt2_2 h	KHt2_2 h	KHt2_2 h	KHt2_2 h	KHt2_2 h plag	KHt2_2 h matrix
Analysis	plag	ksp...	plag	**tern ksp**	plag	poik plag	matrix	plag
SiO2	63.14	65.66	63.78	65.21	63.11	62.75	63.88	63.95
Al2O3	22.59	18.69	23.30	18.60	22.79	23.34	23.24	23.28
Fe2O3	0.00	0.00	0.00	0.00	0.00	0.00	0.00	0.00
CaO	4.22	0.00	4.57	0.02	4.38	4.47	4.53	4.62
Na2O	8.96	2.33	8.74	1.81	8.71	9.00	8.83	8.79
K2O	0.00	13.19	0.18	14.38	0.14	0.00	0.18	0.13
BaO	0.00	0.00	0.00	0.00	0.00	0.00	0.00	0.00
Total	**98.91**	**99.87**	**100.57**	**100.03**	**99.13**	**99.57**	**100.64**	**100.78**
Si	*2.82*	*3.00*	*2.80*	*2.99*	*2.81*	*2.78*	*2.80*	*2.80*
Al	*1.19*	*1.01*	*1.21*	*1.01*	*1.20*	*1.22*	*1.20*	*1.20*
Fe3+	*0.00*	*0.00*	*0.00*	*0.00*	*0.00*	*0.00*	*0.00*	*0.00*
Σ T-site	*4.00*	*4.01*	*4.01*	*4.00*	*4.00*	*4.01*	*4.00*	*4.00*
Ca	*0.20*	*0.00*	*0.21*	*0.00*	*0.21*	*0.21*	*0.21*	*0.22*
Na	*0.77*	*0.21*	*0.74*	*0.16*	*0.75*	*0.77*	*0.75*	*0.75*
K	*0.00*	*0.77*	*0.01*	*0.84*	*0.01*	*0.00*	*0.01*	*0.01*
Ba	*0.00*	*0.00*	*0.00*	*0.00*	*0.00*	*0.00*	*0.00*	*0.00*
Σ A-site	*0.98*	*0.98*	*0.97*	*1.00*	*0.97*	*0.99*	*0.97*	*0.97*
An (Ca)	20.7	0.0	22.2	0.1	21.6	21.5	21.9	22.4
Ab (Na)	79.3	21.2	76.8	16.1	77.6	78.5	77.1	76.9
Or (K)	0.0	78.8	1.0	83.8	0.8	0.0	1.0	0.8

Appendix 2.2.3. a: Major element composition and mineral formulae for Cordierite from the low-grade equivalent rocks.

Sample	USK-1D	USK-1D	USK-1D	USK-1D	USK-2B	USK-2B	USK-2B	USK-5C	USK-5C crd near rim	USK-5C cord near core	USK-5C crd core	USK-5C crd rim	USK-5C crd near rim	USK-5C crd near core
Analysis	cord	cord	crd rim	crd core	crd	crd	crd	cord rim						
SiO2	48.11	48.17	48.90	48.47	48.89	48.92	48.58	47.93	48.69	48.95	48.49	48.97	49.02	48.92
TiO2	0.00	0.00	0.00	0.00	0.00	0.00	0.03	0.00	0.01	0.02	0.00	0.05	0.05	0.00
Al2O3	32.35	32.35	32.98	32.43	32.90	32.97	32.95	32.40	32.96	33.23	32.65	32.84	32.92	32.78
Fe2O3	0.61	0.63	0.54	0.50	0.40	0.23	0.81	1.20	0.84	0.25	0.62	0.51	0.00	1.11
FeO	7.71	7.79	8.04	7.99	7.60	7.61	7.15	7.20	7.56	7.81	7.67	7.85	8.23	7.40
MnO	0.44	0.49	0.46	0.49	1.06	1.12	1.14	0.43	0.51	0.48	0.50	0.41	0.47	0.42
MgO	8.32	8.27	8.33	8.27	8.26	8.24	8.30	8.47	8.46	8.46	8.40	8.53	8.31	8.69
CaO	0.00	0.00	0.00	0.02	0.00	0.00	0.01	0.00	0.02	0.02	0.00	0.01	0.02	0.00
Na2O	0.61	0.61	0.48	0.52	0.62	0.58	0.60	0.43	0.45	0.48	0.47	0.41	0.57	0.53
K2O	0.00	0.00	0.00	0.00	0.00	0.00	0.02	0.00	0.00	0.02	0.00	0.00	0.00	0.00
Total	98.15	98.30	99.72	98.69	99.73	99.67	99.59	98.06	99.50	99.71	98.80	99.58	99.59	99.85
Si	*5.00*	*5.00*	*4.99*	*5.01*	*5.00*	*5.00*	*4.98*	*4.97*	*4.98*	*4.99*	*4.99*	*5.00*	*5.01*	*4.99*
AlIV	*1.00*	*1.00*	*1.01*	*0.99*	*1.00*	*1.00*	*1.02*	*1.03*	*1.02*	*1.01*	*1.01*	*1.00*	*0.99*	*1.01*
Σ T-site	*6.00*	*6.00*	*6.00*	*6.00*	*6.00*	*6.00*	*6.00*	*6.00*	*6.00*	*6.00*	*6.00*	*6.00*	*6.00*	*6.00*
AlVI	*2.96*	*2.95*	*2.96*	*2.95*	*2.97*	*2.98*	*2.96*	*2.93*	*2.95*	*2.99*	*2.96*	*2.95*	*2.98*	*2.93*
Ti	*0.00*	*0.00*	*0.00*	*0.00*	*0.00*	*0.00*	*0.00*	*0.00*	*0.00*	*0.00*	*0.00*	*0.00*	*0.00*	*0.00*
Fe3+	*0.05*	*0.05*	*0.04*	*0.04*	*0.03*	*0.02*	*0.06*	*0.09*	*0.06*	*0.02*	*0.05*	*0.04*	*0.00*	*0.09*
Σ M-site	*3.00*	*3.00*	*3.01*	*2.99*	*3.00*	*3.00*	*3.02*	*3.03*	*3.02*	*3.01*	*3.01*	*3.00*	*2.99*	*3.01*
Mg	*1.29*	*1.28*	*1.27*	*1.27*	*1.26*	*1.26*	*1.27*	*1.31*	*1.29*	*1.29*	*1.29*	*1.30*	*1.27*	*1.32*
Fe2+	*0.67*	*0.68*	*0.69*	*0.69*	*0.65*	*0.65*	*0.61*	*0.62*	*0.65*	*0.67*	*0.66*	*0.67*	*0.70*	*0.63*
Mn	*0.04*	*0.04*	*0.04*	*0.04*	*0.09*	*0.10*	*0.10*	*0.04*	*0.04*	*0.04*	*0.04*	*0.04*	*0.04*	*0.04*
Σ A-site	*2.00*	*2.00*	*1.99*	*2.01*	*2.00*	*2.00*	*1.98*	*1.97*	*1.98*	*1.99*	*1.99*	*2.00*	*2.01*	*1.99*
Ca	*0.00*	*0.00*	*0.00*	*0.00*	*0.00*	*0.00*	*0.00*	*0.00*	*0.00*	*0.00*	*0.00*	*0.00*	*0.00*	*0.00*
Na	*0.12*	*0.12*	*0.10*	*0.10*	*0.12*	*0.12*	*0.12*	*0.09*	*0.09*	*0.09*	*0.09*	*0.08*	*0.11*	*0.10*
K	*0.00*	*0.00*	*0.00*	*0.00*	*0.00*	*0.00*	*0.00*	*0.00*	*0.00*	*0.00*	*0.00*	*0.00*	*0.00*	*0.00*
Σ Channel cations	*0.12*	*0.12*	*0.10*	*0.11*	*0.12*	*0.12*	*0.12*	*0.09*	*0.09*	*0.10*	*0.09*	*0.08*	*0.12*	*0.10*
Mg#	66	65	65	65	66	66	67	68	67	66	66	66	64	68

Appendix 2.2.3. a: Major element composition and mineral formulae for Cordierite from the low-grade equivalent rocks (*continued*).

Sample	USK-5C	USK-6A	USK-6A	USK-6A crd near	USK-6A	USK-6A	USK-6A crd near	USK-6A crd near	USK-6A	USK-7B crd near	USK-7B
Analysis	crd core	crd rim	crd rim	rim	crd core	crd rim	rim	core	crd core	rim	crd
SiO2	48.85	48.18	48.70	48.83	48.78	49.27	48.59	49.25	49.30	49.55	48.21
TiO2	0.01	0.00	0.00	0.00	0.00	0.01	0.00	0.03	0.00	0.00	0.00
Al2O3	33.00	32.52	32.71	32.72	32.98	33.29	32.77	33.20	33.37	33.46	32.54
Fe2O3	0.71	0.74	0.51	0.29	0.51	0.47	0.62	0.16	0.42	0.51	0.29
FeO	7.65	7.73	7.98	8.00	7.95	8.06	8.01	8.24	7.84	8.21	8.08
MnO	0.49	0.43	0.50	0.47	0.45	0.42	0.48	0.50	0.53	0.22	0.30
MgO	8.49	8.30	8.31	8.39	8.34	8.44	8.24	8.34	8.50	8.54	8.24
CaO	0.06	0.02	0.03	0.00	0.03	0.01	0.00	0.01	0.02	0.01	0.00
Na2O	0.49	0.58	0.59	0.67	0.65	0.58	0.56	0.67	0.66	0.47	0.39
K2O	0.00	0.00	0.00	0.00	0.00	0.00	0.01	0.00	0.00	0.00	0.03
Total	99.75	98.49	99.33	99.37	99.69	100.55	99.28	100.40	100.64	100.97	98.08
Si	*4.99*	*4.99*	*5.00*	*5.01*	*4.99*	*4.99*	*4.99*	*5.00*	*4.99*	*4.99*	*5.00*
AlIV	*1.01*	*1.01*	*1.00*	*0.99*	*1.01*	*1.01*	*1.01*	*1.00*	*1.01*	*1.01*	*1.00*
Σ T-site	*6.00*	*6.00*	*6.00*	*6.00*	*6.00*	*6.00*	*6.00*	*6.00*	*6.00*	*6.00*	*6.00*
AlVI	*2.96*	*2.96*	*2.96*	*2.97*	*2.97*	*2.97*	*2.96*	*2.98*	*2.98*	*2.97*	*2.98*
Ti	*0.00*	*0.00*	*0.00*	*0.00*	*0.00*	*0.00*	*0.00*	*0.00*	*0.00*	*0.00*	*0.00*
Fe3+	*0.05*	*0.06*	*0.04*	*0.02*	*0.04*	*0.04*	*0.05*	*0.01*	*0.03*	*0.04*	*0.02*
Σ M-site	*3.01*	*3.01*	*3.00*	*2.99*	*3.01*	*3.01*	*3.01*	*2.99*	*3.01*	*3.01*	*3.00*
Mg	*1.29*	*1.28*	*1.27*	*1.28*	*1.27*	*1.28*	*1.26*	*1.26*	*1.28*	*1.28*	*1.27*
Fe2+	*0.65*	*0.67*	*0.69*	*0.69*	*0.68*	*0.68*	*0.69*	*0.70*	*0.66*	*0.69*	*0.70*
Mn	*0.04*	*0.04*	*0.04*	*0.04*	*0.04*	*0.04*	*0.04*	*0.04*	*0.05*	*0.02*	*0.03*
Σ A-site	*1.99*	*1.99*	*2.00*	*2.01*	*1.99*	*1.99*	*1.99*	*2.01*	*1.99*	*1.99*	*2.00*
Ca	*0.01*	*0.00*	*0.00*	*0.00*	*0.00*	*0.00*	*0.00*	*0.00*	*0.00*	*0.00*	*0.00*
Na	*0.10*	*0.12*	*0.12*	*0.13*	*0.13*	*0.11*	*0.11*	*0.13*	*0.13*	*0.09*	*0.08*
K	*0.00*	*0.00*	*0.00*	*0.00*	*0.00*	*0.00*	*0.00*	*0.00*	*0.00*	*0.00*	*0.00*
Σ Channel cations	*0.10*	*0.12*	*0.12*	*0.13*	*0.13*	*0.12*	*0.11*	*0.13*	*0.13*	*0.09*	*0.08*
Mg#	66	66	65	65	65	65	65	64	66	65	65

Appendix 2.2.3. b: Major element composition and mineral formulae for Cordierite from rocks of the high-grade study area.

Sample	Misc A 1	Misc A 1	Misc A 1	Misc A 1	KH-1_3 B2	KH-1_3 B2	KH-1_3 B3	KH-1_3 B4	KH_1-2 Spectrum 2	KH_1-2	KH_1-2	12/1 D a	12/1 D a	12/1 D a
Analysis	cord?	cord	cord	cord	cord	more cord	cord	cord		cord?	Cordierite	cord!	crd	crd
SiO2	49.15	48.63	49.06	48.00	50.09	49.92	49.22	50.20	51.25	48.89	50.90	47.56	47.29	48.07
TiO2	0.04	0.01	0.00	0.03	0.00	0.00	0.00	0.00	0.00	0.00	0.00	0.04	0.08	0.04
Al2O3	33.38	32.80	33.18	32.48	32.99	32.81	32.45	32.98	32.99	31.57	32.41	32.21	32.32	32.74
Fe2O3	1.94	1.88	1.59	1.97	0.00	0.00	0.00	0.00	0.00	0.00	0.00	2.98	3.12	2.65
FeO	8.04	8.06	8.21	7.79	8.74	9.03	9.06	8.90	9.14	8.85	9.49	8.94	8.87	9.11
MnO	0.36	0.41	0.34	0.40	0.10	0.09	0.12	0.12	0.03	0.02	0.03	0.81	0.76	0.76
MgO	8.27	8.13	8.21	8.10	7.99	8.02	7.78	8.08	7.81	7.57	7.63	6.99	6.93	7.06
CaO	0.00	0.00	0.00	0.03	0.00	0.00	0.00	0.00	0.04	0.04	0.05	0.00	0.03	0.01
Na2O	0.39	0.37	0.37	0.30	0.34	0.39	0.40	0.37	0.00	0.00	0.00	0.47	0.37	0.45
K2O	0.00	0.01	0.02	0.00	0.00	0.00	0.00	0.00	0.03	0.00	0.00	0.00	0.00	0.02
Total	101.57	100.30	100.98	99.09	100.25	100.26	99.03	100.65	101.29	96.94	100.50	100.00	99.77	100.92
Si	*4.94*	*4.96*	*4.96*	*4.95*	*5.09*	*5.08*	*5.07*	*5.08*	*5.15*	*5.13*	*5.16*	*4.92*	*4.90*	*4.92*
AlIV	*1.06*	*1.04*	*1.04*	*1.05*	*0.91*	*0.92*	*0.93*	*0.92*	*0.85*	*0.87*	*0.84*	*1.08*	*1.10*	*1.08*
Σ T-site	*6.00*	*6.00*	*6.00*	*6.00*	*6.00*	*6.00*	*6.00*	*6.00*	*6.00*	*6.00*	*6.00*	*6.00*	*6.00*	*6.00*
AlVI	*2.90*	*2.90*	*2.92*	*2.89*	*3.04*	*3.01*	*3.01*	*3.02*	*3.06*	*3.04*	*3.04*	*2.84*	*2.84*	*2.87*
Ti	*0.00*	*0.00*	*0.00*	*0.00*	*0.00*	*0.00*	*0.00*	*0.00*	*0.00*	*0.00*	*0.00*	*0.00*	*0.01*	*0.00*
Fe3+	*0.15*	*0.14*	*0.12*	*0.15*	*0.00*	*0.00*	*0.00*	*0.00*	*0.00*	*0.00*	*0.00*	*0.23*	*0.24*	*0.20*
Σ M-site	*3.05*	*3.04*	*3.04*	*3.05*	*3.04*	*3.01*	*3.01*	*3.02*	*3.06*	*3.04*	*3.04*	*3.08*	*3.09*	*3.08*
Mg	*1.24*	*1.24*	*1.24*	*1.24*	*1.21*	*1.22*	*1.20*	*1.22*	*1.17*	*1.18*	*1.15*	*1.08*	*1.07*	*1.08*
Fe2+	*0.68*	*0.69*	*0.69*	*0.67*	*0.74*	*0.77*	*0.78*	*0.75*	*0.77*	*0.78*	*0.80*	*0.77*	*0.77*	*0.78*
Mn	*0.03*	*0.04*	*0.03*	*0.03*	*0.01*	*0.01*	*0.01*	*0.01*	*0.00*	*0.00*	*0.00*	*0.07*	*0.07*	*0.07*
Σ A-site	*1.95*	*1.96*	*1.96*	*1.95*	*1.96*	*1.99*	*1.99*	*1.98*	*1.94*	*1.96*	*1.96*	*1.92*	*1.91*	*1.92*
Ca	*0.00*	*0.00*	*0.00*	*0.00*	*0.00*	*0.00*	*0.00*	*0.00*	*0.00*	*0.00*	*0.01*	*0.00*	*0.00*	*0.00*
Na	*0.08*	*0.07*	*0.07*	*0.06*	*0.07*	*0.08*	*0.08*	*0.07*	*0.00*	*0.00*	*0.00*	*0.09*	*0.07*	*0.09*
K	*0.00*	*0.00*	*0.00*	*0.00*	*0.00*	*0.00*	*0.00*	*0.00*	*0.00*	*0.00*	*0.00*	*0.00*	*0.00*	*0.00*
Σ Channel cations	*0.08*	*0.07*	*0.07*	*0.06*	*0.07*	*0.08*	*0.08*	*0.07*	*0.01*	*0.00*	*0.01*	*0.09*	*0.08*	*0.09*
Mg#	65	64	64	65	62	61	60	62	60	60	59	58	58	58

Appendix 2.2.3. b: Major element composition and mineral formulae for Cordierite from rocks of the high-grade study area (*continued*).

Sample	12/1 D a	12/1 D a	12/1 D a	14/5 A	14/5 A	14/5 A	14/5 A	14/5 A	14/5 A	14/5 A	11/7 D	11/7 D	11/7 D	11/7 D
Analysis	crd	crd	crd	crd	crd	crd poik	crd adjacent gt	crd adjacent gt	crd poik 2	crd poik 3	crd	crd	crd	crd
SiO2	46.96	48.02	48.22	47.32	47.80	48.46	48.55	48.67	48.56	48.52	47.96	48.60	48.40	49.06
TiO2	0.01	0.03	0.00	0.02	0.06	0.00	0.04	0.00	0.00	0.03	0.00	0.00	0.00	0.00
Al2O3	32.19	32.69	32.55	32.01	32.96	32.82	32.83	33.06	32.83	32.98	32.37	32.82	32.79	33.11
Fe2O3	2.64	2.28	2.17	2.43	2.76	2.35	2.40	2.63	2.31	2.30	2.13	2.48	1.90	2.21
FeO	9.01	9.73	9.37	7.61	7.44	7.86	7.97	7.49	7.91	8.03	6.69	6.68	6.91	6.79
MnO	0.79	0.74	0.88	0.55	0.46	0.53	0.42	0.46	0.45	0.38	0.68	0.59	0.59	0.61
MgO	6.76	6.75	6.98	7.88	8.02	8.05	8.09	8.31	8.11	8.05	8.53	8.72	8.58	8.80
CaO	0.04	0.01	0.00	0.01	0.00	0.00	0.00	0.00	0.05	0.00	0.01	0.02	0.00	0.01
Na2O	0.38	0.45	0.42	0.31	0.32	0.35	0.36	0.35	0.35	0.35	0.28	0.24	0.37	0.35
K2O	0.00	0.00	0.00	0.00	0.00	0.01	0.01	0.00	0.00	0.00	0.01	0.00	0.00	0.00
Total	98.78	100.71	100.59	98.13	99.83	100.44	100.67	100.96	100.57	100.64	98.66	100.15	99.54	100.94
Si	*4.91*	*4.93*	*4.95*	*4.94*	*4.90*	*4.94*	*4.94*	*4.93*	*4.94*	*4.93*	*4.95*	*4.94*	*4.95*	*4.95*
AlIV	*1.09*	*1.07*	*1.05*	*1.06*	*1.10*	*1.06*	*1.06*	*1.07*	*1.06*	*1.07*	*1.05*	*1.06*	*1.05*	*1.05*
Σ T-site	*6.00*	*6.00*	*6.00*	*6.00*	*6.00*	*6.00*	*6.00*	*6.00*	*6.00*	*6.00*	*6.00*	*6.00*	*6.00*	*6.00*
AlVI	*2.88*	*2.89*	*2.88*	*2.87*	*2.88*	*2.88*	*2.87*	*2.87*	*2.88*	*2.89*	*2.89*	*2.87*	*2.90*	*2.88*
Ti	*0.00*	*0.00*	*0.00*	*0.00*	*0.00*	*0.00*	*0.00*	*0.00*	*0.00*	*0.00*	*0.00*	*0.00*	*0.00*	*0.00*
Fe3+	*0.21*	*0.18*	*0.17*	*0.19*	*0.21*	*0.18*	*0.18*	*0.20*	*0.18*	*0.18*	*0.17*	*0.19*	*0.15*	*0.17*
Σ M-site	*3.09*	*3.07*	*3.05*	*3.06*	*3.10*	*3.06*	*3.06*	*3.07*	*3.06*	*3.06*	*3.05*	*3.06*	*3.05*	*3.05*
Mg	*1.05*	*1.03*	*1.07*	*1.23*	*1.23*	*1.22*	*1.23*	*1.25*	*1.23*	*1.22*	*1.31*	*1.32*	*1.31*	*1.32*
Fe2+	*0.79*	*0.84*	*0.80*	*0.66*	*0.64*	*0.67*	*0.68*	*0.63*	*0.67*	*0.68*	*0.58*	*0.57*	*0.59*	*0.57*
Mn	*0.07*	*0.06*	*0.08*	*0.05*	*0.04*	*0.05*	*0.04*	*0.04*	*0.04*	*0.03*	*0.06*	*0.05*	*0.05*	*0.05*
Σ A-site	*1.91*	*1.93*	*1.95*	*1.94*	*1.90*	*1.94*	*1.94*	*1.93*	*1.94*	*1.94*	*1.95*	*1.94*	*1.95*	*1.95*
Ca	*0.00*	*0.00*	*0.00*	*0.00*	*0.00*	*0.00*	*0.00*	*0.00*	*0.01*	*0.00*	*0.00*	*0.00*	*0.00*	*0.00*
Na	*0.08*	*0.09*	*0.08*	*0.06*	*0.06*	*0.07*	*0.07*	*0.07*	*0.07*	*0.07*	*0.06*	*0.05*	*0.07*	*0.07*
K	*0.00*	*0.00*	*0.00*	*0.00*	*0.00*	*0.00*	*0.00*	*0.00*	*0.00*	*0.00*	*0.00*	*0.00*	*0.00*	*0.00*
Σ Channel cations	*0.08*	*0.09*	*0.08*	*0.06*	*0.06*	*0.07*	*0.07*	*0.07*	*0.07*	*0.07*	*0.06*	*0.05*	*0.07*	*0.07*
Mg#	57	55	57	65	66	65	64	66	65	64	69	70	69	70

Appendix 2.2.3. b: Major element composition and mineral formulae for Cordierite from rocks of the high-grade study area (*continued*).

Sample	14_2 gem Crd	14_2 gem Crd	14_2 gem Crd	14_2 gem Crd	11_1stub	11_1stub	11_1stub	11_1stub	12_1A c	12_1A c	12_1A c crd near core	12_1A c	12_1A c crd near rim	KH1_1B
Analysis	crd	crd	crd	crd	crd	crd	crd	crd	crd	crd		crd		cord
SiO2	47.49	48.07	48.54	47.85	49.73	49.97	50.40	49.94	50.13	50.77	50.79	50.67	50.46	51.90
TiO2	0.00	0.00	0.00	0.00	0.00	0.00	0.00	0.00	0.00	0.00	0.00	0.00	0.00	0.00
Al2O3	32.40	32.41	32.72	32.34	30.95	31.41	31.45	30.95	31.39	32.01	32.03	32.01	31.67	34.80
Fe2O3	2.59	2.57	2.34	2.30	0.00	0.00	0.00	0.00	0.00	0.00	0.00	0.00	0.00	0.00
FeO	7.71	7.78	7.93	7.96	10.11	10.50	10.27	10.20	9.14	9.26	9.30	9.18	8.73	7.07
MnO	0.40	0.45	0.47	0.38	0.43	0.44	0.38	0.47	0.45	0.58	0.50	0.50	0.48	0.21
MgO	7.88	8.03	8.09	7.94	7.26	7.49	7.31	7.32	7.58	7.52	7.56	7.67	7.61	6.98
CaO	0.00	0.00	0.00	0.00	0.00	0.00	0.00	0.00	0.00	0.00	0.00	0.00	0.00	0.00
Na2O	0.35	0.41	0.36	0.38	0.39	0.40	0.33	0.39	0.00	0.50	0.55	0.55	0.56	0.70
K2O	0.00	0.00	0.00	0.00	0.00	0.00	0.00	0.00	0.00	0.00	0.00	0.00	0.00	2.43
Total	98.82	99.73	100.44	99.14	98.86	100.21	100.14	99.28	98.70	100.63	100.74	100.58	99.51	104.09
Si	*4.92*	*4.94*	*4.95*	*4.94*	*5.17*	*5.12*	*5.17*	*5.17*	*5.18*	*5.17*	*5.17*	*5.16*	*5.20*	*5.22*
AlIV	*1.08*	*1.06*	*1.05*	*1.06*	*0.83*	*0.88*	*0.83*	*0.83*	*0.82*	*0.83*	*0.83*	*0.84*	*0.80*	*0.78*
Σ T-site	*6.00*	*6.00*	*6.00*	*6.00*	*6.00*	*6.00*	*6.00*	*6.00*	*6.00*	*6.00*	*6.00*	*6.00*	*6.00*	*6.00*
AlVI	*2.88*	*2.86*	*2.87*	*2.88*	*2.96*	*2.92*	*2.97*	*2.95*	*3.00*	*3.02*	*3.02*	*3.01*	*3.04*	*3.34*
Ti	*0.00*	*0.00*	*0.00*	*0.00*	*0.00*	*0.00*	*0.00*	*0.00*	*0.00*	*0.00*	*0.00*	*0.00*	*0.00*	*0.00*
Fe3+	*0.20*	*0.20*	*0.18*	*0.18*	*0.00*	*0.00*	*0.00*	*0.00*	*0.00*	*0.00*	*0.00*	*0.00*	*0.00*	*0.00*
Σ M-site	*3.08*	*3.06*	*3.05*	*3.06*	*2.96*	*2.92*	*2.97*	*2.95*	*3.00*	*3.02*	*3.02*	*3.01*	*3.04*	*3.34*
Mg	*1.22*	*1.23*	*1.23*	*1.22*	*1.12*	*1.14*	*1.12*	*1.13*	*1.17*	*1.14*	*1.15*	*1.17*	*1.17*	*1.05*
Fe2+	*0.67*	*0.67*	*0.68*	*0.69*	*0.88*	*0.90*	*0.88*	*0.88*	*0.79*	*0.79*	*0.79*	*0.78*	*0.75*	*0.59*
Mn	*0.04*	*0.04*	*0.04*	*0.03*	*0.04*	*0.04*	*0.03*	*0.04*	*0.04*	*0.05*	*0.04*	*0.04*	*0.04*	*0.02*
Σ A-site	*1.92*	*1.94*	*1.95*	*1.94*	*2.04*	*2.08*	*2.03*	*2.05*	*2.00*	*1.98*	*1.98*	*1.99*	*1.96*	*1.66*
Ca	*0.00*	*0.00*	*0.00*	*0.00*	*0.00*	*0.00*	*0.00*	*0.00*	*0.00*	*0.00*	*0.00*	*0.00*	*0.00*	*0.00*
Na	*0.07*	*0.08*	*0.07*	*0.08*	*0.08*	*0.08*	*0.07*	*0.08*	*0.00*	*0.10*	*0.11*	*0.11*	*0.11*	*0.14*
K	*0.00*	*0.00*	*0.00*	*0.00*	*0.00*	*0.00*	*0.00*	*0.00*	*0.00*	*0.00*	*0.00*	*0.00*	*0.00*	*0.31*
Σ Channel cations	*0.07*	*0.08*	*0.07*	*0.08*	*0.08*	*0.08*	*0.07*	*0.08*	*0.00*	*0.10*	*0.11*	*0.11*	*0.11*	*0.45*
Mg#	65	65	65	64	56	56	56	56	60	59	59	60	61	64

Appendix 2.2.3. b: Major element composition and mineral formulae for Cordierite from rocks of the high-grade study area (*continued*).

Sample	KH1_1B	KH1_1B	KH1_1B	KH1_1B	KHt2_2 c	KHt2_2 c	KHt2_2 c	KHt2_2 c	KHt2_2 c	KHt2_2 c	KHt2_2 c	KHt2_2 c	KHt2_2 c	KHt2_2 c	KHt2_2 h	KHt2_2 h	KHt2_2 h	KHt2_2 h
Analysis	cordierite	cord fresh	Fresh cord	cord	leucosome crd? hydrated	leucosome crd	matric crd	matric crd	leucosome crd	leucosome crd? hydrated	leucosome crd	matric crd	matric crd	leucosome crd	crd	crd poik	crd poik	crd poik
SiO2	50.29	50.80	49.86	50.48	47.56	47.81	47.60	47.52	47.27	49.94	49.70	50.14	50.99	50.45	50.63	50.83	50.19	50.67
TiO2	0.00	0.00	0.00	0.00	0.00	0.00	0.00	0.00	0.00	0.00	0.00	0.00	0.00	0.00	0.00	0.00	0.00	0.00
Al2O3	33.46	34.20	33.59	34.15	32.44	32.37	32.06	32.02	31.89	31.60	31.22	31.33	31.87	31.58	31.66	31.60	31.55	31.63
Fe2O3	0.00	0.03	0.00	0.53	3.03	2.35	2.20	2.41	2.52	0.00	0.00	0.00	0.00	0.00	0.00	0.00	0.00	0.00
FeO	7.80	8.82	8.65	8.30	7.37	8.35	8.77	8.65	8.18	9.89	10.15	10.56	10.83	10.40	9.62	9.83	9.46	9.83
MnO	0.00	0.16	0.00	0.19	0.34	0.31	0.49	0.50	0.44	0.33	0.30	0.48	0.50	0.44	0.49	0.34	0.36	0.32
MgO	7.45	8.64	8.46	8.74	8.08	7.73	7.38	7.40	7.60	7.89	7.47	7.23	7.38	7.54	7.80	7.77	7.61	7.55
CaO	0.00	0.00	0.00	0.00	0.00	0.00	0.00	0.00	0.00	0.00	0.00	0.00	0.00	0.00	0.00	0.00	0.00	0.00
Na2O	0.36	0.00	0.36	0.39	0.32	0.32	0.43	0.00	0.39	0.32	0.31	0.42	0.00	0.38	0.34	0.28	0.37	0.33
K2O	1.70	0.00	0.00	0.00	0.00	0.00	0.00	0.00	0.00	0.00	0.00	0.00	0.00	0.00	0.00	0.00	0.21	0.00
Total	101.07	102.64	100.91	102.77	99.15	99.23	98.93	98.49	98.30	99.97	99.15	100.17	101.56	100.79	100.53	100.65	99.76	100.32
Si	*5.15*	*5.01*	*5.02*	*4.99*	*4.91*	*4.94*	*4.95*	*4.94*	*4.94*	*5.11*	*5.14*	*5.15*	*5.14*	*5.14*	*5.16*	*5.17*	*5.16*	*5.18*
AlIV	*0.85*	*0.99*	*0.98*	*1.01*	*1.09*	*1.06*	*1.05*	*1.06*	*1.06*	*0.89*	*0.86*	*0.85*	*0.86*	*0.86*	*0.84*	*0.83*	*0.84*	*0.82*
Σ T-site	*6.00*	*6.00*	*6.00*	*6.00*	*6.00*	*6.00*	*6.00*	*6.00*	*6.00*	*6.00*	*6.00*	*6.00*	*6.00*	*6.00*	*6.00*	*6.00*	*6.00*	*6.00*
AlVI	*3.19*	*2.99*	*3.00*	*2.97*	*2.86*	*2.88*	*2.88*	*2.87*	*2.86*	*2.92*	*2.94*	*2.94*	*2.93*	*2.93*	*2.96*	*2.96*	*2.99*	*2.98*
Ti	*0.00*	*0.00*	*0.00*	*0.00*	*0.00*	*0.00*	*0.00*	*0.00*	*0.00*	*0.00*	*0.00*	*0.00*	*0.00*	*0.00*	*0.00*	*0.00*	*0.00*	*0.00*
Fe3+	*0.00*	*0.00*	*0.00*	*0.04*	*0.24*	*0.18*	*0.17*	*0.19*	*0.20*	*0.00*	*0.00*	*0.00*	*0.00*	*0.00*	*0.00*	*0.00*	*0.00*	*0.00*
Σ M-site	*3.19*	*2.99*	*3.00*	*3.01*	*3.09*	*3.06*	*3.05*	*3.06*	*3.06*	*2.92*	*2.94*	*2.94*	*2.93*	*2.93*	*2.96*	*2.96*	*2.99*	*2.98*
Mg	*1.14*	*1.27*	*1.27*	*1.29*	*1.24*	*1.19*	*1.14*	*1.15*	*1.18*	*1.20*	*1.15*	*1.11*	*1.11*	*1.15*	*1.18*	*1.18*	*1.17*	*1.15*
Fe2+	*0.67*	*0.73*	*0.73*	*0.69*	*0.64*	*0.72*	*0.76*	*0.75*	*0.71*	*0.85*	*0.88*	*0.91*	*0.91*	*0.89*	*0.82*	*0.84*	*0.81*	*0.84*
Mn	*0.00*	*0.01*	*0.00*	*0.02*	*0.03*	*0.03*	*0.04*	*0.04*	*0.04*	*0.03*	*0.03*	*0.04*	*0.04*	*0.04*	*0.04*	*0.03*	*0.03*	*0.03*
Σ A-site	*1.81*	*2.01*	*2.00*	*1.99*	*1.91*	*1.94*	*1.95*	*1.94*	*1.94*	*2.08*	*2.06*	*2.06*	*2.07*	*2.07*	*2.04*	*2.04*	*2.01*	*2.02*
Ca	*0.00*	*0.00*	*0.00*	*0.00*	*0.00*	*0.00*	*0.00*	*0.00*	*0.00*	*0.00*	*0.00*	*0.00*	*0.00*	*0.00*	*0.00*	*0.00*	*0.00*	*0.00*
Na	*0.07*	*0.00*	*0.07*	*0.07*	*0.06*	*0.06*	*0.09*	*0.00*	*0.08*	*0.06*	*0.06*	*0.08*	*0.00*	*0.08*	*0.07*	*0.06*	*0.07*	*0.07*
K	*0.22*	*0.00*	*0.00*	*0.00*	*0.00*	*0.00*	*0.00*	*0.00*	*0.00*	*0.00*	*0.00*	*0.00*	*0.00*	*0.00*	*0.00*	*0.00*	*0.03*	*0.00*
Σ Channel cations	*0.29*	*0.00*	*0.07*	*0.07*	*0.06*	*0.06*	*0.09*	*0.00*	*0.08*	*0.06*	*0.06*	*0.08*	*0.00*	*0.08*	*0.07*	*0.06*	*0.10*	*0.07*
Mg#	63	64	64	65	66	62	60	60	62	59	57	55	55	56	59	59	59	58

Appendix 2.2.4. a: Major element composition and mineral formulae for Biotite from the low-grade equivalent rocks.

Sample no.	USK-1D	USK-1D	USK-1D	USK-2B	USK-2B	USK-2B	USK-3D	USK-3D	USK-4A Bottom Bed	USK-4A Bottom Bed	USK-4A Middle Bed	USK-4A Middle Bed	USK-4A Middle Bed
Analysis	bio incl	matrix bio	bio in crd	bio	bio	bio in crd	bio	bio in musc	bio in ksp	bio	bio	bio	bio
SiO2	35.06	36.54	36.89	36.36	36.99	37.74	36.97	37.43	36.72	36.98	36.50	36.85	36.89
TiO2	2.36	2.49	2.69	2.43	2.55	2.24	2.63	2.52	2.27	2.68	2.53	2.18	2.30
Al2O3	20.10	20.63	20.78	21.12	21.39	21.98	20.07	20.59	20.69	20.64	20.57	20.81	20.54
FeO	18.48	18.30	18.92	17.02	17.56	18.21	16.64	15.48	17.30	17.68	17.10	17.04	17.11
MnO	0.15	0.21	0.19	0.31	0.38	0.33	0.17	0.18	0.18	0.20	0.16	0.22	0.17
MgO	9.09	9.60	9.47	9.41	9.78	9.80	10.60	11.05	9.54	9.70	9.71	10.26	9.99
Na2O	0.36	0.40	0.43	0.32	0.24	0.24	0.25	0.22	0.23	0.26	0.21	0.26	0.25
K2O	8.99	9.15	9.30	9.25	9.46	9.46	9.57	9.73	9.55	9.62	9.48	9.52	9.33
Total	**94.58**	**97.32**	**98.66**	**96.22**	**98.34**	**100.01**	**96.90**	**97.19**	**96.48**	**97.76**	**96.24**	**97.15**	**96.58**
Si (5-6)	*5.34*	*5.38*	*5.37*	*5.39*	*5.37*	*5.39*	*5.44*	*5.45*	*5.44*	*5.41*	*5.41*	*5.41*	*5.44*
AlIV (3-2)	*2.66*	*2.62*	*2.63*	*2.61*	*2.63*	*2.61*	*2.56*	*2.55*	*2.56*	*2.59*	*2.59*	*2.59*	*2.56*
Σ T-site	***8.00***	***8.00***	***8.00***	***8.00***	***8.00***	***8.00***	***8.00***	***8.00***	***8.00***	***8.00***	***8.00***	***8.00***	***8.00***
AlVI	*0.95*	*0.97*	*0.94*	*1.08*	*1.03*	*1.09*	*0.92*	*0.99*	*1.05*	*0.97*	*1.01*	*1.01*	*1.02*
Ti	*0.27*	*0.28*	*0.29*	*0.27*	*0.28*	*0.24*	*0.29*	*0.28*	*0.25*	*0.30*	*0.28*	*0.24*	*0.26*
Σ XX-site (0-2)	***1.22***	***1.24***	***1.24***	***1.35***	***1.31***	***1.33***	***1.21***	***1.26***	***1.30***	***1.27***	***1.29***	***1.25***	***1.27***
Fe2+	*2.35*	*2.25*	*2.30*	*2.11*	*2.13*	*2.17*	*2.05*	*1.88*	*2.14*	*2.16*	*2.12*	*2.09*	*2.11*
Mn	*0.02*	*0.03*	*0.02*	*0.04*	*0.05*	*0.04*	*0.02*	*0.02*	*0.02*	*0.02*	*0.02*	*0.03*	*0.02*
Mg	*2.06*	*2.11*	*2.06*	*2.08*	*2.12*	*2.09*	*2.33*	*2.40*	*2.11*	*2.12*	*2.15*	*2.25*	*2.20*
Σ M-site (6-4)	***4.44***	***4.39***	***4.39***	***4.23***	***4.30***	***4.30***	***4.39***	***4.31***	***4.27***	***4.30***	***4.29***	***4.37***	***4.33***
Na	*0.11*	*0.11*	*0.12*	*0.09*	*0.07*	*0.07*	*0.07*	*0.06*	*0.07*	*0.07*	*0.06*	*0.08*	*0.07*
K	*1.75*	*1.72*	*1.73*	*1.75*	*1.75*	*1.72*	*1.80*	*1.81*	*1.80*	*1.80*	*1.79*	*1.78*	*1.76*
Σ A-site (2)	***1.85***	***1.83***	***1.85***	***1.84***	***1.82***	***1.79***	***1.87***	***1.87***	***1.87***	***1.87***	***1.85***	***1.86***	***1.83***
Cation Sum	*15.51*	*15.47*	*15.47*	*15.42*	*15.43*	*15.42*	*15.47*	*15.44*	*15.44*	*15.45*	*15.43*	*15.48*	*15.43*
Mg#	47	48	47	50	50	49	53	56	50	49	50	52	51

Appendix 2.2.4. a: Major element composition and mineral formulae for Biotite from the low-grade equivalent rocks (*continued*).

Sample no.	USK-4A Top Bed	USK-4A Top Bed	USK-4A Top Bed	USK-5C	USK-5C	USK-5C	USK-5C	USK-5C	USK-5C	USK-6A	USK-6A	USK-6A	USK-6A
Analysis	bio	bio in ksp	bio	bio	bio in crd	bio in crd core	bio	bio in crd	bio in crd core	bio	bi in crd	bio in crd core	bio
SiO2	36.87	35.86	37.02	35.72	37.05	36.96	36.44	36.41	36.85	35.84	37.07	37.55	36.77
TiO2	2.98	2.61	2.62	2.66	2.53	2.47	2.90	2.45	2.70	2.44	2.13	2.18	2.47
Al2O3	20.07	19.86	20.48	19.70	20.71	20.67	19.96	20.44	20.48	20.01	20.93	20.94	20.55
FeO	18.16	18.75	18.12	19.17	18.77	18.55	19.05	18.76	18.98	18.57	18.24	19.00	19.43
MnO	0.18	0.17	0.16	0.12	0.13	0.10	0.06	0.22	0.16	0.19	0.16	0.16	0.15
MgO	9.49	10.05	10.02	9.63	10.15	9.72	9.77	9.75	9.83	9.57	9.83	10.36	9.96
Na2O	0.22	0.25	0.19	0.32	0.37	0.39	0.45	0.42	0.26	0.38	0.42	0.38	0.45
K2O	9.66	8.82	9.73	8.92	9.06	9.05	9.09	8.94	9.05	8.96	8.96	8.92	8.94
Total	**97.63**	**96.37**	**98.34**	**96.24**	**98.77**	**97.90**	**97.71**	**97.39**	**98.31**	**95.96**	**97.74**	**99.49**	**98.72**
Si (5-6)	*5.42*	*5.35*	*5.40*	*5.35*	*5.38*	*5.41*	*5.37*	*5.37*	*5.38*	*5.37*	*5.42*	*5.40*	*5.36*
AlIV (3-2)	*2.58*	*2.65*	*2.60*	*2.65*	*2.62*	*2.59*	*2.63*	*2.63*	*2.62*	*2.63*	*2.58*	*2.60*	*2.64*
Σ T-site	***8.00***	***8.00***	***8.00***	***8.00***	***8.00***	***8.00***	***8.00***	***8.00***	***8.00***	***8.00***	***8.00***	***8.00***	***8.00***
AlVI	*0.90*	*0.84*	*0.92*	*0.84*	*0.92*	*0.97*	*0.84*	*0.92*	*0.91*	*0.91*	*1.02*	*0.95*	*0.89*
Ti	*0.33*	*0.29*	*0.29*	*0.30*	*0.28*	*0.27*	*0.32*	*0.27*	*0.30*	*0.27*	*0.23*	*0.24*	*0.27*
Σ XX-site (0-2)	***1.23***	***1.14***	***1.21***	***1.14***	***1.20***	***1.24***	***1.16***	***1.19***	***1.20***	***1.18***	***1.26***	***1.19***	***1.16***
Fe2+	*2.23*	*2.34*	*2.21*	*2.40*	*2.28*	*2.27*	*2.35*	*2.31*	*2.32*	*2.33*	*2.23*	*2.29*	*2.37*
Mn	*0.02*	*0.02*	*0.02*	*0.02*	*0.02*	*0.01*	*0.01*	*0.03*	*0.02*	*0.02*	*0.02*	*0.02*	*0.02*
Mg	*2.08*	*2.24*	*2.18*	*2.15*	*2.20*	*2.12*	*2.15*	*2.14*	*2.14*	*2.14*	*2.14*	*2.22*	*2.16*
Σ M-site (6-4)	***4.34***	***4.60***	***4.41***	***4.57***	***4.49***	***4.40***	***4.50***	***4.49***	***4.48***	***4.49***	***4.39***	***4.53***	***4.55***
Na	*0.06*	*0.07*	*0.05*	*0.09*	*0.10*	*0.11*	*0.13*	*0.12*	*0.07*	*0.11*	*0.12*	*0.11*	*0.13*
K	*1.81*	*1.68*	*1.81*	*1.71*	*1.68*	*1.69*	*1.71*	*1.68*	*1.69*	*1.71*	*1.67*	*1.64*	*1.66*
Σ A-site (2)	***1.87***	***1.75***	***1.87***	***1.80***	***1.78***	***1.80***	***1.84***	***1.80***	***1.76***	***1.82***	***1.79***	***1.74***	***1.79***
Cation Sum	*15.44*	*15.48*	*15.48*	*15.50*	*15.47*	*15.44*	*15.49*	*15.48*	*15.44*	*15.50*	*15.44*	*15.46*	*15.50*
Mg#	48	49	50	47	49	48	48	48	48	48	49	49	48

Appendix 2.2.4. a: Major element composition and mineral formulae for Biotite from the low-grade equivalent rocks (*continued*).

Sample no.	USK-6A	USK-7B	USK-7B	USK-7B
Analysis	bio in crd core	bio in crd	bio	bio in crd
SiO2	38.61	38.29	36.70	36.19
TiO2	2.17	2.44	2.55	2.20
Al2O3	21.75	21.90	20.35	20.68
FeO	18.86	19.96	19.27	19.14
MnO	0.19	0.13	0.09	0.17
MgO	10.56	9.97	9.72	9.19
Na2O	0.47	0.36	0.35	0.33
K2O	9.15	9.25	9.09	8.76
Total	**101.74**	**102.29**	**98.12**	**96.68**
Si (5-6)	*5.41*	*5.37*	*5.38*	*5.38*
AlIV (3-2)	*2.59*	*2.63*	*2.62*	*2.62*
Σ T-site	***8.00***	***8.00***	***8.00***	***8.00***
AlVI	*1.01*	*0.99*	*0.90*	*1.00*
Ti	*0.23*	*0.26*	*0.28*	*0.25*
Σ XX-site (0-2)	***1.24***	***1.25***	***1.18***	***1.25***
Fe2+	*2.21*	*2.34*	*2.36*	*2.38*
Mn	*0.02*	*0.01*	*0.01*	*0.02*
Mg	*2.21*	*2.08*	*2.13*	*2.04*
Σ M-site (6-4)	***4.44***	***4.44***	***4.50***	***4.44***
Na	*0.13*	*0.10*	*0.10*	*0.10*
K	*1.64*	*1.65*	*1.70*	*1.66*
Σ A-site (2)	***1.76***	***1.75***	***1.80***	***1.76***
Cation Sum	*15.44*	*15.44*	*15.48*	*15.44*
Mg#	50	47	47	46

Appendix 2.2.4. b: Major element composition and mineral formulae for Biotite from rocks of the high-grade study area.

Sample no.	Misc A1	Misc B1	Misc C1	Misc C1	Misc C1	KH1-2	KH1-2	KH1-2	KH 1_3 B1	KH 1_3 B1	KH 1_3 B1	KH 1_3 B1	KH 1_3 B2
Analysis	bio	bio	bio	bi	bi inclusion	bi	bi2	bi3	bio	bi	bi in garnet	bio outside garnet	bi
SiO2	38.46	34.82	35.95	37.12	35.98	37.23	34.94	35.42	35.28	36.28	35.86	36.20	35.64
TiO2	0.00	2.82	0.52	0.88	3.79	3.68	3.58	4.56	4.24	4.31	4.67	3.33	3.99
Al2O3	23.55	18.19	21.86	20.82	18.72	20.04	18.74	18.25	18.48	18.86	18.24	18.94	18.88
FeO	19.09	18.59	18.03	19.14	18.31	21.51	21.91	19.16	16.06	16.43	18.11	20.36	20.58
MnO	0.11	0.03	0.14	0.08	0.14	0.01	0.00	0.00	0.01	0.01	0.00	0.02	0.00
MgO	11.12	9.44	9.53	10.69	10.09	9.60	8.83	10.16	11.27	11.55	10.48	9.55	8.78
Na2O	0.38	0.48	0.19	0.44	0.46	0.00	0.00	0.00	0.55	0.56	0.39	0.32	0.32
K2O	8.41	8.04	9.19	8.79	8.83	9.76	9.42	9.05	8.97	9.23	9.21	9.27	9.34
Total	**101.12**	**92.41**	**95.41**	**97.95**	**96.33**	**101.83**	**97.42**	**96.60**	**94.85**	**97.22**	**96.96**	**97.98**	**97.54**
Si (5-6)	*5.39*	*5.42*	*5.39*	*5.43*	*5.37*	*5.32*	*5.27*	*5.30*	*5.31*	*5.33*	*5.33*	*5.37*	*5.33*
AlIV (3-2)	*2.61*	*2.58*	*2.61*	*2.57*	*2.63*	*2.68*	*2.73*	*2.70*	*2.69*	*2.67*	*2.67*	*2.63*	*2.67*
Σ T-site	***8.00***	***8.00***	***8.00***	***8.00***	***8.00***	***8.00***	***8.00***	***8.00***	***8.00***	***8.00***	***8.00***	***8.00***	***8.00***
AlVI	*1.28*	*0.76*	*1.25*	*1.02*	*0.67*	*0.70*	*0.60*	*0.52*	*0.59*	*0.59*	*0.52*	*0.68*	*0.65*
Ti	*0.00*	*0.33*	*0.06*	*0.10*	*0.43*	*0.40*	*0.41*	*0.51*	*0.48*	*0.48*	*0.52*	*0.37*	*0.45*
Σ XX-site (0-2)	***1.28***	***1.09***	***1.31***	***1.12***	***1.09***	***1.09***	***1.00***	***1.04***	***1.07***	***1.07***	***1.05***	***1.05***	***1.10***
Fe2+	*2.24*	*2.42*	*2.26*	*2.34*	*2.29*	*2.57*	*2.76*	*2.40*	*2.02*	*2.02*	*2.25*	*2.52*	*2.57*
Mn	*0.01*	*0.00*	*0.02*	*0.01*	*0.02*	*0.00*	*0.00*	*0.00*	*0.00*	*0.00*	*0.00*	*0.00*	*0.00*
Mg	*2.33*	*2.19*	*2.13*	*2.33*	*2.25*	*2.04*	*1.99*	*2.27*	*2.53*	*2.53*	*2.32*	*2.11*	*1.96*
Σ M-site (6-4)	***4.58***	***4.62***	***4.41***	***4.68***	***4.55***	***4.62***	***4.75***	***4.67***	***4.55***	***4.55***	***4.57***	***4.64***	***4.53***
Na	*0.10*	*0.14*	*0.06*	*0.12*	*0.13*	*0.00*	*0.00*	*0.00*	*0.16*	*0.16*	*0.11*	*0.09*	*0.09*
K	*1.50*	*1.60*	*1.76*	*1.64*	*1.68*	*1.78*	*1.81*	*1.73*	*1.72*	*1.73*	*1.75*	*1.75*	*1.78*
Σ A-site (2)	***1.61***	***1.74***	***1.81***	***1.76***	***1.81***	***1.78***	***1.81***	***1.73***	***1.88***	***1.89***	***1.86***	***1.85***	***1.87***
Cation Sum	*15.47*	*15.45*	*15.53*	*15.56*	*15.46*	*15.49*	*15.57*	*15.44*	*15.51*	*15.51*	*15.48*	*15.53*	*15.50*
Mg#	51	48	48	50	50	44	42	49	56	56	51	46	43

Appendix 2.2.4. b: Major element composition and mineral formulae for Biotite from rocks of the high-grade study area (*continued)*.

Sample no.	KH 1_3 B4	KHt3	GL-1	GL-1	GL-1	GL-1	GL-1	GL-1	GL-1	GL-1	GL-1	12-1D a	12-1D a
Analysis	bio in this cord	grain with exsolution	bt	bt2	bt3	bt4	gb-bi	gb2-bi	bi cummulate	Spectrum 21	gb3-bi	bio	bio in kspar
SiO2	36.91	47.70	36.17	35.74	36.04	36.52	35.97	34.98	35.85	35.62	35.95	34.72	34.59
TiO2	4.28	0.09	2.74	2.77	2.87	2.52	1.78	1.82	2.85	2.99	1.88	2.08	2.69
Al2O3	19.46	10.81	19.19	19.17	19.07	19.74	19.18	18.61	19.00	19.19	19.26	20.06	19.86
FeO	20.21	3.19	20.88	20.81	20.87	20.46	19.93	20.91	20.50	19.79	21.36	21.72	22.18
MnO	0.01	0.05	0.15	0.17	0.15	0.18	0.13	0.06	0.16	0.05	0.16	0.21	0.25
MgO	9.02	27.06	9.41	9.46	9.32	9.37	11.15	10.41	9.29	9.01	10.02	7.76	7.02
Na2O	0.35	0.00	0.38	0.38	0.31	0.27	0.39	0.31	0.25	0.32	0.43	0.33	0.32
K2O	9.52	8.62	9.24	9.39	9.24	9.33	8.38	8.73	9.35	8.92	8.99	9.05	9.10
Total	**99.75**	**97.52**	**98.16**	**97.90**	**97.86**	**98.39**	**96.91**	**95.83**	**97.25**	**95.89**	**98.06**	**95.93**	**96.01**
Si (5-6)	*5.36*	*6.43*	*5.37*	*5.33*	*5.37*	*5.39*	*5.36*	*5.32*	*5.37*	*5.38*	*5.35*	*5.30*	*5.30*
AlIV (3-2)	*2.64*	*1.57*	*2.63*	*2.67*	*2.63*	*2.61*	*2.64*	*2.68*	*2.63*	*2.62*	*2.65*	*2.70*	*2.70*
Σ T-site	***8.00***	***8.00***	***8.00***	***8.00***	***8.00***	***8.00***	***8.00***	***8.00***	***8.00***	***8.00***	***8.00***	***8.00***	***8.00***
AlVI	*0.69*	*0.15*	*0.72*	*0.70*	*0.71*	*0.82*	*0.73*	*0.66*	*0.72*	*0.79*	*0.73*	*0.91*	*0.88*
Ti	*0.47*	*0.01*	*0.31*	*0.31*	*0.32*	*0.28*	*0.20*	*0.21*	*0.32*	*0.34*	*0.21*	*0.24*	*0.31*
Σ XX-site (0-2)	***1.16***	***0.16***	***1.03***	***1.01***	***1.03***	***1.10***	***0.93***	***0.87***	***1.04***	***1.13***	***0.94***	***1.15***	***1.19***
Fe2+	*2.45*	*0.36*	*2.59*	*2.59*	*2.60*	*2.52*	*2.48*	*2.66*	*2.57*	*2.50*	*2.66*	*2.77*	*2.84*
Mn	*0.00*	*0.01*	*0.02*	*0.02*	*0.02*	*0.02*	*0.02*	*0.01*	*0.02*	*0.01*	*0.02*	*0.03*	*0.03*
Mg	*1.95*	*5.44*	*2.08*	*2.10*	*2.07*	*2.06*	*2.48*	*2.36*	*2.07*	*2.03*	*2.22*	*1.77*	*1.60*
Σ M-site (6-4)	***4.41***	***5.80***	***4.69***	***4.72***	***4.69***	***4.61***	***4.98***	***5.03***	***4.66***	***4.53***	***4.90***	***4.57***	***4.47***
Na	*0.10*	*0.00*	*0.11*	*0.11*	*0.09*	*0.08*	*0.11*	*0.09*	*0.07*	*0.09*	*0.12*	*0.10*	*0.10*
K	*1.76*	*1.48*	*1.75*	*1.79*	*1.75*	*1.75*	*1.59*	*1.70*	*1.79*	*1.72*	*1.71*	*1.76*	*1.78*
Σ A-site (2)	***1.86***	***1.48***	***1.86***	***1.90***	***1.84***	***1.83***	***1.71***	***1.79***	***1.86***	***1.81***	***1.83***	***1.86***	***1.87***
Cation Sum	*15.43*	*15.44*	*15.58*	*15.62*	*15.56*	*15.53*	*15.61*	*15.69*	*15.56*	*15.48*	*15.67*	*15.58*	*15.54*
Mg#	44	94	45	45	44	45	50	47	45	45	46	39	36

Appendix 2.2.4. b: Major element composition and mineral formulae for Biotite from rocks of the high-grade study area (*continued)*.

Sample no.	12-1D a	12-1D a	12-1D a	12-1D a	12-1D a	12-1D a	12-1D a	12-1D a	12-1D a	12-1D a	12-1D a	12-1D a	12-1D a
Analysis	matrix bio	bio in gt core	bio in gt core	bio in gt core	bio in gt	bio around gt	bio around gt	bio around gt	bio around gt 2	Spectrum 34	bio in gt2	bio in gt	bio in crd
SiO2	33.98	35.71	35.87	36.12	35.70	35.19	34.27	35.02	34.96	35.17	34.78	35.53	35.08
TiO2	2.38	4.24	3.94	2.31	4.72	1.78	2.11	2.35	0.07	1.73	1.79	1.83	2.59
Al2O3	19.69	18.54	19.11	19.66	18.41	20.77	20.48	20.34	20.10	20.98	20.92	20.99	20.22
FeO	22.52	18.57	18.11	17.74	19.36	21.81	22.28	22.39	32.41	22.49	23.36	22.36	22.35
MnO	0.28	0.06	0.07	0.07	0.08	0.27	0.32	0.23	8.68	0.19	0.31	0.25	0.28
MgO	7.35	10.08	10.40	11.07	9.44	7.74	7.38	7.61	1.86	7.37	7.37	7.52	7.53
Na2O	0.26	0.61	0.56	0.68	0.51	0.33	0.33	0.32	0.20	0.30	0.29	0.34	0.32
K2O	9.05	8.59	8.80	8.90	8.94	9.17	9.12	9.15	0.01	9.21	9.26	9.00	9.27
Total	**95.51**	**96.40**	**96.86**	**96.55**	**97.16**	**97.05**	**96.30**	**97.39**	**98.29**	**97.44**	**98.08**	**97.82**	**97.64**
Si (5-6)	*5.25*	*5.34*	*5.32*	*5.36*	*5.32*	*5.30*	*5.24*	*5.28*	*5.38*	*5.29*	*5.23*	*5.31*	*5.28*
AlIV (3-2)	*2.75*	*2.66*	*2.68*	*2.64*	*2.68*	*2.70*	*2.76*	*2.72*	*2.62*	*2.71*	*2.77*	*2.69*	*2.72*
Σ T-site	***8.00***	***8.00***	***8.00***	***8.00***	***8.00***	***8.00***	***8.00***	***8.00***	***8.00***	***8.00***	***8.00***	***8.00***	***8.00***
AlVI	*0.83*	*0.60*	*0.66*	*0.80*	*0.56*	*0.99*	*0.93*	*0.89*	*1.02*	*1.02*	*0.94*	*1.01*	*0.87*
Ti	*0.28*	*0.48*	*0.44*	*0.26*	*0.53*	*0.20*	*0.24*	*0.27*	*0.01*	*0.20*	*0.20*	*0.21*	*0.29*
Σ XX-site (0-2)	***1.11***	***1.08***	***1.10***	***1.06***	***1.09***	***1.20***	***1.17***	***1.16***	***1.03***	***1.21***	***1.15***	***1.22***	***1.16***
Fe2+	*2.91*	*2.32*	*2.25*	*2.20*	*2.41*	*2.75*	*2.85*	*2.82*	*4.17*	*2.83*	*2.94*	*2.80*	*2.81*
Mn	*0.04*	*0.01*	*0.01*	*0.01*	*0.01*	*0.03*	*0.04*	*0.03*	*1.13*	*0.02*	*0.04*	*0.03*	*0.04*
Mg	*1.69*	*2.25*	*2.30*	*2.45*	*2.10*	*1.74*	*1.68*	*1.71*	*0.43*	*1.65*	*1.65*	*1.68*	*1.69*
Σ M-site (6-4)	***4.64***	***4.57***	***4.56***	***4.66***	***4.52***	***4.52***	***4.57***	***4.56***	***5.73***	***4.51***	***4.63***	***4.50***	***4.54***
Na	*0.08*	*0.18*	*0.16*	*0.20*	*0.15*	*0.10*	*0.10*	*0.09*	*0.06*	*0.09*	*0.08*	*0.10*	*0.09*
K	*1.78*	*1.64*	*1.67*	*1.69*	*1.70*	*1.76*	*1.78*	*1.76*	*0.00*	*1.77*	*1.78*	*1.72*	*1.78*
Σ A-site (2)	***1.86***	***1.81***	***1.83***	***1.88***	***1.85***	***1.86***	***1.87***	***1.85***	***0.06***	***1.86***	***1.86***	***1.82***	***1.87***
Cation Sum	*15.61*	*15.46*	*15.48*	*15.60*	*15.45*	*15.58*	*15.61*	*15.57*	*14.82*	*15.58*	*15.64*	*15.54*	*15.57*
Mg#	37	49	51	53	47	39	37	38	9	37	36	37	38

Appendix 2.2.4. b: Major element composition and mineral formulae for Biotite from rocks of the high-grade study area (*continued)*.

Sample no.	12-1D a	14-5A	14-5A	14-5A	14-5A	14-5A	14-5A	14-5A	14-5A	14-5A	14-5A	14-5A	14-2A leucosome bi
Analysis	bio matrix	bio in crd	bio in crd	bio in crd	bio around crd	bio around crd	bio around crd	bt in gt core	bt in gt core	bt in gt core	matrix bio	matrix bio	bt
SiO2	34.88	35.58	35.18	35.63	35.34	35.26	35.55	35.87	35.62	35.77	35.76	35.49	35.94
TiO2	2.73	2.81	3.05	2.28	2.95	3.03	3.06	2.74	1.58	1.19	2.65	3.37	2.78
Al2O3	20.51	19.43	19.33	19.72	19.21	19.11	19.12	19.40	19.63	19.52	19.42	18.72	19.86
FeO	21.82	20.47	20.31	20.52	19.92	20.61	19.89	19.33	18.15	17.68	20.47	20.49	18.33
MnO	0.26	0.16	0.14	0.20	0.27	0.21	0.21	0.07	0.08	0.12	0.10	0.20	0.19
MgO	7.46	9.07	8.72	9.19	9.03	9.05	9.40	10.60	11.35	12.18	9.57	9.21	9.39
Na2O	0.20	0.37	0.31	0.34	0.24	0.36	0.27	0.36	0.30	0.30	0.36	0.32	0.36
K2O	9.23	9.05	9.13	9.20	8.97	9.25	9.16	9.14	9.12	9.01	9.26	9.15	8.91
Total	**97.09**	**96.94**	**96.18**	**97.08**	**95.93**	**96.88**	**96.65**	**97.51**	**95.83**	**95.77**	**97.60**	**96.93**	**95.76**
Si (5-6)	*5.26*	*5.34*	*5.33*	*5.34*	*5.35*	*5.31*	*5.34*	*5.32*	*5.35*	*5.36*	*5.33*	*5.34*	*5.39*
AlIV (3-2)	*2.74*	*2.66*	*2.67*	*2.66*	*2.65*	*2.69*	*2.66*	*2.68*	*2.65*	*2.64*	*2.67*	*2.66*	*2.61*
Σ T-site	***8.00***	***8.00***	***8.00***	***8.00***	***8.00***	***8.00***	***8.00***	***8.00***	***8.00***	***8.00***	***8.00***	***8.00***	***8.00***
AlVI	*0.91*	*0.77*	*0.77*	*0.82*	*0.77*	*0.71*	*0.73*	*0.71*	*0.82*	*0.80*	*0.74*	*0.65*	*0.90*
Ti	*0.31*	*0.32*	*0.35*	*0.26*	*0.34*	*0.34*	*0.35*	*0.31*	*0.18*	*0.13*	*0.30*	*0.38*	*0.31*
Σ XX-site (0-2)	***1.22***	***1.09***	***1.12***	***1.08***	***1.11***	***1.05***	***1.07***	***1.02***	***1.00***	***0.94***	***1.04***	***1.03***	***1.21***
Fe2+	*2.75*	*2.57*	*2.57*	*2.57*	*2.52*	*2.60*	*2.50*	*2.40*	*2.28*	*2.21*	*2.55*	*2.58*	*2.30*
Mn	*0.03*	*0.02*	*0.02*	*0.03*	*0.03*	*0.03*	*0.03*	*0.01*	*0.01*	*0.02*	*0.01*	*0.02*	*0.02*
Mg	*1.68*	*2.03*	*1.97*	*2.05*	*2.04*	*2.03*	*2.11*	*2.34*	*2.54*	*2.72*	*2.13*	*2.06*	*2.10*
Σ M-site (6-4)	***4.47***	***4.62***	***4.56***	***4.65***	***4.59***	***4.66***	***4.63***	***4.75***	***4.83***	***4.95***	***4.69***	***4.67***	***4.42***
Na	*0.06*	*0.11*	*0.09*	*0.10*	*0.07*	*0.11*	*0.08*	*0.10*	*0.09*	*0.09*	*0.10*	*0.09*	*0.10*
K	*1.78*	*1.73*	*1.76*	*1.76*	*1.73*	*1.78*	*1.76*	*1.73*	*1.75*	*1.72*	*1.76*	*1.76*	*1.70*
Σ A-site (2)	***1.83***	***1.84***	***1.86***	***1.86***	***1.80***	***1.88***	***1.83***	***1.83***	***1.83***	***1.81***	***1.86***	***1.85***	***1.81***
Cation Sum	*15.52*	*15.55*	*15.53*	*15.59*	*15.50*	*15.59*	*15.54*	*15.59*	*15.66*	*15.69*	*15.60*	*15.55*	*15.45*
Mg#	38	44	43	44	45	44	46	49	53	55	45	44	48

Appendix 2.2.4. b: Major element composition and mineral formulae for Biotite from rocks of the high-grade study area (*continued)*.

Sample no.	14-2A leucosome bi	14-2A leucosome bi	14-2A leucosome bi	14-2A melanosome bi	14-2A melanosome bi	14-2A melanosome bi	14-2A host-rock bi	14-2A host-rock bi	14-2A host-rock bi	11-7D	11-7D	11-7D	11-7D
Analysis	bi	bi	bt	bt	bt	bt	bt	bi incl	matrix bi	matrix bio	matrix bio	bio in crd	bio in crd
SiO2	36.16	37.10	36.33	36.91	36.62	36.19	37.87	36.31	35.87	35.16	34.96	35.79	35.69
TiO2	3.02	2.88	3.22	2.96	3.15	3.03	3.00	3.28	3.25	2.94	3.13	3.18	3.07
Al2O3	19.94	20.45	19.72	19.87	20.22	19.77	20.50	19.62	19.35	18.61	18.53	19.77	18.42
FeO	18.11	18.66	19.60	17.96	18.26	17.62	17.89	19.54	19.81	19.25	19.02	18.69	20.43
MnO	0.12	0.19	0.11	0.17	0.20	0.22	0.15	0.21	0.20	0.23	0.23	0.24	0.20
MgO	9.37	9.39	9.31	9.92	9.76	9.66	10.05	9.53	9.32	10.06	9.90	10.06	10.08
Na2O	0.38	0.53	0.30	0.36	0.46	0.42	0.31	0.37	0.43	0.34	0.30	0.34	0.18
K2O	8.88	8.85	9.27	8.46	8.49	8.64	8.62	9.09	9.06	9.28	9.40	9.30	9.32
Total	**95.98**	**98.05**	**97.86**	**96.61**	**97.16**	**95.55**	**98.39**	**97.95**	**97.29**	**95.87**	**95.47**	**97.39**	**97.39**
Si (5-6)	*5.40*	*5.42*	*5.37*	*5.45*	*5.39*	*5.41*	*5.47*	*5.36*	*5.34*	*5.33*	*5.32*	*5.31*	*5.34*
AlIV (3-2)	*2.60*	*2.58*	*2.63*	*2.55*	*2.61*	*2.59*	*2.53*	*2.64*	*2.66*	*2.67*	*2.68*	*2.69*	*2.66*
Σ T-site	***8.00***	***8.00***	***8.00***	***8.00***	***8.00***	***8.00***	***8.00***	***8.00***	***8.00***	***8.00***	***8.00***	***8.00***	***8.00***
AlVI	*0.91*	*0.94*	*0.80*	*0.90*	*0.89*	*0.90*	*0.96*	*0.77*	*0.74*	*0.65*	*0.65*	*0.76*	*0.59*
Ti	*0.34*	*0.32*	*0.36*	*0.33*	*0.35*	*0.34*	*0.33*	*0.36*	*0.36*	*0.33*	*0.36*	*0.35*	*0.35*
Σ XX-site (0-2)	***1.25***	***1.26***	***1.16***	***1.23***	***1.24***	***1.24***	***1.28***	***1.13***	***1.11***	***0.99***	***1.00***	***1.11***	***0.94***
Fe2+	*2.26*	*2.28*	*2.42*	*2.22*	*2.25*	*2.20*	*2.16*	*2.41*	*2.47*	*2.44*	*2.42*	*2.32*	*2.56*
Mn	*0.02*	*0.02*	*0.01*	*0.02*	*0.02*	*0.03*	*0.02*	*0.03*	*0.03*	*0.03*	*0.03*	*0.03*	*0.03*
Mg	*2.09*	*2.04*	*2.05*	*2.18*	*2.14*	*2.15*	*2.16*	*2.10*	*2.07*	*2.27*	*2.25*	*2.22*	*2.25*
Σ M-site (6-4)	***4.36***	***4.35***	***4.49***	***4.42***	***4.41***	***4.38***	***4.34***	***4.53***	***4.56***	***4.74***	***4.70***	***4.57***	***4.83***
Na	*0.11*	*0.15*	*0.09*	*0.10*	*0.13*	*0.12*	*0.09*	*0.11*	*0.12*	*0.10*	*0.09*	*0.10*	*0.05*
K	*1.69*	*1.65*	*1.75*	*1.59*	*1.59*	*1.65*	*1.59*	*1.71*	*1.72*	*1.79*	*1.83*	*1.76*	*1.78*
Σ A-site (2)	***1.80***	***1.80***	***1.83***	***1.70***	***1.72***	***1.77***	***1.67***	***1.82***	***1.85***	***1.89***	***1.91***	***1.86***	***1.83***
Cation Sum	*15.41*	*15.40*	*15.48*	*15.35*	*15.37*	*15.39*	*15.30*	*15.48*	*15.52*	*15.62*	*15.61*	*15.54*	*15.60*
Mg#	48	47	46	50	49	49	50	47	46	48	48	49	47

Appendix 2.2.4. b: Major element composition and mineral formulae for Biotite from rocks of the high-grade study area (*continued)*.

Sample no.	11-7D	11-7D	11-7D	11-7D	11-7D	11-7D	11-7D	11-7D	11-7D	KHt2_2 c	KHt2_2 c	KHt2_2 c	KHt2_2 c
Analysis	matrix bio	bio in gt	bio in gt	bio in gt	matrix bio	bio in crd	bio in crd	matrix bio	bio in plag	bi in gt crack	bi in gt crack	bi adjacent to gt	matrix bio
SiO2	35.67	36.12	36.07	36.14	35.59	36.19	35.77	35.71	36.12	36.69	35.85	35.97	34.83
TiO2	3.11	2.31	2.40	2.36	3.09	3.08	3.11	3.25	3.39	0.00	0.00	1.60	3.16
Al2O3	18.53	18.76	18.73	18.88	18.45	18.97	19.12	18.45	18.61	19.64	19.53	20.54	18.93
FeO	19.93	16.59	16.43	16.79	19.81	19.77	19.66	19.85	19.66	22.00	24.39	21.93	20.82
MnO	0.28	0.07	0.04	0.14	0.18	0.25	0.24	0.23	0.30	0.20	0.20	0.00	0.00
MgO	10.33	12.49	12.54	12.52	10.31	10.16	9.93	10.30	10.46	9.62	9.81	8.97	8.76
Na2O	0.32	0.34	0.29	0.36	0.26	0.34	0.33	0.32	0.27	0.00	0.00	0.00	0.00
K2O	9.46	9.29	9.29	9.48	8.47	9.74	9.65	9.62	9.65	8.75	8.90	8.93	8.97
Total	**97.63**	**95.97**	**95.78**	**96.67**	**96.16**	**98.50**	**97.81**	**97.72**	**98.46**	**96.90**	**98.69**	**97.93**	**95.46**
Si (5-6)	*5.32*	*5.38*	*5.38*	*5.36*	*5.36*	*5.34*	*5.32*	*5.33*	*5.34*	*5.51*	*5.36*	*5.35*	*5.32*
AlIV (3-2)	*2.68*	*2.62*	*2.62*	*2.64*	*2.64*	*2.66*	*2.68*	*2.67*	*2.66*	*2.49*	*2.64*	*2.65*	*2.68*
Σ T-site	***8.00***	***8.00***	***8.00***	***8.00***	***8.00***	***8.00***	***8.00***	***8.00***	***8.00***	***8.00***	***8.00***	***8.00***	***8.00***
AlVI	*0.58*	*0.67*	*0.67*	*0.65*	*0.63*	*0.65*	*0.67*	*0.57*	*0.57*	*0.98*	*0.80*	*0.94*	*0.73*
Ti	*0.35*	*0.26*	*0.27*	*0.26*	*0.35*	*0.34*	*0.35*	*0.37*	*0.38*	*0.00*	*0.00*	*0.18*	*0.36*
Σ XX-site (0-2)	***0.93***	***0.93***	***0.94***	***0.92***	***0.98***	***0.99***	***1.02***	***0.93***	***0.95***	***0.98***	***0.80***	***1.12***	***1.09***
Fe2+	*2.49*	*2.07*	*2.05*	*2.08*	*2.49*	*2.44*	*2.44*	*2.48*	*2.43*	*2.76*	*3.05*	*2.72*	*2.66*
Mn	*0.04*	*0.01*	*0.00*	*0.02*	*0.02*	*0.03*	*0.03*	*0.03*	*0.04*	*0.03*	*0.03*	*0.00*	*0.00*
Mg	*2.30*	*2.77*	*2.79*	*2.77*	*2.31*	*2.24*	*2.20*	*2.29*	*2.30*	*2.15*	*2.19*	*1.99*	*2.00*
Σ M-site (6-4)	***4.82***	***4.85***	***4.84***	***4.87***	***4.83***	***4.71***	***4.67***	***4.79***	***4.77***	***4.94***	***5.26***	***4.71***	***4.65***
Na	*0.09*	*0.10*	*0.08*	*0.10*	*0.08*	*0.10*	*0.09*	*0.09*	*0.08*	*0.00*	*0.00*	*0.00*	*0.00*
K	*1.80*	*1.77*	*1.77*	*1.79*	*1.63*	*1.83*	*1.83*	*1.83*	*1.82*	*1.67*	*1.70*	*1.69*	*1.75*
Σ A-site (2)	***1.89***	***1.86***	***1.85***	***1.90***	***1.70***	***1.93***	***1.93***	***1.92***	***1.90***	***1.67***	***1.70***	***1.69***	***1.75***
Cation Sum	*15.65*	*15.65*	*15.63*	*15.68*	*15.51*	*15.63*	*15.62*	*15.65*	*15.62*	*15.59*	*15.77*	*15.52*	*15.49*
Mg#	48	57	58	57	48	48	47	48	49	44	42	42	43

Appendix 2.2.4. b: Major element composition and mineral formulae for Biotite from rocks of the high-grade study area (*continued)*.

Sample no.	KHt2_2 c	KHt2_2 c	KHt2_2 h	KHt2_2 h	KHt2_2 h	KHt2_2 h	KHt2_2 h	KHt2_2 h	KHt2_2 h	KHt2_2 h
Analysis	matrix bio	bi incl in matrix ksp	bio	bio	bi in crd	bi in crd	bi in crd rim	bi around crd	bi around crd	matrix bio
SiO2	35.53	35.75	35.01	34.24	35.26	35.31	35.23	35.04	34.24	34.01
TiO2	2.99	2.78	3.08	3.06	2.42	2.60	2.68	3.00	3.04	2.88
Al2O3	19.62	19.95	19.22	18.85	20.00	19.74	19.71	19.07	18.98	18.74
FeO	20.78	20.31	19.54	20.07	19.50	20.09	19.84	20.14	19.66	19.95
MnO	0.20	0.16		0.15		0.16		0.15	0.15	0.15
MgO	8.71	8.49	8.56	8.53	8.65	8.69	8.44	8.63	8.33	8.27
Na2O	0.32	0.00	0.28	0.30		0.34		0.28	0.33	
K2O	9.29	9.46	9.10	8.98	8.95	9.12	9.07	9.26	9.14	8.96
Total	**97.44**	**96.91**	**94.78**	**94.19**	**94.78**	**96.05**	**94.97**	**95.57**	**93.86**	**92.96**
Si (5-6)	*5.32*	*5.36*	*5.36*	*5.30*	*5.37*	*5.34*	*5.37*	*5.34*	*5.31*	*5.33*
AlIV (3-2)	*2.68*	*2.64*	*2.64*	*2.70*	*2.63*	*2.66*	*2.63*	*2.66*	*2.69*	*2.67*
Σ T-site	***8.00***	***8.00***	***8.00***	***8.00***	***8.00***	***8.00***	***8.00***	***8.00***	***8.00***	***8.00***
AlVI	*0.78*	*0.88*	*0.82*	*0.74*	*0.96*	*0.86*	*0.91*	*0.77*	*0.79*	*0.79*
Ti	*0.34*	*0.31*	*0.35*	*0.36*	*0.28*	*0.30*	*0.31*	*0.34*	*0.35*	*0.34*
Σ XX-site (0-2)	***1.11***	***1.20***	***1.18***	***1.10***	***1.24***	***1.16***	***1.22***	***1.11***	***1.14***	***1.13***
Fe2+	*2.60*	*2.55*	*2.50*	*2.60*	*2.48*	*2.54*	*2.53*	*2.57*	*2.55*	*2.62*
Mn	*0.03*	*0.02*	*0.00*	*0.02*	*0.00*	*0.02*	*0.00*	*0.02*	*0.02*	*0.02*
Mg	*1.94*	*1.90*	*1.95*	*1.97*	*1.96*	*1.96*	*1.92*	*1.96*	*1.93*	*1.93*
Σ M-site (6-4)	***4.57***	***4.46***	***4.45***	***4.59***	***4.45***	***4.52***	***4.45***	***4.55***	***4.50***	***4.57***
Na	*0.09*	*0.00*	*0.08*	*0.09*	*0.00*	*0.10*	*0.00*	*0.08*	*0.10*	*0.00*
K	*1.77*	*1.81*	*1.78*	*1.77*	*1.74*	*1.76*	*1.76*	*1.80*	*1.81*	*1.79*
Σ A-site (2)	***1.87***	***1.81***	***1.86***	***1.86***	***1.74***	***1.86***	***1.76***	***1.88***	***1.91***	***1.79***
Cation Sum	*15.55*	*15.47*	*15.49*	*15.55*	*15.43*	*15.53*	*15.43*	*15.54*	*15.55*	*15.49*
Mg#	43	43	44	43	44	44	43	43	43	43

Appendix 2.3.1: Garnet compositions for Experiments by type:

	Type 1a:				Type 1b:			Type 2:			Type 3:	
	Exp 1	Exp 3	Exp 6	Exp 9	Exp 2	Exp 7	Exp 10	Exp 15	Exp 16	Garnet	Exp 19	Garnet
Temp	1000	950	900	850	1000	900	850	800	750	seeds	800	seeds
SiO_2	*39.13*	*37.87*	*38.32*	*36.71*	*39.79*	*37.49*	*37.10*	*37.97*	*37.52*	*37.67*	*37.80*	*38.89*
TiO_2	*0.54*	*0.92*	*0.77*	*0.48*	*0.00*	*0.63*	*0.58*	*0.65*	*0.00*	*0.00*	*0.63*	*0.00*
Al_2O_3	*22.31*	*20.89*	*21.10*	*19.97*	*22.16*	*21.18*	*17.84*	*21.49*	*21.36*	*21.31*	*20.82*	*21.59*
FeO	*27.79*	*30.89*	*31.26*	*38.63*	*31.69*	*31.35*	*41.05*	*28.12*	*29.25*	*29.59*	*30.16*	*29.19*
MgO	*8.08*	*6.60*	*5.70*	*2.34*	*4.52*	*6.01*	*3.04*	*8.17*	*5.16*	*5.31*	*6.12*	*7.32*
MnO	*1.08*	*1.34*	*1.84*	*1.58*	*1.33*	*1.17*	*0.55*	*1.57*	*4.57*	*4.43*	*1.12*	*0.38*
CaO	*1.41*	*1.05*	*1.70*	*1.00*	*0.85*	*1.72*	*0.80*	*1.55*	*1.54*	*1.47*	*3.00*	*3.41*
Total	*100.34*	*99.56*	*100.69*	*101.01*	*100.33*	*99.57*	*100.95*	*99.52*	*99.40*	*99.77*	*99.66*	*100.79*
Si	*3.02*	*3.00*	*3.01*	*2.96*	*3.15*	*2.97*	*3.01*	*2.96*	*2.99*	*2.99*	*2.98*	*3.00*
AlIV	*0.00*	*0.00*	*0.00*	*0.04*	*0.00*	*0.03*	*0.00*	*0.04*	*0.01*	*0.01*	*0.02*	*0.00*
Σ T-site	*3.02*	*3.00*	*3.01*	*3.00*	*3.15*	*3.00*	*3.01*	*3.00*	*3.00*	*3.00*	*3.00*	*3.00*
AlVI	*2.03*	*1.94*	*1.96*	*1.87*	*2.07*	*1.95*	*1.70*	*1.94*	*2.00*	*1.98*	*1.92*	*1.97*
Fe^{3+}	*0.00*	*0.00*	*0.00*	*0.09*	*0.00*	*0.00*	*0.21*	*0.02*	*0.01*	*0.03*	*0.02*	*0.03*
Ti	*0.03*	*0.05*	*0.05*	*0.03*	*0.00*	*0.04*	*0.04*	*0.04*	*0.00*	*0.00*	*0.04*	*0.00*
Σ M-site	*2.06*	*2.00*	*2.00*	*2.01*	*2.07*	*1.99*	*1.95*	*2.00*	*2.01*	*2.01*	*1.98*	*2.00*
Fe^{2+}	*1.80*	*2.04*	*2.05*	*2.52*	*2.10*	*2.07*	*2.57*	*1.82*	*1.94*	*1.94*	*1.97*	*1.85*
Mg	*0.93*	*0.78*	*0.67*	*0.28*	*0.53*	*0.71*	*0.37*	*0.95*	*0.61*	*0.63*	*0.72*	*0.84*
Mn	*0.07*	*0.09*	*0.12*	*0.11*	*0.09*	*0.08*	*0.04*	*0.10*	*0.31*	*0.30*	*0.07*	*0.02*
Ca	*0.12*	*0.09*	*0.14*	*0.09*	*0.07*	*0.15*	*0.07*	*0.13*	*0.13*	*0.13*	*0.25*	*0.28*
Σ A-site	*2.91*	*3.00*	*2.99*	*2.99*	*2.79*	*3.01*	*3.04*	*3.00*	*2.99*	*2.99*	*3.02*	*3.00*
XAlm	*61.62*	*68.10*	*68.77*	*84.07*	*75.13*	*68.91*	*84.41*	*60.54*	*64.80*	*64.83*	*65.27*	*61.72*
XPyr	*31.96*	*25.94*	*22.35*	*9.42*	*19.10*	*23.61*	*12.08*	*31.66*	*20.48*	*21.02*	*23.84*	*28.06*
XSps	*2.42*	*2.99*	*4.10*	*3.62*	*3.19*	*2.61*	*1.23*	*3.47*	*10.33*	*9.96*	*2.48*	*0.82*
XGrs	*4.01*	*2.97*	*4.78*	*2.89*	*2.57*	*4.87*	*2.28*	*4.33*	*4.39*	*4.19*	*8.41*	*9.39*
Mg#	*34*	*28*	*25*	*10*	*20*	*26*	*13*	*34*	*24*	*24*	*27*	*31*

Appendix 2.3.2: Biotite compositions for Experiments by type:

	Type 1a:				Type 1b:						Type 2:			Type 3:		
	Exp 3	Exp 6	Exp 9	Exp 11	Exp 2	Exp 4	Exp 7	Exp 10	Exp 12	Starting material	Exp 15	Exp 16	Exp 17	Exp 19	Exp 18	Starting material
Temp	950	900	850	800	1000	950	900	850	800		800	750	700	800	750	
SiO_2	*37.51*	*38.51*	*38.34*	*37.93*	*40.96*	*38.06*	*36.68*	*36.56*	*37.01*	*36.20*	*38.12*	*37.11*	*37.48*	*36.60*	*39.29*	*37.11*
TiO_2	*3.25*	*2.95*	*2.62*	*2.68*	*5.14*	*2.30*	*2.35*	*2.40*	*2.42*	*2.45*	*2.03*	*2.85*	*2.65*	*2.79*	*2.42*	*2.65*
Al_2O_3	*17.91*	*19.43*	*19.83*	*20.25*	*16.85*	*20.18*	*19.88*	*20.24*	*20.85*	*19.99*	*20.62*	*20.03*	*20.63*	*19.63*	*19.72*	*20.60*
FeO	*17.84*	*17.88*	*19.15*	*19.31*	*8.53*	*12.50*	*18.33*	*18.24*	*17.98*	*19.20*	*15.28*	*19.54*	*18.17*	*17.40*	*18.11*	*18.39*
MgO	*11.21*	*9.81*	*8.80*	*8.04*	*16.04*	*14.69*	*9.85*	*9.58*	*9.00*	*9.41*	*13.20*	*9.08*	*9.34*	*10.64*	*8.92*	*9.00*
MnO	*0.00*	*0.00*	*0.18*	*0.15*	*0.00*	*0.00*	*0.00*	*0.00*	*0.00*	*0.00*	*0.00*	*0.14*	*0.23*	*0.00*	*0.24*	*0.15*
Na_2O	*0.70*	*0.70*	*0.75*	*0.57*	*0.95*	*0.00*	*0.50*	*0.56*	*0.54*	*0.00*	*0.59*	*0.48*	*0.42*	*0.62*	*0.86*	*0.45*
K_2O	*8.74*	*8.21*	*8.18*	*8.49*	*8.240*	*9.208*	*8.76*	*8.848*	*9.102*	*8.988*	*8.61*	*8.95*	*8.78*	*8.66*	*7.79*	*8.53*
Total	***97.17***	***97.49***	***97.85***	***97.40***	***96.71***	***96.93***	***96.36***	***96.42***	***96.90***	***96.24***	***98.45***	***98.17***	***97.70***	***96.34***	***97.35***	***96.88***
Si (5-6)	*5.52*	*5.60*	*5.59*	*5.57*	*5.75*	*5.46*	*5.45*	*5.43*	*5.45*	*5.41*	*5.44*	*5.44*	*5.47*	*5.42*	*5.70*	*5.46*
AlIV (3-2)	*2.48*	*2.40*	*2.41*	*2.43*	*2.25*	*2.54*	*2.55*	*2.57*	*2.55*	*2.59*	*2.56*	*2.56*	*2.53*	*2.58*	*2.30*	*2.54*
Σ T–site	*8.00*	*8.00*	*8.00*	*8.00*	*8.00*	*8.00*	*8.00*	*8.00*	*8.00*	*8.00*	*8.00*	*8.00*	*8.00*	*8.00*	*8.00*	*8.00*
AlVI	*0.63*	*0.93*	*1.00*	*1.07*	*0.54*	*0.87*	*0.93*	*0.97*	*1.07*	*0.93*	*0.90*	*0.90*	*1.02*	*0.84*	*1.08*	*1.04*
Ti	*0.36*	*0.32*	*0.29*	*0.30*	*0.54*	*0.25*	*0.26*	*0.27*	*0.27*	*0.28*	*0.22*	*0.31*	*0.29*	*0.31*	*0.26*	*0.29*
Σ XX-site (0-2)	*0.99*	*1.25*	*1.28*	*1.36*	*1.08*	*1.11*	*1.19*	*1.23*	*1.34*	*1.20*	*1.12*	*1.21*	*1.31*	*1.15*	*1.34*	*1.33*
Fe2+	*2.20*	*2.17*	*2.33*	*2.37*	*1.00*	*1.50*	*2.28*	*2.26*	*2.22*	*2.40*	*1.82*	*2.40*	*2.22*	*2.15*	*2.20*	*2.26*
Mg	*2.46*	*2.13*	*1.91*	*1.76*	*3.36*	*3.14*	*2.18*	*2.12*	*1.98*	*2.10*	*2.81*	*1.98*	*2.03*	*2.35*	*1.93*	*1.97*
Mn	*0.00*	*0.00*	*0.02*	*0.02*	*0.00*	*0.00*	*0.00*	*0.00*	*0.00*	*0.00*	*0.00*	*0.02*	*0.03*	*0.00*	*0.03*	*0.02*
Σ M-site (6-4)	*4.66*	*4.30*	*4.27*	*4.15*	*4.36*	*4.64*	*4.46*	*4.38*	*4.19*	*4.49*	*4.63*	*4.40*	*4.28*	*4.50*	*4.16*	*4.26*
Na	*0.20*	*0.20*	*0.21*	*0.16*	*0.26*	*0.00*	*0.14*	*0.16*	*0.15*	*0.00*	*0.16*	*0.14*	*0.12*	*0.18*	*0.24*	*0.13*
K	*1.64*	*1.52*	*1.52*	*1.59*	*1.48*	*1.68*	*1.66*	*1.68*	*1.71*	*1.71*	*1.57*	*1.67*	*1.63*	*1.64*	*1.44*	*1.60*
Σ A-site (2)	*1.84*	*1.72*	*1.73*	*1.75*	*1.74*	*1.68*	*1.80*	*1.84*	*1.86*	*1.71*	*1.73*	*1.81*	*1.75*	*1.81*	*1.68*	*1.73*
Cation Sum	***15.49***	***15.27***	***15.29***	***15.26***	***15.18***	***15.43***	***15.45***	***15.45***	***15.40***	***15.41***	***15.48***	***15.42***	***15.34***	***15.47***	***15.19***	***15.32***
Mg#	*53*	*49*	*45*	*43*	*77*	*68*	*49*	*48*	*47*	*47*	*61*	*45*	*48*	*52*	*47*	*47*

Appendix 2.3.3: Feldspar compositions for Experiments by type (all are plagioclase unless ksp is specified):

	Type 1a:						Type 1b:							Type 2:			Type 3:	
	Exp 1		Exp 3	Exp 6	Exp 9	Exp 11	Exp 2	Exp 7		Exp 10	Exp 12		Starting material	Exp 16	Exp 17		Exp 18	Starting material
Temp	1000		950	900	850	800	1000	900		850	800			750	700		750	
	Core	**Rim**						**Ksp**	**Plag**		**Ksp**	**Plag**			**Core**	**Rim**		
SiO_2	*61.41*	*59.51*	*61.66*	*61.76*	*62.32*	*61.98*	*64.09*	*65.36*	*65.80*	*65.01*	*63.56*	*65.93*	*66.13*	*62.25*	*62.08*	*59.01*	*62.20*	*62.66*
Al_2O_3	*23.79*	*25.19*	*23.56*	*23.44*	*23.64*	*23.70*	*20.01*	*19.48*	*22.04*	*21.54*	*21.11*	*21.49*	*22.04*	*23.73*	*23.96*	*25.69*	*23.96*	*23.87*
FeO	*0.42*	*0.32*	*0.28*	*0.26*	*0.28*	*0.25*	*0.38*	*0.33*	*0.17*	*0.22*	*0.20*	*0.21*	*0.22*	*0.17*	*0.26*	*0.39*	*0.26*	*0.18*
CaO	*5.54*	*7.04*	*5.33*	*5.10*	*4.84*	*4.93*	*1.03*	*0.74*	*2.81*	*2.65*	*2.60*	*2.19*	*2.62*	*5.24*	*4.85*	*7.53*	*5.12*	*4.94*
Na_2O	*7.52*	*6.38*	*7.67*	*8.50*	*8.92*	*8.76*	*5.37*	*3.05*	*10.09*	*10.09*	*7.54*	*10.54*	*10.44*	*8.73*	*9.13*	*7.26*	*8.81*	*8.91*
K_2O	*1.10*	*0.91*	*1.11*	*0.39*	*0.16*	*0.10*	*7.37*	*11.25*	*0.11*	*0.10*	*3.60*	*0.00*	*0.00*	*0.10*	*0.00*	*0.00*	*0.12*	*0.00*
BaO	*0.00*	*0.00*	*0.00*	*0.00*	*0.00*	*0.00*	*1.35*	*0.00*	*0.00*	*0.00*	*0.00*	*0.00*	*0.00*	*0.00*	*0.00*	*0.00*	*0.00*	*0.00*
Total	*99.78*	*99.36*	*99.62*	*99.45*	*100.16*	*99.72*	*99.61*	*100.21*	*101.02*	*99.61*	*98.61*	*100.36*	*101.45*	*100.22*	*100.28*	*99.87*	*100.46*	*100.56*
Si	*2.74*	*2.67*	*2.75*	*2.76*	*2.76*	*2.75*	*2.92*	*2.95*	*2.87*	*2.87*	*2.87*	*2.89*	*2.87*	*2.75*	*2.75*	*2.64*	*2.75*	*2.76*
Al	*1.25*	*1.33*	*1.24*	*1.23*	*1.23*	*1.24*	*1.07*	*1.04*	*1.13*	*1.12*	*1.12*	*1.11*	*1.13*	*1.24*	*1.25*	*1.35*	*1.25*	*1.24*
Fe^{3+}	*0.02*	*0.01*	*0.01*	*0.01*	*0.01*	*0.01*	*0.01*	*0.01*	*0.01*	*0.01*	*0.01*	*0.01*	*0.01*	*0.01*	*0.01*	*0.01*	*0.01*	*0.01*
Σ T-site	*4.01*	*4.01*	*4.00*	*4.00*	*4.00*	*4.01*	*4.01*	*4.00*	*4.00*	*4.00*	*4.00*	*4.00*	*4.00*	*4.00*	*4.00*	*4.00*	*4.00*	*4.00*
Ca	*0.26*	*0.34*	*0.26*	*0.24*	*0.23*	*0.23*	*0.05*	*0.04*	*0.13*	*0.13*	*0.13*	*0.10*	*0.12*	*0.25*	*0.23*	*0.36*	*0.24*	*0.23*
Na	*0.65*	*0.56*	*0.66*	*0.74*	*0.77*	*0.75*	*0.47*	*0.27*	*0.85*	*0.86*	*0.66*	*0.90*	*0.88*	*0.75*	*0.78*	*0.63*	*0.75*	*0.76*
K	*0.06*	*0.05*	*0.06*	*0.02*	*0.01*	*0.01*	*0.43*	*0.65*	*0.01*	*0.01*	*0.21*	*0.00*	*0.00*	*0.01*	*0.00*	*0.00*	*0.01*	*0.00*
Ba	*0.00*	*0.00*	*0.00*	*0.00*	*0.00*	*0.00*	*0.02*	*0.00*	*0.00*	*0.00*	*0.00*	*0.00*	*0.00*	*0.00*	*0.00*	*0.00*	*0.00*	*0.00*
Σ A-site	*0.98*	*0.95*	*0.98*	*1.00*	*1.00*	*0.99*	*0.98*	*0.95*	*0.99*	*1.00*	*0.99*	*1.00*	*1.00*	*1.00*	*1.01*	*0.99*	*1.00*	*0.99*
An	*27.1*	*35.8*	*26.0*	*24.3*	*22.9*	*23.6*	*5.3*	*3.8*	*13.3*	*12.6*	*12.6*	*10.3*	*12.2*	*24.8*	*22.7*	*36.4*	*24.2*	*23.4*
Ab	*66.5*	*58.7*	*67.6*	*73.4*	*76.3*	*75.9*	*49.8*	*28.1*	*86.1*	*86.8*	*66.5*	*89.7*	*87.8*	*74.7*	*77.3*	*63.6*	*75.2*	*76.6*
Or	*6.4*	*5.5*	*6.5*	*2.2*	*0.9*	*0.6*	*44.9*	*68.2*	*0.6*	*0.6*	*20.9*	*0.0*	*0.0*	*0.6*	*0.0*	*0.0*	*0.7*	*0.0*

Appendix 2.3.4: Cordierite compositions for Experiments by type:

	Type 1a:					Type 1b:					
Temp	Exp 1 1000	Exp 3 950	Exp 6 900	Exp 9 850	Exp 11 800	Exp 2 1000	Exp 4 950	Exp 7 900	Exp 10 850	Exp 12 800	Starting material
SiO_2	*49.99*	*50.59*	*49.61*	*50.12*	*50.56*	*50.12*	*50.36*	*50.09*	*49.69*	*50.38*	*49.80*
Al_2O_3	*32.17*	*31.96*	*31.41*	*32.19*	*32.20*	*32.09*	*32.06*	*32.04*	*31.51*	*32.44*	*31.96*
FeO	*8.09*	*8.64*	*8.64*	*8.76*	*8.81*	*7.52*	*8.18*	*8.31*	*8.17*	*8.37*	*8.23*
MgO	*8.03*	*7.94*	*7.77*	*7.82*	*7.89*	*8.48*	*8.41*	*8.33*	*8.09*	*8.43*	*8.09*
MnO	*0.53*	*0.50*	*0.48*	*0.48*	*0.47*	*0.30*	*0.21*	*0.31*	*0.32*	*0.34*	*0.26*
CaO	*0.00*	*0.00*	*0.00*	*0.00*	*0.00*	*0.00*	*0.00*	*0.00*	*0.00*	*0.00*	*0.00*
Na_2O	*0.30*	*0.00*	*0.33*	*0.50*	*0.36*	*0.00*	*0.26*	*0.27*	*0.38*	*0.32*	*0.45*
K_2O	*0.19*	*0.17*	*0.00*	*0.00*	*0.13*	*0.170*	*0.207*	*0.09*	*0.000*	*0.000*	*0.000*
Total	***99.30***	***99.79***	***98.24***	***99.88***	***100.41***	***98.68***	***99.69***	***99.44***	***98.16***	***100.29***	***98.78***
Si	*5.13*	*5.17*	*5.16*	*5.13*	*5.15*	*5.15*	*5.14*	*5.13*	*5.16*	*5.11*	*5.14*
AlIV	*0.87*	*0.83*	*0.84*	*0.87*	*0.85*	*0.85*	*0.86*	*0.87*	*0.84*	*0.89*	*0.86*
Σ T-site	*6.00*	*6.00*	*6.00*	*6.00*	*6.00*	*6.00*	*6.00*	*6.00*	*6.00*	*6.00*	*6.00*
AlVI	*3.03*	*3.01*	*3.00*	*3.01*	*3.01*	*3.03*	*3.00*	*2.99*	*3.01*	*2.99*	*3.02*
Fe^{3+}	*0.00*	*0.00*	*0.00*	*0.00*	*0.00*	*0.00*	*0.00*	*0.00*	*0.00*	*0.00*	*0.00*
Σ M-site	*3.03*	*3.01*	*3.00*	*3.01*	*3.01*	*3.03*	*3.00*	*2.99*	*3.01*	*2.99*	*3.02*
Fe2+	*0.70*	*0.74*	*0.75*	*0.75*	*0.75*	*0.65*	*0.70*	*0.71*	*0.71*	*0.71*	*0.71*
Mg	*1.23*	*1.21*	*1.20*	*1.19*	*1.20*	*1.30*	*1.28*	*1.27*	*1.25*	*1.28*	*1.24*
Mn	*0.05*	*0.04*	*0.04*	*0.04*	*0.04*	*0.03*	*0.02*	*0.03*	*0.03*	*0.03*	*0.02*
Σ A-site	*1.97*	*1.99*	*2.00*	*1.99*	*1.99*	*1.97*	*2.00*	*2.01*	*1.99*	*2.01*	*1.98*
Ca	*0.00*	*0.00*	*0.00*	*0.00*	*0.00*	*0.00*	*0.00*	*0.00*	*0.00*	*0.00*	*0.00*
Na	*0.06*	*0.00*	*0.07*	*0.10*	*0.07*	*0.00*	*0.05*	*0.05*	*0.08*	*0.06*	*0.09*
K	*0.02*	*0.02*	*0.00*	*0.00*	*0.02*	*0.02*	*0.03*	*0.01*	*0.00*	*0.00*	*0.00*
Σ Channel cations	*0.08*	*0.02*	*0.07*	*0.10*	*0.09*	*0.02*	*0.08*	*0.06*	*0.08*	*0.06*	*0.09*
Mg#	*64*	*62*	*62*	*61*	*62*	*67*	*65*	*64*	*64*	*64*	*64*

Appendix 2.3.4: Cordierite compositions for Experiments by type (*continued)*:

	Type 2:				Type 3:			
	Exp 15		Exp 16		Exp 19	Exp 18		Starting material
Temp	800		750		800	750		
	Core	**Rim/new**	**Core**	**Rim/new**		**Core**	**Rim/new**	
SiO_2	*50.46*	*49.70*	*49.28*	*47.68*	*49.25*	*50.21*	*48.72*	*49.89*
Al_2O_3	*32.47*	*33.17*	*31.82*	*31.82*	*31.78*	*32.47*	*32.18*	*32.36*
FeO	*8.23*	*5.15*	*8.55*	*9.41*	*8.80*	*9.13*	*9.95*	*8.77*
MgO	*8.46*	*10.47*	*7.88*	*7.12*	*7.75*	*7.87*	*7.33*	*7.66*
MnO	*0.34*	*0.00*	*0.44*	*0.64*	*0.47*	*0.47*	*0.30*	*0.55*
CaO	*0.00*	*0.12*	*0.00*	*0.26*	*0.00*	*0.00*	*0.21*	*0.00*
Na_2O	*0.00*	*0.57*	*0.49*	*0.83*	*0.32*	*0.44*	*0.66*	*0.60*
K_2O	*0.00*	*0.00*	*0.00*	*0.00*	*0.00*	*0.00*	*0.00*	*0.00*
Total	***99.96***	***99.61***	***98.45***	***97.75***	***98.38***	***100.59***	***99.35***	***99.83***
Si	*5.12*	*5.01*	*5.11*	*5.03*	*5.11*	*5.10*	*5.05*	*5.12*
AlIV	*0.88*	*0.99*	*0.89*	*0.97*	*0.89*	*0.90*	*0.95*	*0.88*
Σ T-site	*6.00*	*6.00*	*6.00*	*6.00*	*6.00*	*6.00*	*6.00*	*6.00*
AlVI	*2.99*	*2.95*	*3.00*	*2.99*	*3.00*	*2.99*	*2.98*	*3.03*
Fe^{3+}	*0.00*	*0.05*	*0.00*	*0.00*	*0.00*	*0.00*	*0.00*	*0.00*
Σ M-site	*2.99*	*2.99*	*3.00*	*2.99*	*3.00*	*2.99*	*2.98*	*3.03*
Fe2+	*0.70*	*0.43*	*0.74*	*0.83*	*1.20*	*0.78*	*0.86*	*0.75*
Mg	*1.28*	*1.57*	*1.22*	*1.12*	*0.76*	*1.19*	*1.13*	*1.17*
Mn	*0.03*	*0.00*	*0.04*	*0.06*	*0.04*	*0.04*	*0.03*	*0.05*
Σ A-site	*2.01*	*2.01*	*2.00*	*2.01*	*2.00*	*2.01*	*2.02*	*1.97*
Ca	*0.00*	*0.01*	*0.00*	*0.03*	*0.00*	*0.00*	*0.02*	*0.00*
Na	*0.00*	*0.11*	*0.10*	*0.17*	*0.06*	*0.09*	*0.13*	*0.12*
K	*0.00*	*0.00*	*0.00*	*0.00*	*0.00*	*0.00*	*0.00*	*0.00*
Σ Channel cations	*0.00*	*0.12*	*0.10*	*0.20*	*0.06*	*0.09*	*0.16*	*0.12*
Mg#	*65*	*78*	*62*	*57*	*61*	*61*	*57*	*61*

Appendix 2.3.5: Orthopyroxene and gedrite compositions for Experiments by type:

Orthopyroxene		Type 1a:	Type 1b:		Type 2:
	Exp 1	Exp 3	Exp 2	Exp 4	Exp 15
Temp	1000	950	1000	950	800
SiO_2	*48.67*	*45.97*	*50.51*	*43.27*	*46.30*
TiO_2	*0.53*	*0.71*	*1.14*	*2.83*	*0.64*
Al_2O_3	*7.62*	*10.51*	*7.77*	*14.58*	*14.59*
FeO	*28.12*	*30.25*	*23.92*	*25.58*	*23.02*
MgO	*15.09*	*11.33*	*16.34*	*13.90*	*13.81*
MnO	*0.42*	*0.47*	*0.20*	*0.23*	*0.46*
CaO	*0.32*	*0.56*	*0.25*	*0.20*	*0.42*
Na_2O	*0.00*	*0.00*	*0.41*	*0.00*	*0.99*
K_2O	*0.14*	*0.50*	*0.60*	*0.65*	*0.00*
Total	***101.10***	***100.28***	***101.14***	***101.25***	***100.22***
Si	*1.84*	*1.78*	*1.87*	*1.63*	*1.73*
Al^{IV}	*0.16*	*0.22*	*0.13*	*0.37*	*0.27*
Σ T-site	*2.00*	*2.00*	*2.00*	*2.00*	*2.00*
Al^{VI}	*0.18*	*0.26*	*0.21*	*0.27*	*0.37*
Ti	*0.02*	*0.02*	*0.03*	*0.08*	*0.02*
Fe^{2+}	*0.80*	*0.72*	*0.74*	*0.65*	*0.62*
Mg	*0.00*	*0.00*	*0.02*	*0.00*	*0.00*
Σ M1-site	*1.00*	*1.00*	*1.00*	*1.00*	*1.00*
Fe^{2+}	*0.09*	*0.26*	*0.00*	*0.16*	*0.10*
Mg	*0.85*	*0.65*	*0.88*	*0.78*	*0.77*
Mn	*0.01*	*0.02*	*0.01*	*0.01*	*0.01*
Ca	*0.01*	*0.02*	*0.01*	*0.01*	*0.02*
Na	*0.00*	*0.00*	*0.03*	*0.00*	*0.07*
K	*0.01*	*0.02*	*0.03*	*0.03*	*0.00*
Σ M2-site	*0.97*	*0.97*	*0.96*	*0.98*	*0.97*
Mg#	*49*	*40*	*55*	*49*	*52*

Gedrite	Type 2:	Type 3:	
	Exp 17	Exp 19	Exp 18
Temp	700	800	750
SiO_2	*45.69*	*44.64*	*42.94*
TiO_2	*0.15*	*0.71*	*0.42*
Al_2O_3	*18.04*	*15.36*	*16.11*
FeO	*16.86*	*23.25*	*26.79*
MgO	*14.69*	*11.93*	*8.83*
MnO	*0.28*	*0.42*	*0.85*
CaO	*0.54*	*0.73*	*0.90*
Na_2O	*3.69*	*1.24*	*1.02*
Total	***99.92***	***98.28***	***97.85***
Si (5-6)	*6.41*	*6.54*	*6.45*
Al^{IV} (3-2)	*1.59*	*1.46*	*1.55*
Σ T-site	*8.00*	*8.00*	*8.00*
Al^{VI}	*1.40*	*1.19*	*1.30*
Ti	*0.02*	*0.08*	*0.05*
Cr	*0.00*	*0.00*	*0.00*
Σ XX-site (0-2)	*1.41*	*1.27*	*1.34*
Fe^{2+}	*1.98*	*2.85*	*3.36*
Mg	*3.07*	*2.60*	*1.98*
Mn	*0.03*	*0.05*	*0.11*
Σ M-site (6-4)	*5.09*	*5.50*	*5.45*
Ca	*0.08*	*0.11*	*0.15*
Na	*1.00*	*0.35*	*0.30*
Σ A-site (2)	*1.09*	*0.47*	*0.44*
Cation Sum	*15.58*	*15.24*	*15.23*
Mg#	*61*	*48*	*37*

Appendix 2.3.6: Average compositions of glasses (quenched melts) for Experiments by type:

	Type 1a				Type 1b				Type 2		Type 3	
Exp:	1	3	6	9	2	4	7	10	15	16	19	18
Temp	1000	950	900	850	1000	950	900	850	800	750	800	750
Average:												
SiO_2	68.64	-	71.69	69.78	64.50	68.36	70.68	68.05	66.78	69.88	69.05	67.80
TiO_2	0.37	-	0.03	0.12	0.25	0.32	0.02	0.00	0.02	0.00	0.31	0.02
Al_2O_3	14.01	-	15.00	14.89	16.53	13.86	14.93	14.56	15.57	15.09	14.71	14.15
FeO	2.09	-	1.61	1.94	0.99	2.19	1.44	1.23	1.91	1.63	2.02	1.57
MnO	0.00	-	0.00	0.00	0.00	0.00	0.00	0.00	0.01	0.02	0.00	0.02
MgO	1.08	-	0.40	0.54	0.67	0.39	0.27	0.06	1.08	0.37	0.48	0.37
CaO	0.80	-	0.62	0.83	0.26	0.67	0.66	0.59	1.98	1.85	1.96	1.27
Na_2O	2.45	-	3.28	3.64	5.18	2.35	2.87	3.00	2.98	3.16	2.77	3.53
K_2O	4.20	-	4.55	3.20	3.69	5.74	4.70	4.50	1.93	1.05	2.68	1.48
Total	93.64	-	97.18	94.95	92.50	93.87	95.57	92.00	92.26	93.05	93.70	90.22
H_2O	6.36	-	2.82	5.05	7.50	6.13	4.43	8.00	7.74	6.95	6.30	9.78
N	4	0	6	6	11	7	8	5	13	8	12	8
CIPW norm												
Quartz	36	-	33	34	20	31	35	34	38	45	39	41
Plagioclase	26	-	32	37	49	25	29	31	38	39	35	40
Orthoclase	27	-	28	20	24	36	29	29	12	7	17	10
Corundum	4	-	4	4	4	3	4	4	5	6	4	5
Hypersthene	6	-	4	5	3	5	3	3	7	4	5	4
Ilmenite	1	-	0	0	1	1	0	0	0	0	1	0
K:Na	1.13	-	0.91	0.58	0.47	1.61	1.08	0.99	0.43	0.22	0.64	0.28
Mg#	48	-	31	33	55	24	25	8	50	29	30	30
ASI	1.40	-	1.31	1.36	1.27	1.23	1.36	1.34	1.47	1.56	1.34	1.45

Appendix 3: LA-ICP-MS

Appendix 3.1. Standard reference material BHVO-2G is used to determine the quality of the LA-ICP-MS data for the trace element composition of garnet.

Element	Certified value	Repl 1	Repl 2	Repl 3	Average	RSD (%)
Sc	**32.86**	36.4	35.9	39.5	37.3	5.2
Ti	**16 239**	17 220	17 210	18 440	17 623	4.0
V	**308.00**	318.0	311.0	362.3	330.4	8.4
Cr	**293.33**	295.0	306.2	324.5	308.6	4.8
Co	**44.25**	53.7	48.9	50.5	51.0	4.8
Ni	**116.33**	126.4	105.6	125.8	119.3	9.9
Cu	**127.40**	175.3	171.2	176.8	174.4	1.7
Zn	**115.03**	124.6	105.2	115.5	115.1	8.4
Ga	**22.18**	22.7	22.4	23.1	22.7	1.5
Rb	**9.18**	9.7	9.2	9.8	9.6	3.2
Sr	**390.80**	346.0	340.7	359.2	348.6	2.7
Y	**25.79**	25.7	25.3	26.6	25.9	2.5
Zr	**168.60**	171.4	175.5	177.0	174.6	1.7
Nb	**18.28**	16.8	17.5	17.8	17.4	2.9
Ba	**125.00**	114.4	117.9	119.3	117.2	2.2
La	**15.40**	14.1	14.2	14.6	14.3	2.1
Ce	**36.91**	33.2	32.3	33.9	33.1	2.4
Pr	**5.35**	4.8	5.1	4.9	4.9	2.9
Nd	**24.48**	23.9	24.5	26.8	25.0	6.3
Sm	**6.05**	5.8	5.9	6.1	6.0	2.4
Eu	**2.48**	1.9	2.0	2.1	2.0	5.8
Gd	**6.09**	5.9	6.9	6.6	6.5	8.1
Tb	**0.92**	0.9	0.9	0.9	0.9	1.9
Dy	**5.23**	5.5	5.2	6.1	5.6	8.1
Ho	**0.98**	1.0	1.1	1.0	1.0	6.0
Er	**2.48**	2.5	2.6	2.6	2.6	2.8
Tm	**0.34**	0.3	0.4	0.3	0.3	6.5
Yb	**2.02**	2.0	2.0	2.4	2.1	9.4
Lu	**0.28**	0.3	0.3	0.2	0.3	**17.3**
Hf	**4.32**	4.1	4.4	4.3	4.3	3.5
Ta	**1.15**	1.0	1.1	1.1	1.1	4.6
Pb	**1.81**	8.1	6.6	7.7	7.5	9.9
Th	**1.22**	1.2	1.4	1.2	1.3	6.1
U	**0.42**	0.4	0.4	0.4	0.4	5.5

Appendix 3.2: LA-ICP-MS results of several analyses on the same poikilitic garnet with average, standard deviation as well as maximum and minimum values.

	Garnet 1	Garnet 5	Garnet 6	Garnet 8	Garnet 9	Garnet 10	Garnet 13	Garnet 15	Garnet 17	Garnet 19	Garnet 20	garnet spot 1	garnet spot 2	garnet spot 4	garnet spot 5		Average	RSD (%)	MAX	MIN
Sc	205.100	247.500	254.400	189.900	236.100	199.800	221.500	197.300	231.600	269.600	208.500	274.100	260.000	249.300	253.000	**Sc**	*233.180*	*11.938*	*274.100*	*189.900*
Ti	53.110	42.140	47.510	57.450	88.850	66.460	74.030	39.310	57.940	52.640	64.940	52.720	82.920	75.510	46.190	**Ti**	*60.115*	*24.834*	*88.850*	*39.310*
V	70.270	69.040	77.110	74.870	89.420	79.250	74.270	76.920	74.280	72.090	72.590	72.630	73.280	83.190	72.800	**V**	*75.467*	*6.945*	*89.420*	*69.040*
Cr	156.000	185.900	191.000	146.800	206.400	191.700	165.400	147.000	167.100	181.800	145.400	150.400	172.300	177.400	152.000	**Cr**	*169.107*	*11.487*	*206.400*	*145.400*
Co	21.170	22.840	19.470	20.870	24.110	23.330	25.070	24.780	26.490	20.710	24.290	21.910	20.760	21.780	23.270	**Co**	*22.723*	*8.713*	*26.490*	*19.470*
Ni	0.000	0.901	0.000	0.000	0.000	0.000	2.862	0.499	0.000	3.794	0.000	0.292	0.000	0.000	0.000	**Ni**	*0.557*	*209.795*	*3.794*	*0.000*
Cu	8.639	12.880	9.022	9.318	9.314	6.692	10.100	7.394	9.445	10.430	8.973	5.812	6.951	7.170	6.496	**Cu**	*8.576*	*21.597*	*12.880*	*5.812*
Zn	72.490	71.890	73.500	66.900	92.290	90.670	98.230	90.940	100.200	62.600	85.630	84.480	80.840	87.970	96.090	**Zn**	*83.648*	*14.069*	*100.200*	*62.600*
Ga	11.660	12.590	12.990	10.660	11.030	11.830	12.200	11.480	11.920	11.760	11.980	12.800	12.340	12.280	11.980	**Ga**	*11.967*	*5.191*	*12.990*	*10.660*
Rb	0.411	0.258	0.382	0.392	0.365	0.319	0.393	0.330	0.459	0.426	0.396	0.300	0.273	0.445	0.280	**Rb**	*0.362*	*17.842*	*0.459*	*0.258*
Sr	1.869	1.872	1.878	1.989	1.956	1.978	1.977	2.375	2.201	2.106	1.876	1.851	1.834	1.863	1.849	**Sr**	*1.965*	*7.837*	*2.375*	*1.834*
Y	464.400	330.100	371.000	814.200	464.200	429.500	355.600	298.100	396.900	297.100	305.000	410.000	431.400	890.500	403.200	**Y**	*444.080*	*39.508*	*890.500*	*297.100*
Zr	19.670	17.290	69.600	26.560	19.160	18.890	16.750	15.270	20.500	14.610	15.600	19.850	20.300	30.010	20.410	**Zr**	*22.965*	*58.916*	*69.600*	*14.610*
Ba	0.144	0.326	0.125	0.079	0.227	0.054	0.514	0.028	0.110	0.163	0.173	0.094	0.045	0.050	0.048	**Ba**	*0.145*	*89.197*	*0.514*	*0.028*
La	0.004	0.000	1.221	1.445	0.000	0.019	0.394	0.000	0.004	0.007	0.112	0.407	0.013	0.002	0.000	**La**	*0.242*	*192.460*	*1.445*	*0.000*
Ce	0.102	0.036	2.970	1.331	0.037	0.007	0.097	0.092	0.165	0.000	0.392	0.740	0.001	0.000	0.000	**Ce**	*0.398*	*201.194*	*2.970*	*0.000*
Pr	0.048	0.080	0.320	0.186	0.018	0.021	0.023	0.072	0.016	0.026	0.045	0.112	0.021	0.015	0.017	**Pr**	*0.068*	*123.992*	*0.320*	*0.015*
Nd	0.082	0.024	1.088	0.729	0.095	0.106	0.047	0.020	0.079	0.066	0.237	0.863	0.140	0.102	0.098	**Nd**	*0.252*	*136.206*	*1.088*	*0.020*
Sm	0.670	0.503	0.475	0.731	0.591	0.305	0.364	0.267	0.670	0.209	0.491	0.595	0.457	0.953	0.332	**Sm**	*0.507*	*39.399*	*0.953*	*0.209*
Eu	0.000	0.000	0.000	0.006	0.003	0.022	0.000	0.047	0.000	0.000	0.000	0.032	0.011	0.050	0.000	**Eu**	*0.011*	*156.556*	*0.050*	*0.000*
Gd	7.299	3.553	4.284	10.440	5.731	5.349	6.099	4.726	5.859	5.463	4.736	6.252	5.943	11.750	5.828	**Gd**	*6.221*	*35.113*	*11.750*	*3.553*
Tb	4.101	2.266	2.686	6.454	3.447	3.266	3.278	2.900	3.330	2.875	3.050	3.634	3.865	6.976	3.601	**Tb**	*3.715*	*35.175*	*6.976*	*2.266*
Dy	57.370	35.460	43.050	96.000	54.230	49.060	45.170	38.440	49.030	37.800	40.730	52.710	50.870	108.600	51.220	**Dy**	*53.983*	*38.500*	*108.600*	*35.460*
Ho	18.760	12.450	14.510	33.590	19.150	16.960	13.480	11.480	15.510	11.200	11.920	15.510	16.470	36.460	16.010	**Ho**	*17.564*	*42.817*	*36.460*	*11.200*
Er	68.550	54.960	58.750	140.300	78.860	70.670	50.070	40.580	57.430	39.350	40.850	56.440	64.950	151.100	56.310	**Er**	*68.611*	*48.544*	*151.100*	*39.350*
Tm	11.430	11.230	10.950	25.070	14.020	12.890	8.320	6.831	9.198	6.414	6.404	9.218	10.560	26.810	9.301	**Tm**	*11.910*	*51.401*	*26.810*	*6.404*
Yb	75.180	89.150	77.490	173.800	97.840	91.430	51.390	44.500	61.540	40.810	40.900	62.160	74.230	184.100	60.800	**Yb**	*81.688*	*53.118*	*184.100*	*40.810*
Lu	11.540	15.820	12.700	27.510	17.050	15.330	8.529	6.610	9.887	5.939	6.132	9.496	11.340	29.940	9.747	**Lu**	*13.171*	*54.531*	*29.940*	*5.939*
Hf	0.454	0.360	1.704	0.456	0.648	0.392	0.458	0.395	0.575	0.360	0.343	0.558	0.486	0.758	0.504	**Hf**	*0.563*	*59.633*	*1.704*	*0.343*
Ta	0.021	0.010	0.007	0.091	0.037	0.016	0.014	0.010	0.050	0.011	0.014	0.012	0.012	0.013	0.013	**Ta**	*0.022*	*101.391*	*0.091*	*0.007*
Pb	3.945	3.325	4.283	3.602	4.973	2.655	5.656	3.639	4.970	5.122	5.057	2.479	2.646	2.968	3.269	**Pb**	*3.906*	*26.726*	*5.656*	*2.479*
Th	0.024	0.110	0.364	0.885	0.029	0.000	0.070	0.059	0.010	0.000	0.027	0.195	0.009	0.000	0.000	**Th**	*0.119*	*196.754*	*0.885*	*0.000*
U	0.001	0.035	0.218	0.121	0.004	0.186	0.000	0.000	0.000	0.078	0.016	0.103	0.009	0.002	0.000	**U**	*0.052*	*142.293*	*0.218*	*0.000*

Appendix 3.3: Chondrite REE composition used for normalisation of garnet trace element data.

CHONDRITE	
Element	Concentration (ppm)
La	4.22
Ce	1.63
Pr	10.78
Nd	2.19
Sm	6.76
Eu	17.76
Gd	5.03
Tb	27.70
Dy	4.07
Ho	18.32
Er	6.25
Tm	40.49
Yb	6.21
Lu	40.65

Gutta cavat lapidem non bis, sed saepe cadendo; sic homo fit sapiens bis non, sed saepe legendo.

"A drop drills a rock by falling not twice, but many times; so too is a human made smart by reading not two, but many books"

(Giordano Bruno).